

Unclassified

USC-110-93-207

2

AD-A265 120



Project Report  
STK-206  
Volume I

DTIC  
ELECTE  
MAY 27 1993  
S C D

## Proceedings of the 1993 Space Surveillance Workshop

R.W. Miller  
R. Sridharan  
Editors

30 March-1 April 1993

**Lincoln Laboratory**  
MASSACHUSETTS INSTITUTE OF TECHNOLOGY  
LEXINGTON, MASSACHUSETTS



Prepared with partial support of the Department of the Air Force  
under Contract F19628-90-C-0002.

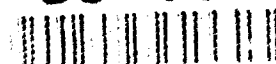
Approved for public release; distribution is unlimited.

Reproduced From  
Best Available Copy

93 5 26 027

Unclassified

93-11884



Prepared with partial support of the Department of the Air Force under Contract F19628-90-C-0002.

This report may be reproduced to satisfy needs of U.S. Government agencies.

The ESC Public Affairs Office has reviewed this report, and it is releasable to the National Technical Information Service, where it will be available to the general public, including foreign nationals.

This technical report has been reviewed and is approved for publication.

FOR THE COMMANDER



Gary Tutungian  
Administrative Contracting Officer  
Directorate of Contracted Support Management

Non-Lincoln Recipients

PLEASE DO NOT RETURN

Permission is given to destroy this document  
when it is no longer needed.

100-44203

# PROCEEDINGS OF THE 1993 SPACE SURVEILLANCE WORKSHOP

30 MARCH-1 APRIL 1993

Approved for public release; distribution is unlimited.

MASSACHUSETTS

**Unclassified**

Accession For	
NTIS CRA&I	<input checked="" type="checkbox"/>
DTIC TAB	<input type="checkbox"/>
Unannounced	<input type="checkbox"/>
Justification	
By	
Distribution /	
Availability Codes	
Dist	Avail and/or Special
A-1	

## PREFACE

The eleventh Annual Space Surveillance Workshop sponsored by MIT Lincoln Laboratory will be held 30-31 March and 1 April 1993. The purpose of this series of workshops is to provide a forum for the presentation and discussion of space surveillance issues.

This *Proceedings* documents most of the presentations from this workshop. The papers contained were reproduced directly from copies supplied by their authors (with minor mechanical changes where necessary). It is hoped that this publication will enhance the utility of the workshop.

Dr. R. Sridharan  
1992 Workshop Chairman

Dr. R. W. Miller  
Co-chair



## TABLE OF CONTENTS

The Maui Space Surveillance Site Infrared Calibration Sources <i>Daron L. Nishimoto, Kenneth E. Kissell, John L. Africano and John V. Lambert - Rockwell International Paul W. Kervin - Phillips Laboratory</i>	1
Infrared Detection of Geosynchronous Objects at AMOS <i>J.K. Lee, Phillips Laboratory and D.L. Nishimoto - Rockwell International</i>	11
LWIR Observations of Geosynchronous Satellites <i>W.P. Seniw - MIT Lincoln Laboratory</i>	21
LAGEOS-2 Launch Support Navigation at JPL <i>T.P. McElrath, K.E. Criddle, and G.D. Lewis - Jet Propulsion Laboratory</i>	31
Space Surveillance Network Sensor Contribution Analysis <i>G.T. DeVere - Nichols Research Corporation</i>	33
NMD-GBR: New X-Band Sensors at Sites in CONUS and USAKA for Space Surveillance <i>J. Krasnakevich, D. Greeley, D. Rypysc, F. Steudel - Raytheon D. Sloan - GPALS PEO; D. Mathis, Teledyne Brown Engineering</i>	39
Recent Improvements at ALTAIR <i>R.B. McSheehy, S.J. Chapman - MIT Lincoln Laboratory R.M. Anderson - GTE Government Systems</i>	49
Enhancements to the ALCOR Imaging Radar <i>R.K. Avent, C.H. Moulton, M.D. Abouzahra - MIT Lincoln Laboratory</i>	57
Fiber Optic Phase Control of the Lake Kickapoo NAVSPASUR Transmitter <i>T.L. Washington and A.A. Bocz - Scientific Research Corp. C.C. Hayden - Naval Space Surveillance Center</i>	65
Coherent Data Recording and Signal Processing Capabilities at Ascension FPQ-15 Radar for Space Surveillance Applications <i>E.T. Fletcher, J.B. Neiger, P.A. Jones, D.B. Green - XonTech, Inc. J.D. Mercier - Phase IV Systems, Inc.</i>	73
Forecasting Trans-Ionospheric Effects to Improve Space Surveillance <i>M.M. Partington - Air Force Space Forecast Center (AWS) G.J. Bishop - Phillips Laboratory</i>	83

Sensor Tasking by the Space Defense Operations Center <i>P.R. Cherry - Loral Command &amp; Control Systems</i>	93
Expert Systems for Sensor Tasking <i>T.D. Tiefenbach - Nichols Research Corp.</i>	99
Pages 109 to 118 have been left intentionally blank	
Tracking Data Reduction for the Geotail, Mars Observer, and Galileo Missions <i>R.L. Mansfield - Loral Command &amp; Control Systems</i>	119
Interferometric Synthetic Aperture Radar Applied to Space Object Identification <i>I. Wynne-Jones - EDS-Scicon Defence plc</i>	125
Pages 135 to 142 have been left intentionally blank	
The Passive Imaging Systems at the Air Force Maui Optical Station's (AMOS) 1.6m Telescope <i>Capt. A.H. Suzuki and Capt. M. VonBokern - Phillips Laboratory</i>	143
All Source Satellite Evaluation Tool <i>G.D. Conner and K. Wilson - Booz-Allen &amp; Hamilton</i> <i>R.D. Oldach - Joint National Intelligence Development Staff</i>	151
Orbital Debris Environment Characteristics Obtained by Means of the Haystack Radar <i>T.E. Tracy, E.G. Stansbery, M.J. Matney, J.F. Stanley - NASA</i>	159
A Study of Systematic Effects in Eglin (AN/FPS-85) RCS Data <i>K.G. Henize - NASA</i> <i>P.D. Anz-Meador and T.E. Tracy - Lockheed</i>	179
Debris Correlation Using the Rockwell WorldView Simulation System <i>M.F. Abernathy, J. Houchard, M.G. Puccetti, J.V. Lambert - Rockwell International</i>	189
Orbital Debris Correlation and Analysis at the Air Force Maui Optical Station (AMOS) <i>R.K. Jessop, J. Africano, J.V. Lambert, R. Rappold and K.E. Kissell - Rockwell International</i> <i>R. Medrano and P. Kervin - Phillips Laboratory</i>	197
Real Time Orbit Determination of Orbital Space Debris <i>S.D. Kuo - Phillips Laboratory</i>	205

**Panel Discussion Session**

Surveillance for Comets and Asteroids Potentially Hazardous to the Earth	213
<i>B.G. Marsden - Harvard-Smithsonian Center for Astrophysics</i>	

Pages 219 to 228 have been left intentionally blank

Signal Processing and Interference Mitigation Strategies in NASA's High Resolution Microwave Survey Project Sky Survey	229
<i>G.A. Zimmerman, E.T. Olsen, S.M. Levin, C.R. Backus, M.J. Grimm, S. Gulkis, and M.J. Klein - Jet Propulsion Laboratory</i>	

## THE MAUI SPACE SURVEILLANCE SITE INFRARED CALIBRATION SOURCES

Daron Nishimoto and Kenneth E. Kissell  
Rockwell Power Systems  
535 Lipoa Parkway, Suite 200  
Kihei, Hawaii 96753

John L. Africano and John V. Lambert  
Rockwell International Corporation  
1250 Academy Park Loop, Suite 130  
Colorado Springs, Colorado 80910-3766

Paul W. Kervin  
Phillips Laboratory  
535 Lipoa Parkway, Suite 200  
Kihei, Hawaii 96753

**BACKGROUND.** In the late 1960's the Air Force Maui Optical Station (AMOS) was opened on Mt. Haleakala to support studies of earth satellites and missiles launched within the Pacific Missile Range. The AMOS Observatory was provided with then state-of-the-art telescope and sensor systems for remote sensing of brightness, color, and trajectory, and resolved imaging of space targets. Several generations of visible and infrared sensors have been installed, tested, and replaced on the 1.6-meter and dual mounted 1.2-meter telescopes, but in the early 1980's it was decided to freeze the sensor suite on the twin 1.2-meter mount and operate it as a standard data acquisition device for the Colorado Springs-based Air Defense Command and North American Aerospace Defense Command, now operating as the Air Force Space Command. This electro-optical addition to the radars and tracking cameras was renamed the Maui Optical Tracking and Identification Facility (MOTIF).

This transition required standardization not only of the instrument configurations but of the stellar calibration procedures, and the archiving of measurement data, including selected calibration information. When the Rockwell Corporation assumed the operation and maintenance of the Maui facilities in 1990, the authors undertook a review of the archived data to look for evidence of aging, filter drift, etc., effects which one might expect in what had been pioneering technologies. Our results indicate that the system has remained stable, and uncovered several nuggets of astronomical data captured within the calibration files. The system, built by Hughes in 1973 and installed on the 1.2-meter telescope in 1974, has remained unchanged since 1980 when the surviving calibration records begin. The instrument is used almost every night for IR radiometry of space objects and calibration stars. The calibration mode of operation employs limited

integration (data are recorded at 50 Hz with a smoothing filter with a time constant of 0.3 seconds). Only 23 bright reference stars are used for calibration. These stars are listed in Table I along with a total number of data points collected and the assigned stellar temperature. Typically an N-band equivalent filter has been used for the observations, and all of the data are archived. It should be noted that the radiometer operates in a chopped mode with a 50-Hz nodding secondary, and the target image moves sequentially back-and-forth from the corner of four adjacent detectors for quadrant tracking to the center of the measuring detector.

## SENSOR DESCRIPTION

Purpose: The Advanced Multicolor Tracker for AMOS (AMTA) was built to provide a day/night capability for acquisition and tracking of space objects and for estimating the object's effective temperature over a range from 200°K to 3000°K. The tracker consists of an array of 25 cadmium-doped germanium (Ge: Cd) photoconductive detectors in a 5x5 pattern at the focus of the 1.2-meter f/20 telescope. The detector array, at a temperature of 12°K, lies behind a set of square light pipes to assure nearly 100% fill factor into the detector configuration. AMTA provides a background-limited performance over the 3 micron to 22 micron spectral region in seven filter bands. The system is calibrated against well-known stellar sources as well as against a standard black-body source injected into a sub-aperture of the primary mirror. Within each filter band, the differential signal at the quadrant detector half-cycle provides an auto-guiding signal as well as the sky/mirror-emission subtraction signal. AMTA can detect and auto-guide on non-solar illuminated targets or daylight targets obscured in the visible by the bright sky or by thin cirrus for measurement of metric position of targets (orbit determination) and radiometric data. For these reasons, we have used bright IR variable stars as part of our metric and bolometric calibrations.

Through observation of a space target with the AMTA in a single band, it is possible to deduce the dynamic motion of the target (stable, periodic tumbling, slow instability) and to infer size from assumptions using Stefan's law. If the target signature is stable or suitably repetitive, the filter bands can be cycled such that color ratios can be used to estimate the temperature and obtain better size estimates. Even object shape and rotation axis can at times be inferred, but frequently other data such as visual-band photometry or resolved imaging are also available to allow synergistic analyses.

This paper will only be concerned with the measurements of stellar reference sources made for AMTA calibration over more than a decade of routine service.

Calibration: The following technique was used to determine the 10.6 micron stellar magnitudes. The stars are assumed to be black body radiators, each with an assigned constant temperature.

The aperture irradiance,  $I_{ap}$  is calculated as

$$I_{ap} = RV_s$$

where:

$R$  = responsivity determined from the standard black body source calibration

$V_s$  = object signal - background signal

The exoatmospheric irradiance  $I_{exo}$  is calculated as

$$I_{exo} = \frac{I_{ap}}{T}$$

where:

$T$  = atmospheric transmittance

The atmospheric transmittance is calculated by

$$T = \frac{\int_0^\infty P(\lambda, t) S(\lambda) T(\lambda) d\lambda}{\int_0^\infty P(\lambda, t) S(\lambda) d\lambda}$$

where:

$P(\lambda, t)$  = Planck function at stellar temperature,  $t$

$S(\lambda)$  = system spectral response

$T(\lambda)$  = atmospheric transmittance model (LOWTRAN 5)

The exoatmospheric irradiance,  $I_{exo}$  is converted to an AMOS 10.6 micron stellar magnitude,  $M(N)$  by

$$\text{AMOS } M(N) = -2.5 \log \frac{I_{exo} K}{I_0 \Delta\lambda}$$

where:

$$K = \left( \frac{\lambda_c}{10.6} \right)^5 \left[ \frac{e^{\left( \frac{1.4388}{\lambda_c t} \right)} - 1}{e^{\left( \frac{1.4388}{10.6 t} \right)} - 1} \right]$$

$I_0$  = 10.6 micron 0th magnitude reference irradiance

$\Delta\lambda$  = effective square bandwidth of AMTA filter

$\lambda_c$  = effective center wavelength of AMTA filter

$T$  = stellar temperature

Both  $\lambda_c$  and  $\Delta\lambda$  are functions of temperature. The effective central wavelength  $\lambda_c$  is found by

$$\int_0^{\lambda_c} P(\lambda, t) S(\lambda) d\lambda = \frac{1}{2} \int_0^{\infty} P(\lambda, t) S(\lambda) d\lambda$$

and the effective square bandwidth  $\Delta\lambda$  is found by

$$\int_{\lambda_c - \Delta\lambda/2}^{\lambda_c + \Delta\lambda/2} P(\lambda, t) d\lambda = \int_0^{\infty} P(\lambda, t) S(\lambda) d\lambda$$

The above procedure does not measure atmospheric extinction, but calculates an atmospheric transmittance as a function of the elevation of the object. This procedure also determines all magnitudes relative to a local blackbody source instead of referencing the observation to astronomical standard stars. The procedure also assumes a constant stellar temperature, i.e., stellar temperature variability was not taken into account. The resulting data set does provide a unique astronomical resource: twelve years of nightly 10.6-micron observations made with the same detector, filters, and telescope; referenced to a laboratory standard blackbody; and reduced using consistent procedures.

### Light Curves:

Light curves are presented for four stars, two variable and two standard stars in Figures 1 through 4. The light curves have been standardized to a range of three magnitudes for the y-axis, and the x-axis covers 5000 days (JD 44000-49000) for direct comparison. The light curves are noisy by astronomical standards. As an operational Space Command asset, we are required to operate even under less than optimum sky conditions. Only a few wildly discrepant data points were removed, those falling outside of the graph boundary. Otherwise no attempt has been made to edit the data.

The data for each star were analyzed using a period-finding routine based upon the published subroutine PERIOD from Press and Teukolsky 1988. Figures 1B and 2B present the light curves as a function of phase. For each star the first data point is assumed to be at phase 0.0 and the remainder of the data are normalized with respect to the calculated period.

Examining the light curves and phase diagrams for all of the variable stars, we find that cycle to cycle differences do occur and there are humps on the rising branch for several of the stars. Table II summarizes the results, ordering the stars by variability and listing the calculated period, peak to

peak amplitude variations, and any comments.

#### Calibration Stars:

As can be seen from Figures 1, 2 and Table II, care must be taken when choosing stars for calibration. One cannot just choose the brightest stars especially in the infrared since most of these objects are long period variable stars. Table I identified Alpha Her and eight other stars which can be used as calibration objects. Studies from the Infrared Astronomical Satellite (IRAS) observations identified a class of stars, Autoclass 23/delta 0 (NASA Reference Publication 1217) which contain stars similar to and including Alpha Her and Alpha Lyr. This class contains 256 stars of which 2% are variable and 73% are probably constant to  $< .3$  magnitudes. Many suitable calibration stars can be obtained from this class of stars.

#### Summary:

We have identified a source list for several hundred possible infrared calibration objects. Data on these new possible calibration stars and stars listed in Table I, will continue to be collected and archived for the foreseeable future, although improvements in data reduction may reduce the scatter without biasing the data integrity. We will be sharing these data with other workers in the long-period variable field who have spectral or brightness measurements at other wavelengths during this decade plus of observation, or may wish to plan some future observing campaign with one or more of these stars.



**Table I**  
**AMOS 10.6 micron Stellar Observation Summary**  
**April 1980 - May 1992**

<u>STAR</u>	<u>Number of Observations</u>	<u>Mean AMOS N Magnitude</u>	<u>Assumed Temperature Deg. K</u>	<u>Figure No.</u>
R AND	48	-2.64	4000	*
Beta AND <sup>1</sup>	145	-2.01	2200	*
Mira	1037	-4.74	4000	1
Alpha TAU <sup>1</sup>	1429	-2.98	3300	*
ALPHA AUR <sup>1</sup>	161	-1.87	6300	*
Alpha ORI <sup>1</sup>	1302	-5.16	500	*
Beta GEM <sup>1</sup>	10	-1.24	10000	*
R CNC	16	-2.24	4000	*
R LEO	1044	-4.29	4000	*
R HYA	1093	-3.83	4000	*
Alpha BOO <sup>1</sup>	1529	-3.09	3700	3
Alpha SCO <sup>1</sup>	1285	-4.59	1000	*
Alpha HER <sup>1</sup>	1409	-3.85	1500	4
CHI CYG	1267	-3.92	4000	2
MU CEP	1336	-3.89	4000	*
Beta PEG <sup>1</sup>	743	-2.45	1800	*
R AQR	66	-3.74	4000	*
VY CMA	776	-5.95	600	*
CW LEO	224	-7.25	650	*
RW LMI	556	-4.48	4000	*
NMLC	994	-5.14	500	*
V HYA	338	-3.76	4000	*
R CAS	360	-4.11	4000	*

<sup>1</sup>These stars should be used as calibration sources since their variability <.3 magnitude.

\*Not reported

**Table II**  
**Summary of Observations**

<u>STAR</u>	<u>Period Days</u>	<u>Peak to Peak Variations AMOS N Magnitude</u>	<u>Comments</u>
R LEO	313.98	.3	possible hump
R. HYA	396.5/347.9	.3	possible hump
V HYA	530.3	.3	
MU CEP	864.78	.3	
VY CMA	No Period Found	.3	
NMLC	942.03	.4	
CHI CYG	406.67	.6	hump lasting .2 period
MIRA	332.61	.8	
R CAS	430.8	.9	possible cycle-to-cycle shape change
RW LMI	623.55	.9	
CW LEO	640.	1.0	long slow decline to minimum light, fast recovery to maximum light

FIGURE 1A: MIRA

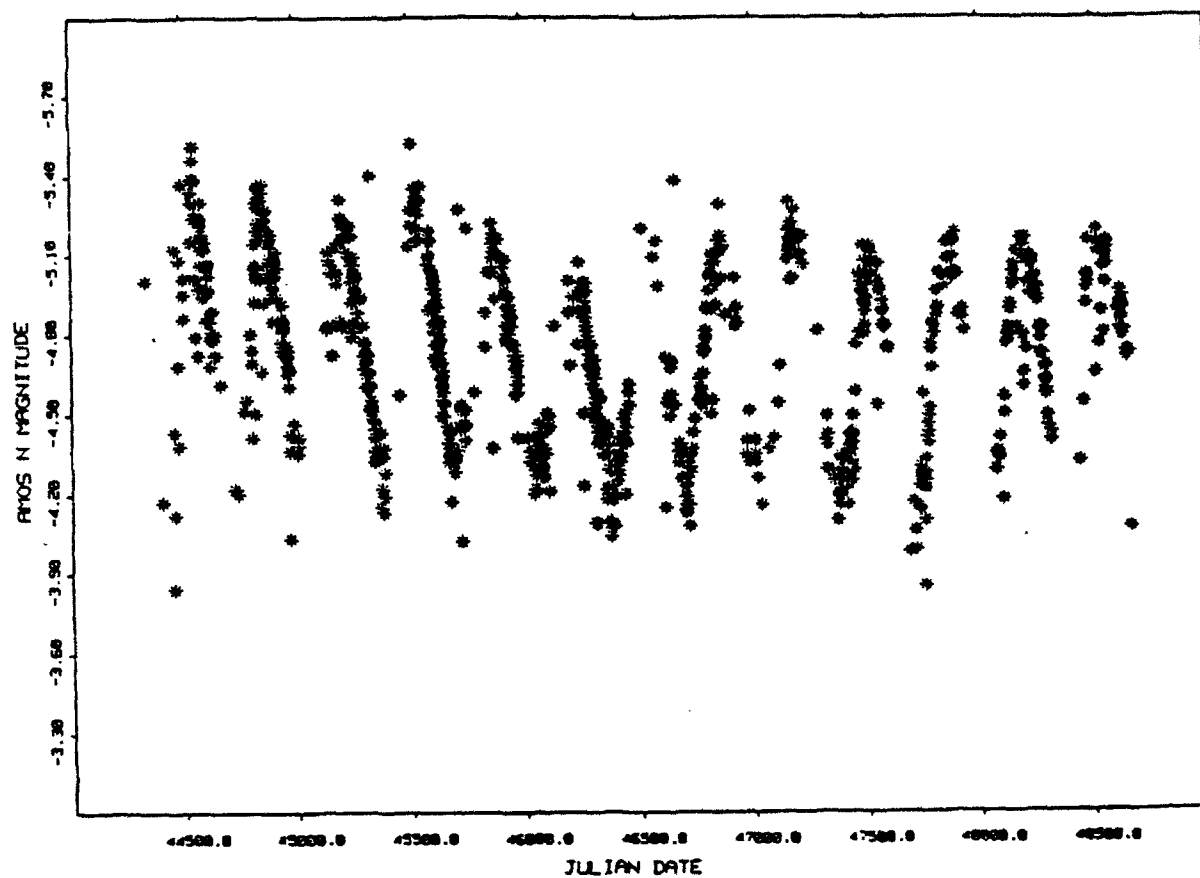


FIGURE 1B: MIRA 332.61 DAY PERIOD

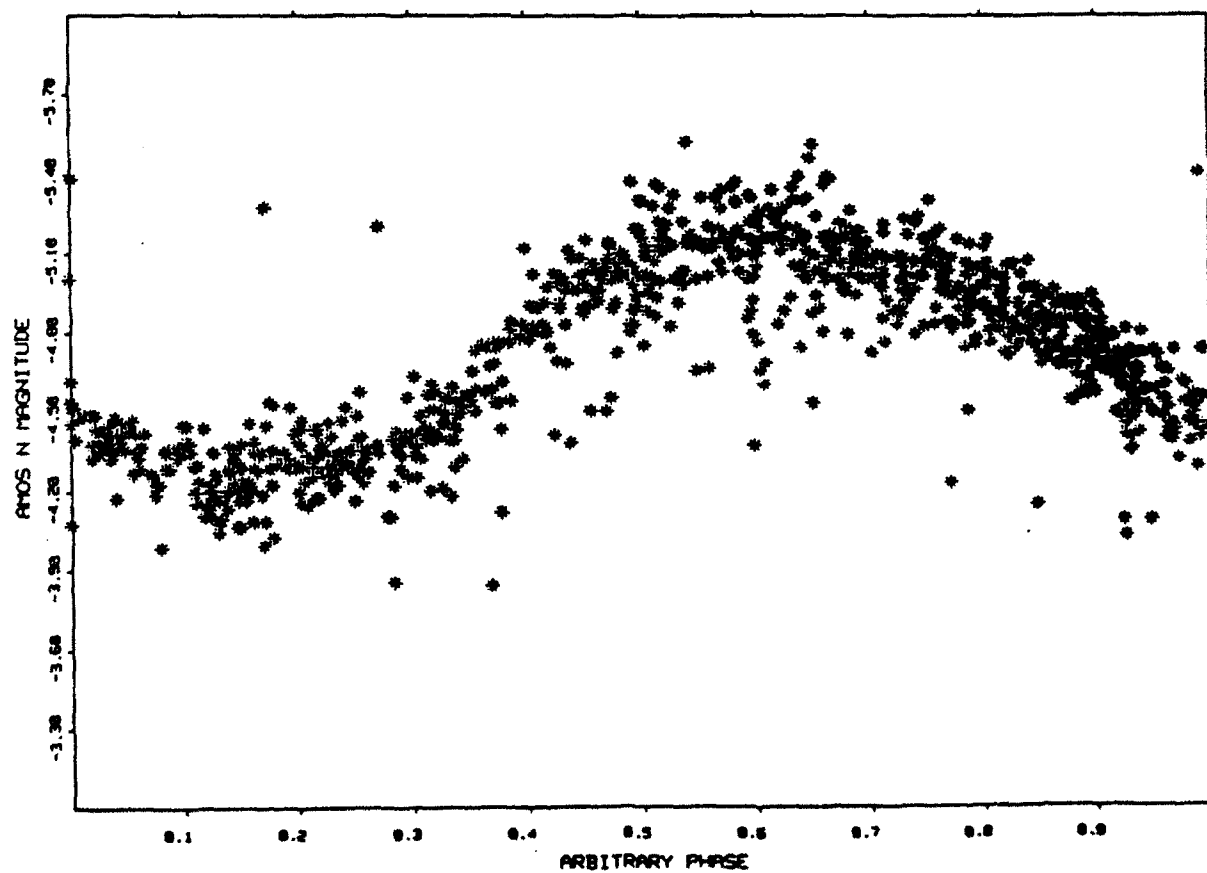


FIGURE 2A: CHI CYG

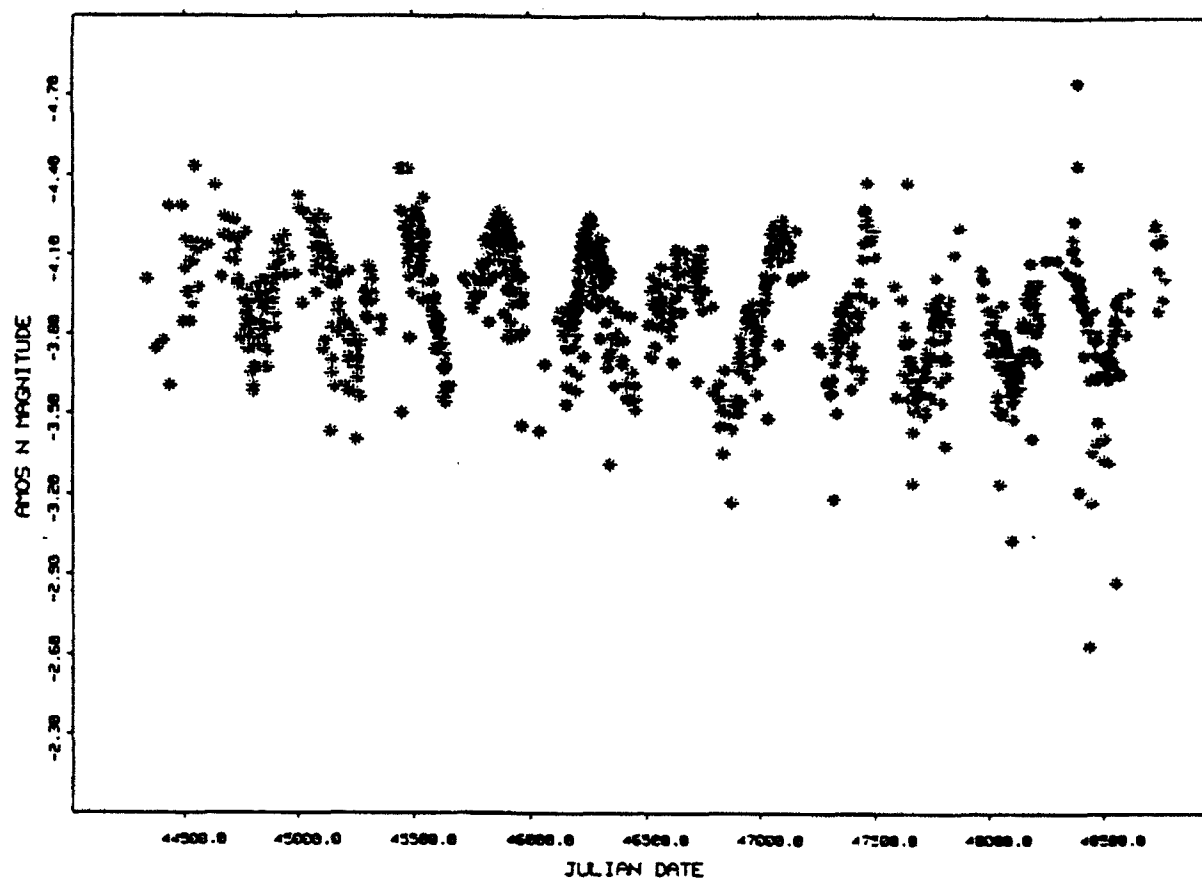


FIGURE 2B: CHI CYG 406.67 DAY PERIOD

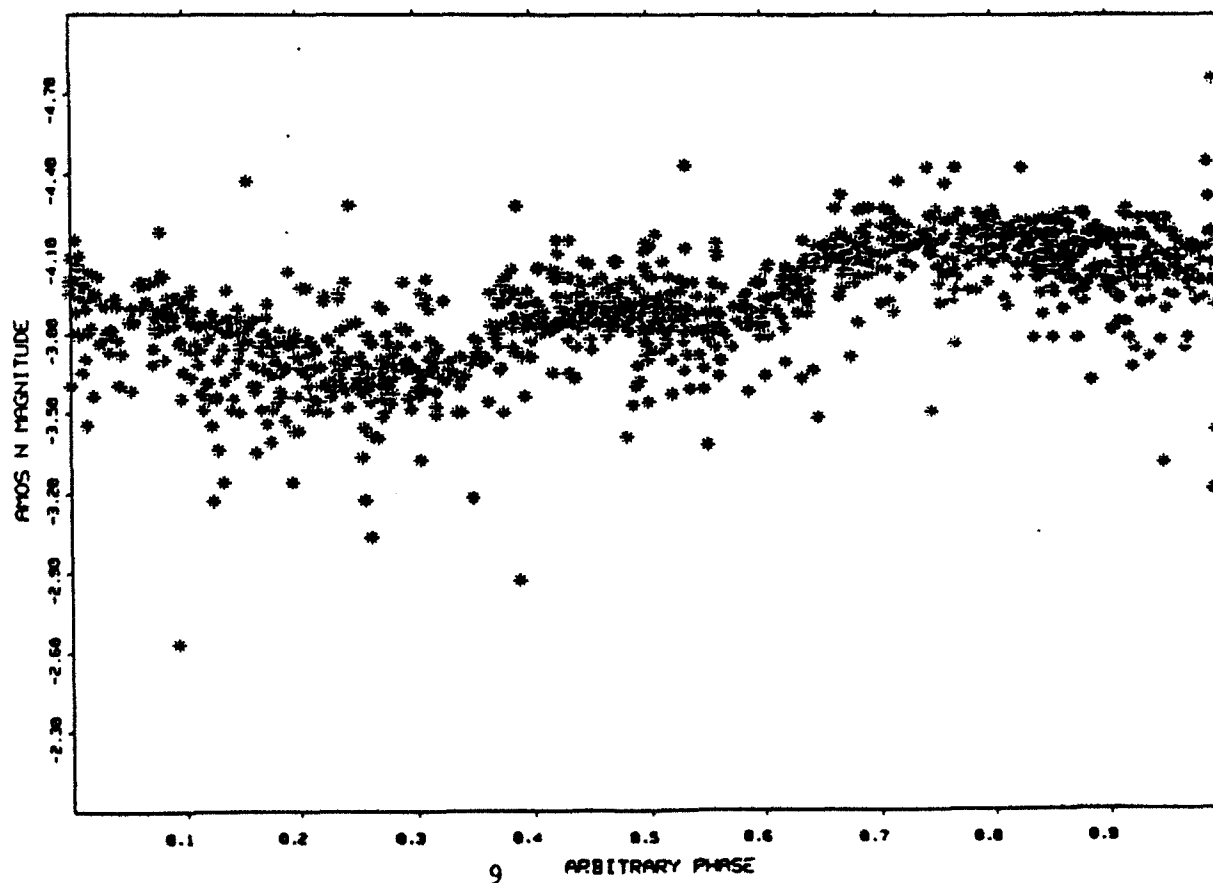


FIGURE 3: ASN 5340 (ALPHA BOO) STANDARD STAR

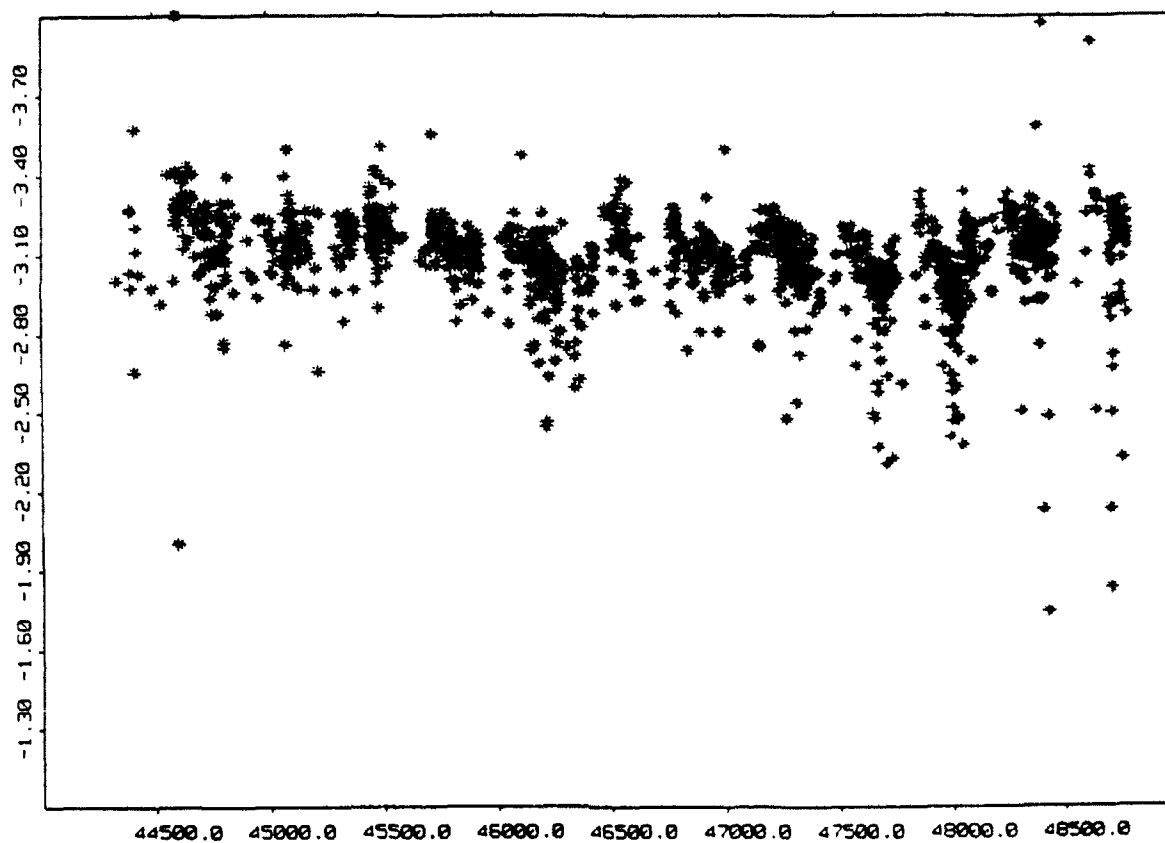
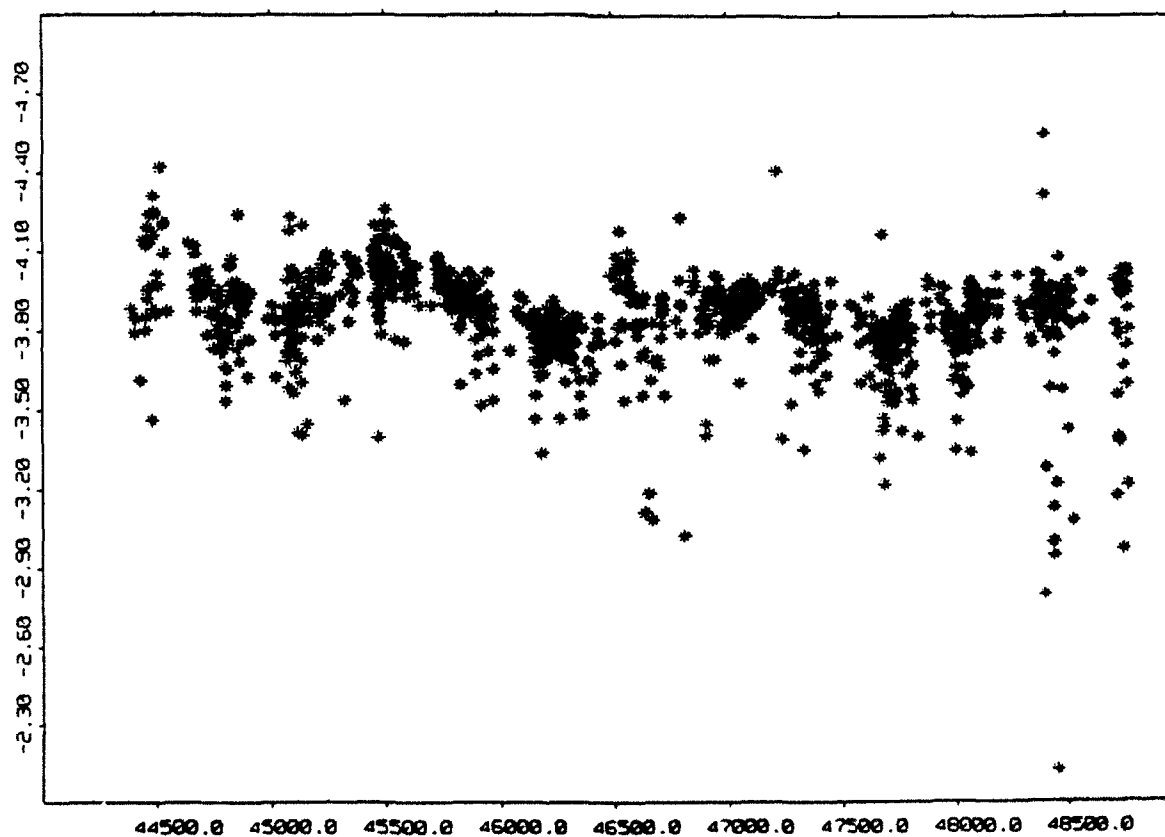


FIGURE 4: ASN 6406 (ALPHA HER)



## Infrared Detection of Geosynchronous Objects at AMOS

J.K. Lee (Air Force Maui Optical Station, PL/OL-YY), D.L. Nishimoto (Rockwell Power Systems - Maui)

Abstract. The most sensitive of the IR radiometers at the Air Force Maui Optical Station (AMOS) has been used in a new operational mode to study the radiometric signatures of geosynchronous satellites as a function of changing solar phase angle. A comparison is made between the measured irradiances and the expected values based on simple thermal balance modeling in which the dominant thermal source is assumed to be the solar panel arrays. Post-processing integration algorithms are also used to increase signal-to-noise levels.

### 1.0 Introduction.

The Air Force Maui Optical Site (AMOS) is one of a small number of electro-optical space surveillance facilities deployed around the world. A chief research mission of AMOS is in the area of Space Object Identification (SOI), in contrast to routine metric tracking and catalog maintenance. With the growing population of man-made objects in geosynchronous orbits, the need to detect, identify, and monitor these objects is ever increasing. Since the technology to image at these large ranges does not yet exist and radar detection is difficult due to minimal object movement and to the large inverse 4th power losses due to range, the use of optical sensors is essential for geosynchronous SOI.

For geosynchronous spacecraft, the illumination power of the sun is almost always present and the range limitation is only inverse square. Currently, techniques must be developed with modest equipment since the largest aperture at AMOS has a collecting area of 1.94 square meters. However, in 1995, the new AEOS telescope now being built for AMOS will provide a 10.5 square meter aperture, which equates to a factor of 5.4X increase in signal or 1.8 stellar magnitudes improvement in limiting magnitude at all wavelengths. Detection and characterization of spacecraft using sensitive infrared sensors exploits the ever-present amount of waste heat dissipated from the large solar panels of geosynchronous satellites.

This research effort focuses on collecting infrared data for two geosynchronous satellites using the AMOS Spectral Radiometer (ASR), an instrument placed into service in its present form some 5 years ago. The objectives of this research were five-fold: to exploit the best wavelength region for these objects based on their expected temperatures; to predict the expected irradiances to be detected by ASR; to develop the techniques necessary for target acquisition and measurement for geosynchronous infrared collection; to conduct data collection over extended periods in a given evening, being particularly mindful of the solar phase angle; and to develop post-processing integration algorithms for enhancing the target signal-to-noise ratio (SNR).

## 2.0 ASR Sensor Overview.

The ASR was designed for and has demonstrated a high degree of versatility in its capability and performance. Since it is AMOS' most sensitive infrared radiometer, the ASR was selected as the primary sensor for collecting radiometric signals emitted by geosynchronous satellites. The ASR's radiometric capability covers a broad spectral range from 2 to 20  $\mu\text{m}$  with filters that match the transmittance windows of the atmosphere. The ASR consists of twenty-four Si:As Blocked Impurity Band (BIB) detectors, which provide high sensitivity in the 6 to 20  $\mu\text{m}$  region, while the high quantum efficiency InSb detector covers the 2 to 6  $\mu\text{m}$  region. The system is cooled with a closed-cycle gaseous helium refrigerator to a temperature of 10 Kelvin. There are several field-of-view options; 4 x 4, 6 x 6, and 12 x 12 arc seconds with the total field-of-view being 12 x 60 arc seconds. The system sensitivity is 5 x 10<sup>-18</sup> watts per cm<sup>2</sup> with one second integration using the 8.1-12.9  $\mu\text{m}$  (wideband) filter. A built-in blackbody IR calibration source was used to routinely monitor the sensitivity and responsivity of the system. The ASR utilizes a 50 Hz nodding tertiary mirror, which has variable spatial scan amplitude in two axes, for background subtraction, target acquisition, tracking and modulation. Target acquisition and tracking are also aided utilizing a visual boresight ISIT camera.

## 3.0 Wavelength Selection Criteria.

Since geosynchronous objects exist at such extreme ranges, the optimal portions of the infrared spectrum must be chosen to insure valid and sufficiently large infrared signals are received by the detectors. The optimal wavelength must be chosen so as to maximize the object's IR signal and avoid the sun's IR radiation. Making the blackbody approximation, the wavelength ( $\lambda_m$ ) at which the radiation distribution is at a maximum can be calculated using Wien's displacement law (Tipler, p. 103):

$$\lambda_m(\mu\text{m}) = \frac{2898}{T(\text{Kelvin})}$$

where T is the temperature of the object of interest. The average temperature of the two geosynchronous satellites used for this study is 320 K (Long). Neglecting other lesser temperature contributors,  $\lambda_m$  is calculated to be 9.05625  $\mu\text{m}$ . In addition, the sun's infrared radiation needs to be approximated. Assuming the sun to be a blackbody radiator with a surface temperature of approximately 5900 K and again using Wien's displacement law, the sun's  $\lambda_m$  is calculated to be .49  $\mu\text{m}$ . One final consideration in choosing an optimal wavelength band is atmospheric transmittance. Therefore, the high-transmittance 8-12 micron region is chosen.

## 4.0 Prediction of Expected Radiant Intensity Collected by ASR.

This radiant intensity prediction is based on the peak projection case when the solar phase angle is either 0 or 180 degrees. The key contributor to radiant intensity from both satellites of interest is wasted heat from the solar energy

conversion; therefore, the radiant intensity prediction is purely based on this excess heat contribution. The average power consumption required by both satellites is known to be approximately 1600 W (Long). Assuming an average 10% solar conversion efficiency for the system's lifespan and equal heat emission from the satellite's front and rear, the total power dissipation toward the observer is 8000 W. The fraction of power dissipated in ASR's 8.1-12.9  $\mu\text{m}$  band must also be determined. Using a standard black body curve, the desired passband radiance can be determined (OSA, p. 1-15). Integrating the flux over ASR's 8.1-12.9  $\mu\text{m}$ , leads to a blackbody radiance of approximately 65  $\text{W}/\text{m}^2\text{-sr}$ . Using Stefan's law, the total blackbody emission is 196.4  $\text{W}/\text{m}^2\text{-sr}$ . Therefore, the fraction in this passband is .331. Applying this fraction to the 8000 W of total dissipated power from the satellite, only 2648 W is contained in the ASR wide passband. Finally, the expected radiant intensity collected by ASR can be computed based on the satellite's range from the observer. Using an average range of 36000 km and assuming an average atmospheric transmittance of 80%, the predicted radiant intensity is  $5.203 \times 10^{-17} \text{ W}/\text{cm}^2$ . Note that this is a "worst case" prediction which could justifiably be higher if other power contributors were considered.

#### 5.0 Data Collection Methodology.

All measurements presented in this paper were collected with the ASR utilizing the wideband 8.1-12.9  $\mu\text{m}$  filter region. Because of the low infrared signals emitted by these geosynchronous objects, sky background noise dominates the signal and needs to be kept to a minimum. Therefore, the small 4 x 4 arc second field-of-view was used to maximize the targets' signal to noise ratio. Target and background signatures are simultaneously recorded at a 10 Hz sampling rate using a 286 microprocessor. The data is processed and analyzed using programs written using the Interactive Data Language (IDL) in a Silicon Graphics/Unix environment.

#### 6.0 Data Analysis and Post-Processing.

Throughout the data collection effort, infrared signatures were collected on two geosynchronous satellites of interest during marginal and excellent weather conditions. Since the resulting signature trends were similar for both satellites, only the data for satellite "A" with the wideband filter is presented in this report.

##### 6.1 Raw IR Signature Trends.

Before any post-processing integration or phase coverage, the raw infrared signatures were examined to first verify sufficient signals for further analysis. Using the Silicon Graphics 4D440 workstation, recorded data is processed to remove background contributions by subtracting the background signature from the target signature on a point-by-point basis. Figure 1 shows the resulting background-removed "target signature" where



the first 3000 data points were collected with the target in the detector field of view. The remainder of the Figure 1 signature shows a diminished signal when the target is stepped out of the detector field of view. Though signal levels are extremely small, Figure 1 shows a recognizable and relatively constant signature when the satellite is tracked. Raw signal levels are slightly higher than expected since only the solar panels were assumed as signal contributors in the previous intensity prediction.

#### 6.2 Post-Processing to Increase Signal-to-Noise Ratio (SNR).

A window integration technique is used for signature conditioning as a post-processing step. Since raw infrared data is recorded at a 10 Hz rate, the windowing algorithm sums and averages every 10t points, where t is the chosen integration time. The beginning of the window is continually shifted until all data points are effectively smoothed. After the window integration is complete, target signal-to-noise ratio (SNR) is calculated using the following relationship (Henden, p. 77):

$$SNR = \frac{SIGNATURE\ AVERAGE}{STANDARD\ DEVIATION}$$

Figure 2 shows the raw, unprocessed infrared signature for Satellite "A" collected using the wideband filter. Figure 3 shows the resulting infrared signature after a 15 second window integration. The effect of window integration on signature smoothness is very noticeable. As a result of this integration technique, increases in SNR by factors greater than two have been achieved (See Figure 4).

#### 6.3 Solar Phase Coverage to Maximize IR Intensity.

As shown in Figure 6, geosynchronous satellite solar panels contain servo motors so as to cause the solar panels to always face the sun for maximum solar energy collection. Excess heat (from the solar conversion) is emitted out the front and back of the solar panel. Therefore, infrared signatures should be maximum at very small solar phase angles around midnight or very large solar phase angles around noon. The data collected in this research effort is consistent with that expected trend. Figure 5 shows a definite increase in average IR intensity as the solar phase angle changes from 80 to 20 degrees.

#### 7.0 Conclusions and Recommendations.

The ASR was successfully used to collect infrared signatures of geosynchronous satellites. Though the unprocessed signal levels were very small, they were shown to be within the sensitivity of ASR. Signal integration as a post-processing step provided significant increases in SNR; however, the integration benefit was not completely exploited due to the existence of coherent or additive noise sources within AMOS systems. The

solar phase angle study proved that the optimum time for infrared collection of non-cylindrical satellites is at very small solar phase angles.

The next challenge within the area of geosynchronous infrared detection is to accurately determine the satellite's temperature. This will require collection of signatures in two separate infrared wavelength bands, thus resulting in even smaller infrared intensities compared to wideband. The 5.4X increase in signal levels provided by the future AEOS 3.57 meter telescope should make this future goal possible.

#### 8.0 Acknowledgements.

We would like to thank Rob Medrano and Tom Nakagawa for their tireless help during the data collection periods of this project. In addition, we would like to thank Dr Ken Kissell for his scientific advice and assistance throughout the project.

#### 9.0 References.

1. Henden, Arne A. and Kaitchuk, Ronald H. Astronomical Photometry. New York: Von Nostrand Reinhold Company, Inc., 1982.
2. Long, Mark. World Satellite Almanac. Indianapolis, Indiana: Howard W. Sams & Company, 1987.
3. Tipler, Paul A. Modern Physics. Rochester, Michigan: Worth Publishers, Inc., 1987.
4. Driscoll, Walter G. (editor). Handbook of Optics (OSA). New York: McGraw-Hill, Inc., 1978.

**Fig 1: IR Intensity for Sat A (Wideband)**

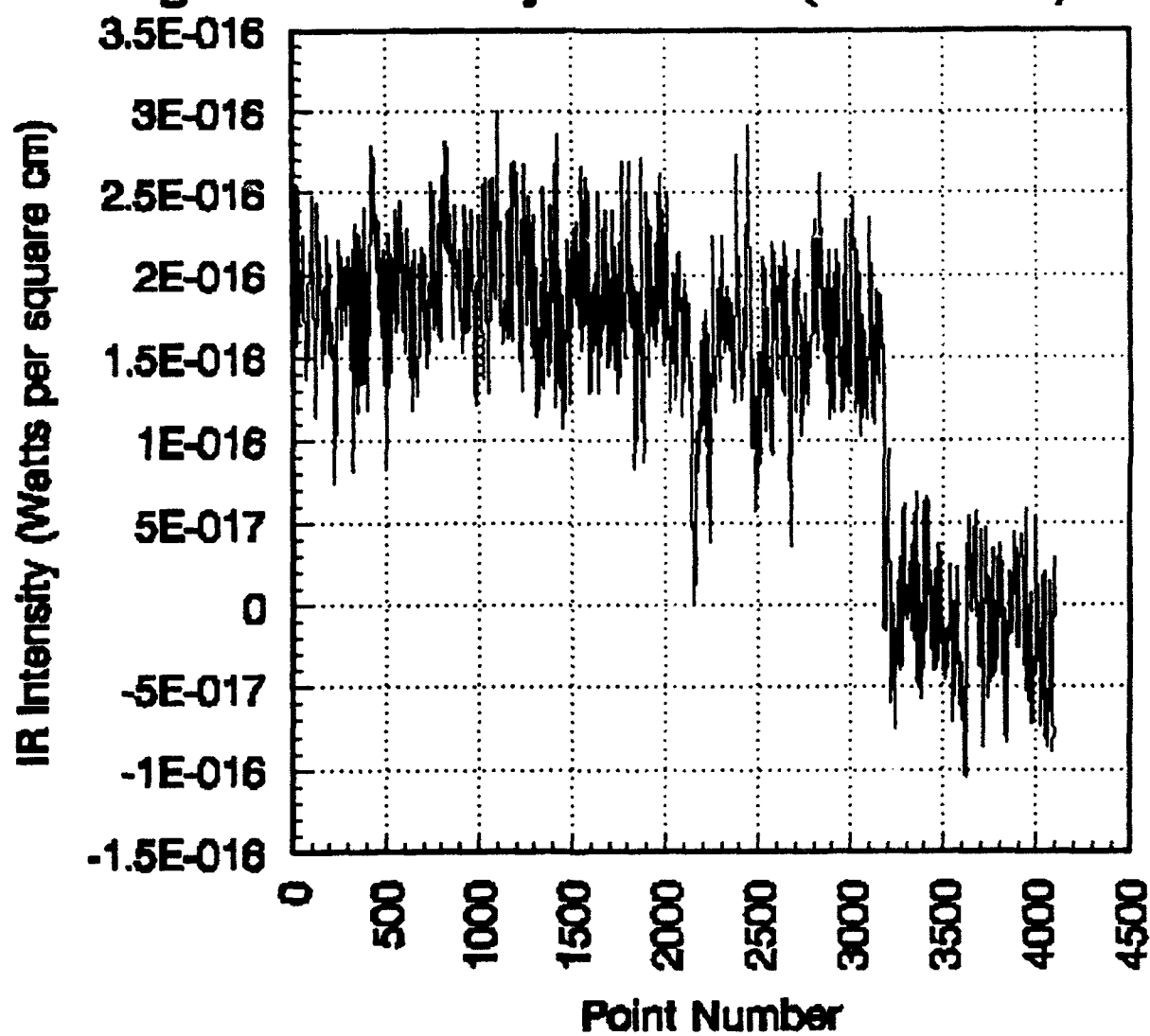


**Fig 2: IR Intensity for Sat A (Wideband, No Int.)**

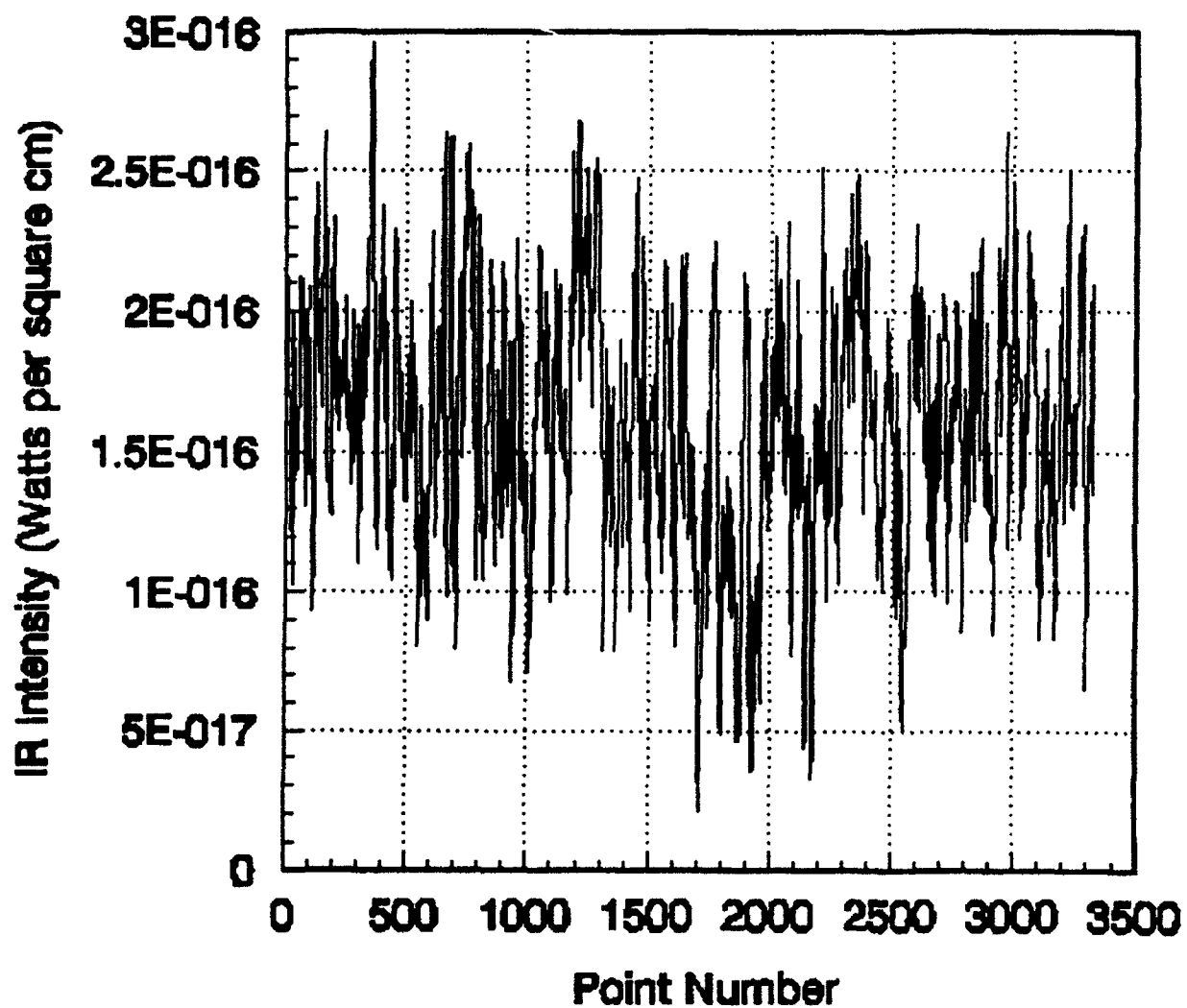


**Fig 3: IR Intensity for Sat A (Wideband, 15 sec)**

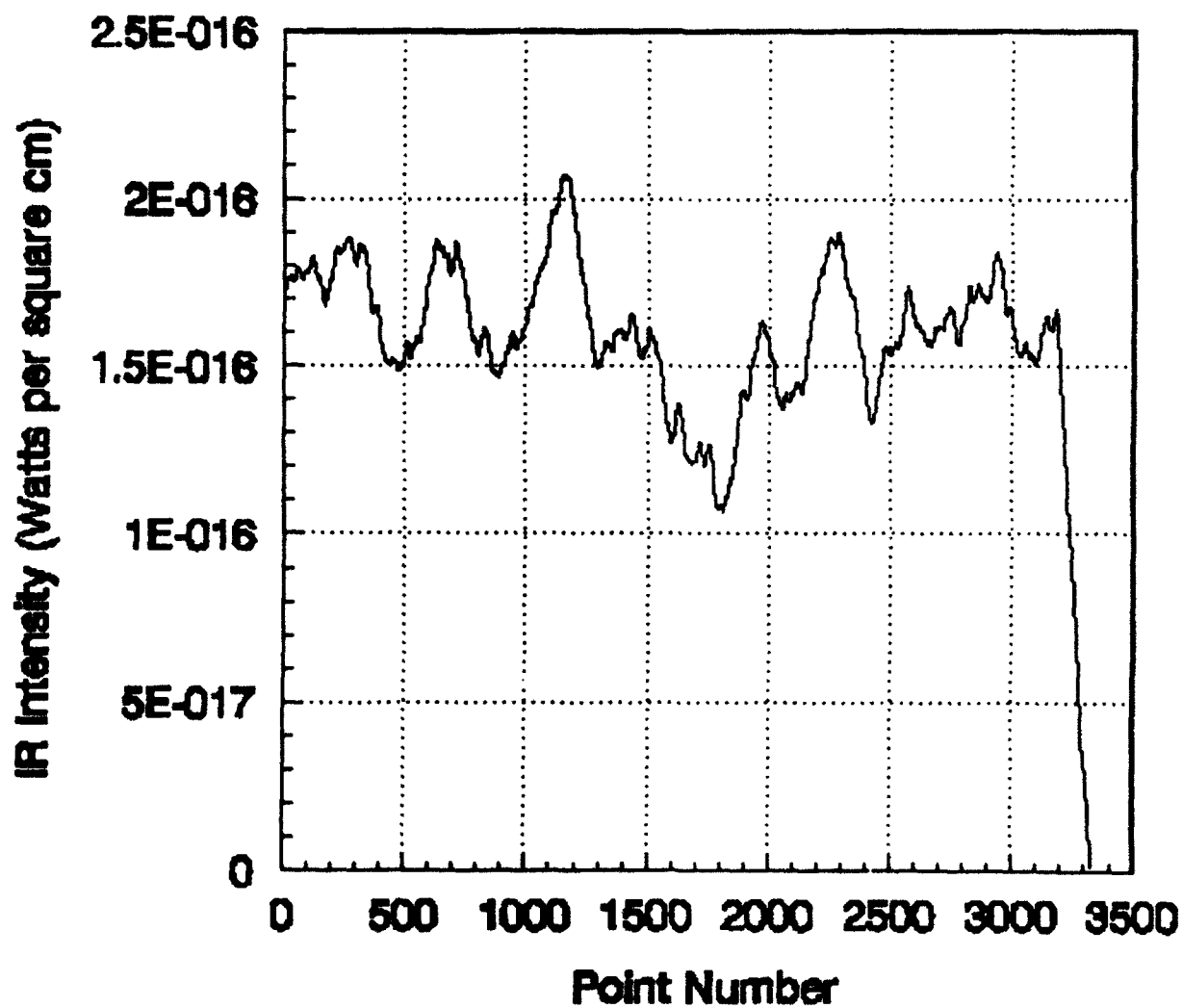


**Fig 4: SNR Plot for Sat A (Wideband)**

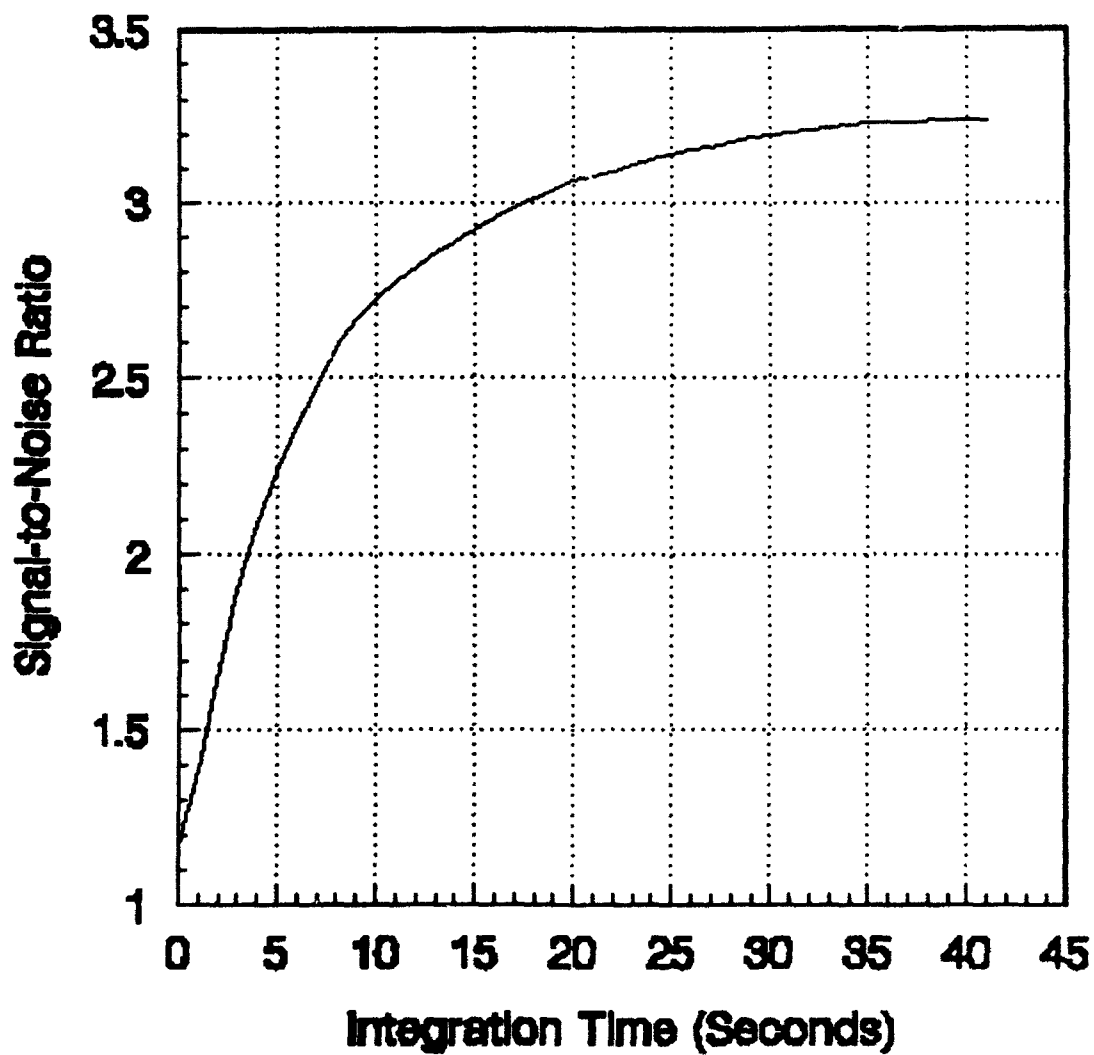
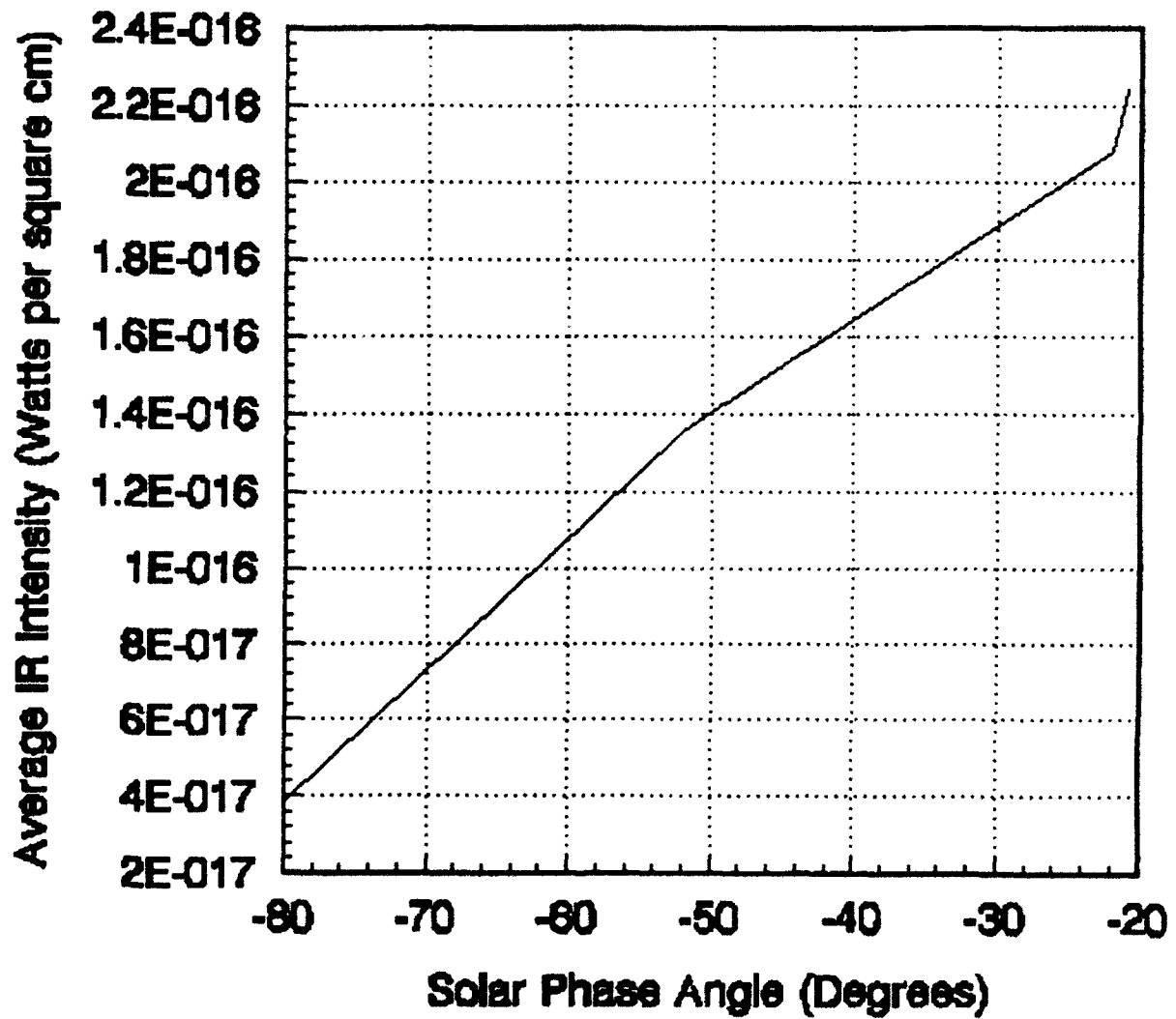


**Fig 5: Avg IR Intensity Versus Phase for Sat A**



## LWIR Observations of Geosynchronous Satellites

W.P.Seniw (MIT Lincoln Laboratory, Surveillance Techniques Group)

### INTRODUCTION

This report documents the measurements and some analysis of Long Wave Infrared (LWIR) observations of geosynchronous satellites using the ground based sensors at the University of Arizona and University of Wyoming between July 1992 and February 1993. The goal of the measurements was to both evaluate the capabilities of ground based sensors to track satellites at geosynchronous (40,000 km.) ranges and measure to thermal emission of a number of satellites in these orbits.

Since many of these satellites in thermal equilibrium are estimated to be at temperatures between 270K and 380K, the peak of the equivalent blackbody temperature flux curves will be within the standard N-Band astronomical filter which spans 8 to 13 microns in wavelength. This wavelength band also is located conveniently in a passband that is relatively transparent for infrared energy passing through the atmosphere so it is a good choice for the observing these objects in the infrared. At this time (January 1993), the data collection activities at Wyoming were not yet completed and data was not yet available, so this report contains data only from measurements at the University of Arizona.

### SENSOR SUMMARY

Table 1 lists some of the relevant sensor characteristics for the two observatories. The infrared bolometer systems were not modified and used the same measurement techniques as used in their standard astronomical measurements. There are several excellent references<sup>1,2</sup> that describe the various infrared astronomical sensor system and measurements techniques in much greater detail than is possible here.

The background thermal radiation from a ground based system is can be up to  $10^7$  times larger than the signal from the target we wish to observe. To remove the background signal, the systems spatially modulate the background and use synchronous ac detection techniques. Typically this is accomplished by rocking the telescope secondary mirror at a frequency between 5 and 20 cycles per second (commonly referred to as chopping). This places two slightly displaced patches of sky on the detector. When observing an object of interest, one patch contains the target signal plus the background. (the source beam) and the other contains only background signal (the reference beam). If the backgrounds of the two sky patches are equal, then the difference between the two samples will equal the signal of the object of interest.

---

<sup>1</sup>Gehrz,R.D, Grasdalen,G.L.,and Hackwell,J.A. (1987), "Infrared Astronomy", *Encyclopedia of Physical Science and Technology*, Vol. 2, 54-80

<sup>2</sup>Low,F.J, and Rieke,G.H. (1974), "The Instrumentation and Techniques of Infrared Photometry", *Methods of Experimental Physics*, Vol. 12, Astrophysics, Part A, 415-462

\*This work sponsored by the Department of the Air Force under Contract No. F19628-90-C-0002



The sampling and differencing is done using a lock-in amplifier with the source in one of the beams and integrated for some period of time, usually 15 seconds in our measurements. Next the object of interest is placed in the other beam position (referred to as nodding) and integrated for the same length of time. The signal from the object is then the average of the source signals measured in each of the nod positions. The beam nodding removes any fixed ac signals remnants from the chopping or spatial background gradients along the chop direction. This technique is valid only when the sky background is relatively uniform spatially and temporally during the sampling. When this is not true, as in the case of high thin cirrus clouds or large atmospheric water vapor content,, then the resulting sky noise can dominate the target signal.

The infrared sensors have an extremely small field of view (8 arcseconds at best) and, coupled with their sensitivities, are not search sensors. It was necessary then to initially acquire and then guide the system using a visible band sensor with a wider (approximately 70 arcsecond or about 20 mdeg.) field of view. This was still a very small field of view, less than 25 times smaller than the Millstone L-band radar's 0.5 degree beam and 2.5 times smaller than the Haystack radar 50 mdeg angular beamwidth. As a consequence, we needed very accurate satellite position predictions for acquisition and tracking, even with our acquisition systems.

**TABLE 1**  
**UNIV OF ARIZONA                      UNIV OF WYOMING**

SITE/SENSOR	STEWART OBSERVATORY - CATALINA	WYOMING INFRARED OBSERVATORY
LOCATION	MT. BIGELOW, ARIZONA	MT. JELM, WYOMING
ALTITUDE (METERS)	2500	2943
TELESCOPE OPTICS (METERS)	1.5	2.3
DETECTOR	GERMANIUM BOLOMETER	Ge:Ga BOLOMETER
APERTURE (ARCSEC)	5.7, 8.5	6
SAMPLE RATE (HZ)	20	7.5 TO 10
SENSITIVITY (W/CM2-MICRON)	1.47E-17	1.80E-17

#### **OBSERVED SATELLITE SUMMARY**

Table 2 summarizes the satellites observed during the measurement campaign. Initially we chose two large three-axis stable payloads, ANIK E-2 (SSC# 21222) and SPACENET 1 (SSC# 14985) and two spinning cylinder payloads, GALAXY 1 (SSC# 14158) and TELSTAR 3A (SSC# 14234) as our baseline list of satellites for our measurements. The physical size, shape and orientations of these objects are

known and our estimates of their radiant flux in the N-Band led us to believe that we should be able to detect them with less than 1 minute of integration with these sensors.

After successfully observing all these objects, we next extended the data collection to a various other objects within our coverage, including active and inactive payloads and rocket bodies.

SSC#	TRACKS	NAME	TYPE
3432	1	TITAN 3C RB	CYLINDER
11145	2	DSCS II	SPIN-STABILIZED CYLINDER
13631	1	RCA SATCOM 5	GE 3000 3-AXIS STABILIZED
13652	1	ANIK C3 (TELESAT 5)	HS-376 SPIN-STABILIZED CYLINDER
14050	1	GOES 6	SPIN-STABILIZED CYLINDER
14158	6	GALAXY 1	HS-376 SPIN-STABILIZED CYLINDER
14234	3	TELSTAR 3A	HS-376 SPIN-STABILIZED CYLINDER
14951	1	SL-12 RB	CYLINDER
14985	7	SPACENET 1	GE-3000 3-AXIS STABILIZED
15643	1	LEASAT	SPIN-STABILIZED CYLINDER
16667	3	COSMOS 1738	INACTIVE
17181	2	USA 20	3-AXIS STABILIZED
17875	2	SL-12 RB	CYLINDER
19017	2	GORIZONT 15	INACTIVE
20872	3	SBS 6	HS-393 SPIN-STABILIZED CYLINDER
20873	3	GALAXY 6	HS-376 SPIN-STABILIZED CYLINDER
21019	2	SL-12 RB	CYLINDER
21135	2	SL-12 RB	CYLINDER
21222	14	ANIK E-2	GE-5000 3-AXIS STABILIZED
21726	3	ANIK E-1	GE-5000 3-AXIS STABILIZED

**TOTAL  
20 SATELLITES, 60 TRACKS**

*Table 2. Observed Satellite Summary*

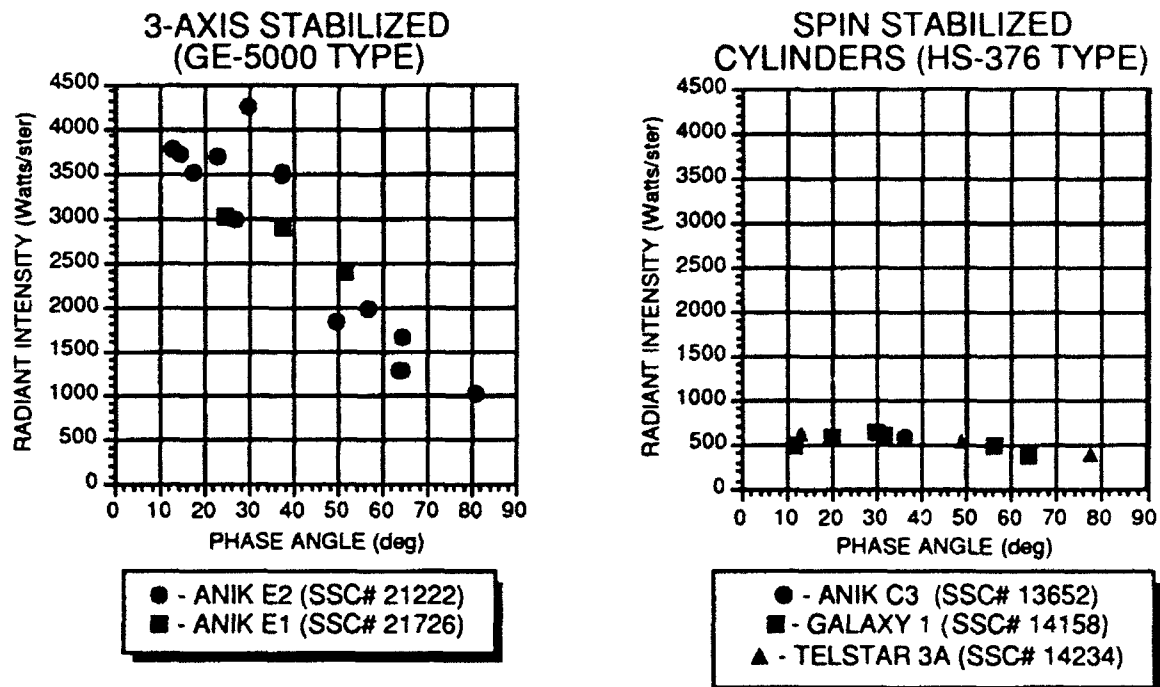
## ANALYSIS EXAMPLES

Next we will present the phase angle curves for a number of the satellite classes that we observed in our measurements. Here we define the phase angle as the angle from the sensor to the satellite to the sun such that a 0° phase angle would place the sun directly behind an observer when viewing a satellite.

Most three-axis stable active payloads have solar arrays that are oriented normal to the sun and the solar panels dominant the total emitted radiant flux. So the measured flux from this type of satellite should be highly dependent on the phase angle. We see this behavior very plainly in Figure 1. As the phase angle increases, the cross sectional area from the solar array as seen from the site becomes smaller until we observe only the radiant flux from the central box and antenna arrays which point toward a fixed point on the earth which does not vary with phase angle.. The GE-5000 class payload has a total of about 36 square meters of solar array, which makes it one of the physically largest objects available.

In contrast, a spinning cylindrical payloads should show very little variation with phase angle since the object is in thermal equilibrium and the cylinder cross-sectional area does not change with phase angle. Figure 1 also shows the observed flux from a number of Hughes HS-376 type satellites, which is the most common type of geosynchronous payload at present.

## N-BAND (8-13 $\mu$ ) RADIANT INTENSITY vs PHASE ANGLE



NOTE: PHASE ANGLE IS DEFINED AS THE ANGLE FROM THE SITE TO THE SATELLITE TO THE SUN

WPS (JAN 93)

*Figure 1. Three axis stable and spinning cylinder payload phase curves*

There seems to be only a slight variation with phase angle in contrast to the three-axis stable case. One possible explanation for this small variation may be contributions from the despun platform and antenna arrays which point toward a fixed location on the earth. As the incident absorbed solar flux varies with the solar illumination angle, there may be some more complicated thermal changes to the platform and antenna arrays that cause this variation.

In Figure 2, we show the observed flux from a number of synchronous rocket bodies. Since these objects are not being maintained in any particular orientation they should not have a predictable phase dependence in general. Since we are integrating for 30 seconds and each point shown is an average of a number of integration cycles, any short term signature behavior is lost in this processing.

## N-BAND (8-13 $\mu$ ) RADIANT INTENSITY vs PHASE ANGLE

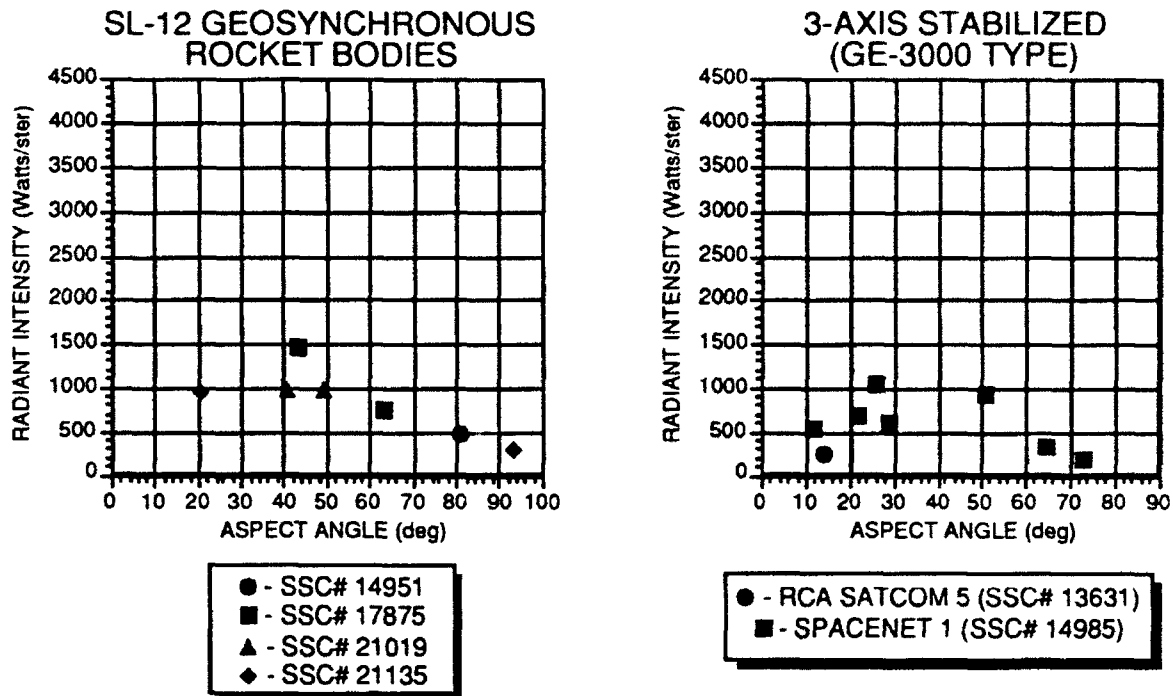


*Figure 2. Rocket body and three axis stable payload phase curves*

In the same figure we also have the phase curve for another three-axis stable payload class of object. These objects are based on the GE-3000 configuration which is a pre-cursor of the GE-5000 satellite class in the previous figure. These objects have significantly smaller solar arrays and central box body gives us a smaller radiant flux.. There may also be an offset in the solar array pointing in these objects which could explain why the peak flux is not at 0 degree phase angle.

In Figure 3 we have some examples of older and assumed inactive Soviet payloads in geosynchronous drift orbits. Since these types of objects are no longer being station kept, they are also probably no longer being actively attitude controlled as well. Their phase curves will be hard to predict in general and these few examples show only the range of average values that may be observed. And any short term flux variation that is smaller than our 30 second integration interval will be averaged out in these observations and not detected.

Finally in this same figure, we show some observed flux values of a several other payloads from a number of different configurations classes.

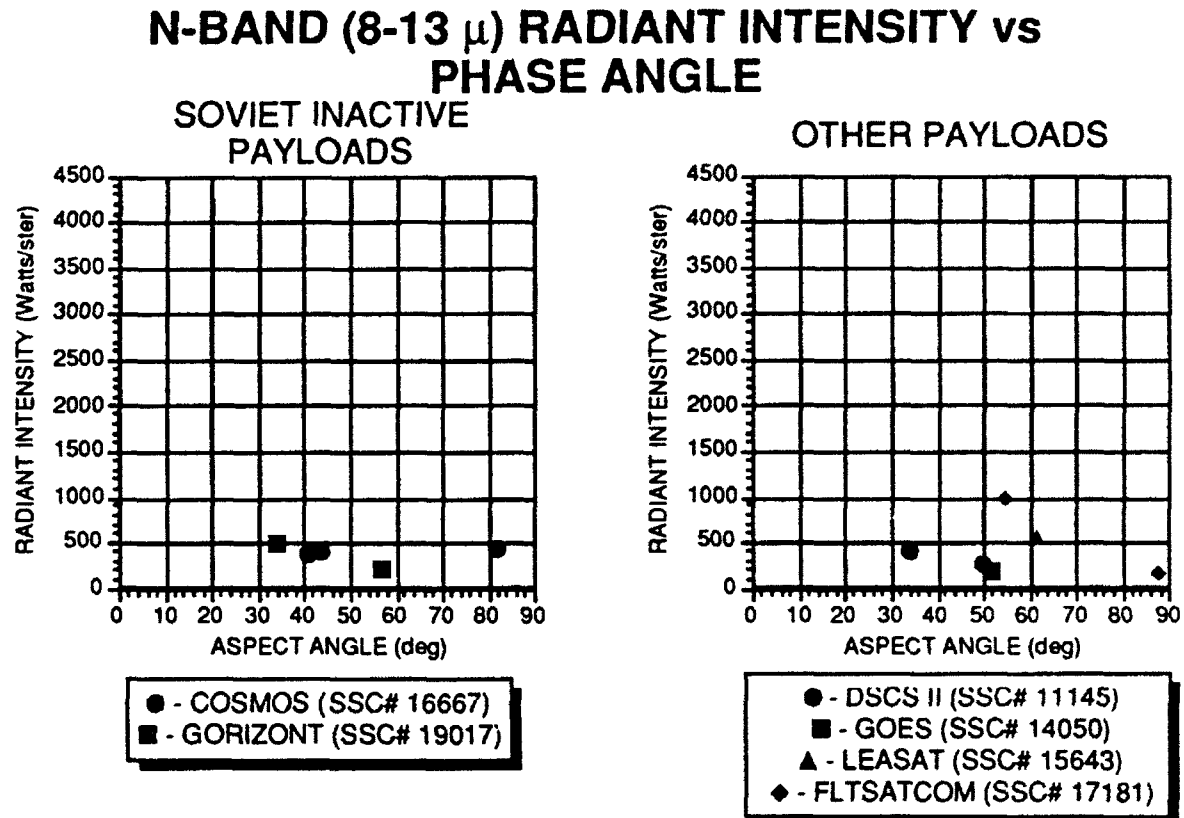
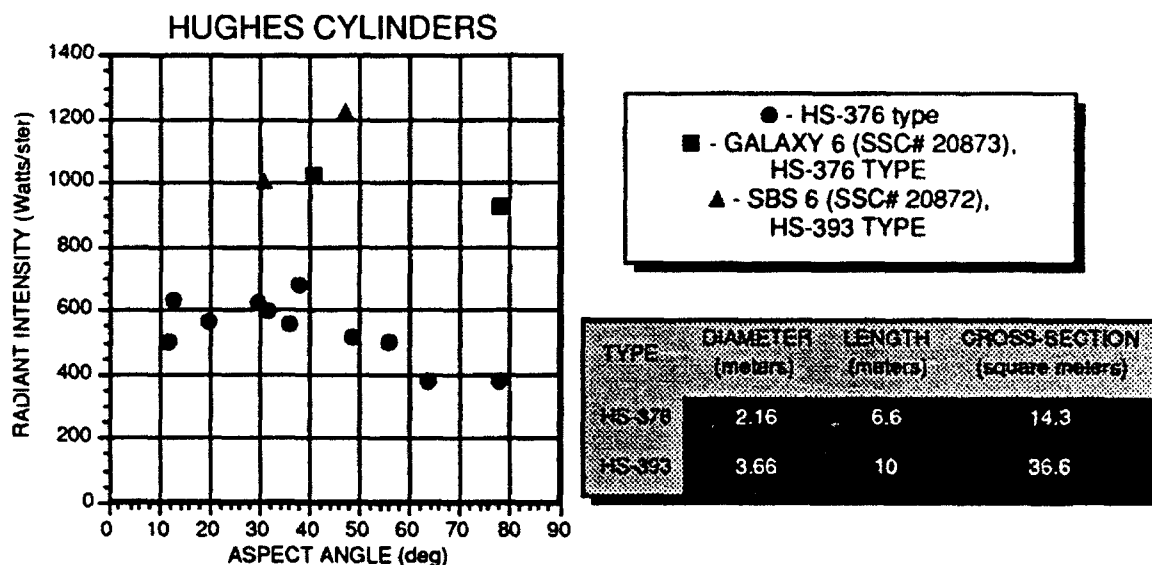


Figure 3. Inactive Soviet payloads and miscellaneous payload phase curves

## N-BAND (8-13 $\mu$ ) RADIANT INTENSITY vs PHASE ANGLE



SBS-6 AND GALAXY ARE WITHIN .1 DEGREES OF ONE ANOTHER WITH FREQUENT SENSOR MISTAGGING. MISTAG ALSO PROBABLE IN THIS CASE WITH THE LARGER OBJECT (SBS-6) THE ONLY OBJECT TRACKED

NOTE: PHASE ANGLE IS DEFINED AS THE ANGLE FROM THE SITE TO THE SATELLITE TO THE SUN

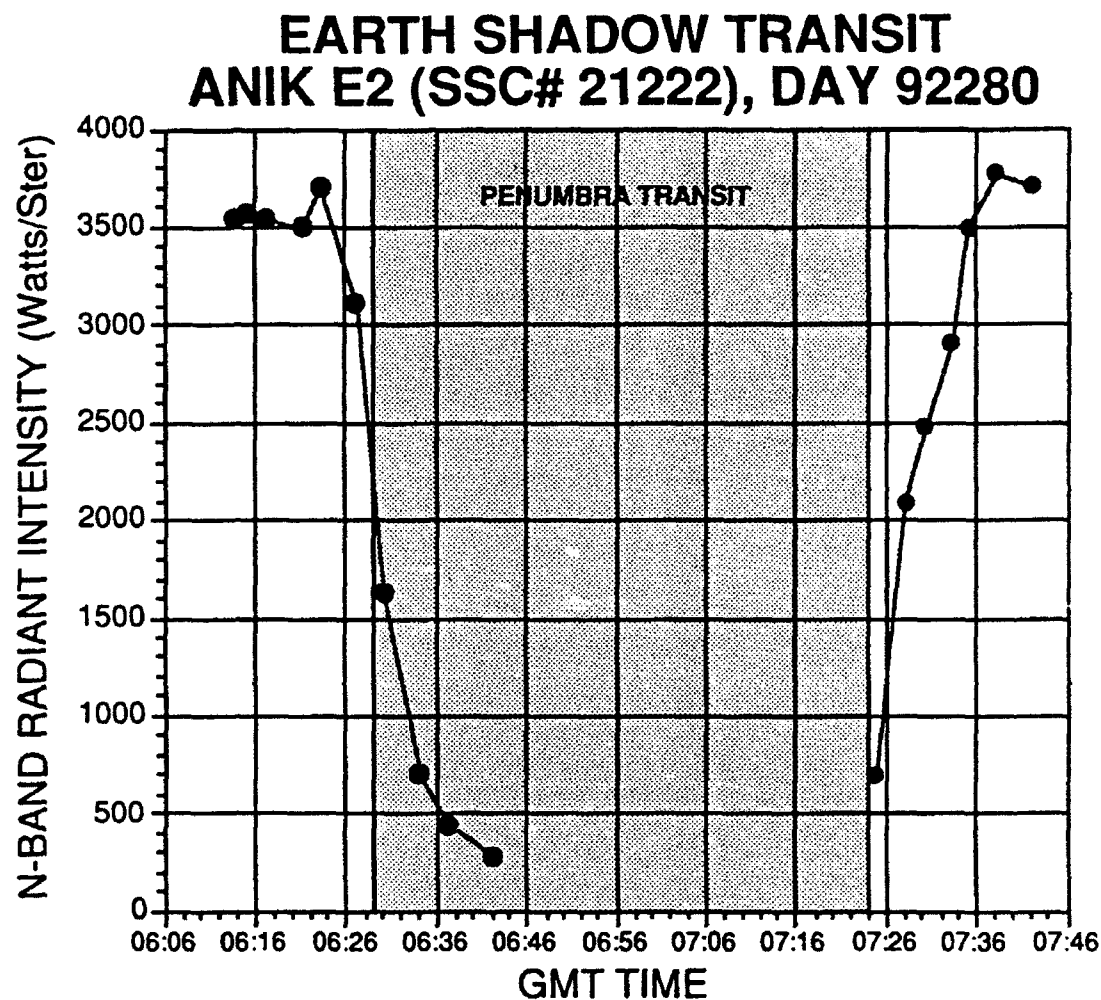
WPS (JAN 93)

*Figure 4 Hughes cylinder possible mistag phase curves*

In Figure 4, we have observations of the two different types of Hughes cylinders. The HS-376 type is the most common type and have N-Band fluxes around 500 Watts/steradian. The new type of Hughes cylinder, HS-393, is physically much larger than the HS-376 series. There is approximately a factor of about 2.5 in the cross sectional area which should give us a much larger flux (by the same scale factor of physical cross section if the temperature and emissivity are identical). We observed a HS-393 payload, SBS 6 (SSC# 20872), and measured a much larger flux, as expected. However, when we tried to observe a co-located (predicted to be within .05 degrees of one another) HS-376 satellite, GALAXY 6 (SSC# 20873), we most measured flux of this object was much more consistent with the flux of the larger HS-393 type of satellite.

The most likely explanation is that we observed the same satellite (the larger HS-393) in both cases. Since the objects are so close together, there is a great deal of mistagged metric data from the SPACETRACK sensors on these objects. The resulting orbital element sets, which are based on this data, are corrupted by

a mixture of data on both objects and the positional predictions from the se element sets are not as accurate as in other cases. So the probability that we tracked only one satellite is not too unlikely.



WPS - JAN 93

*Figure 5 ANIK earth shadow transit*

We also observed several satellites as they entered and exited the earth shadow. this can occur for geosynchronous or about a two week period around the spring and fall equinox. By a lucky scheduling



coincidence, we had our first observation session during the fall equinox. Figure 5 shows ANIK E2 (SSC# 21222) during such a transition.

We can see the rapid drop in radiant flux as it cools down as it enters the shadow. At this point we could no longer actively track the satellite with the visible band guiding system. However we were able to track the object for some period with the IR sensor. We kept the satellite centered in the 8 arcsecond aperture by periodically performing a small scan in RA and DEC and then centering on the measured peak (a standard astronomical technique). This worked reasonably well since the flux was relatively strong and constant during the scan. We acquired the satellite with the visible band system as it exited the shadow and then tracked it as it warmed up and reached thermal equilibrium again.

## **SUMMARY**

We have demonstrated the capability of ground based sensors to observe geosynchronous satellites using long wave infrared sensors in the 8 to 13 micron band. During the program, we observed a number of different classes of satellites, including active and inactive payloads and rocket bodies over a range of phase angles. The sensors were existing astronomical infrared instruments that used their standard measurement techniques for the program.

## **LAGEOS-2 LAUNCH SUPPORT NAVIGATION AT JPL**

**T.P. McElrath, K.E. Criddle, and G.D. Lewis**  
Jet Propulsion Laboratory, California Institute of Technology  
4800 Oak Grove Drive, Pasadena, CA 91109

### **ABSTRACT**

Lageos-2 was launched on October 22, 1992, aboard STS-52, and was deployed the following day. After the successful firing of a perigee and an apogee stage, Lageos-2 was placed in a circular orbit inclined 52 degrees at an altitude of 5900 kilometers. While Lageos-2 contains no radio equipment, both upper stages had a radio transmitter that was tracked to receive telemetry and to obtain angle measurements by the stations of the NASA/JPL Deep Space Network (DSN), and by several other tracking stations. Some of the responsibilities of DSN Multimission Navigation during the first day of the mission were (1) to receive space shuttle state vectors, numerically integrate through both motor firings, and provide state vectors to several different users, and (2) to process upper stage angle data from the DSN, generate improved state vectors for the upper stage and Lageos-2, and send the Lageos-2 state vectors to the satellite laser ranging network located at Goddard Space Flight Center to assist in laser acquisition of Lageos-2. While all these tasks were successfully accomplished, the failure of the laser network to acquire Lageos-2 using DSN state vectors (as opposed to U.S. Space Command element sets) has resulted in ongoing analysis into possible error sources. The proposed paper would discuss pre-launch covariance studies, operational results, and post-mission analysis (including an attempt to combine U.S. Space Command element sets for each Lageos-2 related object in orbit with DSN angle data to determine the actual separation impulses and motor performance), all of which is unclassified.

## Space Surveillance Network Sensor Contribution Analysis

G.T. DeVere (Nichols Research Corporation)

### 1.0 INTRODUCTION

The Space Surveillance Network (SSN) is composed of radar, electro-optical and passive radio frequency sensors disbursed at world-wide locations reporting to a centralized command and control facility located in Cheyenne Mountain AFB called the Space Surveillance Center (SSC). A back-up facility, the Alternate SSC (ASSC) is co-located at Dahlgren, VA with the Naval Space Surveillance (NAVSPASUR) System. In the current era of force reductions, military budget cut-backs and overall defense restructuring, it is important to understand the contributions of the various sensors. As a result, Nichols Research Corporation (NRC) was tasked by Air Force Space Command (AFSPACECOM) to conduct an analysis of this area. This analysis was limited to the importance of sensors to the overall catalog maintenance mission and new foreign launch support. Additional missions performed by sensors that are independent of their satellite tracking function were not addressed, nor were special space surveillance activities, such as decay prediction support because of the randomness of these events.

### 2.0 CATALOG MAINTENANCE ANALYSIS

The catalog maintenance analysis focused on the importance of sensors in the two primary altitude regimes as related to the SSN: near earth (orbital periods less than 225 minutes), and deep space (periods greater than 225 minutes). This separation is important because the sensors that can track satellites in each of these orbital regimes can be different. In particular, there are a limited number of sensors that can track deep space objects, due to the altitudes employed (typically greater than 5000 km), whereas many sensors can observe near earth satellites.

The approach to this task employed a two phased methodology for each of the orbital regimes. The first phase involved a quantification of the contributions of sensors. This assessment involved generation of quantitative statistics for a six month time period concerning numbers of satellites tracked, numbers of observations collected and other parameters. The second phase involved the generation of qualitative statistics for the sensors. In this phase, the importance of sensors was evaluated through the deletion of data from these sensors in the standard SSC element set maintenance process. The element set differential correction software was obtained from AFSPACECOM and is directly compatible with the software in use at the SSC

today. As different sensors were deleted, the impact on output element set quality was monitored. Also, the amount of bad data (defined as exceeding the accepted norm by a specified amount) was measured for each sensor.

To obtain an overall assessment of sensor importance, an equation was developed to allow the rating of sensors using a combination of these quantitative and qualitative factors. The use of this equation provided the following results. For geosynchronous satellite tracking, the most important sensors were Diego Garcia, Socorro and Millstone. For highly elliptical satellite tracking, NAVSPASUR, Socorro and ALTAIR were the highest rated sensors. For overall deep space satellite tracking, the sensors at Diego Garcia, Socorro and Millstone received the highest ratings. It is important to note that these ratings are somewhat subjective and caution should be employed in their use.

The overall near earth sensor importance ranking showed NAVSPASUR, Cavalier and Eglin to be of primary importance in routine element set maintenance of near earth satellites with secondary support provided by Clear, Shemya and Thule. The analysis also revealed that Cavalier data is of significant utility in maintaining orbits on small satellites (those with radar cross sections less than 0.01 square meters).

Sensor ratings for tracking all satellites in all orbit regimes were developed, based on the analysis data. This combination rating showed that the top six sensors, in order of priority for catalog maintenance, were: NAVSPASUR, Eglin, Cavalier, Diego Garcia, Socorro and Millstone. The sensors providing the least valuable data for catalog maintenance, in descending order, were Antigua, Ascension, Kaena Point and the now deactivated Fylingdales mechanical trackers.

### 3.0 NEW FOREIGN LAUNCH ANALYSIS

Tracking New Foreign Launches (NFLs) is an important requirement for the SSN. NFLs are defined as launches of new satellites from countries that have not provided pre-launch information (e.g., data and time of launch and expected orbital parameters). Due to the lack of advance information, these launches stress the SSN in several ways. These satellites may be considered a threat to national security, and it is important to determine their orbital position and status as quickly as possible. Also, some sensors are required to scan across wide coverage areas to compensate for their narrow beam-width and the uncertainty in the new satellite position. The primary emphasis is to acquire the object quickly and provide the data to the SSC, where the

element set generation, update and dissemination process can occur. To facilitate this process, the SSC has developed a series of NFL folders. Each of these folders contains an element set representative of past historical launches with similar orbital characteristics. Non-historic and non-nominal launches were not examined; however, over 95 percent of the launches in the last two years have followed a folder trajectory. NRC examined the contributions of sensors to the NFL tracking mission through the analysis of NFL folders, described below.

The approach used in determining sensor importance in NFL tracking was to quantify each sensor's contribution to the generation of the first element set of a newly launched satellite. Each sensor's importance is a function of its capabilities and limitations. NRC measured each sensor's contribution to the mission and then compared it with other sensors to determine the most important sensors. This permitted an assessment of the sensor importance to the NFL tracking mission. The NFL folders studied in this task were all 71 folders listed in the January 1992 SSC Launch Folder Element Set File.

To quantify each sensor's contribution, the first step was to determine what opportunity each sensor would have for viewing each launch during the period of interest. The NRC software, H Code, was used to determine the opportunities. If the launch involved a parking orbit for a specified period of time, only observations during that time interval were generated. In other words, only the data from the sensor observing the satellite during the time it was in a parking or transfer orbit were considered. If the satellite was in its final orbit, all opportunities were generated until 12 hours after launch. This opportunity file was then used as input to the Launch Simulation Program (LSP), which is a special purpose program written by NRC for this analysis. LSP calculated the importance of each sensor's contribution for each launch.

Besides measuring each sensor's individual contribution, LSP determines how long it takes a sensor suite to obtain the initial element set (often referred to as "Elset-1") on each launch. Elset-1 time is the time from launch to the time of the last observation used to meet the criteria established to ensure adequate element set accuracy, and is the standard measure of NFL performance. Requirements, as listed in United States Space Command (USSPACECOM) Regulation 55-12, for these criteria were used for both near earth and deep space launches.

It should be noted that the communication delays from the sensors to the SSC were not modeled in this analysis. Also, it was assumed that the sensors acquired the NFL satellite 100 percent of the time. In other words there were no sensor down times due to maintenance or support of other missions and that the sensors had the sensitivity to detect all objects regardless of

Radar Cross Section (RCS). NRC recognizes that these factors do influence the generation of NFL element sets, but it was beyond the scope of this analysis to model these parameters. The information generated provides a reasonable assessment of the sensor importance without considering these variables.

To understand sensor importance for NFL tracking, a rating scheme was developed. A rating was calculated for each sensor for each folder. This equated to approximately 1700 values for each sensor suite (24 sensors times 71 folders). An overall sensor importance was calculated for each sensor by summing up each sensor's contribution to each folder and then dividing by the number of folders. This contribution assessment was performed by evaluating the following factors:

- (1) Satellite Mission (SM): the priority of the foreign launch to the military community. The values range from high interest military (rating of 10) to civilian low interest (rating of 2).
- (2) Launch Frequency (LF): how many times a year can the SSN expect to see this launch, based on historical data from the prior two years. If the launch is infrequent then the sensor's ability to see it is of less value when compared to a launch that occurs often.
- (3) Time Delay when the sensor is removed from the network (TD): a value for a sensor if its omission means a large delay in generation of Elset-1 for the launch.
- (4) Time to Next Sensor (TN): a value for a sensor if there is a large time gap before another sensor observes it.
- (5) Sensor Viewing Order (VO): the first sensor to track the final orbit of an NFL will receive the most credit for this factor. Each level of the viewing order is weighted along with the orbit type - - final, parking, or transfer.
- (6) Sensor Unique Capability (SC): the sensor's capability to do Space Object Identification (SOI) and/or piece count of a new launch.
- (7) Sensor Accuracy (SA): based on the sensor's tracking accuracy taken from the AFSPACECOM/DOA Technical Note 89-2, "Sensor Accuracies".

- (8) Sensor Contribution Type (ST): reflects the sensor availability to support the space surveillance mission, e.g., if the sensor is dedicated, contributing or collateral.
- (9) Sensor Availability or Up-Time (SU): whether the sensor is available full time or only part time.

Figure 1 shows the results of applying the rating scheme and shows that Pirincliik scored the highest followed closely by Fylingdales, Shemya and ALTAIR.

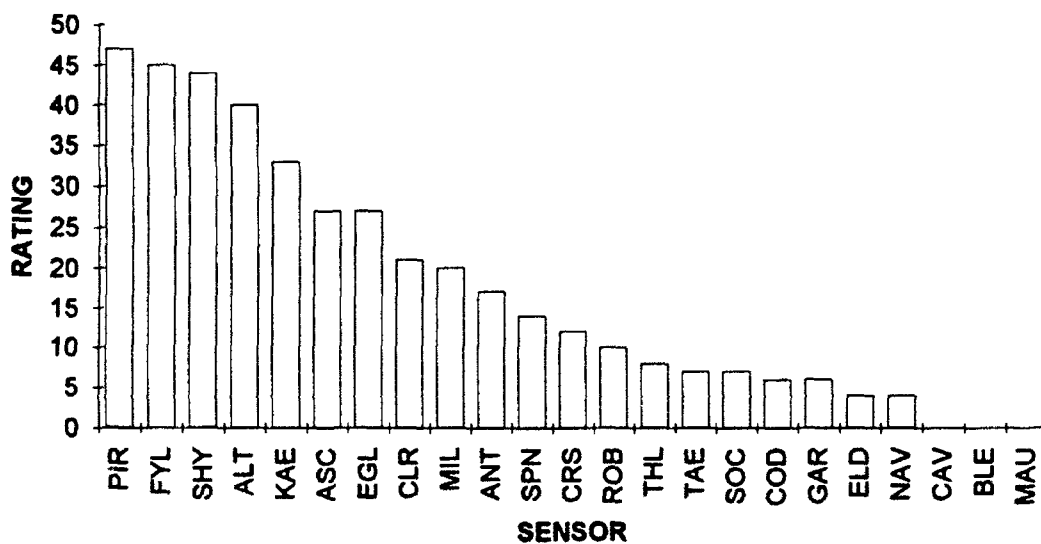


**Figure 1. Sensor Rating, All Factors Considered**

NRC examined the importance of each sensor in tracking folder based NFLs. The conclusions of this analysis suggest that there are three tiers of sensor importance for NFL tracking. Referring to Figure 1, NRC has defined the primary tier to include sensors with ratings greater than 30. The most important sensors for NFL tracking are Pirincliik, Fylingdales, Shemya, ALTAIR and Kaena Point. These four sensors are the highest rated contributors to the generation of Elset-1 on NFLs. A major reason for these sensor's importance is their geographic locations that cover the ground traces of the NFLs from the established Soviet and Chinese launch sites. The second tier of sensors, with ratings between 10 and 30, is composed of Ascension, Eglin, Clear, Millstone, Antigua, Saipan (now deactivated) and CROSS. The third tier is composed of all other sensors. This analysis has permitted the sensor contribution to the NFL

mission to be explicitly quantified considering the variables of importance to the space surveillance mission.

#### 4.0 CONCLUSIONS

Following the development of the sensor importance in the individual mission areas, NRC evaluated the feasibility of combining the importance in these discrete missions to develop an overall sensor rating scheme. Because the various space surveillance functions analyzed in this report are diverse in requirements and importance, this concept did not prove feasible. The main reason for this is that developing a unified rating scheme would have involved prioritizing the space surveillance mission areas, a most difficult task, and one with no correct answer. For example, tracking new launches could be assessed to be the most important SSN mission, with other missions of lower priority. Given this assumption, data from sensors primarily providing catalog maintenance support could be regarded as unnecessary, and therefore could be eliminated. The result would be a degraded satellite catalog, with a portion of the satellites not being tracked. This would increase the unknown target background and potentially result in not tracking the new launch in a timely fashion.

The synergy between space surveillance functions is significant, making a unified rating scheme difficult. Consideration was given to rating all space surveillance mission areas at the same level. However, the outcome of this approach would rate a sensor with mediocre performance in both areas higher than a sensor that was rated the best for catalog maintenance with very low ratings in the other area. For this reason, NRC did not develop a unified rating scheme. The factors discussed above suggest that a mix of sensors is required to provide adequate space surveillance support.

In conclusion, the set of sensors assessed to be most important in all mission areas are, in no order of significance: Pirinlik, Fylingdales, Shemyz, Eglin, Cavalier, NAVSPASUR and other sensors with a deep space capability. Other sensors may be of importance to specific missions, but this list represents the set of "core" sensors around which the current SSN performance is dependent. If any of these sensors were to be deactivated, significant impacts to aspects of SSN mission satisfaction are probable, unless the sensor is replaced with a sensor with very similar operating characteristics.



## NMD-GBR: New X-Band Sensors at Sites in CONUS and USAKA for Space Surveillance

J. Krasnakevich (Raytheon), D. Mathis (TBE), D. Sloan (GPALS PEO), D. Greeley (Raytheon),  
D. Rypysc (Raytheon), F. Steudel (Raytheon)

### 1.0 Summary

The U. S. Army, GPALS PEO, has recently awarded a contract to Raytheon Company to develop the new GBR Family of Radars which consists of three Theater Missile Defense Ground Based Radars (TMD-GBRs), one National Missile Defense Ground Based Radar (NMD-GBR) for use as a DEM/VAL sensor at U.S. Army Kwajalein Atoll (USAKA) facilities and an option for another NMD-GBR to be deployed in continental United States (CONUS). The required milestones in the contract and the proposed completion dates for all five radars are summarized in Figure 1. Recent changes in Raytheon plans may result in a slightly reduced schedule for the TMD configurations. Some adjustments in priorities and funding may result in a delay by the Government to exercise the option for the CONUS based NMD-GBR development.

The DEM/VAL NMD-GBR, also referred to as GBR-T ("T" for test) is scheduled for completion of integration and test at USAKA in 1995. The GBR-T configuration replaces the GBR-X radar previously scheduled for deployment at USAKA in support of DEM/VAL activity for Strategic Defense System Phase I deployment. The GBR-X procurement was canceled by the Government due to changes in requirements and implementation of a new architecture for GPALS.

This GBR-T deployment like GBR-X is planned to be on Building 1500 at Kwajalein in the Marshall Islands.

Although the GBR-X redirection to GBR-T delayed the deployment of an X-Band phased array at USAKA, it provided an opportunity for the U. S. Army to implement new design features which improve the capability of all GBRs in this procurement to perform space surveillance and other range sensor functions needed at USAKA and other deployed sites.

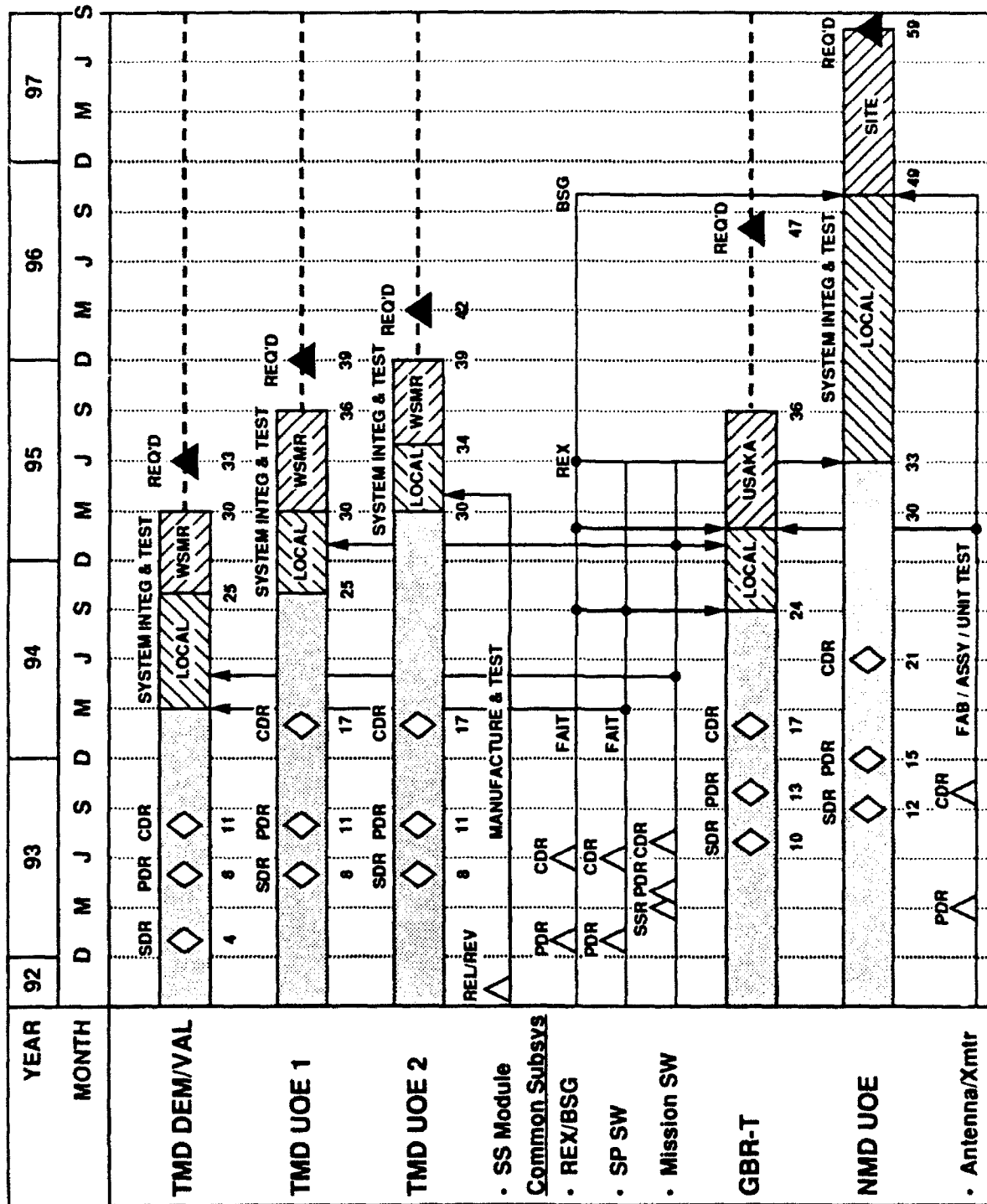
As a result all five radars are state of the art phased array radars operating at X-band that have a number of unique operating features and application flexibility which will become available in a few years to support space surveillance applications as well as other missions.

This presentation defines the new GBR program and describes the radar characteristics and performance. The new design features are described including the enhanced architecture, programmable signal processor, new search capability (e.g. enhanced detection of NFLs (New Foreign Launchers and orbital debris), data processing configuration, recording of both pre and post pulse compressed data, imaging capability and GBR-T range networking with the existing KREMS sensors and KMR facilities using the KMCC (Kwajalein Mission Control Center) which is being developed by MIT/LL.

One application of interest for NMD-GBR at USAKA and the CONUS based site(s) is to provide orbital debris measurement for use in a collision avoidance system being developed by NASA.

Over the past several years Raytheon has analyzed the orbital debris measurement requirements being formulated by NASA as part of the GBR-X Program and recently Raytheon updated this analysis for the new NMD-GBR configuration.

This presentation also provides a summary of the orbital debris measurement capability of the NMD-GBRs in developing an orbital debris catalog and for use in collision avoidance applications.



GBR92-1124-1

FIGURE 1 Solid-State TMD Radar and TWT NMD Radar Development Schedule

The presentation addresses coverage requirements for high drag objects, radar sensitivity requirements, electronic scan benefits for efficient search and track operation, frequency assessments and the application of distributed network of sensors for collision avoidance.

## 2.0 NMD-GBR Configuration

The NMD-GBR design is based on Raytheon's past design and development primarily on GBR-X and related programs like Cobra Dane System Modernization.

Many of the existing hardware designs from GBR-X were applied with minor adjustments to meet the performance requirements for the NMD-GBRs. For example, the NMD-GBR utilizes the TWT and phase shifter designs developed on GBR-X in the array. However, because the requirements for the NMD-GBR imposed a medium field of view (MFOV) operation instead of the GBR-X reduced limited field of view (LFOV) capability, the multi-element phase shifter assembly (MEPSA) and some of the control circuitry has to be redesigned.

Similar modifications were needed in other hardware designs like the receiver/exciter and beam steering generator.

The software design is also based on previous development efforts. The new GBR family software is required to be developed in Ada. Although most of the discrimination, imaging, classifications, resource management and radar scheduling algorithms were directly transferable from GBR-X to the GBR family, the GBR-X software was developed in Fortran.

This conversion challenge was overcome by a combination of ways which include:

- Application of previous designs when code could not be converted
- Select conversion of Fortran to Ada
- Use of equivalent code on Cobra Dane available in Ada

In addition, we were fortunate to utilize existing COTS software employed on Cobra Dane for the real time operating system and the data processing support environment.

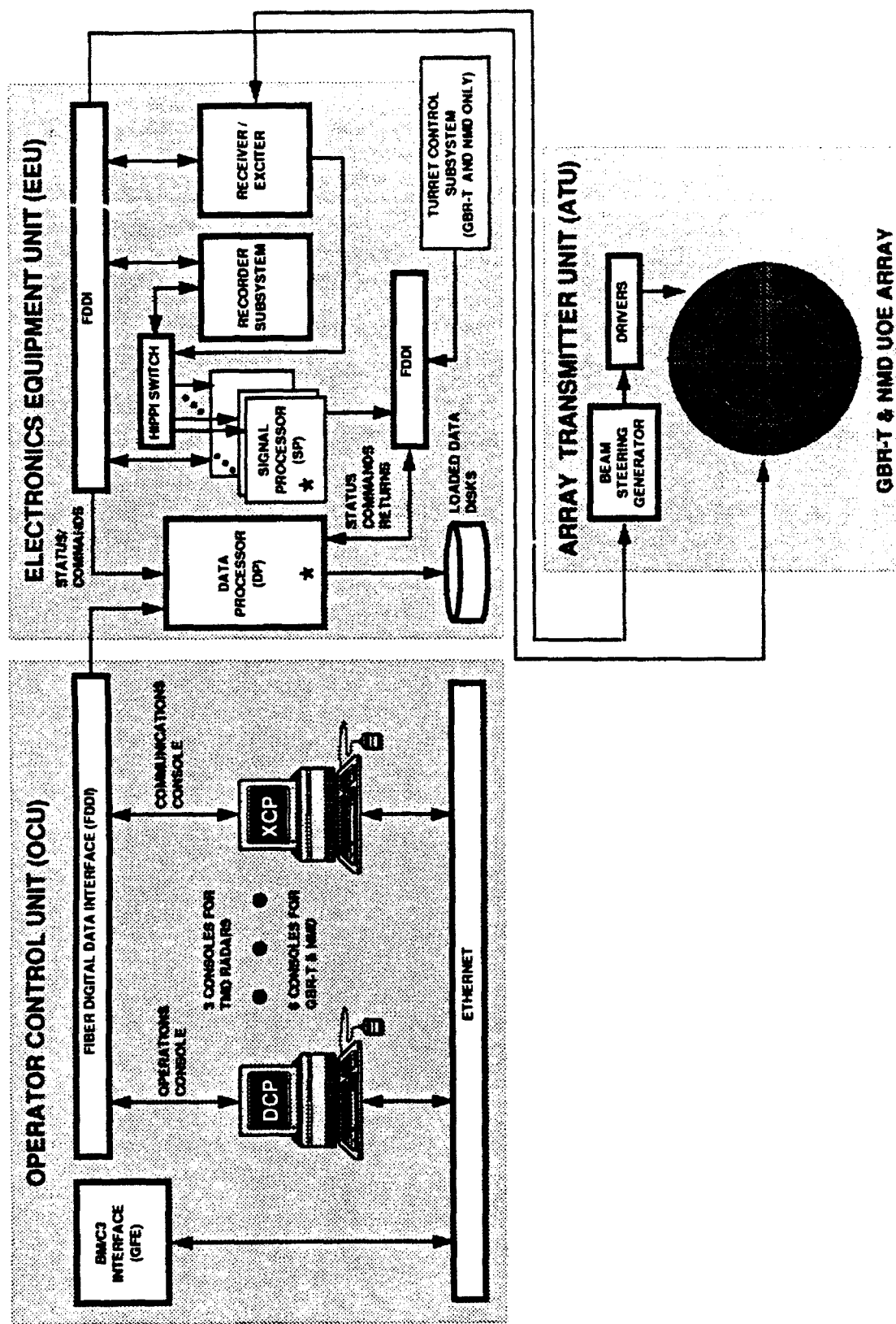
The use of existing designs provided Raytheon with a unique advantage to achieve a challenging schedule, control development cost and reduce risk on the program.

The resultant NMD-GBR design utilizes 48 TWTs which generate 2.4 MW peak power and has an 83.3M<sup>2</sup> array populated with approximately 55,000 active phase shifters. This configuration has a single pulse sensitivity to detect and track a typical ICBM at horizon (over 3000 Km range).

The design uses state of the art data processors, signal processors and workstations in all configurations (TMD and NMD) that provide substantial margin for future mission growth and concurrent operation in peacetime of collateral missions (e.g. concurrent catalog maintenance and orbital debris measurements).

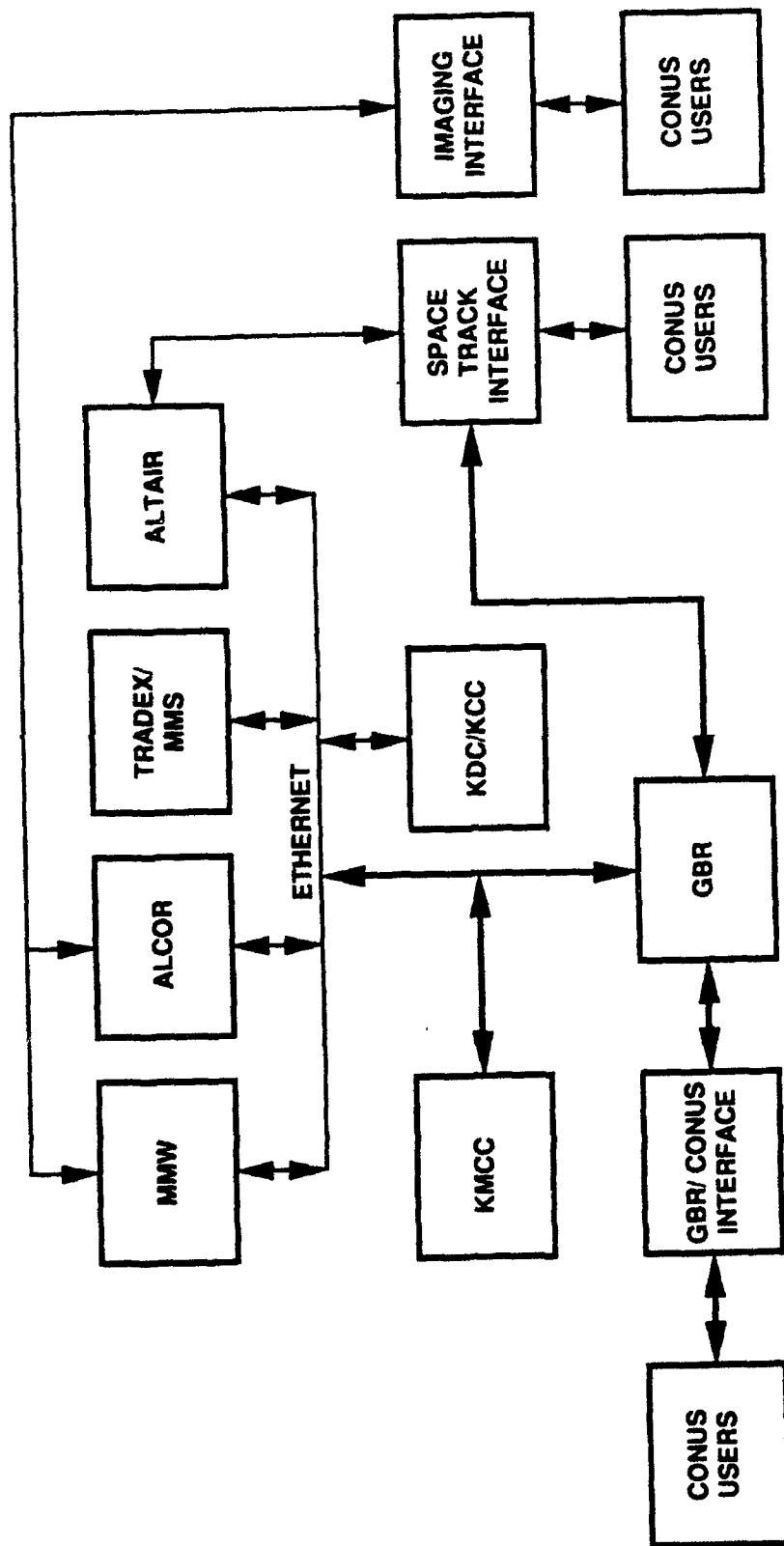
The NMD-GBR block diagram is shown in Figure 2. This diagram illustrates the integration of major system elements in the design and the interface with external BM/C<sup>3</sup> facilities or KMCC at USAKA.

The KMCC interface can be implemented in a form similar to the notional configuration depicted in Figure 3. In this way, the NMD-GBR at USAKA can be integrated with the existing KREMS radars.



GBR92 1094

FIGURE 2 NMD-GBR Block Diagram



GRR92-1159

FIGURE 3 NMD-GBR Interfaces with KREMS Radars

The recording system for the NMD-GBR is being enhanced to provide full capability to record all raw A/D data, select post pulse compressed data for rapid post mission analysis and DP activity log.

The signal processor design is being developed using a programmable array of massively parallel processors. This approach provides the flexibility to change the signal processor execution in the future to adjust to changes in mission and use of the GBRs.

Flexible priority driven resource management and radar scheduling design is being provided using mission profiles to control execution as illustrated in Figure 4. This design approach allows for definition in the mission profiles mission-specific or application specific operating rules which schedule search and execution activity.

### 3.0 TMD-GBR Configuration

The TMD-GBR design retains maximum commonality with the NMD-GBR. Approximately 75% of the software is expected to be common and most of the hardware utilizes common designs between all configurations.

The major differences between the TMD-GBR and the NMD-GBR are in the array and in the facility where the radar equipment is located. The TMD-GBR utilizes solid state transmit/receive modules in the array design and is road transportable with a C-130 air transportability requirement, whereas the NMD-GBR is fixed based and is mounted in a turret with virtually full mechanical coverage in azimuth ( $\pm 178$  deg) and in elevation (horizon to zenith). The TMD-GBR typical deployment is shown in Figure 5.

The TMD-GBR UOE configuration has a significantly smaller array than the NMD-GBR and generates much less peak power which results in a significantly reduced sensitivity in comparison with the NMD-GBR.

Nevertheless, the TMD-GBR with a  $9.2\text{M}^2$  aperture utilizing 25,344 T/R modules with 9.5 watt peak power capability can still have adequate single pulse sensitivity to detect and track a typical TBM at 1000 KM.

This sensitivity results in an adequate range for operation of the TMD-GBR for many space surveillance missions especially for low earth orbit measurements.

### 4.0 Analysis of Orbital Debris Applications of the NMD-GBR

Raytheon reviewed the orbital debris measurement requirements and developed a preliminary operational concept. We also analyzed search, track and debris catalog maintenance operation for various candidate radars.

Our analysis indicates that it is desired to achieve an operating range of 2000 KM on a -40 dBsm object RCS with a single pulse signal to noise ratio greater than 0 dB to minimize integration loss using coherent integration for about a one second limit. The preferred frequency for operation was determined to be at X-band.

Our analysis shows that the preferred acquisition approach is to search near zenith from 300 to 600 KM in order to minimize  $R^4$  loss. We concluded that the NMD-GBR sensitivity and beam agility is desirable to minimize the time needed to detect and catalog the debris.

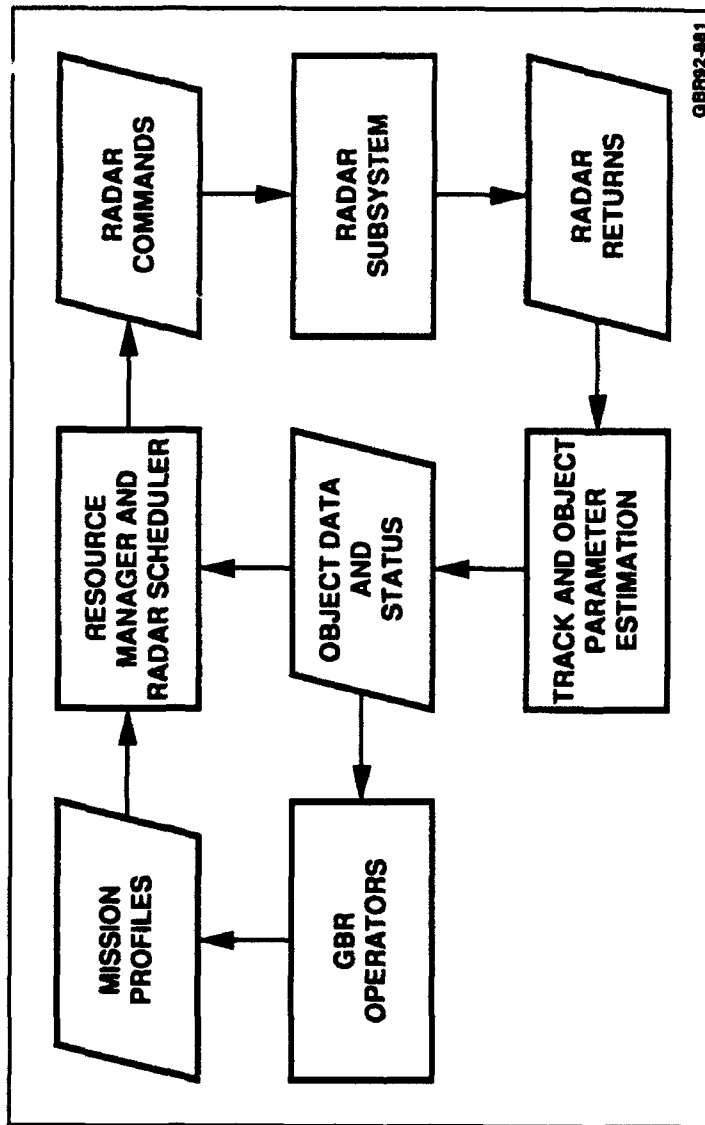
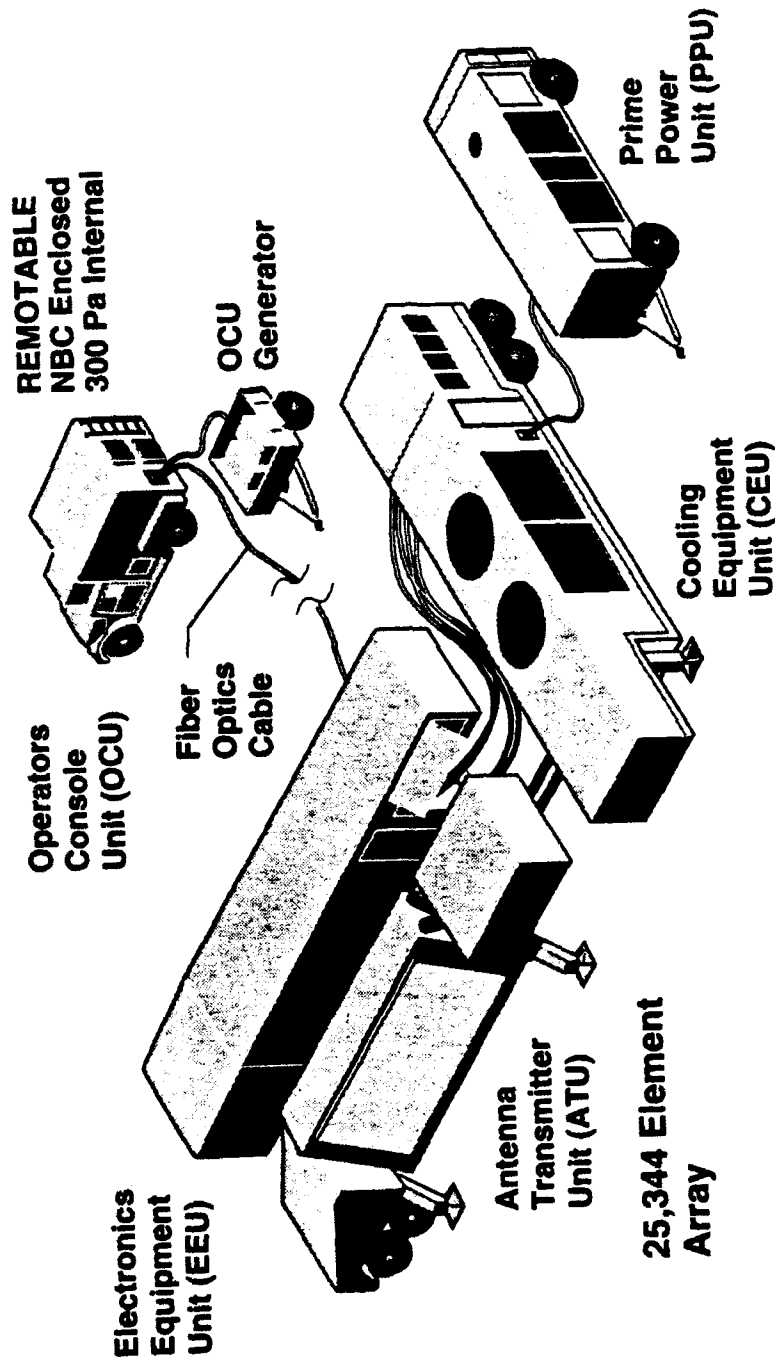


**FIGURE 4 Flexible Mission Profile Control of Radar Execution**

## UOE As Deployed



GBR92-1096

FIGURE 5 Illustrative TMD-GBR Physical Deployment



In this optimal search operation the radar is required to utilize 500 beams per second using a  $\pm 5$  degree field of view which is well within the NMD-GBR capability.

In order to establish the orbital element set the approach includes the following steps:

- Search as described above
- Upon detection schedule verify waveform
- Upon verification track debris
- Predict error at next observation
- Maintain track to minimize reacquisition load
- Estimate orbital element sets
- Update time for next observation
- Update as needed by object drag

Raytheon also considered locations of sensors along the equator and identified optimal locations to maximize performance and developed orbital debris catalog maintenance requirements. We believe that the planned NMD-GBR deployments at USAKA and at Grand Forks are well positioned for effective integration into a larger network.

## 5.0 Conclusion

The GBR Family of Radars have many unique features and capabilities which can be utilized for space surveillance applications in the future.

Although the TMD-GBRs are smaller in size and have significantly less sensitivity than the NMD-GBRs, they still have more than adequate capability for use on targets at lower altitudes.

The orbital debris analysis illustrated shows one possible application of the NMD-GBRs. Other missions that can be supported include NFL detection, track, imaging and catalog maintenance. We are aware of new defense oriented missions beyond BMD applications that are being evaluated by other potential users of the GBR family of radars.

## Recent Improvements at ALTAIR

R. B. McSheehy, S. J. Chapman (Lincoln Laboratory, Massachusetts Institute of Technology)  
R. M. Anderson (GTE Government Systems)

The work was sponsored by the U. S. Army Kwajalein Atoll, Department of the Army, under Air Force Contract F19628-90-C-0002.

### Introduction

Three significant improvements have been made to the ALTAIR radar during the past year. Improvements to the signal system, particularly with respect to new capabilities that have resulted from the signal system upgrade; improvements in ionospheric compensation that enhance metric accuracy and sensitivity; lastly, improvements in the UHF transmitter, and its implications for ALTAIR's performance.

### The ALTAIR Signal System Upgrade

As a result of the ALTAIR Signal System Upgrade (SSU), the new signal processors became operational this spring. The SSU is a continuing, multiyear project designed to replace the existing mélange of pulse compression and processing systems with a single flexible and maintainable system and to upgrade ALTAIR's real-time programs (RTPs).

The old ALTAIR signal-processing systems are shown in Figure 1.

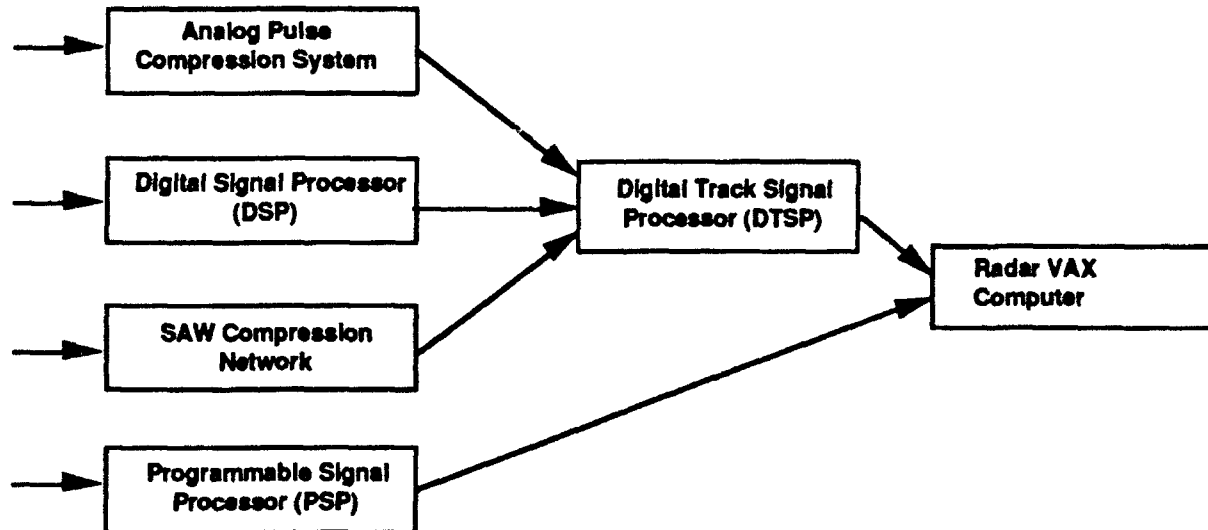


Figure 1 - The Old ALTAIR Signal-processing System.

These systems have grown as the radar added new capabilities. By the late 1980s, the radar had four different parallel pulse-compression systems:

1. Four waveforms (U3, U15, V6, and V30) were compressed by analog lumped-constant compression networks, which were installed in the late 1960s when the radar was originally built.

2. Two waveforms (U238 and V238) were compressed by an obsolete early-1970's vintage digital signal processor.
3. One waveform (U120) was compressed by a surface acoustic wave (SAW) device, which was installed in the mid-1980s.
4. Four waveforms (U1000, U400, V600N, and V600W) were compressed by the Programmable Signal Processor (PSP), a late-1970's vintage array processor.

The compressed pulses from the first three pulse-compression systems were fed into a Digital Track Signal Processor (DTSP) for noncoherent integration, detection, range marking, and monopulse angle calculation. The DTSP was itself of early 1970's vintage and was quite difficult to maintain. Pulses that were compressed in the PSP were also integrated, detected, and range marked within the PSP.

The new ALTAIR Signal System is shown in Figure 2. It replaces all four of the old pulse compression networks with a single Universal Signal Processor (USP). The USP consists of eight parallel channels (UHF and VHF, PP and OP, AZ and EL). Each channel contains a 3072-tap Finite Impulse Response (FIR) filter, permitting it to compress any waveform with a time-bandwidth product less than or equal to 3072. The USP can compress any existing ALTAIR waveform, and has room for growth.

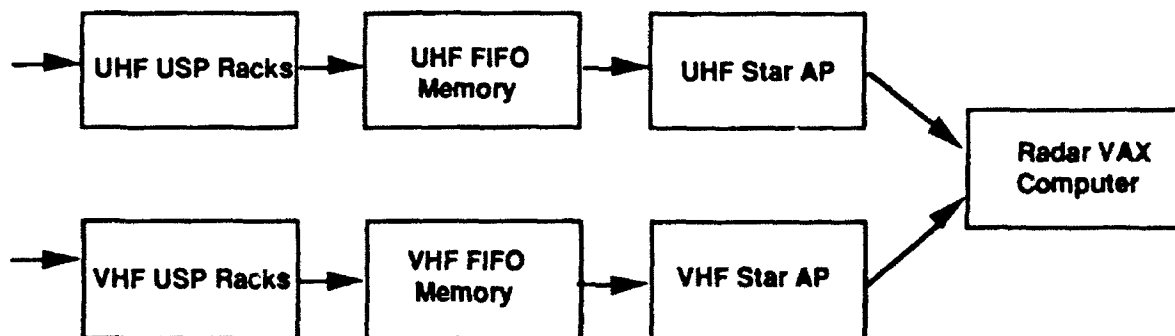


**Figure 2 - The Upgraded ALTAIR Signal-processing System.**

The output of the USP is fed through a pair of First-in First-out (FIFO) buffers into two Star VP-2 Array Processors (APs). The Star APs perform coherent or noncoherent integration, detection, range marking, and monopulse calculations, then report the results to the RTP running in the radar VAX computer. The Star APs are programmed in a FORTRAN-like language, and they are an order of magnitude more flexible than the DTSP and PSP that they replaced.

#### New Near-Earth Waveforms

The flexibility of the new signal system has made possible the installation of a new set of near-earth and reentry waveforms with increased sensitivity and bandwidth compared to the waveforms available under the old signal system. All of the new waveforms are up-chirps and all have Hamming weighting applied. A table of the new waveforms is shown below.

**Table 1 - New Near-Earth Waveforms**

Name	Length ( $\mu$ s)	BW (MHz)	Max PRF	Use
U1000M	1000	1	50	Acq
V260M	260	1	50	Acq
U150	150	18	333	Exo trk
V40	40	7.06	333	Exo trk
U15	15	18	1488	Endo trk
V6	6	7.06	1488	Endo trk

The new near-Earth acquisition waveforms are U1000M and V260M. U1000M is 9 dB more sensitive than the old UHF acquisition waveform (U120); V260M is both slightly more sensitive and of higher resolution than the old VHF acquisition waveform (V238). The net effect of this change is to make near-earth acquisitions and New Foreign Launch (NFL) handovers easier and smoother.

The new near-Earth tracking waveforms are U150 and V40. They are both more sensitive than the waveforms that they replaced (U120 and V30), yet maintain the same range resolution. The new waveforms described above have already been implemented and are in use during routine SPACETRACK operations.

#### Deep-space VHF Tracking

There has been interest for some years now in developing a deep-space VHF tracking capability. The capability would have two purposes: to provide a real-time ionospheric correction to improve UHF metrics and to gather RCS information.

In the new signal system, the UHF and VHF signal paths are essentially identical. This design makes it relatively easy to develop a new deep-space VHF tracking capability. The Star AP code, which contains all of the complex signal processing, will be completely identical in both the existing UHF deep-space system and the new VHF deep-space system.

A substantial amount of work is still required on the radar VAX computer to support deep-space VHF tracking. A second tracker must be added to the VAX for the VHF information, and a display must be provided for the VHF information. Because the VHF signal is 17 dB down relative to the UHF signal, a method will have to be developed to specify integration times for VHF independently of integration times for UHF.

#### High-Resolution Deep-space UHF Waveforms

The old PSP pulse compression system limited the maximum resolution available during deep space satellite tracking. A 1000  $\mu$ s, 50 kHz waveform (U1000) was used for acquisition, and a 400  $\mu$ s, 250 kHz waveform (U400) was used for tracking. While these waveforms were adequate for most deep-space tracking tasks, the operators experienced frequent problems with interference between unresolved objects during transfer orbits and right after injection into final orbits.

The new signal system provides much higher resolution waveforms than the old system did. With the new system, it is possible to develop a high resolution, 400  $\mu$ s, 5 MHz waveform with

20 times the range resolution of the existing U400. This waveform will be added to the deep-space tracking system to allow the easy separation of closely spaced objects when necessary. The new waveform will be the same length as the existing tracking waveform (400  $\mu$ s), so the sensitivity of the system with the new waveform will be identical to that of the system with the current waveform.

### Improvements in Ionospheric Compensation

In the past year, two significant advances in ionospheric compensation have been made at ALTAIR. The first achievement involves the use of a new Global Positioning System (GPS) receiver that can track up to eight GPS satellites simultaneously, and receive the two-frequency L-band information from each satellite. The two frequency information can be used to obtain total electron content along the line of sight to the GPS satellite, as well as correct errors in radar range, range rate, and elevation measurements. The method used to implement these corrections will be explained in this paper.

In addition to the improvements to radar observables, a new technique has been created that allows one to compensate for pulse distortion due to ionospheric dispersion. The amount of ionospheric dispersion can be predicted by a model or by real-time measurements, and then compensation for the effect can be made in the transmitted waveform. The method of implementation for this improvement will also be described in this paper.

### Use of GPS Satellites

ALTAIR has obtained an Allen Osborne Associates model ICS-4Z mini-rogue ionospheric calibration system/GPS receiver that tracks up to eight GPS satellites simultaneously. This receiver can supply ephemeris data and total electron content data to the ALTAIR VAX 8650 radar computer. Historically, ALTAIR has used a Stanford Telecommunications GPS receiver to obtain ephemeris information in order to evaluate the metric performance of the radar. Radar tracks of the GPS satellites are compared with state vectors derived from the GPS element sets in order to accomplish this. In the past the element set information has also been used to calibrate the ionospheric model.

The residual range error obtained from the above procedure is considered to be due to ionospheric delay; accordingly, once every four hours throughout the day the ALTAIR ionospheric model is recalibrated to eliminate any measured range error. Updates are not performed during the nighttime hours due to spatial and temporal nonuniformities in the ionosphere. These nonuniformities could cause a calibration to be valid only for a very short period of time or for a small part of the sky. Between the hours of 8 PM to 8 AM, local time, the ALTAIR ionospheric model has been used with no updates. Historically, ALTAIR's range bias sigma is about 50 m, due to these infrequent ionospheric updates.

The ionospheric model uses a quantity termed DRV0, which is the expected correction to the VHF range for a target outside the ionosphere, at zenith. All corrections to either the UHF or VHF range, range rate, or elevation are computed in terms of DRV0. DRV0 is computed continuously throughout the day. The values follow a basically sinusoidal shape; although the nighttime values are limited to a minimum value. Calibration of the ionospheric model essentially consists of modifying the current DRV0 value by an appropriate scale factor. In use, DRV0 is adjusted for the hour angle of the object in track, so that an object that is low on the horizon and may be affected by an ionosphere that is one or two hours earlier or later than that at the local vertical, receives the appropriate correction.

When each of the Total Electron Content (TEC) values are obtained from the GPS receiver, the associated element set for each satellite is used to obtain the hour angle of the satellite. The

ALTAIR ionospheric model is then used to map the TEC value to a corresponding TEC value at the local vertical and then converted to a DRV0 value. These DRV0 values are then averaged to obtain a new estimate of DRV0. This process is repeated once a minute, 24 hours a day. This system is being used experimentally at this time. It is expected that the range bias sigma will be substantially improved with these more frequent ionospheric updates and that routine use of this new method of calibrating DRV0 will occur soon.

### Dispersion Compensation

The ionosphere acts as a dispersive medium at UHF and VHF. Because it is a plasma, the refractive index is less than one, and the group velocity is decreased while the phase velocity becomes greater than the speed of light. The result of these effects is the well-known radar range error due to the slowing of the group velocity and the range rate error due to errors in coherent Doppler tracking. Both of these are corrected by the ionospheric model. Elevation error is also corrected by a knowledge of the group velocity change. Another error is introduced by the dispersion caused by the change in phase velocity. The phase velocity error is frequency dependent and is therefore a significant problem in wideband VHF waveforms.

It has been shown<sup>1</sup> that ionospheric dispersion can increase the pulsewidth and decrease the peak height by a factor of:

$$F = [1 + (\frac{2\Delta R}{w_0 c T})^2]^{\frac{1}{2}}$$

Where  $w_0$  is the transmit frequency,  $c$  is the speed of light, and  $T$  is the compressed pulsewidth and  $\Delta R$  is the range error due to group delay. When transmitting the V30 waveform, a 7.06 MHz linear FM chirp, ionospheric dispersion can result in a decrease in measured RCS by 5 to 7 dB. This decrease is due to the received waveform being mismatched in frequency with the receiver matched filter. As the waveform sweeps in frequency, the amount of phase shift changes, resulting in a different slope than intended for the transmitted waveform. Because the ionosphere causes the phase velocity to increase, the frequency slope is greater than expected. The resulting mismatch in the receiver leads to pulse broadening and a resultant decrease in observed RCS.

The Digital Waveform Generator, part of the signal system upgrade, adjusts the transmitted waveform to precompensate for ionospheric dispersion. Estimates of DRV0 can be obtained from real-time, two-frequency track information, or they can be obtained from the ionospheric model. The DRV0 values are converted to DRV values (VHF range correction along the radar line of sight), and then to adjustments to the transmitted slope frequency. Figure 3 shows the improvement obtained in pulsewidth and amplitude when using the new dispersion correction capability.

---

<sup>1</sup> T. M. Pass - "Ionospheric Correction Using Two Frequency Measurements", 25 Aug 1971, MIT Lincoln Laboratory Project Report PPP-112.

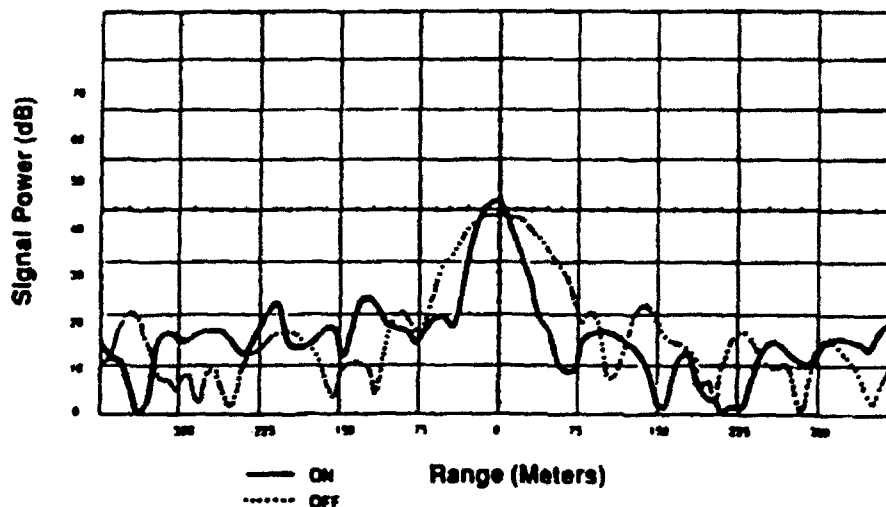


Figure 3 - Ionospheric Dispersion Correction.

#### ALTAIR UHF Transmitter Expansion

##### History

ALTAIR's original UHF transmitter consisted of a single Varian VA812 klystron. This tube operated at a 415 MHz center frequency with a peak power output of approximately 20 MW and a maximum pulsewidth of 40  $\mu$ s. With a maximum duty factor of 0.005, the average output power was limited to approximately 110 kW. This was somewhat of a liability for the new space surveillance operation that began in 1982.

During 1982, the UHF transmitter from the USNS *Arnold* was declared surplus and became available. This transmitter offered several significant advantages over ALTAIR's single-tube klystron for example, graceful power degradation due to a failure of any single Travelling Wave Tube (TWT) or group. The long pulse, high duty cycle, high average power capability of the new transmitter resulted in an overall power increase of 5 dB over the klystron transmitter.

The USNS *Arnold* transmitter was installed during late 1983, and became operational in November of 1984. During its first year of operation, the TWT transmitter was used primarily for deep space operations and the klystron transmitter was used for near-earth tracks. During this time frame, new waveforms were developed and implemented that utilized the long pulse capability of the TWT transmitter to improve its single-pulse sensitivity. Once this waveform upgrade was fully implemented, the klystron transmitter was decommissioned.

The configuration of the USNS *Arnold* transmitter consisted of 24 Raytheon PPA-200 TWTs arranged in three groups of eight tubes each. Each group was self contained, having its own modulator, power supply, and energy storage complement. The RF output power of each pair of TWTs within a group was combined in a 3 dB coaxial hybrid. These combined outputs were subsequently combined again in a series of similar but higher-power hybrids to produce a single output from each group of approximately 1.6 MW.

The outputs of each of the three groups were then combined in another series of hybrids to produce a final output power of approximately 4.8 MW peak (240 kW average). Several major modifications have since been incorporated to improve even further on system reliability. The most significant modification was the addition of an individual solid-state RF driver for each of the 24 TWTs. This gave the transmitter "graceful power degradation" in the truest sense.

In mid-1991, the UHF transmitter from the USNS *Vandenberg* became available. This was the sister ship of the USNS *Arnold*; and its UHF transmitter was identical to the ALTAIR transmitter originally installed on the USNS *Arnold*. Obtaining this transmitter and its spares has many advantages for ALTAIR. No spares existed for many of the ALTAIR transmitter components. Portions of the new transmitter could be installed at ALTAIR, contributing to an overall increase in sensitivity. The remaining transmitter components could be utilized to support the installed system.

The decision was made to remove the transmitter hardware from the *Vandenberg* and ship it to ALTAIR. Once this is accomplished, an additional group of eight TWTs will be integrated into the existing UHF TWT transmitter, increasing the average power of the system by approximately 60 kW or 1.25 dB, as shown in Figure 4. Additionally, failure of a group of eight TWTs in the new configuration would result in a power output only 1.25 dB down from our current full-up power.

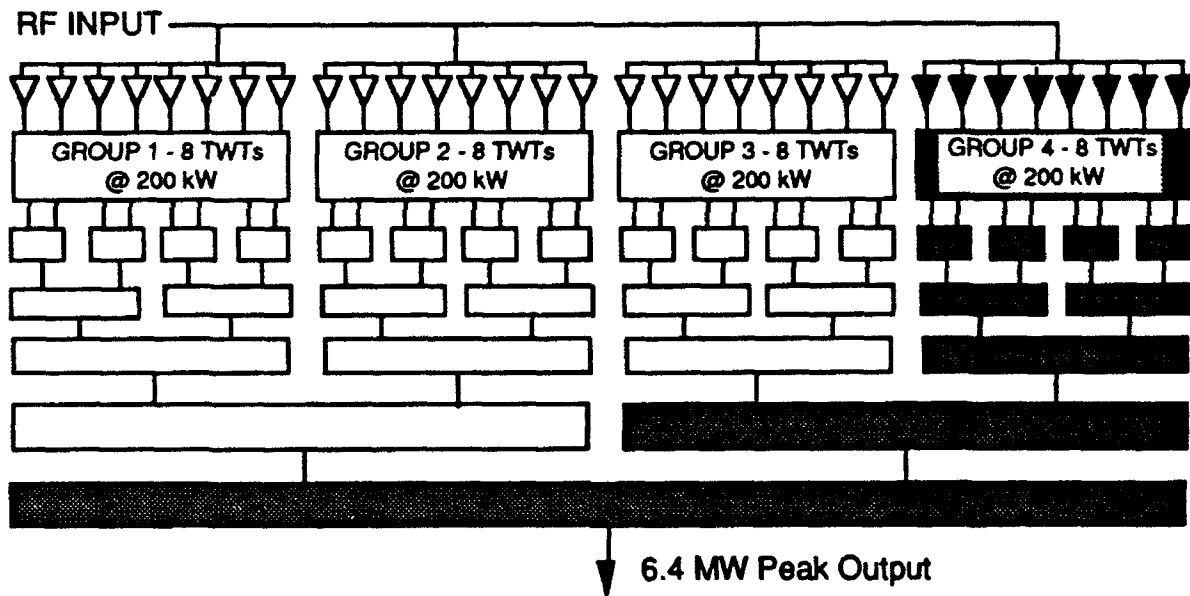


**Figure 4 - ALTAIR Four-group TWT Configuration**

### Modifications

Accommodation of the newly acquired transmitter hardware required some major modifications to the ALTAIR facility and existing transmitter control hardware. These modifications included expansion of the current TWT transmitter second and third level decking to support the new RF amplifier, power distribution unit and capacitor filter cabinets.

A complete redesign of the high-power microwave combiner assembly was required to accommodate a new power-combining scheme. Many of the microwave components from the *Vandenberg* required rework to operate satisfactorily at the ALTAIR frequency.



### Additional Benefits

Many spare parts that were previously unavailable are now on hand to support the modified transmitter. An additional 30 TWTs in various condition were also made available as part of the transmitter equipment. Of the first eleven of these TWTs that were shipped to site, all have been processed and 10 of the 11 are good spares. One tube is currently installed in our existing transmitter. The remaining 19 TWTs are expected to arrive on site within the next year, and it is anticipated that many of these will prove to be good spares as well.

### Operational Impact

The increased power output from the UHF transmitter upgrade will result in an increased sensitivity of 1.25 dB over the existing system. This increase will lead to a greater ability to acquire and track lower cross section objects and a reduction in the metric variance on low signal to noise objects. An overall reduction of as much as 33% in integration is expected when compared to the existing system, resulting in more tracks per hour.

Additional benefits of the upgrade become even more apparent when the loss of a single group is considered. In the present configuration, the loss of one group results in a reduction of power output from the nominal 4.8 MW to approximately 2.13 MW, a reduction of 3.5 dB. A similar loss of one group when the expanded transmitter becomes operational will result in a degraded output power from the nominal 6.4 MW to approximately 3.6 MW, a reduction of 2.5 dB. When the output of the upgraded system is compared to that of the existing configuration while each is operating in a degraded manner as outlined above, the new configuration is 2.3 dB better.

### Conclusion

As a result of ALTAIR's signal system upgrade, several new waveforms have been created that will improve ALTAIR's sensitivity and resolution for various applications. A new suite of software has been created to duplicate the New Foreign Launch (NFL) and Deep-space system capabilities with the new signal system; and these are now in use. A new operational Deep-space VHF capability will soon be created. Improvements in ionospheric compensation have provided the capability to significantly enhance Deep-space metric accuracy and wideband VHF sensitivity. ALTAIR's upgraded UHF transmitter will increase the radiated UHF power, resulting in the ability to track more satellites in Deep-space; and, in the event of tube failures, the new TWT configuration will make the transmitter system more robust than the present system.

## Enhancements to the ALCOR Imaging Radar

R. K. Avent, C. H. Moulton, M. D. Abouzahra (Lincoln Laboratory, Massachusetts Institute of Technology)<sup>1</sup>

### **1 Introduction**

The Kwajalein Atoll is located approximately 3500 km southwest of Hawaii and is home to four high-power instrumentation radars operated under the direction of MIT Lincoln Laboratory [1]. These four radars are part of the Kwajalein Missile Range (KMR), U.S. Army Kwajalein Atoll (USAKA), and are located on the northernmost island of Roi-Namur. They form the backbone of the Kiernan Re-Entry Measurements Site (KREMS). Although originally designed for ballistic missile data collection, each of these radars now support a wider variety of functions. One of the fastest growing areas within the current scope is the space surveillance operations.

The space surveillance operations consist of two major functions. The first function includes tracking new foreign launches, near-earth satellites, and deep-space satellites and requires a radar with large search volumes and long detection ranges. ALTAIR, which supports the largest portion of the KREMS-based U.S. Space Command operations, fulfills this category while TRADEX functions as a backup. The second function is Space Object Identification (SOI) and requires a high-resolution radar capable of generating range-Doppler images. Both ALCOR and MMW fulfill this need and are regularly tasked to provide range-Doppler images on foreign and domestic near-earth satellites. Table 1 lists ALCOR's operating parameters and illustrates the fact that its combination of range resolution and sensitivity makes it an excellent radar for imaging satellites. In addition, due to its near-equatorial location of 9 degrees N latitude, the viewing geometry on all near-earth satellites is extremely good. The level of support provided by ALCOR/MMW for U.S. Space Command has consequently increased steadily during the past years. For instance, the number of SOI tracks has grown from 60 in FY87 to 160 in FY92 and to an estimated 200 in FY93.

Lately, both ALCOR and MMW have been undergoing a number of upgrades to improve their ability to track and subsequently image satellites. A recent paper detailed the upgrades being conducted at the MMW radar, which include the installation of the dual-tube transmitter, the restoration of the 95 GHz system, and the increase in FM bandwidth to 2 GHz [2]. The purpose of this paper is to describe the modifications being conducted at the ALCOR imaging radar as they pertain to space surveillance operations. These modifications fall into the two broad categories: those currently completed and those planned for the upcoming year.

---

<sup>1</sup>This work was sponsored by the Department of the Army. The views expressed are those of the authors and do not necessarily reflect the official policy or position of the U.S. government.

ALCOR OPERATING PARAMETERS	
Frequency (GHz)	5.7
Peak Power (kW)	3000
Bandwidth (MHz)	512
Range Resolution (m)	0.5
Peak Range Sidelobe Level (dB)	-30
Antenna Gain (dB)	55
Beamwidth (mrad)	5.2
Maximum PRF	323
Single Pulse SNR on a 0 dBsm target at 1000 km range and 30 degree elevation (dB)	23
First Near Real-Time Image	Oct 84

**Table 1:** A list of ALCOR's operating parameters pertinent to range-Doppler image generation.

## 2 Recent Improvements

During the past two years there have been various improvements at ALCOR, resulting primarily from software modifications to the Real-Time Program (RTP). The impetus for these improvements are founded in the migration from the DDP 224 computer, which was coded in assembly language and fully utilized, to the upgraded Gould/Encore 9780. Once this upgrade was complete, significant capacity for RTP improvements existed because the Gould/Encore utilization was low, more memory was available, and the code was written in FORTRAN. The most modifications completed to date that significantly enhance the satellite imaging applications are (1) a 60% increase in the maximum radar PRF, (2) the addition of full angle sampling, (3) the capability to simultaneously track two targets on alternate PRIs and (4) the addition of extended NB PP sampling. Each of these topics, including the computer upgrade itself, will be discussed in the following section; current improvements will be addressed in the subsequent section.

### 2.1 Computer Upgrade

Prior to 1990 the ALCOR radar system was controlled by a pair of 1960s technology Honeywell DDP-224 computers. These computers restricted improvements at the radar because the RTP was written in assembly language, which made it difficult to modify, and memory was limited to 120 kbytes. In late 1988 an effort was initiated to replace the antiquated DDP-224s with a Gould/Encore 9780 system. This new system was sized to produce a CPU utilization of less than 50% in order to accommodate a number of long-term upgrades. The new system was deemed fully operational in the spring of 1991 and now provides a CPU utilization of 40-50% with a coprocessor utilization peaking at 70%. Both the hardware and software have been extremely reliable and a number of significant upgrades have already been accommodated.

In addition to the ALCOR computer upgrade, a new imaging computer was also installed during 1991. The motivation for this improvement was to port the imaging software to a Silicon Graphics (SGI) workstation. Prior to the completion of this modification, range-Doppler images were compiled on a Gould 6750 and required the printing of hard copies before the image parameters could be adjusted. Because this printing normally took on the order of 10 minutes/image, there was often a significant delay and effort in producing quality images. The implementation of the new capability using a graphics-based workstation permits adjustments to be made almost instantaneously and provides for much faster processing.

Although both the radar control and imaging computers were enhanced, there still existed an approximate 35-minute lag in transferring images to U.S. Space Command after the completion of a satellite pass. The reason for this delay is that ALCOR data is recorded to multiple 9-track ALCOR Signature Tapes (AST). A multiple drive system was required since the data rate exceeds a single drive capacity. The net result is that sequential PRIs are sometimes recorded on different drives. After the satellite pass is completed, then, a program that merges and time-aligns the two tapes is initiated. These processed tapes are read into the SGI and converted to a Calibrated ALCOR Data Tape (CADT). The CADT format is used by the Near Real-Time Imaging (NRTI) software. As can be seen, the majority of this 35 minute processing time was spent in tape transfers. Thus, in 1992 a modification was initiated that allowed direct recording from the Gould/Encore 9780 to the SGI workstation. With this new direct disk recording modification, data is transferred in real-time into a CADT format directly to the SGI via an HSD interface. As a result, average imaging times have decreased from 35 minutes to approximately 10 minutes for a 5-minute stable satellite pass.

## **2.2 PRF Increase**

The maximum PRF of ALCOR was recently increased from 203 to 323 Hz while maintaining the same peak power per pulse. There are plans for yet another increase to 400 Hz in the near future. The increase in PRF results in two immediate advantages for image generation. The first advantage is that there is less chance for Doppler aliasing, which can occur on large tumbling satellites [3]. The second advantage is that the higher PRF yields 60% more pulses for integration on weak targets.

The PRF increase was possible because of a number of peripheral modifications. One of the most important modifications was again the computer upgrade. The DDP-224 computers restricted the PRF processing to a maximum 203 Hz; however, in addition to the computer upgrade, modifications to the waveguide cooling system were also completed, allowing operations at high PRFs for sustained periods of time. The maximum video duty for the current FPA is 0.0048; the maximum RF duty is 0.0041. Although we have demonstrated video duties of 0.0045 and RF duties of 0.004 into a dummy load, we are currently restricting our operation to a video duty of 0.0043 until we have more spare FPAs at site.

Because ALCOR can transmit any combination of narrowband (NB), wideband (WB), doublet (DBLT) and beacon (BCN) pulses, a need for a PRF algorithm that protects the maximum duty limit existed. The resulting PRF algorithm inputs waveform type and not only generates the maximum PRF for the given waveform sequence but also accommodates dual-target track spacings up to 150 km. Earlier testing pushed the PRF to 380 Hz, which is the current limit of the Timing and Data Unit (TADU). With the new TADU this restriction will be removed, paving the path to a full 400-Hz operation.

### **2.3 Full Angle Sampling**

The ALCOR receiver consists of five channels, REF, AZ, EL, PP, and OP, of which the PP and OP channels form the signature data paths. Prior to the new computer upgrade, three WB contiguous PP windows and one OP window were fully recorded. Fully recorded in this sense means that all 170 samples per window were both sampled and recorded. On the other hand, only 10 samples about the target track point were sampled and recorded in the REF, AZ, and EL channels. Because of this sampling limitation ALCOR was not able to offset track or form optimal WB monopulse error calculations on extended targets.

Recently, a number of TADU database and hardware modifications were performed along with improvements in the RTP, allowing all 170 samples of the REF, AZ, and EL channels to be sampled and recorded. By implementing this modification the path is now paved for improved WB angle tracking on extended targets and more importantly, offset tracking. One application of offset tracking deals with extended targets larger than 120 gates but less than the full 170 gates. For targets this size, the extended WB mode has to be employed in which all three PP WB windows are sampled and recorded; however, the primary disadvantage associated with using three WB windows is that the direct recording capability can not be utilized. By offset tracking, the most in-range portion of the satellite can be moved to the front of the sampling window so that only one WB window is needed. Yet another application of offset tracking is that stable returns, such as outrange booms, can be tracked without the in-range portions lying outside the sampling window.

### **2.4 Dual Target Tracking**

ALCOR efforts in multitarget tracking were originally restricted to two closely spaced targets, one in NB/BCN and the other in WB. Initially, the capability to track dual targets with no waveform restrictions was added and then tested; however, the one limitation associated with this initial multitarget tracking capability was that for simultaneous tracks on beacon bearing objects, the beacons had to operate at the same frequencies. The constraint lies in the fact that multitarget tracking is implemented as a shared PRF task. The beacon synthesizers, although capable of switching code spacings on a PRF basis, were not able to switch frequencies at PRF rates. This restriction was recently removed when the old synthesizers were replaced with newer fast switching units.

One reason for having dual target tracking is to image satellites when dispensing a payload. By initiating a WB track on each object, simultaneous images of both objects could be generated. The only modification needed is to change the CADT generation program so it filters tracker pulses. A recent example was the space shuttle Endeavour mission, in which the Intelsat 6A satellite was to be picked up. Although the NRTI software allows multiple objects to be imaged during different sessions, dual tracks are easier in that the state vector for the second object would not have to be modified.

## **2.5 Extended NB PP Sampling**

The current PP data path consists of three separate branches routed through various delay networks so that three independent contiguous WB PP data windows can be sampled and recorded; however, in the case of the NB PP data path only one of these branches are utilized, and thus the receiver consists of only one NB PP data window. A number of years ago a modification was requested that would incorporate the three branches into the NB PP channel, resulting in three contiguous NB PP data windows. The impetus for this modification, of course, was that larger data windows meant increased probability of sampling on intercepts, deployments, and breakups. To this end, with the redesign of the new TADU, it was determined that in fact nine contiguous NB PP windows could be implemented for a total NB window size of 22.5 km [4]. As it turns out this was also an important modification for the new console, the reason being that the new scopes are digital; therefore a large acquisition window needed to be sampled for display.

The introduction of the extended NB sampling is important to SOI operations in that it will allow us to maintain the current level of functionality once we transition to the new console. The support to SOI will increase to an all-time new level of 200 taskings in FY93. This new level of tasking is possible only because of a new structure in which taskings are handled, i.e., ALCOR/MMW gets a list of weekly taskings and based on a database resident at the radar, these taskings are scheduled when possible. This structure differs from that previously used in that the KREMS Control Center (KCC) is not involved in most of these passes; therefore the radar has more flexibility in scheduling tasks. However, to execute the new structure ALCOR must be capable of acquiring the object on its own. The incorporation of the new 22.5-km window, coupled with coherent integration, allows ALCOR to acquire objects in range and thus permits the current structure to be used once we transition to the new console.

## **3 Planned Improvements**

The two major improvements now being completed are the console upgrade and the addition of coherent processing. Although these two improvements are integrated in that the coherent processor is hosted in the new console, this section will independently address each topic.

### 3.1 Console Upgrade

Because the current ALCOR console is 20 years old and has not appropriately evolved, it has been long proposed that a new integrated console was needed. This console brings to ALCOR a number of advantages. The primary advantage is that the input structures are generalized enough to support multitarget tracking, coherent processing and future system upgrades. In addition, because site displays are migrating from a Masscomp-based architecture to a SGI-based graphics system, the new console becomes a unified base upon which to incorporate the new site standards. Work has begun on the new console in mid-1992, and completion is expected in the late spring of 1993.

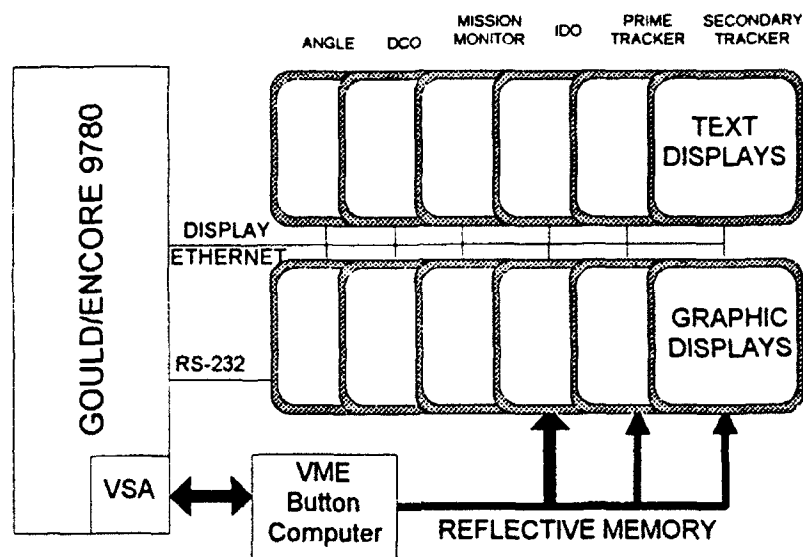
The new console consists of two displays per operator position. For the most part the upper display is textual and provides system status information, track file parameters and directing source data. The lower unit is typically a dedicated graphics display. Both range operator graphic displays are unified and consists of an A-scope and color RTI for each tracker. The ID Operator's (IDO) graphic displays will be driven by the coherent processor and is fully configurable in that various displays have been implemented to aid in the ID process. The current displays are a strip chart, color RTI, color DTI, color-coded stacked pulse display and real-time range-Doppler images. These range-Doppler images are useful for discriminating payloads in NFL launches where multiple targets are deployed. There is also a long-term plan to implement real-time bandwidth extrapolation methods to drive these displays. The real-time range-Doppler imaging will, for the short term, correct the state vector by phase referencing to a specific scatterer. Although this type of phase referencing can produce satellite images, a long-term goal of the new console is to implement real-time state-vector correction somewhat similar to Haystack.

Figure 1 illustrates the data flow for the new console. As can be seen, radar data is transferred to the range operator and IDO computer via a reflective memory link. This reflective memory serves as a data pool for the SGIs, the signal processing elements, and the new recording upgrades and is connected to the Gould/Encore 9780 using a VME-to-Sel bus Adapter (VSA). Peripheral information such as track files, recording system status, and button configurations is displayed on the text displays using an Ethernet link, which is connected to all graphics and text displays. Because of I/O overhead and latencies associated with the ethernet in the Gould/Encore, a RS-232 link sends angle information to that display.

### 3.2 Coherent Integration

To improve ALCOR sensitivity and thus increase the target acquisition envelope a coherent processor system is currently being developed at site [5]. This coherent processing system will have the capability to coherently integrate up to 256 pulses, noncoherently integrate up to 256 pulses, and also incorporate a post-summing option. In addition to the increase in detection range afforded by this processor, Doppler measurements to improve the tracking filter quality will also be provided. The digital A-scopes and color RTIs will be driven directly from the coherent processor as will the

tracking loop. In addition, the coherent processing system will provide a number of new digital graphics displays as discussed in the above section.



**Figure 1.** The network for the new C-band console.

Coherent processing is accomplished on a Skybolt application accelerator hosted by an SGI Crimson workstation. Data is provided to the Skybolt over the reflective memory path that links the Gould/Encore 9780, the Skybolt application accelerator and the graphic display system as shown in Figure 2. Data transfer is accomplished once radar and control data are written into the reflective memory by the Gould/Encore. The Skybolt card then, based on input processing parameters, decides whether or not to move the data into its own memory and executes that decision. Once processing according to the control data is completed, the Skybolt IO Processor (IOP) moves the data back into reflective memory for the graphics display system and the Gould/Encore. The display system subsequently displays the integrated data while the Gould/Encore uses the information to close the tracking loop. The synchronization of data transfers is provided via mailbox interrupts provided by the reflective memory interface.

The Skybolt Arithmetic Processor (AP) actually performs the signal processing functions and will be coded to allow various input parameters concerning the data processing. This data processing begins with a phase correction algorithm, of which a number of methods exist. Cross-range FFTs are then performed and the resulting data can be post summed and peak picked. As in the phase correction stage, there are a number of candidate methods for Doppler collapsing of which most will be provided. Cross-range FFTs on the AZ and EL channels will also be performed to extract monopulse I and Q values.



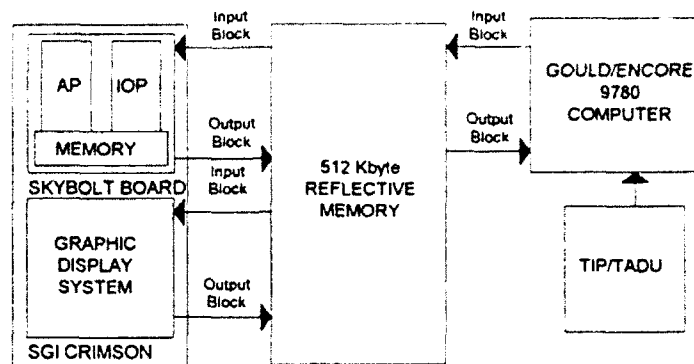


**Figure 2.** The architecture for the ALCOR Coherent Processor.

#### 4 Summary

This paper has attempted to describe a few of the modifications being implemented at the ALCOR imaging radar. Those modifications most influencing SOI operations have been discussed, although there are a number of additional upgrades that have not been addressed in this paper. For instance, ALCOR is aggressively replacing the old TADU system and eliminating the TADU Interface Processor (TIP). In addition, a new color weather integrator is being developed and will become part of the new console effort. With the addition of these new upgrades ALCOR has become a more flexible sensor and should be capable of providing high quality range-Doppler images to U.S. Space Command well into the future.

#### REFERENCES

1. Roth, K., M. Austin, D. Frediani, G. Knittel and A. Mrstik, "The Kiernan Reentry Measurements System on Kwajalein Atoll," *Lincoln Laboratory Journal* 2:2, pg. 247 (1989).
2. Jones, G.A. and M.D. Abouzahra, "Major Improvements at the KREMS Millimeter Wave Radar," *Proceedings of the 1992 Space Surveillance Workshop*, MIT Lincoln Laboratory Project Report STK-193, Volume 1, pg 239 (1992).
3. Boisvert, R.E. and R.K. Avent, "Recent and Planned Improvements to Satellite Imaging at ALCOR/MMW," *Private Communication*.
4. Kentosh, G., "NB Data Collection for 7.5 km Mod and TADU Upgrade", *KREMS Memorandum* AM1042, (1992).
5. Rejto, S.B., "Alcor Coherent Processor System", *KREMS Memorandum*, AM1080, November 19, 1992.

## Fiber Optic Phase Control of the Lake Kickapoo NAVSPASUR Transmitter

T.L. Washington, (Scientific Research Corporation),

A.A. Bocz, (Scientific Research Corporation),

C.C. Hayden, (Naval Space Surveillance Center)

### **1.0 INTRODUCTION**

Nine naval facilities constructed during the early 1960's currently provide the United States with the capability to accurately detect and track space-borne objects. The Navy is currently executing several concurrent modernization programs for these sites. The goal of these programs is to increase overall system operational performance and reliability. This document discusses the modernization of the phase monitoring and control system at the Lake Kickapoo Site which is the primary transmitting station in the NAVSPASUR sensor system and also the largest continuous wave (CW) transmitter in the world. The new system will utilize optical fiber signal paths to monitor and control the phase distribution for the Kickapoo transmitter.

### **1.1 Background**

The Naval Space Surveillance (NAVSPASUR) sensor system originated in 1958 as a research project; the goal of which was to develop, install, and operate a space surveillance system for the detection and orbital prediction of passive (non-radiating or noncooperative) satellites. The system was commissioned as an operational command in 1961 to provide the Naval fleet with the predicted orbital ground paths (ephemerides) of surveillance satellites for the purpose of denying potential enemies the exact position of naval vessels.

The NAVSPASUR system is comprised of equipments performing three operational functions: data acquisition of detected satellites is performed by a complex of three transmitting and six receiving stations located on a great circle across the southern United States; satellite detection and correlation with predictions is performed by high speed computers at the NAVSPASUR Center in Dahlgren, Virginia; data storage, retrieval, and updating of orbital elements of past, present, and future paths of all known orbital objects is also performed by the computer center at Dahlgren.

The NAVSPASUR system operates as a large interferometer which detects orbital objects whose paths cross the continental United States. Transmitting stations emit a continuous wave of energy in a fan-shaped pattern known as the NAVSPASUR "fence"; the north-south dimension of this pattern is very narrow and the east-west dimension is very wide. This fan-shaped pattern of energy consisting of the overlapping beams of both transmitter and receiver sites, illuminates all satellites passing through it. Some of that energy is reflected to the receiving stations. Each receiving station operates as an interferometer to measure the angle between stations vertical and an imaginary line to the object. The exact space-time position of an unpredicted object is then determined at the NAVSPASUR Center by triangulation of coincident data from two or more receiving stations. A very narrow beamwidth and controlled sidelobes are required from the transmitting stations to provide directed energy towards a narrow sector of space. This is the reason for modernization of phase control equipment at the primary transmitter site.

The Lake Kickapoo site is the primary transmitter station and is responsible for the majority of the total surveillance coverage. High power RF radiation is performed at this site with a two mile, linear phased-array antenna structure consisting of 18 bays of radiating dipole elements. The system relies on one common RF exciter located at a central location to feed each of the 18 bays via a coaxial cable distribution system. The transmitter delivers approximately 800 kilowatts of CW energy at a frequency of 216.98 MHz through 2,556 dipole elements; each with it's own 300 watt solid state amplifier[1]

For optimal performance, it is essential that all 18 bays of radiating elements transmit in phase to within a few degrees. In order to keep the phase constant at the center of each bay, the existing phase monitoring and control system samples the RF signal at the bay and returns it to the central location via calibrated coaxial cables. The return signal is phase compared to the RF source using a vector voltmeter. Using computer controlled phase shifters, the system computer controls the distributed RF based on information derived from the RF comparison. This group of electronics, inter-cabling, and interface components required to monitor and control the electrical phase at the bay centers is referred to as the phase monitoring and control system (PMCS)[2].

## 1.2 Statement of Problem

The current PMCS relies on calibrated lengths of coaxial cable for return of the RF samples from the bays to the central sites. The primary cause of irregular phase measurements is thermally-induced changes in electrical path length of the coaxial cables. In the past, the system has relied on the use of a thermatic control system to prevent the formation of temperature gradients on portions of the distribution network. The coax cables were buried in the ground and temperature-controlled water was circulated through insulated jackets surrounding the cables. The water system is no longer operational, consequently, temperature gradients have been introduced which are producing variations in the electrical length of the cable resulting in random phase errors. Phase delay characteristics are also altered by oxidation of coax conductors and the long-term deterioration of dielectric material contained in the coaxial cable.

Typical coaxial cable such as that used at the Kickapoo site experiences a change in physical length when there is a change in temperature. A change in the physical length of the transmission medium relates to a change in the electrical length. If the electrical length of the cable changes relative to other cables in the system, phase imbalances will occur. Hysteresis effects in coax cables relating to physical length versus temperature cycling (see figure 2) compound the problem since the change in the cable is neither predictable nor repeatable.

The combination of increased phase delay resulting from a large thermal coefficient of delay (TCD) and unpredictable fluctuations arising from temperature gradients as well as the deterioration of the coax cables themselves has degraded the performance of the Kickapoo transmitter.

## 1.3 General Discussion of Improved PMCS

NAVSPASUR has performed a preliminary assessment of the transmitter requirements and has proposed a conceptual design to eliminate the current problems in the signal distribution system. The concept involves substituting optical fibers in place of coaxial cables currently being used to return the RF samples from the bays. As part of the NAVSPASUR modernization program, a design and prototype testing of a replacement to the existing PMCS has been performed. The goal of the technical effort is to replace the aged PMCS and associated coaxial cabling with a reliable, long term phase stable system for optimum antenna field intensity. Rationale for the utilization of fiber was evidenced by the fact that fiber optic cable typically experiences less than half the thermal expansion of a coaxial cable of similar length. Moreover, fiber optic cable is much less susceptible to long-term deterioration than coaxial cable and provides stable and predictable performance.

To maintain the proper beam pattern required for system operation, phase stability must be maintained to within four electrical degrees across all of the 18 bays of radiating elements. The PMCS system must be able to withstand severe environmental conditions due to the harsh desert environment for a lifetime of fifteen years. A straightforward approach to system design was chosen for implementing the optical fiber PMCS. The system relies on equal length runs of single mode optical fiber to each of the 18 bays. The fibers return a portion of the RF signal from the bay distribution point to the control center for comparison to the reference frequency source. An error signal is used to control digital phase shifters for the required phase alignment. A block diagram

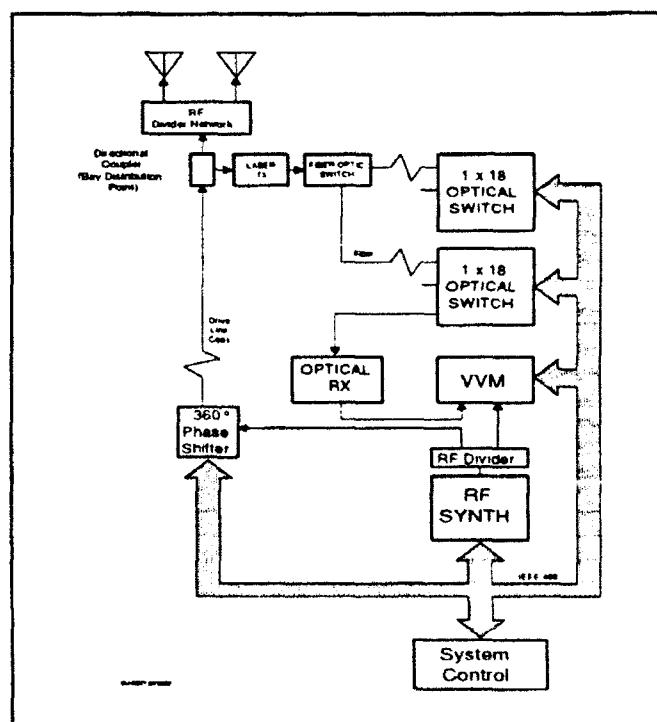


Figure 1. Block Diagram of the PMCS

of the PMCS is presented in figure 1. The fiber system is expected to meet the specification of no more than four electrical degrees variation across all eighteen bays of radiating elements.

## 2.0 DESIGN APPROACH

The approach chosen for system design takes advantage of the inherent phase stability of optical fiber and excellent phase noise characteristics of solid state laser transmitters. The simplicity of the design provides low risk development and uses much of the same equipment and facilities of the existing PMCS. The primary differences in optical fiber versus coaxial cable signal distribution systems are discussed in terms of overall system design.

### 2.1 Optical Fiber versus Coaxial Cable for Signal Distribution

As previously described, coaxial cable experiences a change in physical length, and therefore electrical length, when there is a change in temperature. Relative changes in signal distribution cables result in phase imbalances between bay distribution points. Physical length and therefore phase delay through the transmission medium is directly proportional to the thermal coefficient of delay. The TCD is a measure of time delay through a medium and is expressed in parts per million of phase delay per degree Celsius (ppm/°C). Since the electrical length in degrees for a length of fiber is given as:

$$\text{Electrical Length} = \frac{360 \cdot \text{freq} \cdot \text{IOR} \cdot \text{length}}{c} \quad (1)$$

It is evident that the change in phase delay through a coaxial cable or fiber due to temperature change is directly proportional to its characteristic TCD[3]:

$$\Delta \text{ Phase Delay} = \text{Electrical Length} \cdot \text{TCD} \cdot 10^{-6} \cdot \Delta T \quad (2)$$

where:

freq	=	Frequency of Operation	(Hertz)
TCD	=	Thermal Coefficient of Delay	(ppm/°C)
length	=	Fiber Length	(meters)
IOR	=	Index of Refraction	(unitless)
ΔT	=	Change in Temperature	(°C)
c	=	Speed of Light	(meters/second)

The Index Of Refraction (IOR) of a media is the ratio of the velocity of light in free space to the velocity of light in that media and in this case is 1.47. The frequency of operation is 216.98 MHz and the length of fiber is 2500 meters. Optical fiber demonstrates lower TCD values than coaxial cable as well as predictable and repeatable phase delay characteristics. A typical coaxial cable has a TCD of 15 ppm/°C while an optical fiber has a typical TCD of 7 ppm/°C. Figure 2 illustrates a comparison of the measured TCD over a range of temperatures for a 7/8" #64-875 RG-254/U coaxial cable and a loose tube construction fiber optic cable. This coaxial cable has one of the lowest average TCDs for any coaxial cable. It is evident that coaxial cable reacts differently to temperature changes depending on whether the temperature is increasing or decreasing[4]. The optical fiber demonstrates almost minimal change in TCD as the temperature is varied. An important characteristic of optical fiber for this application is the relative consistency of TCD from one fiber to the next. The new PMCS will rely on this important factor to maintain phase stability from bay to bay. This will allow relative matching of fiber lengths instead of absolute matching. Optical fiber is also very advantageous for long distance distribution of signals due to its low insertion loss. Fiber typically demonstrates only 0.7 dB/km electrical loss compared to approximately 19.6 dB/km for RG-254/U coaxial cable. This very important characteristic of fiber allows the implementation of the calibration system.

### 2.2 Discussion of Overall System Design

The PMCS system illustrated in figure 1 provides fiber optic paths between the bay distribution points and the central control facility. As previously discussed, a portion of the RF energy at the distribution point is returned to the central control facility for comparisons to the primary RF synthesizer used for signal distribution. Error signals resulting from variations along the 18 bays are measured with the vector voltmeter (VVM) and used to control a digital phase shifter. The system uses an eighteen-to-one optical switch to cycle through each of the eighteen bays.

This switch allows the use of only one optical receiver to convert the modulated light into an electrical signal which the VVM can compare to the RF reference. All control signals and measurement results are transferred over an IEEE 488 interface bus.

A continuous wave frequency source is used to supply RF to the array. The individual links from central site to bay do not require exact matching in electrical length since a constant fixed frequency is propagated throughout the distribution system. However, the phase modulo (a portion of a wavelength) at the end of the link must be matched for all links. Consequently, fibers may have different physical lengths as long as they are matched in electrical length, modulo one wavelength. This can be accomplished with a 360 degree phase shifter in each link implemented using the computer controlled digital phase shifters in each RF drive line.

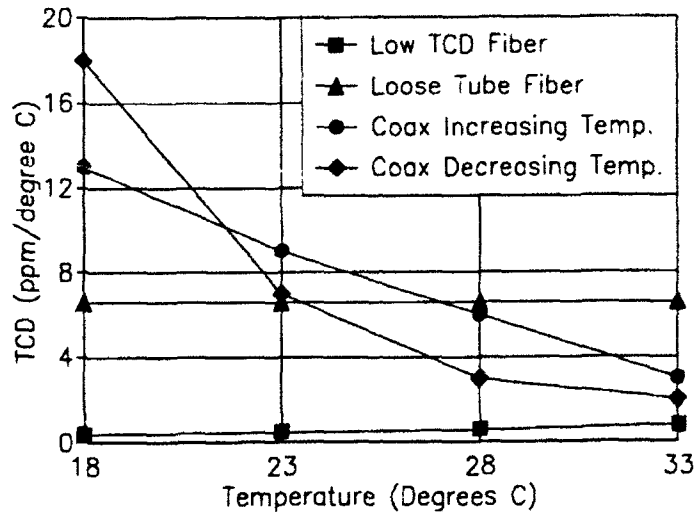


Figure 2. Measured TCD - Fiber Optic Cable vs. Best Coax

Calibration for this system will be required to minimize relative changes in fiber paths and drift and aging effects of control components and test equipment. Seasonal changes in temperature may dictate the frequency of calibration, however, diurnal changes in temperature will have a minimal effect on relative phase delay. The inherent phase stability of the fiber itself allows system operation with acceptable performance without frequent calibration. The approach taken for system design will utilize calibration procedures similar to those used in the existing PMCS. The difference however, is that these procedures will be automated by the system controller and will not require user interaction. This automated calibration system will allow calibrations as frequent as approximately once per minute while being transparent to transmitter operation. This system will allow tight control of fiber paths for increased phase stability. Details of the calibration procedures are presented in a companion paper entitled "Calibration of the Lake Kickapoo Phase Control System."

### 2.3 Optical Component Considerations

The PMCS system utilizes optical components operating at a wavelength of 1310 nm. Optical fiber at this wavelength provides high performance for long distance analog links due to a high bandwidth-length product. Single mode operation is a requirement for these links due to modal dispersion effects experienced with multi-mode fiber. Optical fiber with these characteristics is readily available and widely used for indoor and outdoor applications. Optical components at this wavelength pose very minimal risk to the human eye.

Direct burial loose-tube construction optical fiber was chosen for paths between the central control site and bay distribution points. This cabling configuration consists of a slow helix of fiber floating in a petroleum based jelly, which is in turn enclosed by an outer jacket. This configuration is water proof, minimizes microbending, provides crush resistance, and transfers very little external stress or thermal expansion/contraction to the fiber itself. The fiber is protected by a dielectric center and an armor sheathing to allow for direct burial. A cable consisting of six individual loose tube construction optical fibers will be buried in a common trench to each of the eighteen distribution points. Only two of these fibers will be used in the system leaving four other fibers for spares or future expansion. Low TCD fiber was not chosen for this design because the system relies on the consistency of TCD from standard fiber to fiber instead of the absolute value of TCD. The use of low TCD fiber would therefore add unnecessary cost to the system.

All short distance indoor jumper fibers use a tightly buffered configuration. Tightly buffered fiber allows a tighter bend radius and is suited for indoor usage where cables may be rerouted frequently.

The laser transmitters and optical receivers required for this system must provide excellent phase noise characteristics and high thermal stability. Other factors such as reliability, phase stability due to input RF power variations, and immunity to power supply variations had to be considered in the system design to determine if the overall link performance would meet the stability requirements. Laser transmitters and optical receivers from Ortel Corporation were chosen based on published specifications which were later verified in laboratory evaluations.

A 4 mW, 1310 nm InGaAsP semiconductor laser transmitter module using a distributed feedback (DFB) configuration was selected for this application. This module utilizes a Peltier effect reverse thermoelectric (TE) cooler to heat or cool the semiconductor diode substrate as needed to keep its temperature to within  $\pm 2$  degrees C. The estimated mean time to failure (MTTF) for the laser module is 1,000,000 hours ( $\approx 114$  years).

A PIN diode fiber optic receiver is used at the other end of the fiber link to convert the light into electrical current. The receiver package provides bias, monitor, and alarm circuitry as well as an integrated 16 dB RF amplifier.

Reflections from optical components such as connectors and splices translate into increased phase noise. Several factors were considered to reduce these reflections. The chosen laser transmitter uses an integrated optical isolator to reduce the amount of reflections coupled back into the laser cavity. The isolator eliminates laser noise due to bulk fiber back-scattering. The isolator also provides better laser to fiber coupling thereby increasing the effective optical power output. Angled FC/PC optical connectors were chosen to provide high return loss (typically greater than 65 dB) which helps to reduce the phase noise.

### 3.0 PREDICTED PERFORMANCE

As previously discussed, optical fiber demonstrates high consistency in TCD from one fiber to the next. Phase delay through fiber depends on the variables listed in equations 1 and 2. It is evident that phase delay is affected by TCD and the change in temperature ( $\Delta T$ ). However, as long as the temperature changes are similar to within a few degrees for each fiber, the absolute change is of no concern. Relative changes in phase delay are the primary issue. If equation 2 is plotted with change in TCD as the independent variable and change in phase delay as the dependent variable, it can be seen that the phase delay through a fiber can approach several degrees over a certain amount of temperature change. A plot of equation 2 using typical values for the Kickapoo transmitter is illustrated in figure 3. The plot demonstrates the expected amount of change in phase delay for the fiber link.

The fiber cable will be buried 3 feet underground. At that depth there will be no diurnal effects on fiber temperature[5,6,7]. Since all fibers will be buried in the same trenches, the expected variance in temperature from fiber to fiber is not expected to exceed  $2^{\circ}\text{C}$ . This means that the change in temperature does not play a major role in fiber phase delay if the TCD is sufficiently low. A typical value of TCD for an optical fiber is 7 ppm/ $^{\circ}\text{C}$ . Since relative change in fiber delay is of importance, it is the variance in TCD between fibers that is of issue. Preliminary data reveals approximately  $1/4$  ppm/ $^{\circ}\text{C}$  variance in TCD between fibers[5]. On the plot in figure 3 this translates into less than 0.5 electrical degrees for a  $2^{\circ}\text{C}$  change in temperature.

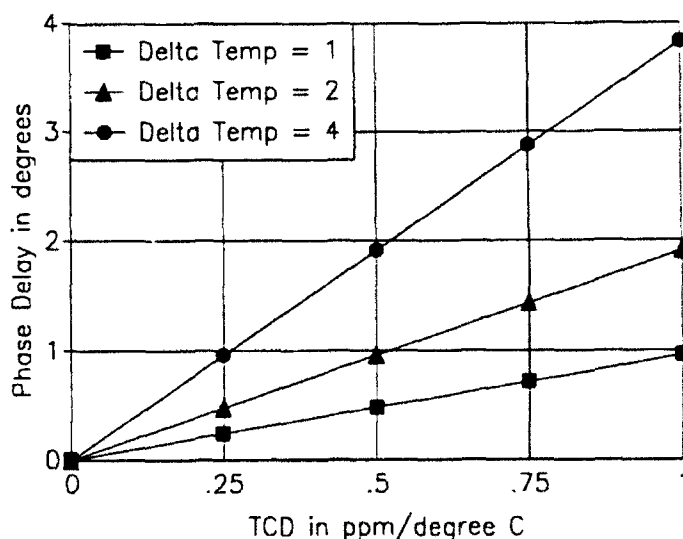


Figure 3. Change in Phase Delay vs. TCD for Different  $\Delta T$ s

Relative phase delay between bay to bay links should be sufficiently low to meet the needed requirements. Frequent automatic calibration of the fiber links will further reduce the effects of temperature variations.

The primary reason for matching all optical fibers in length is so that each fiber experiences the same change in phase delay due to temperature fluctuations. According to equations 1 and 2, phase delay is directly proportional to length. At 1/2 ppm/°C change in TCD, a 50 meter difference in fiber length equates to approximately 0.02 degrees of change in phase delay. It is evident that small changes in fiber length do not contribute greatly to relative phase delay between fibers. However, to minimize phase variations resulting from fiber length imbalances, all fibers will be matched to within one meter and buried in common trenches since this can be accomplished at no extra cost.

The optical path from distribution point to control site contains many connectors, splices, and switches. Consideration had to be given to the available optical power budget. An excess of RF power is available at the input of the laser transmitter. RF power has to be scaled to the proper level to prevent signal compression. An input RF power level of approximately +2 dBm was chosen based on specifications from Ortel Corporation concerning input signal levels.

#### **4.0 LABORATORY RESULTS**

The fiber optic link from bay to central point must be able to maintain extremely high phase stability in order to meet the stated requirements. Several factors such as temperature and input RF signal characteristics can affect the phase stability of the signal. A verification unit was constructed to determine what effect these factors have on the overall stability of a typical fiber link connecting each bay and the Kickapoo central control site.

##### **4.1 Laser Transmitter Stability Measurements**

In the fielded system, the laser transmitter will be mounted in an outside enclosure close to the antenna and the optical fiber will be buried in the ground. Temperature fluctuations caused by these adverse environmental conditions will affect the phase stability of the fiber link. The Ortel laser transmitter will operate over a wide temperature range (-40 to 70 degrees celsius) but small fluctuations in phase stability could result from a change in temperature. The enclosure used to house the transmitter will be temperature controlled over a range of 21 to 32 degrees celsius using an additional TE cooler[8]. The laser transmitter was evaluated in an environmental test chamber to determine the phase variation over that temperature range. In addition, the laser transmitter phase stability was measured when the temperature range was varied from -10 to 50 degrees celsius. This is the temperature range that the transmitter could experience inside the electronics bay enclosure if the TE cooler (used to control the temperature inside the electronics bay enclosure) failed. Phase stability for the 21 to 32 degree temperature range was measured to be 0.9 electrical degrees. The measured phase stability for the -10 to 50 degree temperature range was 4.3 degrees. Extreme temperature changes over 60 degrees are very unlikely. If one of the TE coolers fail, then the temperature differential from one bay box to another would not exceed 42 degrees instead of the full 60. This test demonstrates however, that even during TE cooler failures, the laser transmitter will continue to provide degraded but acceptable performance until repairs can be made.

The RF input to the laser transmitter will be provided by the directional coupler at each of the 18 bay central distribution points. The RF energy taken from each bay may or may not be of equal power at the input of the laser transmitter. Additionally, time dependent variations may also be detected within the bay. It is these variations within the bay that can not be calibrated out of the system. This time varying RF signal is of primary concern if it affects the phase stability of the fiber link. A phase stability test was performed to determine these effects using a varying RF input signal to the laser. Based on expected power levels at the directional couplers (with proper attenuation), the laser transmitter phase stability was measured when the RF input power varied from -10.0 to +9.0 dBm while the input signal phase remained stable. The measured phase variation for the optical link (with the above RF power variations) did not exceed 0.3 degrees. It is anticipated that power levels will vary over a smaller range of -2 dBm to +2 dBm. Over this range, phase variation did not exceed 0.1 degrees.

The laser transmitter along with other components will be mounted in an enclosure at the antenna location. The power supplies which are required to power the laser will be supplied AC power from the AC distribution system at the antenna. This distribution system is subject to variations in power loading and environmental effects such as lightning. These AC power fluctuations could result in variations in the DC power supplied to the laser. The laser

was monitored while the 5 and 15 volt DC power supplies as well as AC voltages to the DC supplies were varied. The results of these measurements indicate that phase variations due to DC power supply and AC voltage fluctuations of  $\pm 10\%$  resulted in less than 0.025 electrical degrees fluctuation[9].

The fiber link was tested for short term phase noise using a stable RF source as an input. The system should at least demonstrate phase noise characteristics lower than the RF source used for frequency distribution and comparisons. The current specification states that noise and spurious levels must be 70 dB below the carrier into a 1 Hz bandwidth from 6 Hz to 600 kHz away from the carrier and slope down to -80 dBc/1 Hz BW above 1.5 MHz[1]. Using standard test equipment, the measured short term phase noise for the link was -90 dBc/3 Hz bandwidth (equivalent to -95 dBc/1 Hz bandwidth) from 3 Hz to 600 kHz. Phase noise has been measured to levels better than -115 dBc at 1 Hz and -120 dBc  $\geq 10$  Hz using special test equipment[10]. Very low phase noise characteristics from the laser transmitter will allow signal distribution without degradation of signal purity.

#### **4.2 Optical Fiber Stability Measurements**

Phase stability was measured for a 12 meter fiber jumper over the 21 to 32 degree celsius temperature range. This is the temperature range that the fiber might experience inside the electronics bay enclosure. In addition, a 2.2 kilometer length of fiber was tested over the 24 to 26 degree celsius temperature range. This is the temperature range that the fiber will experience 36 inches below the ground surface. The measured phase variation for the twelve meters of fiber was 0.38 degrees. The measured phase variation for the 2.2 kilometers of fiber was 11.4 degrees. The results from these tests agreed very well with predictions based on equation 2 and verified the value of TCD stated in Section 2.1.

As discussed previously, the fiber link will consist of several kilometers of fiber and numerous splices and connectors. Attenuation through typical connectors, splices, and switches was measured and compared with published specifications. A typical value of attenuation for the entire link was measured to be approximately 12 dB and a maximum level is estimated to be 23 dB based on published specifications. Phase variation resulting in loss of optical signal was then measured using an optical attenuator to vary the link through the expected ranges of attenuation. The measurements exhibited less than 0.3 degrees of phase fluctuation at typical values and 1.0 degree at maximum levels.

#### **5.0 SUMMARY AND CONCLUSIONS**

The PMCS system specification requires bay to bay phase similarity within four electrical degrees. A complete phase error analysis is provided in a companion paper entitled "Calibration of the Lake Kickapoo Phase Control System." In summary, phase errors associated with various components of the system are not expected to exceed 3.0 electrical degrees[11]. Based on this analysis, the PMCS system should meet the stated system requirements.

This discussion of the PMCS system at the NAVSPASUR Lake Kickapoo Transmitter station has concentrated on the use of optical fiber for highly stable frequency distribution over long distances in a harsh environment. The described design approach was chosen for its inherent stability and because it offered a simplistic substitution for the existing PMCS by taking advantage of equipment and facilities currently in place[12]. The system will facilitate automated calibration equipment to continuously monitor and control any changes in optical fiber paths. The companion paper will discuss this calibration system.

The system design specification has been completed along with test and evaluation of the verification unit. System construction and integration is currently underway and is expected to provide greatly improved performance for the transmitter facility. This modernization effort along with other concurrent upgrades will allow the NAVSPASUR system to provide space-object target detection and tracking well beyond the turn of the century.

#### **6.0 ACKNOWLEDGEMENTS**

This work was performed by Scientific Research Corporation in Atlanta, Georgia under contract to the Naval Electronic Systems Engineering Center (NAVELEXCEN) in Charleston, South Carolina. The success of this program could not have been realized without much help and direction from Francis Allston (NAVELEXCEN) and Roy Braddy (NAVSPASUR).



## 7.0 REFERENCES

- [1] Raytheon Company, NAVSPASUR, LAKE KICKAPOO STATION MANUAL, Raytheon Company Equipment Division, Wayland, MA, November 1986.
- [2] Braddy, Roy, "Lake Kickapoo Transmitter Phase Control System", Naval Space Surveillance Center, Dahlgren, VA, May, 1990.
- [3] Logan, R., Lutes, G., and Maleki, L., "Microwave Analog Fiber-Optic Link for Use in the Deep Space Network", Jet Propulsion Laboratory, Pasadena, CA, February 15, 1990.
- [4] Lutes, G. and Primas, L., "State-of-the-Art Optics for Reference Frequency Distribution Over Short Distances", Jet Propulsion Laboratory, Pasadena, CA.
- [5] Conversation with George Lutes, NASA, Jet Propulsion Laboratory, 19 July 1990.
- [6] Rieger, S., The Genesis and Classification of Cold Soils, Academic Press, New York, 1983.
- [7] Ashcroft, G., Hanks, R., Applied Soil Physics, Springer-Verlag, Berlin Heidelberg, New York, 1980.
- [8] Allston, Francis G., Bocz, Andrew A., Hayden, Carroll, C., Washington, Tim L., "Standard Engineering Installation Package, Phase Monitoring and Control System, NAVSPASUR Transmit Antenna, Texas", Naval Electronic Systems Engineering Center, Charleston; Scientific Research Corporation, Atlanta, GA; Naval Space Surveillance Center, Dahlgren, VA, June 1991.
- [9] Lanza, Joe B., "Lake Kickapoo Transmitter Phase Monitoring and Control System Verification Unit Test Report", Scientific Research Corporation, Atlanta, GA, March 1992.
- [10] Logan, R., Primas, L., Lutes, G., Maleki, L., "Phase Noise and optical Isolation in RF Fiber Systems", Jet Propulsion Laboratory, Pasadena, CA.
- [11] Bocz, Andrew A., Hayden, Carroll C. Hayden, Washington, Tim L., "Calibration of the Lake Kickapoo Transmitter Fiber Optic Phase Monitor and Control System", Scientific Research Corporation, Atlanta, GA, Naval Space Surveillance Center, Dahlgren, VA, 1992.
- [12] Washington, Tim L., Watt, Michael L., "Lake Kickapoo Transmitter Phase Monitoring and Control System Design Trade-off Analysis Report", Scientific Research Corporation, Atlanta, GA, October 1990.

## **Coherent Data Recording and Signal Processing Capabilities at Ascension FPQ-15 Radar for Space Surveillance Applications**

E. T. Fletcher, J. B. Neiger, P. A. Jones, D. B. Green (XonTech, Inc.)  
J. D. Mercier (Phase IV Systems, Inc.)

### **Summary**

The USAF 45th SPW FPQ-15 C-band tracking radar on Ascension Island recently underwent a modification program, sponsored by the Navy Strategic Systems Programs Office (SSPO), to enhance its single-pulse sensitivity by 12 dB and to add a coherent data recording and real-time coherent signal processing and display capability. In the radar's maximum pulse width mode (10  $\mu$ s), single pulse sensitivity of the enhanced system yields a 27 dB SNR on a 0 dBsm target at 10<sup>6</sup> meters range. The system has been successfully utilized to collect tracking and coherent signature data on selected space objects to ranges in excess of 40,000 km. Coherent integration of 25 seconds of Intelsat VI geosynchronous Objects 20523, 20667, and 21653 data, having +5 dB single pulse SNR, yielded a post integration SNR of 40 dB at 36,000 km range, thus indicating good long term coherent system phase stability. Coincident metric measurements on Object 21653 made with Millstone indicate excellent agreement with range and angle differences less than 30 meters and .005°, consistent with the FPQ-15 metric calibration accuracy. The system has good doppler resolution capability ( $\sim$  .01 m/s for 2 seconds of coherent integration) and thus can aid the identification and monitoring of both large and relatively small space objects using conventional ISAR techniques.

The coherent data collection system is routinely used to support the Navy's TRIDENT missile flight tests conducted into the South Atlantic test areas and could be used to routinely support space surveillance functions with appropriate coordination and approval from the Navy SSPO, owner-operator of the coherent data collection system. Navy SSPO currently has plans to develop and install a similar coherent data collection system at the Antigua FPQ-14 site, with a goal for initial operational capability by early 1994. The Antigua system will be capable of 320 Hz PRF (versus 160 at Ascension) and will have real-time motion-compensated coherent RTI and DTI color-graphics displays and will have capabilities to coherently integrate up to 4096 pulses in real-time.

### **Introduction**

The FPQ-15 C-Band radar was originally installed on Ascension Island in the 1960's as the prototype Target Tracking Radar (TTR-2) element of the Nike-Zeus ABM system. Over the past twenty-five years, however, this radar has fulfilled an important role for the USAF Eastern Range in support of satellite and missile reentry tracking requirements. Currently, the Ascension FPQ-15 provides 24-hour support to DoD and NASA space-track missions, particularly in the areas of space object identification (SOI) and in the maintenance of orbital elements. The FPQ-15

is also vital to the success of the U.S. Navy TRIDENT II D-5 Fleet Ballistic Missile (FBM) operational performance demonstration flight tests.

In 1989, the Navy Strategic Systems Program Office entered into an agreement with the USAF Eastern Space and Missile Center (ESMC) in which the Navy would provide the funding, contractor team, and hardware for a major upgrade to the FPQ-15 radar. The stated objective of the C-Band Sensitivity Improvement Program (CSIP) was the quadrupling of the range of the radar on TRIDENT MK-4 and MK-5 reentry bodies, a 24-dB performance enhancement. Naturally, the radar's space-track mission would also benefit from the Navy's CSIP modifications.

The following paper describes the pertinent details of CSIP, the FPQ-15 radar performance characteristics today, and the use of coherent pulse integration to extend the useful range of the FPQ-15 to geosynchronous equatorial orbits.

#### C-Band Sensitivity Program (CSIP)

The Ascension FPQ-15 C-Band Sensitivity Program (CSIP) consisted of two basic elements: the replacement of an existing 28-ft parabolic reflector with a new 40-ft reflector and high performance feed, a 60-ft diameter metal space-frame radome, and the addition of a coherent data recording and real-time coherent tracking system which adds the sensitivity improvement of coherent pulse integration. The objective of these improvements was to obtain an approximately 12-dB sensitivity enhancement from the new antenna and feed system as well as an additional 12-dB system enhancement from the coherent integration of typically 16 pulses (0.1 second at the radar's 160 Hz PRF).

Figure 1 summarizes the key elements of the sensitivity upgrades that have been successfully implemented and used at the Ascension FPQ-15. Table 1 displays the radar's performance characteristics before and after the CSIP modification. The system characteristics in this table show that an 11-dB enhancement in the single-pulse sensitivity has been achieved with the CSIP modification, including a two-way loss of 1-dB with the metal-space-frame radome installation.

Visible in Figure 1 are the coherent Data Acquisition System (DAS) and the real-time display of the Coherent Designate and Tracking System (CODATS). Up to 4000 pulses (25 seconds at 160 Hz PRF) have been successfully coherently integrated post-mission with DAS, yielding an effective enhancement of 36 dB to the target signal-to-noise ratio. This is directly attributable to the long-term stability of the DAS and the excellent doppler phase noise characteristics ( $< 5^\circ$  RMS) of the system. CODATS provides the operator with a menu that allows for the selection of real-time coherent pulse integration in steps of up to 360 pulses (2.25 seconds), for an SNR enhancement of up to 25 dB.

Figures 2 and 3 display post-modification system performance data on orbiting radar calibration targets Objects 6212 and 5398. These figures demonstrate that

the primary system performance objectives of coherent data recording and sensitivity enhancement have been attained.

### Geosynchronous Observations

While the traditional spacetrack role of the Ascension FPQ-15 radar is the near-earth observation of satellites for orbital element set maintenance, tracking and impact prediction (TIP), NASA support, New Foreign Launch (NFL) detection, and space object identification (SOI), the Navy CSIP modification has extended the reach of the radar to ranges heretofore not considered feasible.

In close cooperation with USAF Space Command and the Millstone Radar, two test periods were established at the FPQ-15 radar during February and May 1992. These periods were scheduled on a non-interference basis with normal site operations, in which efforts were made to detect and "track" certain select geosynchronous satellites. The targets, at ranges of approximately 36,000 km, possessed radar cross sections in the range from approximately +15 dBsm to +40 dBsm. With the radar operating in its normal mode of 160 Hz PRF and 10  $\mu$ sec pulse width, the expected single pulse signal-to-noise ratio would lie in the range from -20 to +5 dB for this class of targets. By employing the real-time CODATS system with 64 to 360 pulse integration selected, targets could be detected and tracked with expected signal-to-noise ratios from +5 to +30 dB. Using NORAD 2-card element sets for acquisition, a number of geosynchronous objects were successfully detected and tracked with the FPQ-15, including Objects 12089, 14077, 13083, 20667, 21653, 21789, 20523, and 18384. The majority of these were at high elevations (60°-85°) relative to the radar, but in one interesting case, Object 20667 was tracked at an elevation angle of 5° and a range of approximately 41,000 km.

Figure 4 presents a section of a coherently derived RCS and Doppler-Time-Intensity history for a track of Object 18384, as recorded on the FPQ-15 Data Acquisition System. Two second, 320-pulse, coherent integration was used to develop this history. Figure 5 displays a comparison of non-coherent pulse shapes and coherent doppler spectra with 4000 pulse integration (25 seconds). The doppler spectra shows good agreement with an expected 36 dB reduction in the noise floor for this level of integration.

During the February test period, Object 21653 was also simultaneously tracked by the Millstone and FPQ-15 radars. As shown in Figures 6, there was excellent agreement in the metric data gathered by the respective sensors.

### Future Plans

The Navy SSPO Mid-Course Radar (MCR) Program will add a real-time coherent signal processing, display, and data recording capability to the C-band FPQ-14 radar at the USAF Tracking Station, Antigua, West Indies. These modifications will

ultimately provide improved sensitivity and coherent data recording capabilities for coverage of TRIDENT FBM powered flight and reentry body deployment for typical trajectories launched off the Florida coast into South Atlantic test areas. The ability of the Coherent Signal Processor (COSIP) system to integrate up to 4096 pulses (12.8 seconds at 320 Hz PRF) in real-time will also give the Antigua FPQ-14 radar a limited geosynchronous orbit capability, i.e., an RCS threshold  $\geq 17$  dBsm for a 7 dB post integration S/N at 36,000 km.

The MCR COSIP is scheduled to be operational in early 1994.

**TABLE 1**  
**ASCENSION FPQ-15 RADAR PRE-CSIP AND CS'P**  
**PERFORMANCE SUMMARY**

PARAMETER	PRE-CSIP	CSIP
<b><u>ANTENNA</u></b>		
Frequency	5.4 - 5.9 GHz	5.4 - 5.9 GHz
Type	Parabolic	Parabolic
Diameter	28 Ft	40 Ft
Gain	48 dBi	55 dBi
Polarization	Linear-Vertical	Circular-RHCP or LHCP
Beamwidth	0.46 Deg.	0.27 Deg.
Feed	Cassegrainian	Cassegrainian
<b><u>PEDESTAL</u></b>		
Azimuth Velocity	23.3 Deg/Sec	20.6 Deg/Sec
Azimuth Acceleration	18.9 Deg/Sec <sup>2</sup>	19.9 Deg/Sec <sup>2</sup>
Elevation Velocity	13.0 Deg/Sec	10.8 Deg/Sec
Elevation Acceleration	21.7 Deg/Sec <sup>2</sup>	9.6 Deg/Sec <sup>2</sup>
<b><u>SYSTEM</u></b>		
Radome	No	60 Ft
Sensitivity* (10 $\mu$ Sec PW)	16	27
Coherent	No	Yes
Doppler Sidelobes (40 dB S/N)	N/A	$\leq 34$ dB
Doppler Phase Noise (40 dB S/N)	N/A	$< 5^\circ$ RMS

\* Single Hit S/N on 1-m<sup>2</sup> Target at 1,000 Km Range.

## Figure 1 Overview of Ascension FPQ-15 C-Band Radar After Recent Navy Sensitivity Upgrades

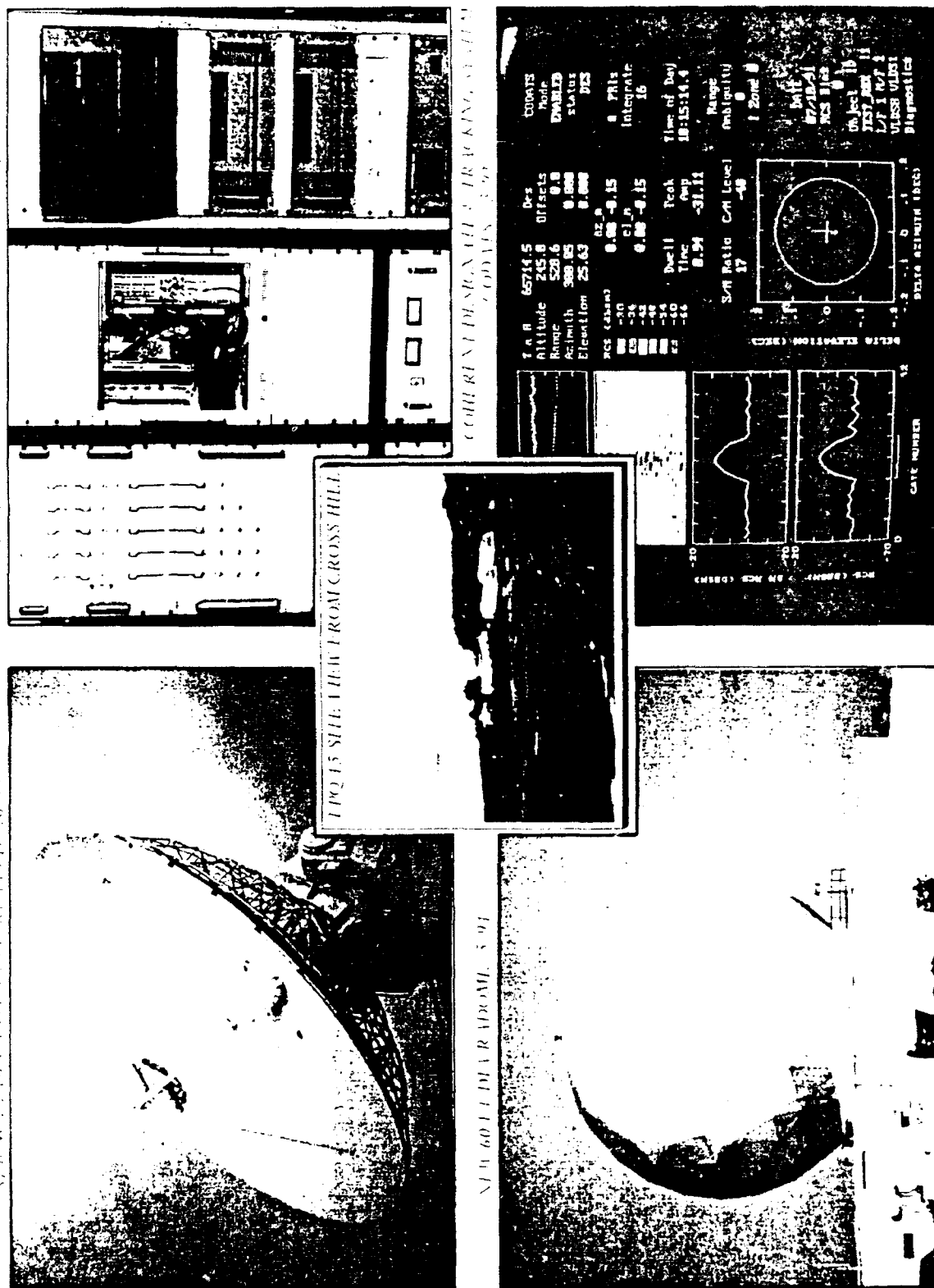
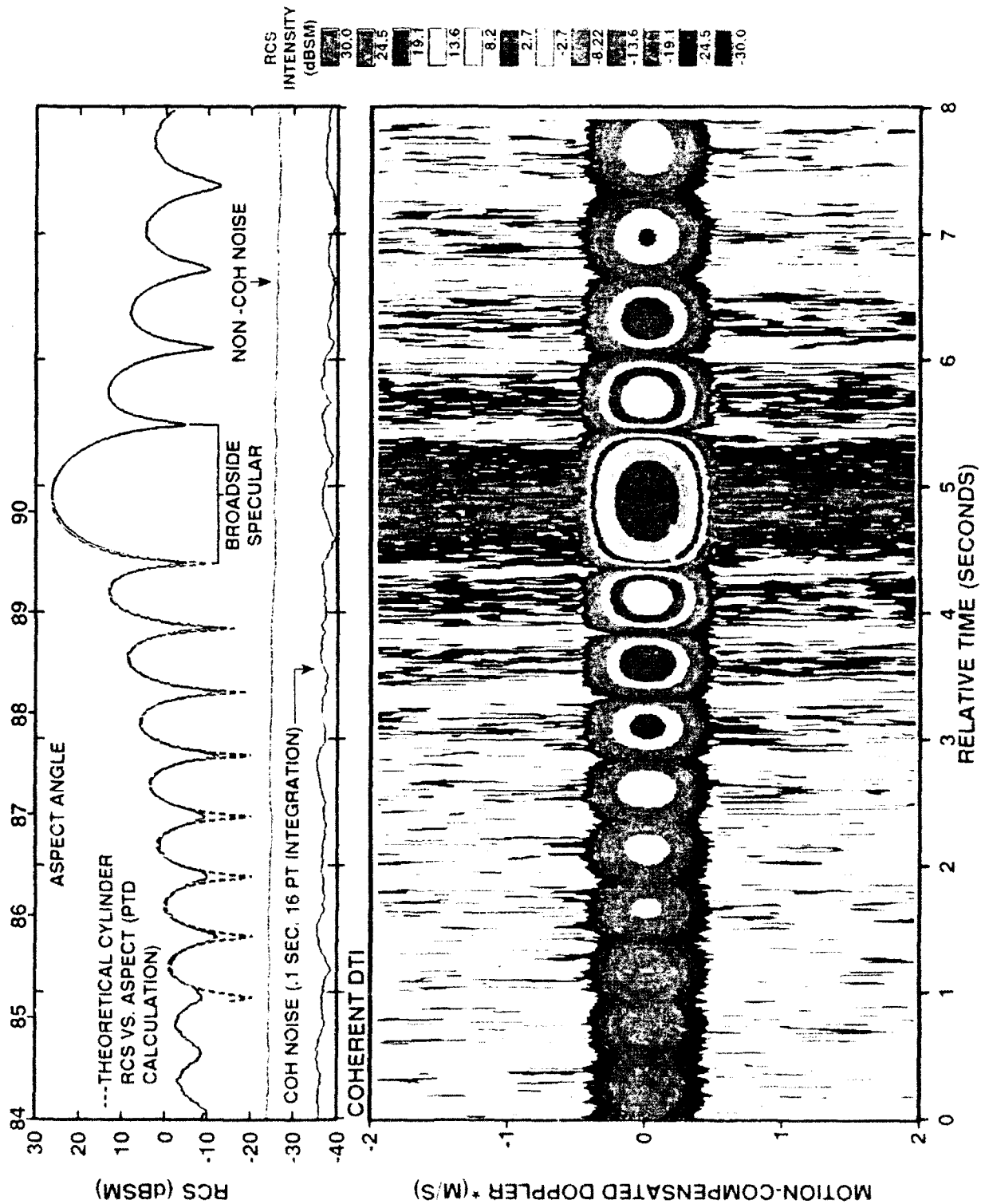


**Figure 2 Ascension FPQ-15 Coherent Data Recording on Object 6212  
(Tumbling Cylinder Radar Calibration Satellite), 11/07/92**



\* .1 SEC (16 PULSE) COHERENT INTEGRATION, RANGE 1.15 x 10<sup>6</sup> METERS, 2.3MW, 10/US PULSE WIDTH

Figure 3 Ascension FPQ-15 Coherent Data Recording on Object 5398, 6/18/92, Comparison of Typical Non-Coherent RCS Pulse Shape & Coherent Doppler Spectra, 2 Sec. Average

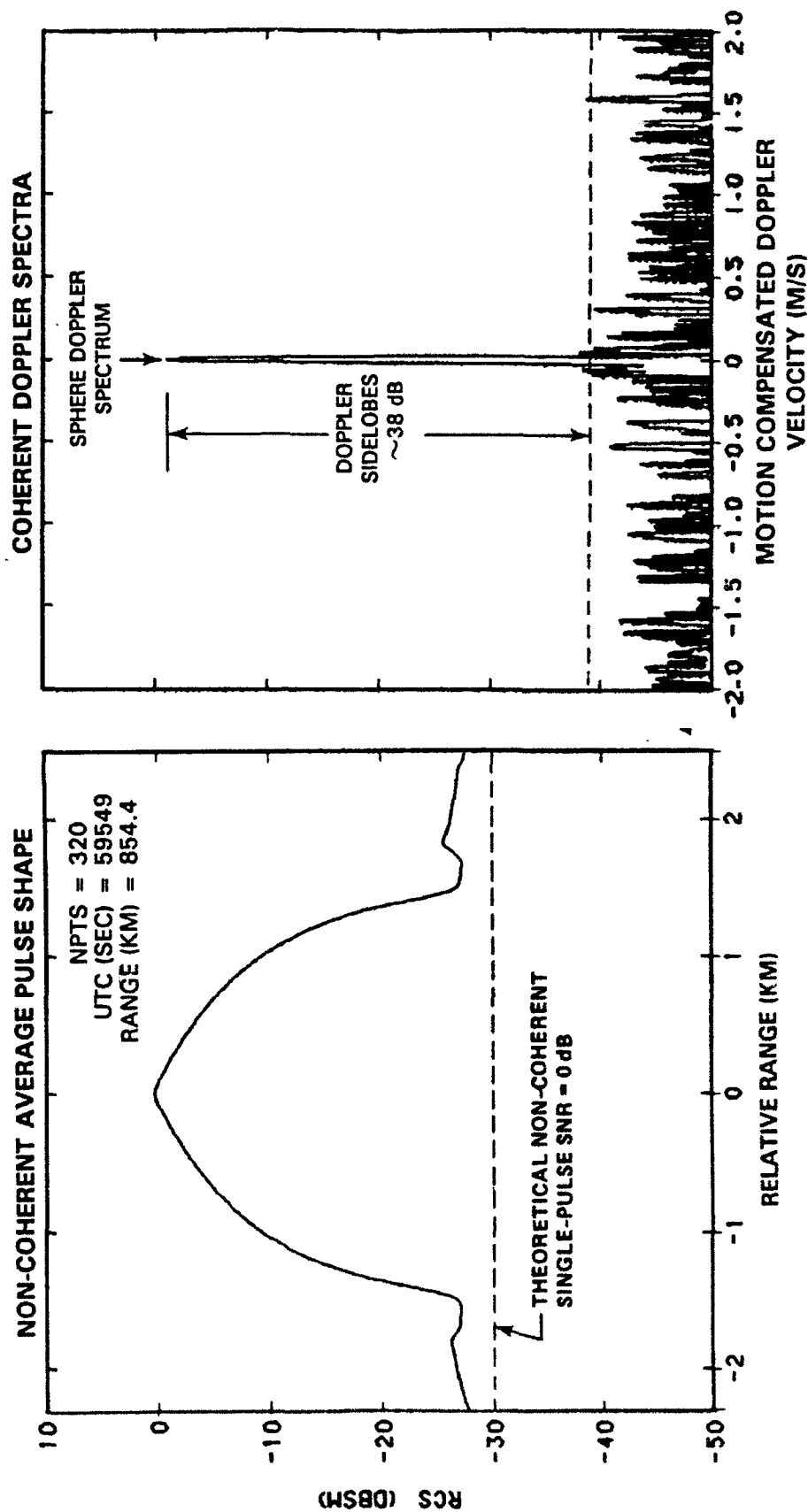




Figure 4 Representative Segment of Geosynchronous Object 18384 (5/07/92), Ascension FPQ-15 C-Band, LC/RC Coherently Derived RCS and Doppler-Time-Intensity\*



\*320 Point (2.0 sec) Coherent Integration

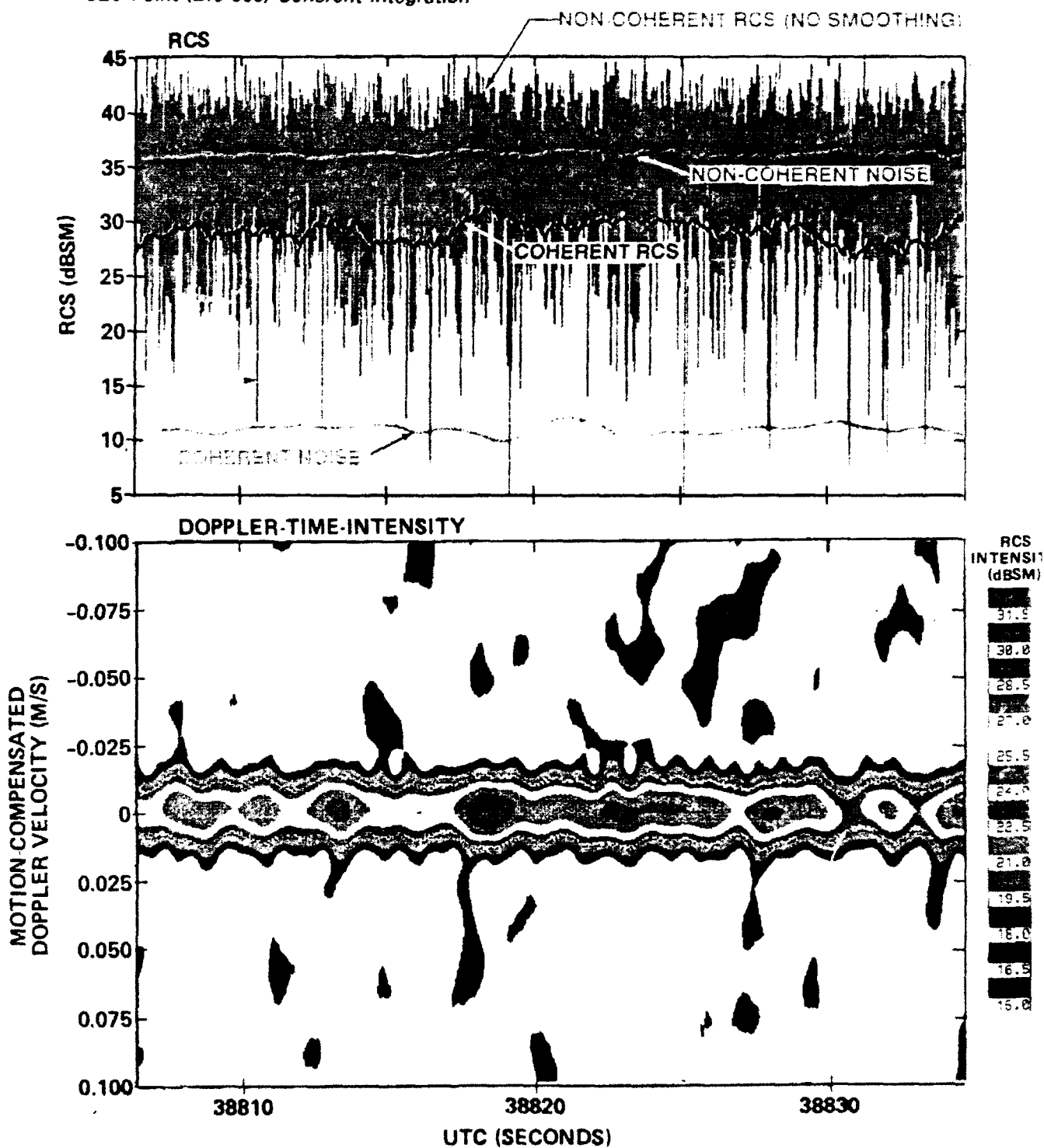


Figure 5 Geosynchronous Object 18384, Ascension FPQ-15 C-Band,  
5/07/92, Comparison of Non-Coherent Pulse Shapes and Coherent  
Doppler Spectra With 25 Second(4000 Pulse) Integration

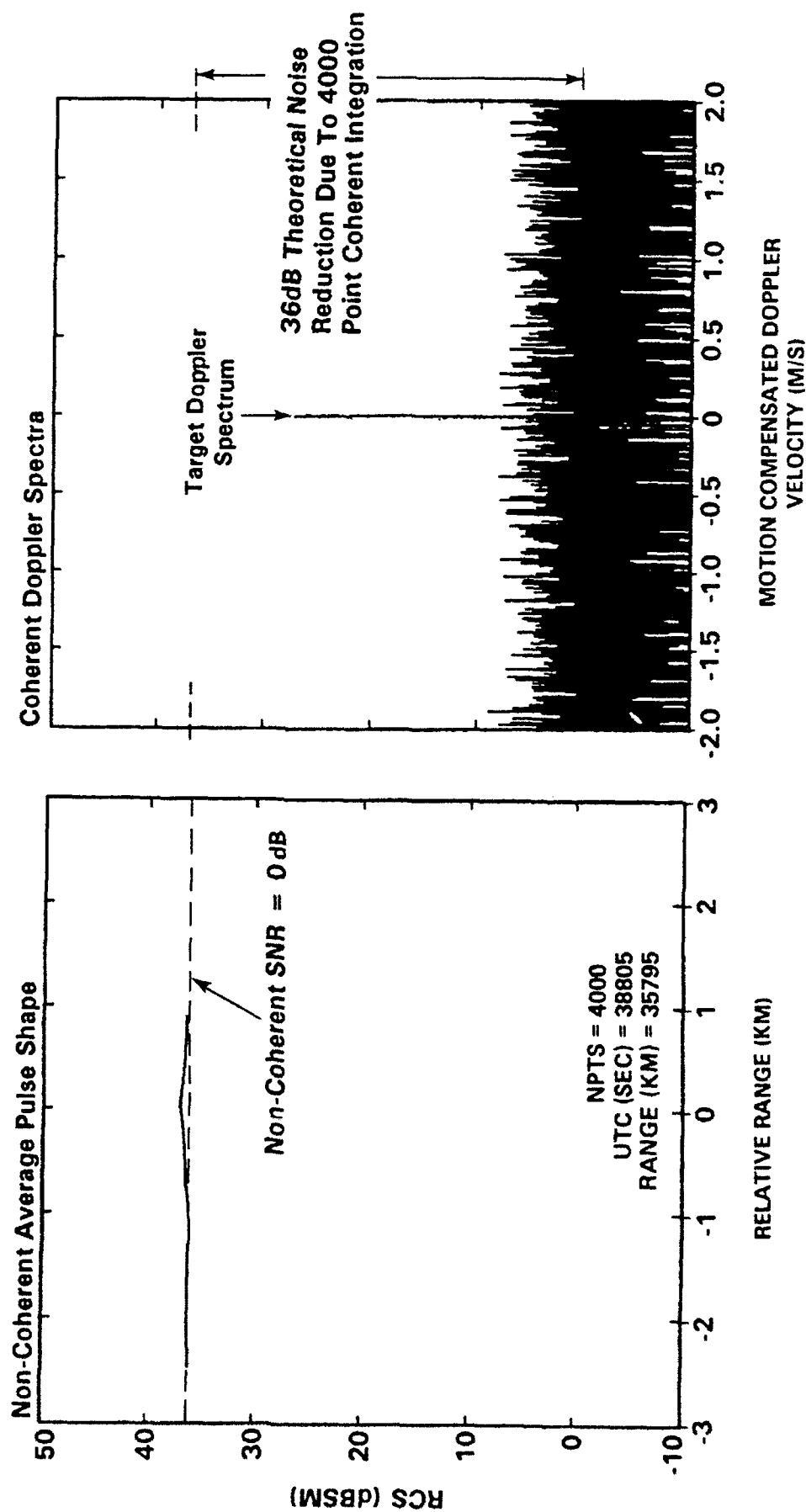
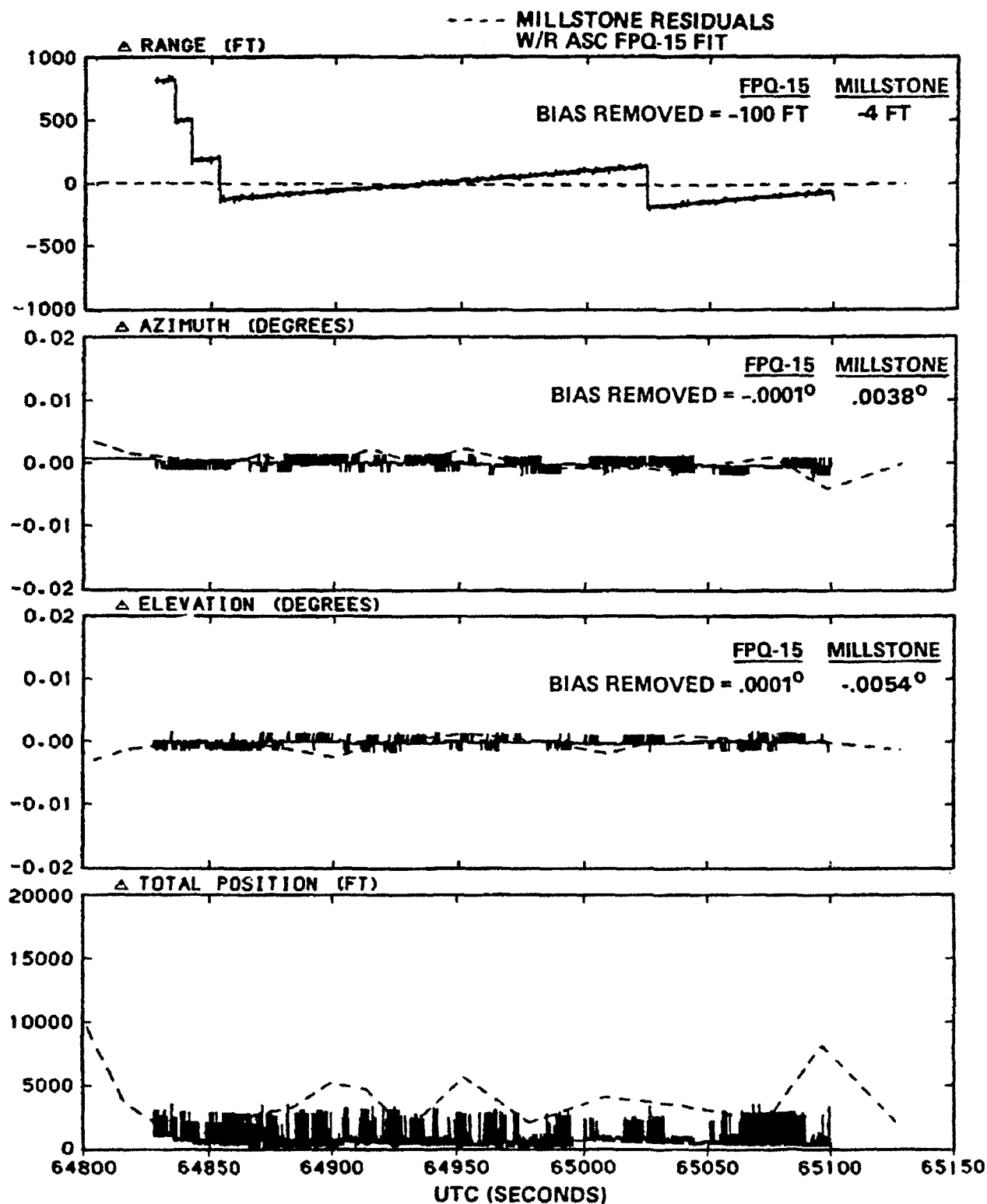


Figure 6 Geosynchronous Object 21653 (2/24/92),  
Ascension FPQ-15 Designate R, A, E and Total Position  
Residuals With Respect to Self-Fit Trajectory



## Forecasting Trans-Ionospheric Effects to Improve Space Surveillance

M.M. Partington (Air Force Space Forecast Center [AWS]), G.J. Bishop (Phillips Laboratory [AFMC])

### Abstract

With Air Force Space Forecast Center (AFSFC) now fully operational it will soon be possible to support surveillance system requirements for new products to specify trans-ionospheric effects such as range error (due to ionospheric total electron content, [TEC]), signal phase noise, and target radar cross section noise, (which can both be caused by ionospheric scintillation). Such specification products have potential for high accuracy and near-real-time capability through combining the outputs of improved models at AFSFC with real-time updates from sensors which may be co-located with surveillance radars. Such timely and accurate specification of effects will support improved surveillance capability through improved mitigation. Previously, the need to specify these ionospheric effects could only be supported by climatology "forecasts" projecting mean monthly conditions, updated, in some cases by the previous day's observations. This paper reviews the status of AFSFC, including its mission, capabilities, and customers, and discusses the more important data sources, particularly the new Trans-Ionospheric Sensing System (TISS), being procured by Air Weather Service. Measurement data is presented which contrasts the predictions of a present climatological model with observations from a TISS-type sensor.

### The Air Force Space Forecast Center

The Air Force Space Forecast Center (AFSFC) is operated by the USAF Air Weather Service (AWS) to serve the needs of the Department of Defense (DOD) and other Federal agencies. Indirectly, through its joint operations with National Oceanic and Atmospheric Administration's (NOAA) Space Environment Services Center (SESC) at Boulder, Colorado, the AFSFC also serves the private and academic sectors. AFSFC has the mission and responsibility to provide, or arrange for the provision of such tailored space environmental observing and forecasting services as are necessary to meet unique military requirements in support of programs dealing with national security. To implement this responsibility, AWS and the AFSFC have entered into a number of agreements and contracts to obtain the observational solar, ionospheric, and geophysical data required to support a world-wide space environmental forecast and warning service.

### Mission and Organization of the AFSFC

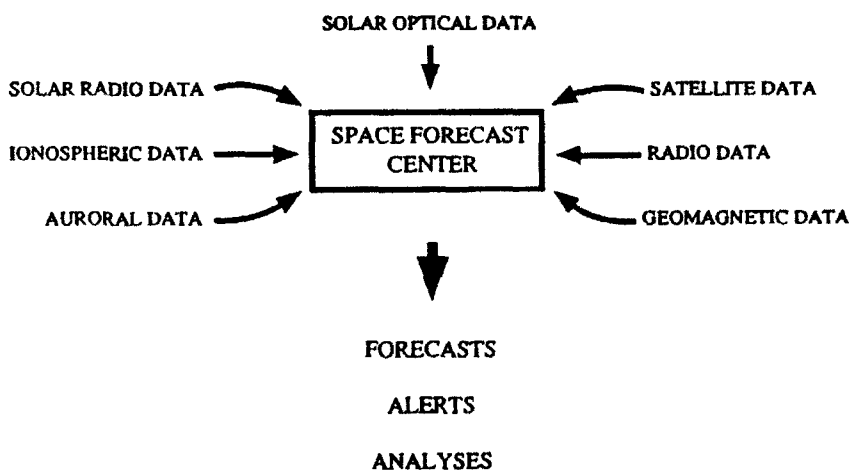


Figure 1. The AFSFC production center

The AFSFC mission includes specifying and forecasting the condition of the near-earth space environment. This environment may impact many DOD systems, including communication (both ground-based and satellite), radar, and surveillance systems. The AWS's AFSFC provides both broad and mission-tailored support in many areas. These areas include: solar flare activity, ionospheric variability, energetic particle events, geomagnetic and solar indices required to determine atmospheric density

variations, and post analysis of operational system problems to determine if the space environment was a contributing factor. Customer support includes real-time notification of solar and geophysical events, forecasts with lead times ranging from hours to months, products tailored to specific user requirements, and detailed

post-analysis studies. The AFSFC is staffed by USAF military and civil service employees. The forecast center itself, located at Falcon AFB, Colorado, serves as the DOD's only space environmental forecast and warning center, providing round-the-clock, world-wide mission support to the DOD and other Federal agencies which can be adversely impacted by disturbances in the near-earth environment. Figure 1 provides an overview of the data processing and product generation at the AFSFC. A number of products are jointly issued by the AFSFC and the NOAA's Space Environment Services Center.

The AFSFC has seven direct subordinate units. One is the Air Force contingent (AFSFC Operating Location A) at the Joint USAF-NOAA Space Environment Services Center (SESC) at Boulder, Colorado. The other six units are USAF Solar Electro-Optical Network (SEON) observatories located at Sagamore Hill, Massachusetts; Ramey, Puerto Rico; Holloman AFB, New Mexico; Haleakala, Hawaii; San Vito, Italy; and Learmonth, Australia. This network of solar optical and radio observatories maintains near continuous monitoring of solar activity using the Solar Observing Optical Network (SOON) telescope, Radio Solar Telescope Network (RSTN) telescope, and their associated computer subsystems.

#### AFSFC Data Sources

The AFSFC receives solar, ionospheric, and geophysical data from world-wide networks of space environment sensors. These data come from ground-based and satellite observing networks.

#### Ground-Based Observing Networks

The SOON telescope gathers standardized photospheric, chromospheric, and coronal data in either computer assisted ("automatic") or non-computer ("semiautomatic") mode. The SOON consists of five solar optical observatories geographically positioned to allow a 24-hour per day optical observation of the sun (weather permitting). The system provides the capability to observe, analyze, and report such solar phenomena as flares, sunspots, magnetic fields, and disk and limb activity.

The RSTN telescopes gather standardized solar radio data in either computer assisted or non-computer ("manual") mode. The RSTN system produces discrete (fixed) frequency radio observations at 245, 410, 610, 1415, 2695, 4995, 8800, and 15400 MHz. The RSTN system also produces swept frequency spectral radio observations over a continuous band of frequencies. The USAF optical (SOON) and radio (RSTN) observatory networks were specifically designed to provide consistent, rapid flare observations and data for short-term solar flare forecasting. Solar flares are the primary source of solar X-ray and radiowave bursts, as well as high energy particle emissions.

Ground-based geomagnetic data are available from a network of automated magnetometers owned and operated by the US Geological Survey. Magnetometers measure the strength and orientation of the earth's geomagnetic field as observed at a particular point on, or near, the earth's surface. Although magnetometers are sometimes flown on satellites, most are ground-based. When the Air Force Space Forecast Center became operational in mid 1992, it started using a larger network of automated magnetometers owned and operated by the US Geological Survey, which produce hourly geomagnetic indices. The magnetic indices derived provide a near real-time indicator of the average planetary geomagnetic activity.

The AFSFC receives data from a world-wide (primarily northern hemisphere) network of ionosondes. Data from these vertical incidence ionospheric sounders are very important in determining radio propagation conditions in all frequency bands. These devices measure ionospheric parameters (primarily free electron density vs altitude) up to the maximum level of ionization (F-Layer) directly above the sounder. The Air Force has access to data from several dozen sounders located worldwide, and is in the process of installing a network of automated Digital Ionospheric Sounder System (DISS) instruments at critical locations. Ionospheric models use the data obtained from these geographically separated sounders to "fill in the gaps" and produce a global, 3-dimensional specification of the ionosphere's structure.

Polarimeters measure total electron content (TEC) of the ionosphere along a path through the ionosphere from

the ground-based instrument to an orbiting reference satellite by monitoring the Faraday rotation, or polarization twist, of a linearly polarized VHF radio wave transmitted from the satellite. TEC data are used to adjust for errors in satellite range and bearing measured by ground-based radars. Polarimeters will be replaced by Transionospheric Sensing System (TISS) instruments, which use signals from Global Positioning System (GPS) satellites.

Riometers (Relative Ionospheric Opacity Meters) instruments record the strength of High Frequency (HF) "cosmic radio noise" (i.e., radio waves emanating from extraterrestrial sources) received at the earth's surface. A decrease in power represents an increase in ionospheric opacity or absorption. Riometers can detect ionospheric disturbances such as: Short Wave Fades (SWF), Auroral Zone Absorption (AZA), and Polar Cap Absorption (PCA) events.

Neutron Monitor are used for ground based detection of secondary neutrons produced during collisions between cosmic rays and atmospheric molecules or atoms. It provides an indirect measure of the cosmic ray flux encountered by the earth, whether from solar or non-solar (i.e., "galactic") sources. The most interesting event detected by a neutron monitor is a Ground Level Event (GLE), which is a sudden increase in secondary neutrons produced by collisions between solar cosmic rays and atmospheric gases. GLEs are important as an indicator that a very energetic solar flare has occurred, and a Polar Cap Absorption event and geomagnetic storm are almost certain to follow.

#### Satellite Observations

Satellite sensors provide early warning of changes in the near-earth environment. In particular, the AFSFC and SESC receive near-continuous data from two major satellite networks, the Defense Meteorological Satellite Program (DMSP) and Geosynchronous Operational Environmental Satellite (GOES). DMSP satellites are in low altitude polar orbits, and provide visual aurora, low energy particle, and ionospheric parameter data. GOES satellites are in geostationary orbits, and provide solar X-ray, energetic particle, and magnetometer data. Additional energetic particle data are received from a series of DOD geostationary satellites. From time to time, other satellites have provided useful solar-geophysical data on a temporary basis. For example, in the early 1980s, ISEE-3 provided real-time solar wind, interplanetary magnetic field, and X-ray data from its position 930,000 miles from earth toward the sun. Another example was Sky Lab, which provided a capability to image the sun at ultraviolet and X-ray wavelengths.

#### Current AFSFC Support

The state of the art in accurately forecasting solar and geophysical events is limited. However, rapid event notification provides warning to operators of conditions that could degrade the performance of their systems. Typical types of notification include: solar X-ray events which may disrupt high frequency (HF) communications on sunlit paths, solar radio bursts which may disrupt communication systems and/or cause interference on radar systems, solar proton events which can produce radiation hazards to satellites and spacecraft, ionospheric disturbances which can degrade HF and satellite communication systems, and geomagnetic disturbances which can affect the orbital parameters of low altitude satellites or cause spacecraft charging near geostationary altitudes.

The state of the ionosphere is monitored to provide a variety of notifications and forecasts of irregularities that can affect performance of ionospheric dependent systems. These services consist of real-time and long-range forecasts, along with specification and forecasting of electron density profiles and total electron content. Large scale fields of parameters such as foF2 are also available. As one of its routine general-use products, the AFSFC provides real-time specification and forecast of HF propagation conditions every six hours.

Magnetospheric monitoring is accomplished using real-time particle data from the GOES and DOD geostationary satellites. Variation of the magnetosphere is also monitored using ground based magnetometers, which provide 3-hour ap and 24-hour Ap indices. These indices are indicators of the influx of energy into the upper atmosphere due to energetic particle bombardment, and are a prime input for atmospheric density models.

Another prime density model input is the 10.7 cm (2800 MHz) solar radio flux (F10), which correlates with the influx of energy into the atmosphere due to solar X-ray and extreme ultraviolet radiations. F10 observations are received daily from a standard observatory (the Dominion Radio Astrophysical Observatory) at Penticton, British Columbia, Canada.

The AFSFC provides timely, solar and geophysical alerts, analyses, forecasts, and environmental specifications directly to DOD and other Federal agencies, as well as through the NOAA Space Environment Services Center (SESC) at Boulder, Colorado. AFSFC Pamphlet 105-4 describes all space environment analysis and forecast products available from the AFSFC. Most of these products can be received by U.S. military units. Additional specialized products can be arranged.

#### Future Plans for the AFSFC

To improve customer support at the AFSFC, plans and projects are underway to obtain new real-time data and advanced space environmental models. The models will utilize the data to improve specifications and forecasts of the space environment. Enhancements in operational support capabilities will be seen through the implementation of such data systems as TISS.

#### New Data Sources

As mentioned previously, the Air Force is in the process of installing a network of automated Digital Ionosonde Sounder System (DISS) instruments to provide electron density profiles and developing Transionospheric Sensing System (TISS) instruments to provide total electron content and scintillation data. A project is currently underway to obtain real-time ionosonde data from locations in the southern hemisphere. All of these data will be used primarily by the new ionospheric models.

Many new satellite data sources are projected to provide the AFSFC with space environmental observations to be used as input to the space environmental models as well as other analysis and display techniques used for specification and forecasting. DMSP will provide special sensor data such as precipitating particles (SSJ/5), ion and electron drift and scintillation (SSIES-II), magnetometer (SSM), ultraviolet spectrographic imager (SSUSI), and ultraviolet limb imager (SSULI). NASA has proposed to launch a satellite into an L1 orbit to provide interplanetary solar wind data (SWIM) which the AFSFC would have access to in near-real time. Solar x-ray image data should be available to the AFSFC from the GOES-NEXT satellites.

#### Space Environmental Models

The Space Environmental Technology Transition (SETT) Models program involves the transition of a suite of prototype scientific models into operational models capable of interfacing with the real-time databases within the AFSFC operating environment. These models will specify and forecast the space environment from the sun to the Earth's upper atmosphere. In addition, new applications software will be developed to retrieve model output and allow forecasters to effectively use the data for operational customer support. The research-grade models are undergoing advanced development by Air Force Material Command contracted universities and civilian laboratories. The contract for transitioning the SETT models to the AFSFC operating environment was awarded in September 1992. Ten space environmental models are being developed in a planned, phased fashion, which means the transition process and operational software development will also be phased. The transition process is expected to be completed by 1998. Figure 2 demonstrates the planned transition schedule for data and model acquisitions. Follow-on space models are planned to improve model output accuracy by replacing parameterization techniques with first principle physics schemes wherever possible. The currently planned suite of ten models include: two magnetospheric models, three ionospheric models, one neutral atmosphere model, two interplanetary models, a coupling model, and an executive routine.

#### Magnetospheric Models

The magnetospheric models will enable the AFSFC to provide specification and forecasts of the following:

	1993	1994	1995	1996	1997	1998	
<u>DATA</u>							
DISS				X			charged particle population and geomagnetic field line geometry in the near-Earth region, energy fluxes and characteristic energies of precipitating energetic electrons, and global electric fields mapped into the ionosphere and neutral atmosphere. The Magnetospheric Specification Model (MSM) was designed to provide only the most basic capability for post-analysis of satellite anomalies. The MSM concentrates on specifying low-energy charged particle fluxes that cause surface charging on spacecraft and satellites. The Magnetospheric Specification and Forecast Model (MSFM) is a follow-on to the MSM. The
TISS		X					
SSIES-II	X						
SSJ/5						X	
SSM	X						
SSUSI						X	
SSULI						X	
SWIM		X					
<u>MODELS</u>							
MSM / MSFM		X	X				
PRISM / IFM			X	X			
WBMOD				X			
VSH			X				
SWT		X					
ISP					X		
COUPLING / EXEC SYSTEM					X	X	

Figure 2. Operational dates for data and model acquisitions at the AFSFC

MSFM concentrates on increasing accuracy, increasing spatial coverage to include more of the magnetosphere, and establishing a significant magnetospheric forecast capability (0-3 hours) for warning satellite operators before an anomaly occurs.

#### Ionospheric Models

Current ionospheric specification models are limited to the region between 20 degrees South and 80 degrees North geomagnetic latitude. Since the current ionospheric support products are developed manually from the specification analyses, their quality varies according to the experience of the duty forecaster. The new ionospheric models will enable the AFSFC to provide real-time ionospheric specification and forecasts of electron density profiles, total electron content (TEC), critical frequencies, and ionospheric scintillation parameters. The Parameterized Real-time Ionospheric Specification Model (PRISM) is a global ionospheric specification model that will use near real-time data from both ground-based and space-based sources to provide accurate specification of electron density profiles and TEC. The Ionospheric Forecast Model (IFM) is a 3-dimensional, time-dependent model that will use PRISM as input to produce global ionospheric forecasts.

The Wide Band Scintillation Model (WBMOD) models the effects of ionospheric plasma density irregularities on transionospheric radio frequency propagation. It provides specifications and predictions of the world-wide occurrence and behavior of the plasma density irregularities, and uses these to estimate the levels of ionospheric scintillation that the irregularities will cause on transionospheric propagation channels.

#### Neutral Atmosphere Model

The Vector Spherical Harmonic Model (VSH) will specify and predict global neutral particle densities, winds, and temperatures from 90 to 1500 km in the atmosphere. The primary objective of VSH is to reduce the average error in density specification to 5% in the region below 500 km.

#### Integrated Space Environmental Models (ISEM)

These models include two interplanetary models, as well as an integrated software system that links all the space environmental models together and an executive routine. The Solar Wind Transport Model (SWT) will predict the effect of the solar wind and interplanetary magnetic field on the Earth's magnetosphere. The Interplanetary Shock Propagation Model (ISP) will provide an early warning (1-4 days) of geomagnetic storms resulting from



IONOSPHERIC TERM	RADIO (RF) EFFECT	SYSTEMS EFFECT	POTENTIAL DEGRADATION OF:
Total electron content (TEC)	Signal delay Faraday rotation (polarization -	Range error Signal loss fading)	Target location Coverage
Amplitude scintillation	Fades & enhancements	Signal fades Target fades	Discrimination Target update
Phase scintillation	Rapid changes in signal delay	Rapid changes in apparent range	Detection Tracking Imaging
Clutter	Partial signal reflection	Anomalous signal returns	Detection Tracking

Figure 3. Ionospheric effects and potential surveillance impacts

solar flares. A Model Coupling effort will link the interplanetary, magnetospheric, ionospheric, and neutral atmosphere models together with physically-based, self-consistent interfaces. Coupling will allow output from PRISM to be used as input by VSH, etc., resulting in more accurate customer support. Finally, an Executive Routine will provide a single framework to coordinate and facilitate the

execution of all the regional space models using scientific expertise and decision making capability within the program. This will increase the consistency of the outputs, optimize run times, and decrease the workload of forecasters.

#### Operational Support Enhancements from the New TISS System

To mitigate an environmental effect, or to limit its impact, an operational system needs to know what the effect is, where it is occurring, and when or how much it will occur today. Among the more important ionospheric effects on trans-ionospheric RF surveillance at typical system frequencies are:<sup>1</sup> 1) signal delay, 2) Faraday rotation of linearly polarized signals, 3) rapid changes in signal delay (phase)<sup>2</sup>, 4) signal fades and enhancements<sup>2</sup>. The TISS system will support real-time specification of these effects<sup>3</sup> through its capability to monitor TEC and scintillation (phase and amplitude) in multiple directions (possibly up to 12) from each site. TISS data will be available to update the WBMOD and PRISM models every 15 minutes.

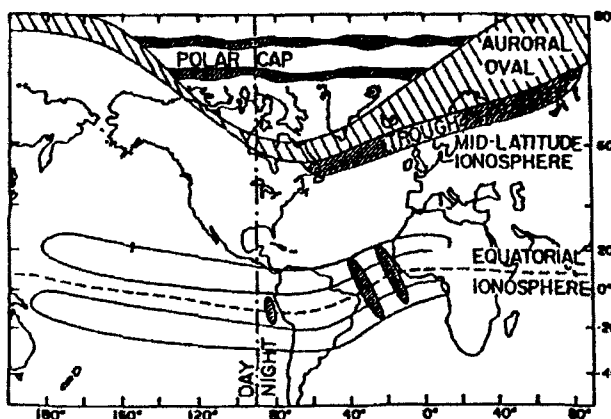


Figure 4. Major geographic regions of the ionosphere

The major ionospheric effects, and related systems effects and potential impacts are shown in Figure 3. These effects vary greatly among the geographic regions of the ionosphere, Figure 4. For example, scintillation occurs frequently in the high latitude auroral region, and associated with gradients in the trough region<sup>4</sup>, but seldom in the mid-latitudes (CONUS), except during large magnetic storms. Figure 5 illustrates how both TEC and amplitude scintillation can vary in the vicinity of the trough, (after ref. 4). Diurnal TEC is plotted in the TEC vs Time (UT) plane. The trough itself may be observed here as a "valley" in TEC along the TEC vs latitude lines between 1800 and 2200. After midnight, the equatorward wall of the trough appears to fade away, leaving a standing poleward wall. The intensity of shading

measures the level of observed amplitude scintillation, which is seen here to associate with the TEC gradients in the trough region.

Figure 6a shows an example of the regional coverage currently available to a TISS-type monitor over 24 hours of GPS observation from the mid-latitudes, and Figure 6b the portion of that coverage applying to a single hour. Judicious selection of satellites to be monitored can allow TISS to obtain very extensive regional coverage from a single station, due to the wide radius of coverage at lower elevations, (approximately 1000 km at 15° and 1500 km at 5°)<sup>1</sup>. Figures 7a, b, and c, show respectively: a) a typical diurnal profile of mid-latitude TEC (looking vertically), b) several days' observation of TEC from the same sequence of GPS satellites (during a magnetically quiet period), and c) predictions from the Bent<sup>4</sup> model for the same times and directions as in (b). The

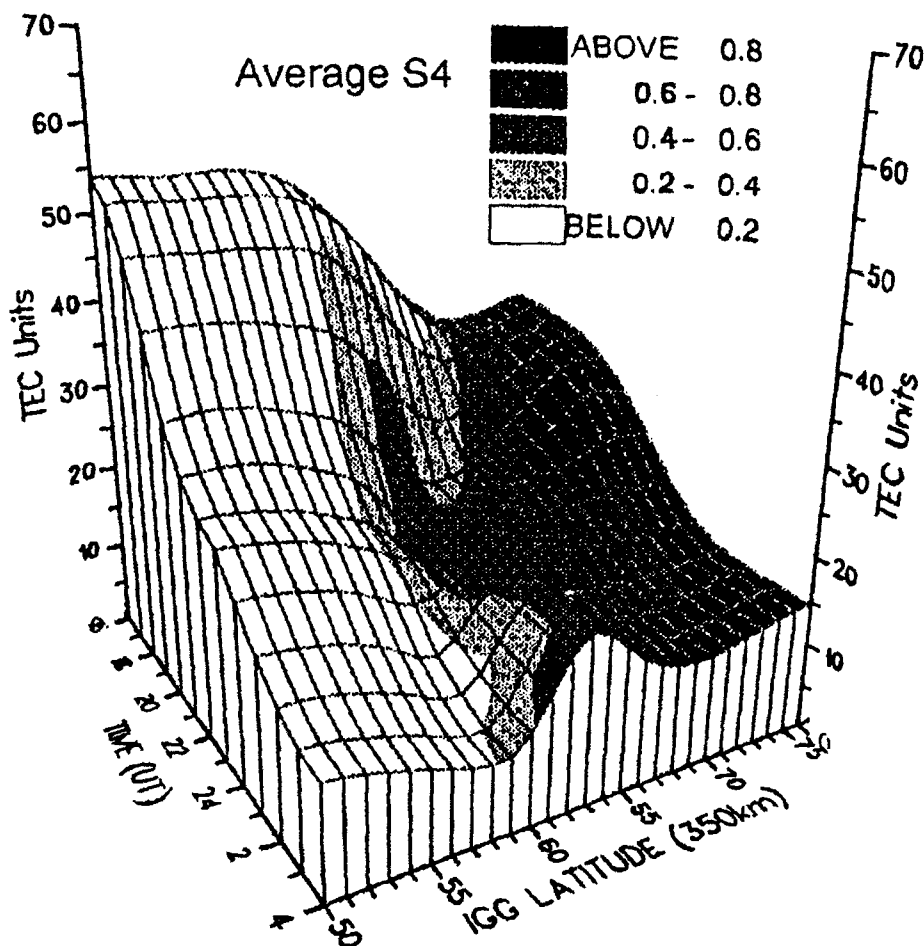


Figure 5. Example of electron content (1 unit =  $1 \times 10^6$  e/m<sup>2</sup>) and amplitude scintillation ( $S_4$  = power std. dev./ mean) morphology in the ionospheric trough region (after Kersley<sup>4</sup>).

raypath to the GPS satellite penetrates the ionosphere peak, and by separating the observations by latitude region. The middle plot in Figure 8 (which shows observations within  $\pm 2^\circ$  latitude of the station), now has the expected appearance, as Figure 7a. But we can also look into latitude regions north and south of the station, and, in the northern region we appear to see the wall of the trough at about 1600-1700 in the top plot, and the standing poleward wall at 0100-0400 in the middle plot.

Figure 9 gives a sample 1-week data set, from December 1991 at the Shetland islands, contrasting the Bent<sup>5</sup> model predictions of TEC behavior with GPS (TISS-type) observations. The full data set is plotted, in addition to low, medium, and high-elevation subsets, and morning, midday, afternoon, and night subsets. If observation agreed fully with Bent all the points would lie on the diagonals. Just this small data set (from a quiet period) clearly shows that the various subsets of the data systematically differ from the climatological model. This illustrates the need for models like PRISM, supported by real-time sensor input.

With the capability to monitor as many as 12 satellites per station, TISS' inputs will greatly enhance AFSFC (WBMOD and PRISM) capability to specify current locations of important boundaries where scintillation or TEC change rapidly, such as the auroral scintillation boundary, the trough, and the equatorial anomaly. This will, in turn, improve operational systems' capability to apply mitigation or avoidance of effects, where appropriate.

disjoint appearance of the plot in Figure 7b is due to the switching among satellites that are seen in different directions, i.e. hopping among tracks such as seen in Figure 6b, and is generally predicted by the Bent model as shown in Figure 7c. In doing this, the observation may change time zones, or even ionospheric regions, as one might if this observation were on the day shown in Figure 5.

Since TISS will be observing in four (and possibly up to 12) directions at once, it will be recording at least four, different, records like Figure 7b, simultaneously. To clarify the value of the TISS wide coverage, it is necessary to improve the presentation such data. In Figure 8 this is accomplished by plotting each TEC value against the local time at the point where the

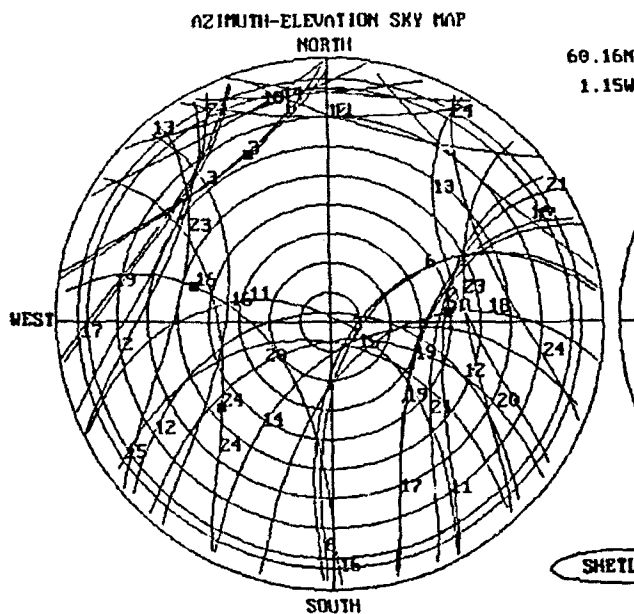


Figure 6a. Example of regional coverage available to a TISS-type monitor, Shetland Islands.

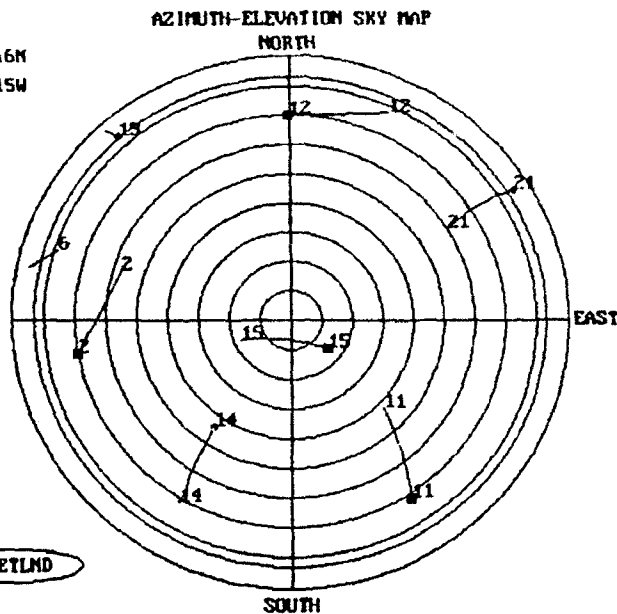


Figure 6b. Portion of coverage in (6a) obtained in a single hour.

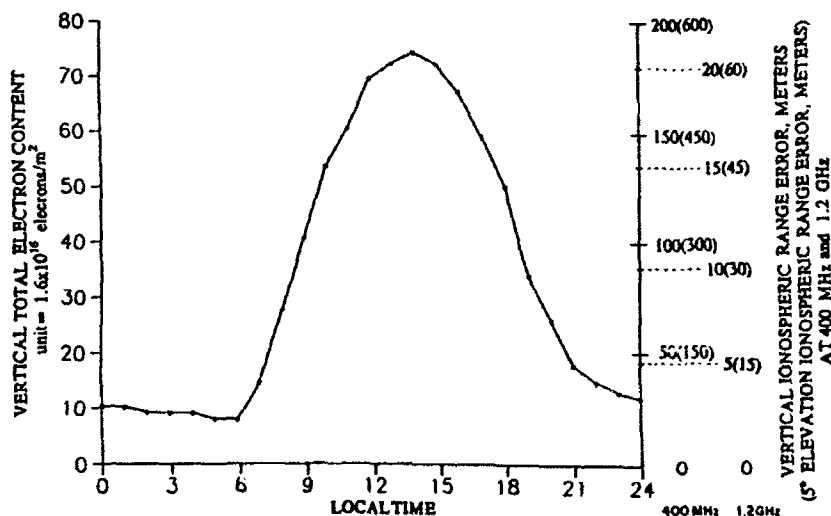


Figure 7a. Typical mid-latitude diurnal behavior of TEC during high solar activity years, with scale to convert to range error at 400 MHz and 1.2 GHz.

## SUMMARY

The AFSFC currently provides such products as rapid solar event notifications, forecasts of ionospheric irregularities, and indices of geomagnetic activity. These products are useful for operators of space surveillance systems. However, with increased real-time monitoring of the space environment and more accurate modeling capabilities, the AFSFC will have increased capability to provide more tailored products for the space surveillance community. Highly accurate real-time specifications and forecasts of trans-ionospheric effects will be possible.

## References

1. Bishop, G. J., and P. H. Doherty, "Trans-Ionospheric Effects on Space Surveillance," Proceedings of the 1991 Space Surveillance Workshop, Lincoln Laboratory Project Report STK-175, Vol. 1, Contract F19628-90-C-0002, April, 1991.
2. Basu, S., E. MacKenzie, and Su. Basu, "Ionospheric Constraints on VHF/UHF Communication Links During Solar Maximum and Minimum Periods," Radio Sci., 23, 361, 1988.
3. Bishop, G. J., "Specification of Trans-Ionospheric Effects for Space Surveillance," Proc. of the 1992 Space Surveillance Workshop, Lincoln Lab. Proj. Rpt. STK-193, Vol. 1, Contract F19628-90-C-0002, Apr., 1992.

4. Kersley, L. K., C. D. Russell, and G. J. Bishop, "Mapping of Total Electron Content and Scintillation in the Sub-Auroral Ionosphere," Proc. of the International Beacon Satellite Symposium, MIT, Cambridge, MA 1992.

5. Llewellyn, S. K., and R. B. Bent, "Documentation and Description of the Bent Ionospheric Model," AFCRL-TR-73-0657, AD 772733, 1973.

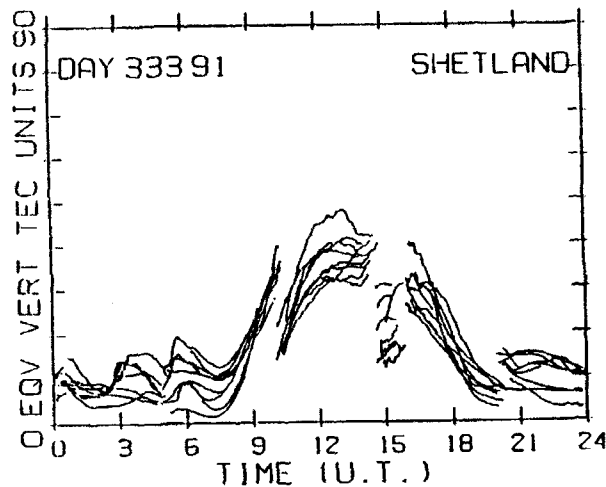


Figure 7b. Several days' TEC observation from the same sequence of GPS satellites, during a magnetically quiet period.

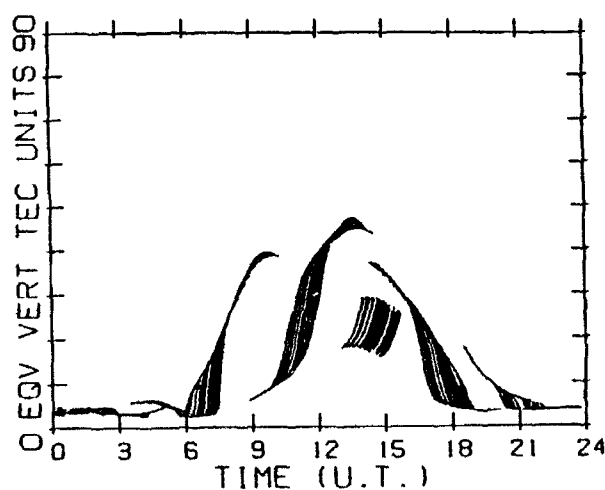


Figure 7c. TEC predictions from the Bent model<sup>5</sup> for the same times and directions as (7b).

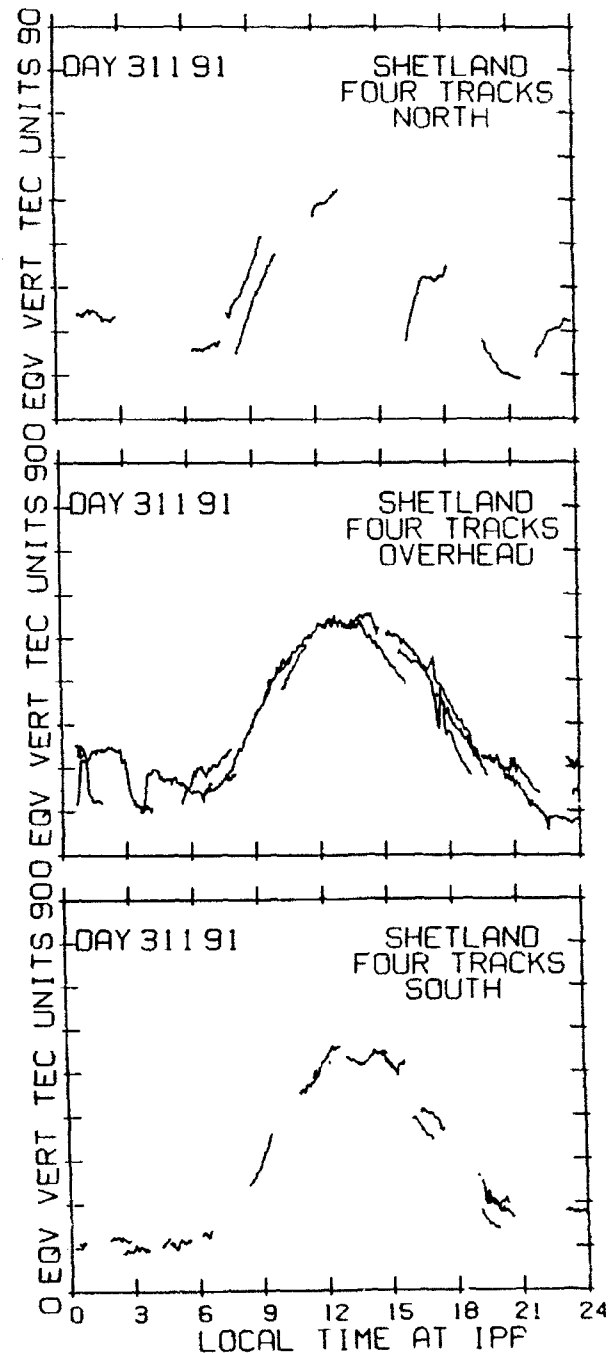


Figure 8. Four-direction GPS observations of TEC vs local time at the longitude where the raypath to the satellite penetrates 350 km altitude, 'overhead' =  $\pm 2^\circ$  latitude.

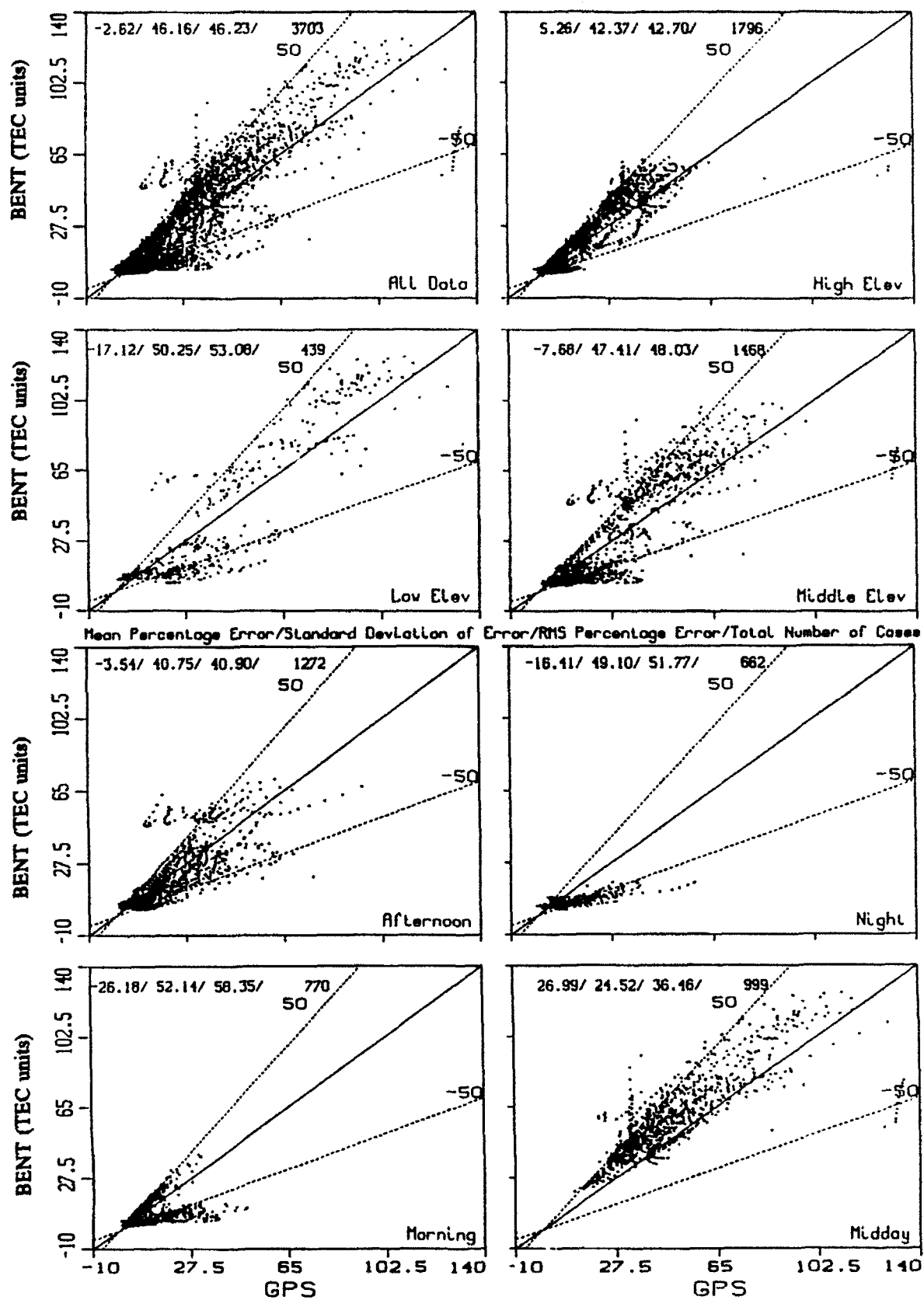


Figure 9. Comparison of one week of GPS TEC observations to predictions of the Bent model.

## Sensor Tasking by the Space Defense Operations Center

Paul R. Cherry (Loral Command & Control Systems, Colorado Springs, CO USA)

The proliferation of new satellites in orbit, and a desire to track ever-smaller pieces, will cause the number of cataloged space objects to rise dramatically. This will place an ever-increasing strain on the network of sensors that must track them. With greater demands being placed on the network in the face of dwindling budgets, it is imperative to make the most efficient use possible of network resources.

To meet this challenge, a new functional area is being developed for the Space Defense Operations Center (SPADOC) system in Cheyenne Mountain. Its mission is to task the Space Surveillance Network (SSN) with a minimum of human interaction required, while at the same time, allowing SPADOC analysts to control as much of the process as desired. The program will integrate tasking for both near-earth and deep-space objects, and will monitor day-to-day variations in each sensor's visibility for the objects to which it is tasked. This function will become operational with the 4C phase of SPADOC, scheduled for early 1995.

As an integrated part of the SPADOC system, this new program component will have "built-in" access to the catalog maintenance and observation processing components, and will have interfaces to other functional areas, such as breakup, lost, and decay processing, and automated message handling.

### 1. Purpose

The SPADOC Sensor Tasking program component supports the collection of metric observations from the SSN sensors to maintain current element sets in the Satellite Catalog. It is designed to automate what is currently a labor-intensive operation performed by the Space Surveillance Center (SSC).

It is not the intent of the program to schedule each sensor site's daily operations; each site will generate its own schedule for the satellites to which it is tasked. The program is intended instead to allocate tasking assignments for the entire catalog across the network, such that every object is being observed with the desired frequency, and that sensors are not being tasked for objects they cannot see.

The program is also intended to provide analysis of the network's performance, as measured by each sensor's response to its assigned tasking. The analysis function is designed to track observations expected and received down to the level of satellite/sensor/day, and to enable this data to be sorted and formatted into a variety of reports.

### 2. Theory

To use the SSN resources most effectively, a balance must be achieved for each object based on its relative importance in the catalog. An object should be tasked for enough observations to adequately maintain its element set to the desired level of accuracy. Conversely, it should not be tasked for excess observations, to the point that it is using resources that are needed elsewhere. The program must make decisions on both quantity and type of sensor to use to adequately cover as much of the catalog as possible.

The program must also be able to adjust tasking as needed, in a timely manner. Objects that are not being seen frequently enough must have their tasking increased. Tasking should be decreased on objects that are being seen more than necessary. In a further effort to free resources, objects that are close to their "optimum" level of tasking may be periodically decreased to see if they can be maintained at a lower level.

Balanced against the observation needs are the network resources that are available. The program must know the "capacity" of each sensor in the network, and as objects are tasked to individual sensors, must record a decrease in capacity at that sensor for subsequent objects tasked. Likewise, when tasking for an

object is deleted from a sensor, that capacity should be made available for tracking other objects. This means that the satellites in the catalog need to be processed in a predictable order to give objects of a high priority or with limited visibility an early opportunity at the sensors that are most appropriate for them. The program must also be able to determine where an object of a given priority would fit into the workload of a given sensor.

### 3. Design

The actual design process has been a unique team effort initiated by the government SPADOC program office located at the Electronic System Center (ESC). ESC identified the tasking development as challenging, and assigned a team of Government, MITRE, and Loral engineers to conduct early requirements definition meetings with the user. The results of these meetings were used by the MITRE Corporation to build a rapid prototype used in an off-line workstation.

As the prime contractor for the SPADOC program, Loral Command & Control has the responsibility for translating the stated requirements and objectives into a cohesive software design, integrated into the SPADOC architecture. The result of this effort is the SPADOC Sensor Tasking (TSK) program component.

The TSK program is designed to execute on a daily basis against the entire catalog, and to automatically handle as much of the tasking process as possible while operating within constraints and parameters established by the user. The program also permits the user to over-ride any of its decisions, even to the point of placing individual objects in the catalog under complete user control. The program tasks objects for a 24-hour period beginning with the next "midnight-Zulu" time following the time of execution.

#### 3.1. Establish Tasking Groups

A key concept in the TSK program design is that of "tasking groups", which are essentially collections of objects that have similar tasking requirements. In general, an object is assigned to a tasking group based upon its orbital characteristics (orbit class) and its object type, although the program allows the user to create a tasking group for any purpose, and assign objects to it.

Tasking groups allow markedly different levels of tasking to be specified for the extremely varied sets of objects in the catalog. The user may set the observation requirements for a tasking group to anything desired, in terms of number of sensors to task, number of tracks to acquire, and number of observations per track based on sensor type. The tasking group also defines the criteria for when and how adjustments to tasking are to be made.

It is desirable to permit different tasking groups to consider different sets of sensors as candidates for tasking. The program permits each tasking group to declare a "ranking list" of sensors to use for the objects assigned to it. Further, each tasking group may have declared preferences for certain sensor types. As an example, it is possible to request that objects in a particular deep-space tasking group be tasked first to a deep-space radar, and then to one or more optical sensors.

#### 3.2. Prioritized Catalog

The order in which satellites are processed is vital in determining what resources are available to an object of its importance, relative to the rest of the catalog. A priority is computed for each satellite in the catalog, and used to determine the order in which each satellite will be tasked.

The major factor in this priority key is the object's tasking "category", which is the mechanism by which sensors are told what objects take precedence over others when resolving scheduling conflicts. This is a number from "1" to "5", where "1" means the most important and "5" means the least. This implies that all

CAT-1 objects will be processed before any CAT-2 objects, which in turn will be handled before any CAT-3 objects, and so forth.

Within a category, the satellites are further prioritized by their orbital characteristics, with higher priority given to objects with a small mean motion and low inclination, both of which may restrict their visibility to the sensors in the network. By processing these objects sooner, they are more likely to find capacity available at the limited number of sensors that can see them.

### 3.3. Evaluate Response

An integral function of the tasking program is on-going evaluation of how well each object's current tasking is maintaining its element set in the catalog. Each time the TSK program executes, it examines the network's response for each previously-tasked object, and determines if any adjustments are needed to correct problems that may be developing.

The TSK program monitors the epoch date of the current element set, to see if it has aged past a threshold defined by that object's tasking group. If so, the program will call for an increase in tasking, in an attempt to get observations on the object before it goes "lost". Should efforts to acquire the object fail before the epoch age exceeds the "lost threshold" (defined by tasking group), the TSK program identifies the object as lost in the catalog, and causes other components of SPADOC to initiate lost processing.

Also computed for each object on a daily basis is its "element set prediction quality". This is a measure of the object's error growth rate, measured over a period of time. In effect, this algorithm examines how well "previous" element sets would have predicted the errors seen in current observations. As the expected error growth rate increases, it may eventually exceed a threshold that is settable by tasking group. If this occurs for a number of consecutive days, the program will call for an increase in tasking on the object. This feature may be "disabled" during periods of high solar activity.

For each object, the TSK program evaluates the response of each individual sensor tasked. If any sensors are reporting considerably fewer obs than tasked over a period of time, the program causes those sensors to be re-evaluated against others that could be tasked instead.

Finally, if tasking on an object has not required any adjustments for a user-defined interval (by tasking group), the program attempts to decrease tasking on the object. This allows each satellite to seek its own optimum level of tasking, within the parameters of its tasking group. The program also contains certain "dampening" controls, to minimize oscillation between different levels.

### 3.4. Determine Observation Needs

The frequency of observation for a given object is parameterized within the tasking group to which that object belongs. Other parameters also prescribe the adjustments to be made to increase and decrease tasking on each object, in response to its changing status. Increasing tasking is accomplished by elevating the object to a higher category, requesting more tracks, or tasking more sensors for the object. Decreasing tasking seeks to lower the category, tracks, and number of sensors, until the object reaches a level at which it can be maintained with minimal resources.

The principal stimuli for increasing tasking on an object are the object's epoch time has aged beyond a given threshold, or the object's computed element set prediction quality has deteriorated past a given threshold for a specified period of time. The thresholds that control these decisions are set by tasking group.

An old epoch age is typically due to out-prioritization at the sites to which the object is tasked, resulting in



insufficient observations being reported. Epoch age adjustments will cause the object to "rise" in category, and may also result in the addition of sensors and/or additional tracks.

A deteriorating element set prediction quality can be the result of many factors, such as perturbations to the orbit that are unaccounted for in the theory type used, the sensitivity and accuracy of the sensors to which the object is tasked, and even poor distribution of observations around the orbit. The common denominator in this situation is that there is something not quite "right" about the combination of sensors that the program has tasked for the object. In general, element quality adjustments will cause the program to completely re-select the sensors to task, with additional tracks and/or sensors requested. Further, a different ranking list is used for this type of adjustment, in which sensors may be ranked by "quality" of observations.

### 3.5. Assign Tasking

When the desired level of tasking for an object has been determined, the TSK program must select the "best available" sensors to task for the needed observations. Many factors go into this decision, and these factors are controlled by user-definable parameters.

The initial list of candidate sensors comes from the ranking list of the tasking group to which the object is assigned. Any sensors that are marked in the database as "down" are removed from this list.

The remaining sensors in the candidate list are checked for visibility on the object. The TSK program utilizes an SGP4 algorithm that is specialized to the task of computing viewing opportunities of a single object, from many different locations. The result of the algorithm is the number of passes of a minimally-acceptable duration that each sensor will have on the object, during the day being tasked. Any sensors that are computed to have no viewing opportunities on the object are removed from the list.

The surviving sensors form the final candidate list. The sensors that will actually be tasked for the object are selected from this list, using a parameter-driven "weighting" algorithm. Each sensor receives a weight for how well it is judged to satisfy certain criteria. The amount of weight to be added for each of the criteria is user-settable in the database. The selection criteria include:

#### Currently Tasked

In an effort to achieve stability of tasking across the network, sensors that are currently tasked to the object will receive additional weight for that object. This weight is intended to be difficult for non-tasked sensors to overcome, but a sensor will lose this weight if it has not responded sufficiently on the object, or if an adjustment for poor element set prediction quality is being made.

#### Sensor Ranking

Every Sensor Ranking list provides two weight values for each of the sensors it contains. One is used specifically when the program is making an adjustment for element set prediction quality. The second ranking value is used in all other cases.

#### Sensor Loading

As the program cycles through the catalog, it maintains a record of how many tracks have been tasked to each sensor at each of the possible tasking categories. This enables the TSK program to determine if an object's category would place it within a sensor's taskable capacity. If so, that sensor receives a substantial weight. A smaller additional weight is also added to each sensor based upon loading at the category of the object. The less-loaded a sensor is, the more weight it receives.

#### Number of Passes Available

A "minimum" number of passes per sensor is determined, by computing the maximum number of

tracks that any one sensor would receive, if they were evenly divided among the taskable sensors. Each sensor that has sufficient passes (as computed in the visibility algorithm) to cover this minimum is given a fixed amount of weight. Sensors then receive a smaller additional weight for each pass over the "minimum" needed.

#### Latitude Separation

As each sensor is selected, the remaining sensors in the candidate list are given a varying amount of weight, depending upon its latitude separation from the "closest" of the sensors that have been previously selected. A greater latitude separation results in a higher weight.

#### Probability of Acquisition

Each sensor's ratio of observations received to observations tasked for an object, over a period of time, is used in two ways. First, if the ratio falls below a user-settable threshold, the extra weight given a currently-tasked sensor will be removed. Secondly, a certain amount of weight is added based on the strength of the ratio itself.

Using these criteria, the specified number of sensors are selected from the highest-weighted rankings. The specified number of tracks are then distributed as evenly as possible among the selected sensors. For each sensor, the program generates the tasking code from the priority category, and the suffix that best approximates the number of tracks and observations allocated to it. The number of expected observations from each sensor is then recorded in the database, for later use by the evaluation and analysis functions.

#### 4. Transmit Tasking to Sensors

Once the tasking for all objects has been computed, reviewed, and accepted, the user may transmit the tasking assignments to the sensors. The TSK program generates tasking message(s) for each sensor, and uses SPADOC's interface to the Communications System Segment Replacement (CSSR) to transmit the messages to the sensors in the network.

The "Sensor Tasking" message, or "consolidated" message, is a complete listing of all objects that are tasked to the sensor. It consists of a list of satellite numbers, organized by tasking code. These messages may be generated or re-generated at any time, upon user request.

The "Sensor Tasking Update" message contains only those satellites whose tasking has changed at that sensor from that assigned the previous day. The message contains separate sections for satellites whose tasking is to be deleted from the sensor, and satellites that are being added to the sensor or are being tasked under a different tasking code than they were previously. Update messages cannot be received by some sensor sites. Whether or not they are sent is user-definable for each site in the tasking database.

"Supplemental Tasking" is a new concept for this program, and results in the output of the "Supplemental Tasking" message. This message contains a list of satellite numbers, organized by tasking code, that could not be "accountably" tasked to the desired number of sensors. This situation arises when all sensors that have visibility on the object are already fully-loaded with higher-priority objects. When this is found to be the case, the TSK program will task the object to sensors in a "non-accountable" status, meaning that if the site has time to take observations it should do so, but it will not be counted as a "missed" object if it can't. Supplemental tasking is also user-definable for each sensor in the database.

#### 5. Sensor Performance Analysis

The TSK program is informed by the observation processing segment of SPADOC as obs are received. It then accesses its historical database, to update the counts of obs received from each sensor on individual objects that coincide with the expected observations that were tasked.

Upon user request, the TSK program will format and present reports of the network's response to tasking. The reports may be organized and sorted in several different ways, and selection criteria may be specified to restrict the report to a subset of satellites and/or sensors. Aside from the obvious purpose of documenting sensor performance, this data may also help to identify changes to key parameters that could be beneficial to certain objects or tasking groups.

Also upon request, statistics for each sensor may be formatted into a "Sensor Analysis Report" message, and transmitted to that sensor site. This feedback message details the observations expected and received on a daily basis, and identifies the specific satellites that had insufficient obs reported.

## 6. Tasking Prototype

The Mitre Corporation has, in a co-operative effort, prototyped the major algorithms of the SPADOC Sensor Tasking program on a stand-alone workstation. This prototype is in the process of being interfaced with the SSC's 427M computer system, from which it will receive observations and current element sets. The prototype will in turn generate tasking messages, and send them out to the network via the 427M interface.

The purpose of this effort is two-fold. First, the prototype will provide validation of the algorithms, with a large enough window to implement any needed adjustments before the SPADOC program is delivered. Secondly, the data that results from this effort will help to establish realistic values for the many parameters that control the tasking process.

## 7. Summary and Conclusion

The future success of the Space Surveillance Network in performing its spacetrack mission will depend upon the ability to make the most of the resources available. This means tracking each object with as few resources as possible, while still maintaining the desired level of accuracy. The key to this is optimizing the use of the SSN through intelligent tasking.

Just as much, the success of the network also depends upon two-way communication and co-operation. Feedback from the sensor sites is vital, to make the adjustments needed to allow the system to function. The SPADOC Sensor Tasking program will enhance the ability of tasking personnel to use that feedback effectively.

## Acknowledgements

The design for this software was made possible through the dedication and teamwork of fellow Loral team engineers Gary Brumfield, Ron Elrod, Brian Gould, Bob Reed, Fred Seitz III, and Howard Tilton. Many of the underlying concepts evolved from numerous interchange meetings with representatives from AFSPACECOM 1st CACS and DOYA, USSPACECOM, Space Applications International Corporation, and especially the Mitre Corporation.

## Expert Systems For Sensor Tasking

T.D. Tiefenbach (Nichols Research Corporation)

### INTRODUCTION

Expert Systems technology has matured sufficiently enough in recent years to allow its application to a wide range of problems in science, business, and industry. However, there is a noticeable lack of existing Expert Systems applications in the area of space surveillance, and in particular, sensor tasking. This paper discusses a research project which was concerned with the evaluation of Expert Systems technology as a solution to some of the problems associated with sensor tasking.

In 1992, Nichols Research Corporation (NRC) received funding from United States Space Command to evaluate the potential offered by Expert Systems to enhance Space Surveillance Center (SSC) sensor tasking. The objective of this project was to review current sensor tasking methodologies, identify those areas which seem well suited to an Expert Systems approach, and if possible, develop a software prototype. As a result of the study, NRC developed two prototype systems that demonstrate the usage of Expert System techniques to solve different tasking problems.

The motivation for considering an Expert System approach to sensor tasking arises from the nature of the tasking problem itself. Sensor tasking is a complex problem requiring the consideration of many factors. Often, a tasking decision will be made by a human tasking officer who draws upon years of experience in his reasoning process. An Expert System allows the human expert's knowledge to be captured in a set of rules that can be easily modified to reflect changing requirements. This approach offers an advantage over more conventional algorithms in which costly software changes might be needed.

### EXPERT SYSTEMS BACKGROUND

Before progressing any further, it may be useful to include a brief discussion of some of the general concepts of Expert Systems (also referred to as ES). Expert Systems is one facet of Artificial Intelligence that involves the use of computer programs to mimic the reasoning of a human expert when he or she is engaged in solving a narrowly defined problem. The essence of ES development is to capture the strategies and rules-of-thumb that the expert may employ, and

reproduce these in a form that can be processed by a computer. Thus, the availability of a human expert is critical to the success of any ES endeavor.

A key feature of ES is the capability to reason with rules. A rule is a collection of knowledge that represents a situation and its immediate consequences. A typical rule consists of conditions, a hypothesis, and actions. The hypothesis represents a conclusion or goal that has a Boolean value, i.e., either True or False. The conditions are mathematical or logical criteria that must be satisfied if the hypothesis is to be proven true. If, upon evaluation, the rule is found to be true, then the rule's actions are performed. Typical rule actions may include evaluating a related hypothesis, or executing a routine to perform numerical calculations. These concepts of rule structure are illustrated by the following example:

*IF*                    *there is evidence of Recent\_Tasking*                    (Conditions)  
                         *and satellite.obs\_age > 5.0 days*

*THEN*                    *Satellite\_Lost* (Hypothesis)

*AND*                    *Search\_Tasking* (Action)

The hypothesis of this example rule is *Satellite\_Lost*. In order for this hypothesis to be confirmed True, the two conditions, *Recent\_Tasking* and *satellite.obs\_age > 5.0*, must both be true. If the hypothesis is True, then the action *Search\_Tasking* is performed. In this example, the first condition is actually the hypothesis of a different rule, which in turn may have other hypotheses for its conditions. Similarly, the action *Search\_Tasking* is the hypothesis of a rule that comes under evaluation if *Satellite\_Lost* is confirmed. Following this example, many rules that share similar data can be linked together to form a rule network.

Expert Systems commonly use two different types of reasoning processes, known as backward and forward chaining. In backward chaining, the system is directed to start at a particular hypothesis. The system evaluates the conditions of the initial hypothesis, and if these conditions include other hypotheses, they are also evaluated. In this way, the reasoning process propagates backward through the rule network until all information necessary to determine the value of the initial hypothesis is found. Forward chaining works in the opposite direction, starting from a set of data and propagating forward in order to see which hypotheses are true as a result.

Keeping the previous discussion in mind, ES are best suited for applications involving complex decision-making processes in which the outcome is initially uncertain. Repetitive numerical calculations are not an area in which ES are likely to be useful. While it is true that a complex decision tree can be implemented in software using the standard If-Then-Else structure, ES have a definite advantage in this area due to their flexibility. Rather than being hard coded in the software, ES rules are stored as data in a "Knowledge Base" file which can be modified with the use of rule editors. The ES software contains only that code which is necessary to read and execute the rule format. Additionally, the ability to start from any hypothesis and reason either forward or backward allows for a virtually unlimited number of decision paths.

## TASKER DEFICIENCY IDENTIFICATION

In evaluating the potential for ES applications in sensor tasking, NRC first conducted a survey of the current tasking process to identify problem areas that need improvement. This list of deficiencies was assembled with the aid of information from SSC tasking personnel and previous NRC tasking studies. While this survey was by no means a comprehensive accounting of all deficiencies, we were able to identify more than a dozen general areas in which the tasking process could be improved. NRC then evaluated this list of problem areas against known ES strengths to determine the areas with the most potential for an ES solution. It became apparent that several of these areas, such as sensor visibility checking and element set quality monitoring, were straightforward numerical processes and therefore not well suited for an ES approach. However, other areas showed promise.

Two areas in particular seemed likely candidates for ES solutions. The first involves how unique sensor resources are exploited by the current tasking process. Many sensors in the network have unique attributes or special capabilities that are not fully realized. Better use of limited sensor resources could be made if these unique capabilities were considered when issuing tasking.

The second area of interest involves the use of feedback in the tasking process. The current method counts the number of observations received from each sensor on each satellite, but the operational use of this data is a manually intensive function and is not always used. The tasking process could be improved if long term trends were monitored and the data used to perform diagnosis of satellite/sensor combinations that produce consistently poor tasking response. This diagnosis could lead to recommendations for changes in tasking.

## APPROACH

Having established that ES technology showed promise as a potential solution for some sensor tasking problems, NRC proceeded to develop a prototype ES tasker. The reasons for this approach were two-fold. First, the use of a functional ES would give better validation of concepts and rules than a purely academic exercise could provide. Second, an operational ES prototype is an excellent way to demonstrate how the technology can be applied.

The knowledge base for the NRC Expert System was derived from interviews with NRC technical staff members who are experienced with the SSC tasking process. The system was implemented on an IBM compatible 486 computer, and runs under the Windows operating system. A commercially available ES shell known as Nexpert Object was used as the inference engine for the system. Nexpert is marketed by Neuron Data Corporation and is widely regarded as an industry standard ES shell. One particularly important feature of Nexpert is its ability to interface with other non-ES applications, allowing the development of a hybrid system that brings together the advantages of both ES and conventional algorithms.

What resulted from our experiments with Nexpert was actually two separate prototype Expert Systems, to which we have assigned the (highly original) names Version 1 and Version 2. The Version 1 prototype was primarily an experimental system, meant to be used as a test bed for various tasking-related ES concepts. Experience with the Version 1 prototype revealed that the sub-area of problem satellite diagnosis and tasking is particularly interesting. We developed the Version 2 prototype in order to more fully explore this area. What follows is a more detailed description of each of these prototypes.

### VERSION 1 PROTOTYPE

The Version 1 ES prototype was designed to address the two problem areas that were discussed earlier: unique sensor resources and tasking feedback. The knowledge base currently consists of approximately 70 rules, and is capable of performing sensor tasking assignments for a limited number of test case satellites. Initially, a small sample of 25 satellites was used in order to keep run times to a reasonable limit. However, larger samples were used later to gauge the effect on system performance.

In order to model a complete feedback loop, a sensor response algorithm was developed to simulate the number of observations (OBS) received from each sensor for each satellite. This

algorithm utilizes a binomial probability distribution to determine the number of OBS received, given the number requested and the probability of receiving one OB with one request. The probability of receiving one OB is a function of the following four independent parameters: 1) Sensor loading (OBS requested from sensor divided by maximum sensor capacity), 2) Age of last satellite element set, 3) Satellite element set error magnitude, and 4) Sensor "effectiveness rating" for the satellite class of interest. Given this model of sensor response, a sensor has a high probability of obtaining OBS on a satellite that has a recent element set of good quality.

A simplified diagram of the Version 1 software architecture is shown in Figure 1. The Nexpert knowledge base is represented by the two darkened blocks, corresponding to two rule sets, one for tasking assignment and one for satellite diagnosis. Tasking assignments generated by the knowledge base are sent to the sensor response module. The simulated sensor response is fed back into the satellite diagnosis portion of the knowledge base, which performs tasking adjustment if necessary.

Some additional functions of the Version 1 Expert Systems prototype tasker can be summarized as follows:

- Satellites are assigned to one or more of the following ten classes:

<u>Class Name</u>	<u>Description</u>	<u>Priority</u>
Pasched_Sats	Active payloads, NFLs, PPLs	10
TIP_Sats	Decaying orbits	9
Special_Interest_Sats	Calibration, DMSP, etc.	8
Marginal_Sats	Few or no OBS	7
Poor_Elset_Sats	Error magnitude > 12.0 km	6
Lost_Sats	OBS age > 5.0 days	5
Small_RCS_Sats	RCS < 0.01 sq. meters	4
Payloads	Inactive payloads	3
Rocket_Bodies		2
Debris		1

- Satellites are ranked in numerical order, based on the priority of the highest class to which they belong. Sensors are tasked for higher ranked satellites before lower ranked ones.



- Each sensor has an "effectiveness" rating for each of the ten satellite classes, that is a measure of how good the sensor is at obtaining OBS for that satellite class. The sensors with higher ratings are assigned tasking before lower rated ones.
- There is one tasking rule for each of the 31 sensors. These rules consider both the capabilities of the sensor and the type of satellite, so that tasking is only assigned to sensors which are appropriate for the satellite. (For example, only deep space sensors can be assigned to track a deep space satellite.)
- If found to be necessary, the knowledge base performs a simulated differential correction to estimate a new value for element set error magnitude. The error magnitude is determined by a probabilistic model which was found to reasonably duplicate actual DC behavior.
- The satellite diagnosis rules change the sensor suite assigned to the satellite and adjust the tasking as necessary to correct problems.
- Satellite events (e.g., new launch, payload deactivation, etc.) can be scheduled to perturb the system and force tasking adjustment.

Because of the cycle of tasking assignment - sensor response - tasking adjustment within which the Version 1 prototype operates, the system runs in an essentially infinite loop, with the current day incremented by one after each tasking assignment phase. We found that in general, satellites that were having problems with poor OBS flow or large error magnitude would eventually be corrected as they were diagnosed and the tasking was adjusted appropriately. Once the satellite had been recovered, the tasking was then restored to normal levels.

#### VERSION 1 PROTOTYPE - CONCLUSIONS

Our experiments led us to draw several conclusions regarding the Version 1 prototype software architecture. One conclusion is concerned with our use of feedback data in the system. While the prototype uses a limited set of data to perform tasking adjustment, it became apparent that a more complete set of data would allow for a more robust diagnostic rule network. Specifically, the Version 1 prototype uses the number of OBS requested and received for the previous day, and the error magnitude and age of the most recent element set. A complete set of feedback data would include a history of the tasking and OBS received for an extended period of time, as well as the actual element set data for the same period of time.

Most importantly, we concluded that our use of the ES to assign tasking for all of the satellites in our sample set was not the most efficient use of ES resources. The Version 1 prototype was designed under the assumption that the ES would act as a "global" tasker, performing tasking assignments for every satellite in the SSC catalog. While this assumption is valid for a satellite sample like our original 25, it breaks down when the number is increased to anything resembling the true catalog of 7000 objects. Because of software constraints, we were able to run a maximum catalog of approximately 700 satellites. For this number of satellites, it took approximately one-half hour to generate one day's worth of tasking.

In retrospect it became clear that with our first prototype, we were asking too much of the ES, by using it to perform routine tasking assignments for non-problem satellites. Although we demonstrated that ES technology is fully capable of handling this function, other non-ES algorithms perform more efficiently in this area. We are convinced that the real payoff comes from using ES for functions that other algorithms do not perform so well, as in the case of non-routine tasking. For this reason, we directed our efforts to the area of problem satellite diagnosis.

Historically, many of the successful applications of ES have been for diagnostic purposes. There are several well publicized examples of medical diagnosis expert systems, as well as applications designed to troubleshoot complex mechanical systems. The complex decision making process involved in many diagnostic problems lends itself well to an ES approach. The area of tasking diagnosis is no exception. In general, the majority of satellites in the SSC catalog can be maintained using a routine set of tasking assignments. However, there is usually some small percentage of satellites which experience detectable problems. For example, one or more sensors may not be responding to tasking for the satellite, or the satellite may have a consistently poor quality element set. It is for these special cases that an ES approach may have the most benefit.

The idea of using an ES to perform diagnosis and tasking recommendation for special case problem satellites led us to develop the Version 2 ES prototype. In addition, we were motivated by a desire to build a more user-friendly system which would be useful for demonstration purposes.

## VERSION 2 PROTOTYPE

The Version 2 ES prototype, while borrowing many aspects of Version 1, represents a change in functionality from the previous version. Rather than generating tasking assignments for all satellites, Version 2 is designed to operate on one satellite at a time. It is assumed that the majority

of tasking assignments are handled by a conventional algorithm such as currently used by the SSC, and that the ES is invoked only when it is determined that a particular satellite appears to be having problems.

In order to provide a basis for rule development in the Version 2 prototype, an analysis of problem satellites was performed. Using SSC element set files for Julian days 92-120 of year 1992, a search was performed to find those satellites that had an element set age of three days or older, for at least 2 days in the time period. Those satellites that had no change in element set epoch date over the time period were removed, in order to screen out ones which were obviously "lost." What resulted from this process was a set of problem satellites that consistently exhibit marginal tasking response. When the number of OBS per day from each sensor was plotted for these satellites, it became obvious that nearly all of these satellites were experiencing fluctuations in OBS flow.

Figure 2 shows a simplified diagram of the Version 2 prototype software architecture. All input and output are handled via an interactive user-friendly windows interface. Nexpert handles all ES functions, but runs in the background and is totally transparent to the user. A database is maintained that contains all necessary satellite and sensor information. Nexpert interacts with the database, both directly and via a set of auxiliary "C" routines that perform functions such as visibility checking and analysis of OBS history data.

The functionality of the Version 2 prototype Expert System tasking "Advisor" can be summarized as follows:

- The system is capable of three different operating modes: Satellite diagnosis, Ideal tasking assignment (no consideration of satellite symptoms), and Tasking recommendation (optimized for satellite symptoms).
- The user has the capability to pick a satellite of interest from a list of all satellite data currently in the system. In addition, the user can enable or disable specific sensors if desired.
- Satellite data used by system includes SSC catalog data, (name, type, radar cross section, launch date, etc.), all element set data for time period, OBS history and tasking history for time period.
- Sensor data used by system includes site data, (name, location, etc.), coverage data (azimuth, elevation, range limits).

- The diagnostic rules execute auxiliary C routines to perform analysis of satellite history data.
- Diagnostic conclusions are output via a window which contains a brief explanation of each conclusion.
- Tasking recommendations are output via a window which contains both the suggested number of OBS per sensor and the equivalent SSC standard category/suffix.
- The visibility of each sensor to the satellite of interest is computed using the sensor look angles program LAMOD.

## VERSION 2 PROTOTYPE - CONCLUSIONS

NRC is currently refining the Version 2 rule network, and experiments are underway to test the validity of this new prototype. Therefore, we have elected to refrain from making conclusions about this version until the date of presentation, at which time the final results are expected to be available.

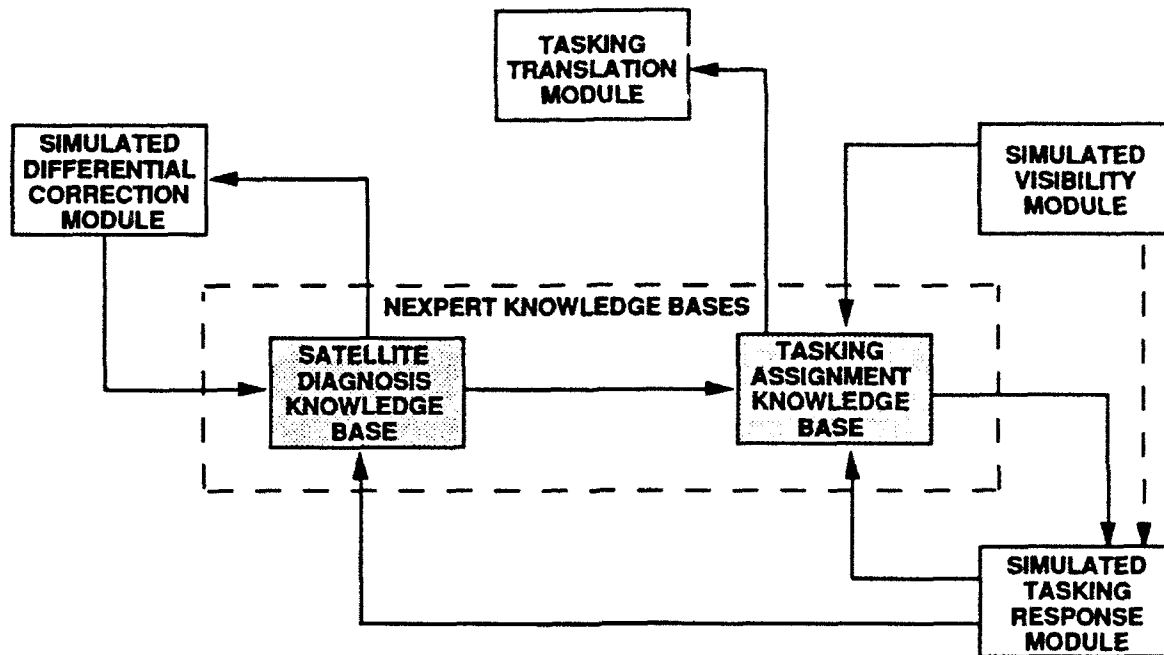


Figure 1. Version 1 Prototype Software Architecture

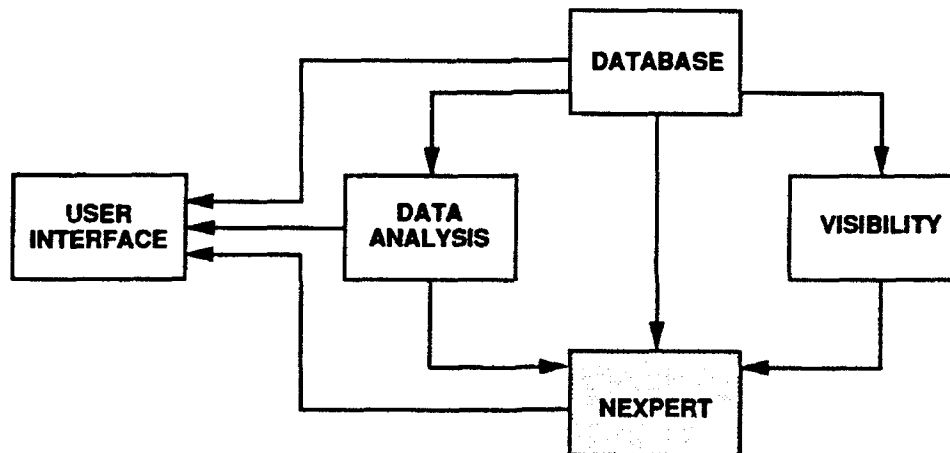


Figure 2. Version 2 Prototype Software Architecture

Pages 109 to 118 are intentionally left blank.

## Tracking Data Reduction for the Geotail, Mars Observer, and Galileo Missions

R. L. Mansfield (Loral Command & Control Systems, Colorado Springs, Colorado U.S.A.)

The first Earth flyby of the space probe Galileo provided the stimulus for synthesizing and testing a uniform path propagation theory ("uniform path mathematics") valid for any orbital eccentricity. The following paragraphs summarize the rationale for, and recent experience with the theory and provide examples based upon operational results obtained in the Space Defense Operations Center, Phase 4B (SPADOC 4B) from Geotail, Mars Observer, and Galileo observations.

### 1. Background

The orbit determination and single-track differential correction processes are fundamental to space surveillance. For radar tracks containing at least three observations, the Herrick-Gibbs preliminary orbit determination method is used in SPADOC 4B to obtain a first estimate of position and velocity. The initial estimate is then improved by differential correction (DC), provided that three or more observations are available. It has been conventional that all space surveillance DC applications programs use the equinoctial form of orbital elements as the orbital state to be corrected. This is because a DC of the equinoctial form will converge for small eccentricity and inclination, while a DC of the classical form of orbital elements will fail to converge in the argument of perigee or right ascension of ascending node correction if either eccentricity or inclination, respectively, is too small.

But in the age of gravity-assist Earth flybys, which was begun by the Galileo space probe at its Earth 1 flyby of 8 December 1990, the equinoctial form of orbital elements no longer suffices to represent all cases of orbital motion of interest to space surveillance analysts. This is true because flyby trajectories are by definition unbound, and are therefore parabolic or hyperbolic when the space object is in the close vicinity of the primary. Since the equinoctial form uses mean motion as a path element, and since mean motion only makes sense for bound (elliptical or circular) orbits, a more general approach to the representation of two-body motion was sought.

An approach based upon merely checking orbital eccentricity and branching to the elliptical, parabolic, and or hyperbolic form of Kepler's equation was rejected immediately since it was known that elliptical and hyperbolic motion in the vicinity of unit eccentricity could pose a problem for convergence of the DC. Further, it was known that Stumpff [1] and Goodyear [2] have provided uniform equations for two-body path representation which do not depend upon the orbital eccentricity. Given these developments, the approach taken was to adopt a cartesian, rather

than an equinoctial state representation, and to use Stumpff's c-functions to calculate position and velocity, then Goodyear's state transition matrix to calculate the necessary partial derivatives. This approach was given the name "uniform path mathematics" to distinguish it from the other methods of path propagation in SPADOC 4B, both two-body and perturbed.

To verify the equations for a case of operational interest, a DC of the hyperbolic trajectory for Galileo's Earth 1 flyby was accomplished using uniform path mathematics with observations from the Millstone Hill and ALTAIR radars [3]. After proof of concept, the challenge was now to analyze the existing, equinoctial-state-based SPADOC 4B DC code and determine how to interface the existing procedures for residuals, partials, and least squares normal equations calculations with the new procedures for state and state partials propagation. This was accomplished during summer 1992, in time for the Mars Observer launch of September 25, for which the Earth-to-Mars transfer orbit was hyperbolic with respect to Earth as the primary.

## 2. Numerical Examples from the Geotail, Mars Observer, and Galileo Missions

To illustrate the application of uniform path mathematics, and to provide examples for numerical validation, the first three SPADOC 4B operational usages are described and numerical data are given in tabular form.

2.1 Geotail's Orbit after Second Lunar Swingby. Geotail was launched on 24 July 1992 into a highly eccentric, but still elliptical orbit whose apogee is kept in Earth's geomagnetic tail in order to enhance Geotail's opportunities to observe the tail. Further, Geotail's orbits have been planned such that lunar swingbys will pull apogee out to more than three times the radius of the moon's orbit. Thus, it is expected that over the probe's three-year-plus mission lifetime, lunar swingbys will make it possible to sample the magnetotail over a wide range of distances along the Earth-sun line on Earth's night side.

On 18 October 1992, just after the second lunar swingby, Space Command analysts Capt. Tim Slauenwhite and First Lt. Dave Correll determined the orbit of Geotail from ALTAIR observations. For an epoch on this date, Table 1 provides the position, velocity, conic elements, and state transition matrix at epoch and at four other equally-spaced points, as calculated using uniform path mathematics.

2.2 Mars Observer's Transfer Orbit. Mars Observer was launched on 25 September 1992 into a hyperbolic transfer orbit toward Mars, with arrival at Mars expected in August 1993. Capt. Derrick Aiken and the author determined the transfer orbit from ALTAIR observations. For an epoch after injection on the launch date, Table 2 provides the position, velocity, conic elements, and state transition matrix at epoch and at four points



post-epoch, as calculated from the solution obtained the day of the launch using a DC based upon uniform path mathematics.

2.3 Galileo's Earth 2 Flyby Trajectory. Galileo was launched on 18 October 1989 into a six-year flight to Jupiter, during which it has received three planned gravity assists, one from Venus (10 February 1990) and two from Earth (8 December 1990 and 8 December 1992). Reductions of Millstone Hill and ALTAIR observations of the Earth 1 gravity-assist flyby, as obtained via a DC using uniform path mathematics, were reported in [3]. For the Earth 2 gravity-assist flyby, Space Command analysts Slauenwhite, Capt. Paul Hartman, Aiken, and Correll determined the flyby parameters from Pirinclik (near-Earth radar) and Taegu (deep-space electro-optical) observations. Table 3 provides the position, velocity, conic elements, and state transition matrix at epoch and at four other equally-spaced points, as calculated from the solution obtained a few minutes after perigee by Space Command via a DC based upon uniform path mathematics.

### 3. Summary and Conclusions

Three operational instances, one involving a very-elongated elliptical path and two involving hyperbolic paths have been described, for which a single mathematical procedure, uniform path mathematics, was used successfully to provide "computed" observations in a DC of cartesian state. Since, as was noted at the outset, reducing tracking data on an unknown or unconfirmed space object is of fundamental interest in space surveillance, it is concluded that (a) a DC based upon uniform path mathematics is well-considered for inclusion in the data reduction software of space surveillance command centers and remote tracking sites, and (b) the algorithm can be used to reduce multiple tracks of observations, subject to the short-arc limitation inherent in the two-body mathematics.

### Acknowledgments

The modifications to SPADOC 4B needed to implement uniform path mathematics in the initial orbit request function, IOR, were carried out with consummate efficiency and skill by Jon Kolb and John Czaja of Loral Command & Control Systems.

### References

- [1] K. J. Stumpff, "Neue Formeln und Hilfstafeln zur Ephemeridenrechnung," Astronomische Nachrichten, Vol. 275 (1947)
- [2] W. H. Goodyear, "Completely General Closed-Form Solution for the Coordinates and Partial Derivatives of the Two-Body Problem," Astronomical Journal, Vol. 70 No. 3 (1965)
- [3] R. L. Mansfield, "Algorithms for Reducing Radar Observations of a Hyperbolic, Near-Earth Flyby," AAS Paper No. 92-110, AAS/AIAA Space Flight Mechanics Meeting, Colorado Springs (Feb. 1992)

TABLE 1 - GEOTAIL AFTER SECOND LUNAR SWINGBY. WITH EPOCH AT  
1992 OCTOBER 18 (DAY 292). 03h 33m 11.398s UTC

POSITION AND VELOCITY AT EPOCH (KM AND KM/SEC):

-36291.2188980	-27384.5436770	-14626.1192510	2.5156940880	-2.8593779340	-.8810831430
----------------	----------------	----------------	--------------	---------------	--------------

CONIC ELEMENTS:

PERIGEE HT ABOVE SPHERE. KM	41380.503	ECCENTRICITY	.83091256
INCLINATION. DEG	22.35579	R.A. OF ASC. NODE. DEG	345.57163
ARGUMENT OF PERIGEE. DEG	233.69941	DELTA T, EPOCH TO PERIGEE. MIN	.25980

POSITION, VELOCITY, AND STATE TRANSITION MATRIX AT EPOCH MINUS 2880 MINUTES:

74123.4432383	247543.8280042	106191.8286552	-.9059455757	-.6961332121	-.3701044099
13.7770560193	2.6640546676	2.9882851452	-322.7316337038	106.6142331358	14.5073866882
-14.8840612184	-8.8709626663	-3.1330506933	355.3787845417	-325.2084074424	-73.2295931556
-4.0210653161	-1.3348012936	-5.7779733205	113.5893988783	-98.7218287970	-77.5984389382
-.0327786465	-.0041075894	-.0070740449	.8812111839	-.3580776273	-.0517918067
.1105705979	.0665617087	.0297614740	-2.8374136611	2.3359270613	.6590726039
.0386018582	.0180097881	.0314168114	-.9804396162	.8928533232	.2598318213

POSITION, VELOCITY, AND STATE TRANSITION MATRIX AT EPOCH MINUS 1440 MINUTES:

-8387.2157172	164847.5007045	64798.6745048	-.9804244520	-1.3163992642	-.8247863621
8.5783846797	1.6777745113	1.7792207476	-188.7178658688	47.5409897005	4.1862785675
-4.2872240500	-2.6280183765	-.5847414838	104.8333284209	-112.4337688982	-16.2774208541
-.5986163917	.0265238595	-2.3135209120	26.9856078144	-22.1484735859	-50.6504942231
-.0861004487	-.0135927307	-.0151157726	1.6517492197	-.7053433602	-.1240913327
.0836074663	.0488447075	.0166412983	-1.9448683848	1.5881664106	.3762267867
.0235987108	.0066806736	.0336535839	-.8177896225	.5032475533	.2583258673

POSITION, VELOCITY, AND STATE TRANSITION MATRIX AT EPOCH PLUS 1440 MINUTES:

172559.1270017	-40613.5417044	1508.8324295	1.5882980158	.8267708890	.4124019583
-2.7927092879	-2.1240463941	-.8999807874	93.8090248748	-88.9142265281	-29.5648749115
3.8522270872	7.1311213925	4.1375736545	-29.4392780373	194.0103180120	56.5317744919
1.4803471313	3.5251529097	-.7101855984	-8.8728128608	50.8420087593	83.9888337509
-.0624208308	-.0591852291	-.0270401117	1.2343387299	-1.8881756246	-.8299127848
.0381135212	.0613490942	.0397279335	-.6253482533	1.9248405745	.8547115550
.0117138252	.0297572096	-.0155370129	-.1348983856	.5273521743	.3163875902

POSITION, VELOCITY, AND STATE TRANSITION MATRIX AT EPOCH PLUS 2880 MINUTES:

276518.1088510	17759.5624982	35409.8601593	.9173893231	.6833327443	.3661787324
-11.2135263301	-10.1298577301	-4.8880129292	270.3291088728	-345.8412427782	-115.1414540539
7.4321208504	12.5600086322	7.8911988345	-98.4870350960	370.2067084691	117.7568843899
2.3068589130	5.8915286708	-2.2550951048	-15.8245839227	92.2040235125	84.8340882047
-.0926659800	-.0866786457	-.0419397179	2.0089880696	-2.8546220182	-.9313056439
.0279586155	.0409093337	.0272404427	-.5691862604	1.3658889841	.4849552087
.0037182913	.0154933586	-.0137382885	-.0210249293	.2507543688	.0995925192

TABLE 2 - MARS OBSERVER TRANSFER ORBIT. WITH EPOCH AT  
1992 SEPTEMBER 25 (DAY 289). 18h 21m 50.985s UTC

POSITION AND VELOCITY AT EPOCH (KM AND KM/SEC):

10706.8508770	15334.9934710	-3588.1358820	.7338454219	7.2824506978	.8634366138
---------------	---------------	---------------	-------------	--------------	-------------

CONIC ELEMENTS:

PERIGEE HT ABOVE SPHERE, KM	287.427	ECCENTRICITY	1.20306738
INCLINATION, DEG	29.30128	R.A. OF ASC. NODE, DEG	74.95105
ARGUMENT OF PERIGEE, DEG	236.52444	DELTA T. EPOCH TO PERIGEE, MIN	-39.56138

POSITION, VELOCITY, AND STATE TRANSITION MATRIX AT EPOCH PLUS 60 MINUTES:

11407.0456889	37912.3136179	-857.7983648	-.0701038025	5.6158976905	.8563033198
.9515069794	.2178920736	-.0351330949	4.3859798966	.1982185408	-.0227507432
.2221611013	1.2315644309	-.0618111077	.1980950856	4.7149958546	-.0456127697
-.0345110414	-.0592974810	.8381600327	-.0224773059	-.0445957642	4.2969281878
-.0191999670	.0891488240	-.0098736827	.9562532577	.0691075688	-.0081052976
.0722213046	.0852629759	-.0185554261	.0907207804	1.1334559062	-.0176757329
-.0094259819	-.0168902758	-.0533829308	-.0078702314	-.0168014426	.9191568455

POSITION, VELOCITY, AND STATE TRANSITION MATRIX AT EPOCH PLUS 120 MINUTES:

10836.3138228	56910.3719834	2419.7802422	-.2179206641	5.0124658366	.8484856528
.8512800128	.5472647070	-.0798308174	8.5331487026	.7119379544	-.0591323440
.5797681003	1.6866532937	-.1495801809	.7329880641	10.0918786105	-.1283588963
-.0750944458	-.1319647605	.5783077215	-.0560650663	-.1149506556	8.2462593808
-.0245679234	.0764049741	-.0100596984	.9052851037	.1353529713	-.0078128399
.0860793083	.1150220024	-.0208130537	.1427643981	1.2694684264	-.0169132650
-.0086502207	-.0153899868	-.0612243142	-.0067299836	-.0128857572	.8562471525

POSITION, VELOCITY, AND STATE TRANSITION MATRIX AT EPOCH PLUS 180 MINUTES:

9943.9365829	74323.1360723	5440.6783858	-.2703445703	4.8888616205	.8297437334
.7375041088	.8914082855	-.1246099697	12.4867989943	1.3867312937	-.0918008040
.9813618331	2.2386524681	-.2446920944	1.4368790816	15.9889790548	-.1902391335
-.1115025553	-.1959411981	.2997878340	-.0813793492	-.1522220944	11.9722371639
-.0261417637	.0774469799	-.0100008094	.8888935035	.1555783019	-.0067573119
.0933808269	.1310872425	-.0219749763	.1702193940	1.3688822469	-.0114846245
-.0076790384	-.0133395287	-.0631997581	-.0048239123	-.0035497917	.8165842668

POSITION, VELOCITY, AND STATE TRANSITION MATRIX AT EPOCH PLUS 240 MINUTES:

8922.6918779	90808.0768201	8396.2210128	-.2942349285	4.4829174452	.8128824900
.8194654809	1.2365031769	-.1890329179	16.3017962805	2.0850391927	-.1197909606
1.4098338802	2.8484075822	-.3453925037	2.2366439795	22.2717712434	-.2283660139
-.1437763558	-.2514548283	.0183992006	-.0977001502	-.1462028370	15.5518132270
-.0288739189	.0771282717	-.0099085917	.8423967727	.1652504287	-.0059233122
.0984189314	.1415876828	-.0231340140	.1870613529	1.4440132022	-.0056490481
-.0068065541	-.0115964897	-.0836949318	-.0027451738	.0061715208	.7894242361

TABLE 3 - GALILEO'S EARTH 2 FLYBY, WITH EPOCH AT  
1992 DECEMBER 08 (DAY 343), 14h 58m 15.922s UTC

POSITION AND VELOCITY AT EPOCH (KM AND KM/SEC):

10071.0678650	-1662.5947910	298.8923300	-9.3302233081	-5.4584285132	-6.3292675115
---------------	---------------	-------------	---------------	---------------	---------------

CONIC ELEMENTS:

PERIGEE HT ABOVE SPHERE, KM	295.285	ECCENTRICITY	2.31994985
INCLINATION, DEG	138.53394	R.A. OF ASC. NODE, DEG	168.72284
ARGUMENT OF PERIGEE, DEG	237.18874	DELTA T, EPOCH TO PERIGEE, MIN	11.14798

POSITION, VELOCITY, AND STATE TRANSITION MATRIX AT EPOCH MINUS 120 MINUTES:

57921.4989715	35375.3772357	40580.0528961	-6.0577299167	-4.9168383936	-5.2964228543
3.5007089722	.0919953091	.7172305581	-10.4655982661	-.5270513141	-.8881543580
.2834072670	-.1276900889	.1089851721	-.5675228048	-8.1463811311	-.2639985460
.8827600391	.0759777469	.0207253636	-.9404489721	-.2535707325	-8.3397143196
-.3189835916	-.0172490055	-.0951999902	1.2319214150	.1002244098	.1533254286
-.0550040237	.1365043239	-.0182192707	.1139279873	.8863856195	.0550934566
-.1278498238	-.0117087268	.1144321642	.1651760281	.0527303868	.9194789836

POSITION, VELOCITY, AND STATE TRANSITION MATRIX AT EPOCH MINUS 60 MINUTES:

35670.9980602	17422.3661212	21217.7079497	-6.3845929070	-5.0845486167	-5.4945427557
2.1041033292	.0171237188	.2989807023	-5.0299825881	-.1408180353	-.2770875552
.0666263480	.4816286747	.0335044525	-.1531729866	-4.1691597371	-.0617277412
.3417896501	.0249881293	.5367018405	-.2879448423	-.0595627427	-4.2294860927
-.3037944183	-.0154104794	-.0907803612	1.1977054622	.0880210121	.1141909854
-.0394514471	.1361416167	-.0147782980	.0751782335	.8995548581	.0327931322
-.1115705404	-.0106328299	.1169295288	.1203804178	.0315589280	.9246752452

POSITION, VELOCITY, AND STATE TRANSITION MATRIX AT EPOCH PLUS 60 MINUTES:

-30468.2510065	-4349.6841754	-9015.5259791	-10.0978745966	.8718219258	-.9873260263
.5568831578	-.7694550476	-.2617913004	3.6153088402	.6307981081	.8824915649
-2.4654798832	1.7828630724	2.8591884223	-.8422480494	5.5124368071	3.2198226857
-1.7284818555	2.9516340209	.4707285088	-.2184149408	3.4393490735	4.5977101928
-.3003023367	-.0213090287	.0546387550	.8104413389	.4727380957	.5289751908
-.5447189675	.2088463592	.7127918503	-.0271356913	1.2254790356	.9568391903
-.3979963719	.8030498098	-.0981875442	.0966954191	1.0430379879	1.0322898894

POSITION, VELOCITY, AND STATE TRANSITION MATRIX AT EPOCH PLUS 120 MINUTES:

-85379.2788487	-1074.7092236	-12203.5098531	-9.4489298869	.9227653413	-.8314003989
-.8527782392	-.7975945765	.0117532543	7.5204226253	3.0014603021	3.5300093089
-4.7889235990	2.6440673432	5.7161487783	-.6956543123	10.7578664180	7.3656718573
-3.4398734299	8.4044207917	.0244410622	.3328137419	8.0032090066	9.0801847589
-.3284040782	.0013316777	.0836654452	.9175275801	.5653697121	.6314431681
-.5061251237	.1841093588	.8677070012	-.0058261107	1.1438433812	.9094450050
-.3751737051	.7552137724	-.1005262957	.1374837023	1.0079430486	.9863924553

# INTERFEROMETRIC SYNTHETIC APERTURE RADAR APPLIED TO SPACE OBJECT IDENTIFICATION

Ian Wynne-Jones (EDS-Scicon Defence plc)

## 1. INTRODUCTION

An overview of the theory of Interferometric Synthetic Aperture Radar (INSAR) and its application to Space Object Identification (SOI) is presented, some results from computer simulations are described. The requirements for a bistatic radar system are discussed and circumstances in which interferometry can be performed with a monostatic radar are appraised. Range Doppler imaging is not explained. Introductions to range Doppler imaging are given in references 1 and 2. In this paper space objects are assumed to be rigid.

## 2. THEORY

An ISAR interferometer needs two range Doppler or extended coherent images of an object viewed from slightly different aspects. Subtle differences in the phase of the complex images, enable information about the three dimensional structure of the object to be extracted from the pair of images. The images can be acquired by many different radar configurations and operating strategies. In the discussion below, bistatic operation is assumed. It is easy to adapt the theory to other radar configurations.

Figure 1 shows a schematic diagram of 2 radars, space object and object feature. Symbols used in this theory tabulated in section 9. The distances from the radars to a feature on the space object are given by

$$\begin{aligned} l_1 &= |\mathbf{p} + \mathbf{s}| = (\mathbf{p} \cdot \mathbf{p} + 2\mathbf{p} \cdot \mathbf{s} + \mathbf{s} \cdot \mathbf{s})^{1/2} \\ l_2 &= |\mathbf{p} + \mathbf{s} + \mathbf{r}| = (\mathbf{p} \cdot \mathbf{p} + 2\mathbf{p} \cdot \mathbf{s} + \mathbf{s} \cdot \mathbf{s} + 2\mathbf{p} \cdot \mathbf{r} + \mathbf{r} \cdot \mathbf{r} + 2\mathbf{r} \cdot \mathbf{s})^{1/2} \end{aligned} \quad (1)$$

Object sizes and distances are typically of the order of 10m and 1000km respectively for LEO space objects. Assuming the object size and distance between the radars is much smaller than the distance from the radars to the object then to first order the Taylor expansion of the difference in the distances is given by

$$\Delta l = l_2 - l_1 = (\mathbf{p} \cdot \mathbf{r} + 2\mathbf{r} \cdot \mathbf{s}) / p. \quad (2)$$

This distance comprises two components, a centring component

$$(\Delta l_c = (\mathbf{p} \cdot \mathbf{r} + 2\mathbf{r} \cdot \mathbf{s}) / p) \text{ and a height component } (\Delta l_h = \mathbf{r} \cdot \mathbf{s} / p).$$

For a feature at the origin of the object's coordinate system the equation shows that the centring term is the difference in distance to the origin from the two radars. To estimate the position of the features in 3 dimensions the centring component must be eliminated. The height component is proportional to the projection of the feature vector onto the radar difference vector. See figure 2. The height component enables the height of a feature above or below the image plane to be deduced, after correction for the centring component.

Pulses from the radars are centred by orbit estimation using range, range rate, azimuth and elevation measurements of the object from the radars. The pulses received by each radar are processed resulting in a sequences of images, given an estimate of the object's attitude history. The images are paired, each pair being formed from the same set of transmitted pulses. The image pairs are then used to compute phase difference and geometric mean power images. The following expressions are used

$$\begin{aligned}\phi_1 &= \tan^{-1}(i_1/r_1), \phi_2 = \tan^{-1}(i_2/r_2) \\ \Delta\phi &= \phi_1 - \phi_2 = \tan^{-1}\left(\frac{i_1 r_2 - i_2 r_1}{r_1 r_2 + i_1 i_2}\right) \\ P &= \sqrt{(r_1^2 + i_1^2)(r_2^2 + i_2^2)}.\end{aligned}\quad (3)$$

Assuming there are no centring errors then the phase differences is also given by

$$\Delta\phi = \frac{2\pi}{\lambda} \Delta l_h = \frac{2\pi}{\lambda} \frac{\mathbf{r} \cdot \mathbf{s}}{P}.\quad (4)$$

Each image is considered to be formed in the XY plane of an image coordinate system whose origin is coincident with that of the object coordinate system. The orthogonal triad of unit vectors of the image coordinate system are deduced from the radar line of sight vector, and the instantaneous net angular velocity vector of the object. The image coordinate system unit vectors are given by

$$\hat{\mathbf{x}} = \mathbf{p}/|\mathbf{p}|, \quad \hat{\mathbf{y}} = \boldsymbol{\omega} \times \mathbf{p}/|\boldsymbol{\omega} \times \mathbf{p}|, \quad \hat{\mathbf{z}} = \mathbf{p} \times \boldsymbol{\omega} \times \mathbf{p}/|\mathbf{p} \times \boldsymbol{\omega} \times \mathbf{p}|.\quad (5)$$

For a particular feature in an image, its phase difference and X and Y image coordinates are known. The radar difference vector and distance to the object are also known. These can be rotated into the image coordinate system with the matrix formed from the image coordinate system unit vectors. Re-arranging the expression for phase difference we can derive an expression for the height of the feature above or below the image plane, ie the Z image coordinate of the feature

$$s_z = \left( \frac{\Delta\phi \lambda P}{2\pi} - r_x s_x - r_y s_y \right) / r_z.\quad (6)$$

This equation shows that the phase difference is constant in planes which are orthogonal to the radar difference vector. See figure 2. When the radar difference vector is orthogonal to the image plane the estimated height is least sensitive to phase errors. When the radar difference vector lies in the image plane a feature height cannot be estimated.

Two constraints on the radar placement can be inferred from equation 6. The radars must be sufficiently close so that the total phase difference variation across an object is less than  $2\pi$ . This avoids the need to unwrap the phase difference and so simplifies processing. Ideally the radars must also be placed so that the bearing of one radar with respect to the other is orthogonal to the plane of motion of the object.

To avoid phase ambiguities the total phase variation across the object should be less than  $2\pi$ . This constraint places an upper limit on the separation of the radars. For example, assuming a maximum object size of 50m, a minimum range at closest approach of 250km and a radar carrier frequency of 10Ghz, we have a maximum separation of 150m. Table 1 shows maximum separations for other frequencies and ranges. Allowing the phase to wrap round would improve feature height measurements, provided the phase can be unwrapped unambiguously. This is less of a problem with interferometric SAR for topography measurements, where phase wrap round cannot be avoided, see references 3 and 4. However phase wrap round is anticipated to be more a problem for space objects since their structures are more discontinuous on the scale of a resolution element. For this reason phase ambiguities are best avoided for the purposes of demonstrating the technique. However, in an operational system, it is expected phase ambiguities will be resolved given a sequence of images of the object within a pass.

Object feature height is most sensitive to image phase difference when the radar line of sight vector is orthogonal to the radar to radar vector. Thus for radars with an East-West bearing, high elevation satellite passes which ascend or descend North-South are best observed. Were the radars on a North-South bearing, East-West satellite passes are best observed. The optimal bearing will clearly depend on the distribution of space object passes.

The height accuracy of a feature is proportional to its signal to noise ratio and hence dependent upon its Radar cross-section. Before displaying the phase difference image it is thresholded such that the phase of pixels below a given geometric mean power are set equal to zero, thus excluding regions in the image dominated by noise. This simplifies interpretation of the phase image by removing a considerable amount of clutter.

Given the three coordinates of a feature in the image coordinate system it is possible to form projections of the object in the YZ and ZX planes, as well as the XY plane of the image, and indeed onto any plane. The projections of the object in its own coordinate system can be formed. This has the added benefit of enabling the projections from several pairs of images to be added incoherently to obtain a more complete 3 dimensional representation of the object.

Returning to the centring problem, centring errors should be a small fraction of a wavelength. Errors in centring will produce systematic errors in the height term which distort the perceived structure of the object. By accurately surveying the radar position difference vector before observations, and measuring azimuth and elevation and pulse times accurately during observations, the centring term can be computed. This can be tested in practice by observing a calibration sphere. Another method would be to correlate the images for residual shifts in range, or compute several images with different shifts, over half a wavelength should suffice, and select the least distorted image.

Range, range rate and phase errors manifest themselves in different ways. Range errors result in a range displacement of the object in the image, range rate errors result in a cross range displacement of the object and phase errors result in a displacement of the object out of the image plane. Systematic errors over a sequence of images can be used to infer corrections to improve image quality and the height measurements.

### 3. SIMULATIONS

To illustrate the technique simulated data was used. Range compressed and centred pulses were generated of an object comprising 31 isotropic scatterers of equal radar cross section. In the objects coordinate system the scatterers are placed so that one is at the origin, 10 each lie along the X,Y and Z axis respectively at intervals of one metre from 5m to -5m, excluding the origin. The radar wavelength was taken to be 3cm, and the separation of the radars 1500m, placed on a NW to SE bearing with respect to one another. The object distance at the image centre time was 1000km. The object ascended in the SW and descended in the NE, reaching a maximum elevation of 25degrees. No noise was added.

Figure 3 is a Range Doppler geometric mean power image showing the 3 lines of scatterers along the axes of the object, that is as projected onto the image plane. The axes are labelled. The image size is 15m by 15m, sampled with a pixel spacing of 3.625cm by 3.625cm. The image range resolution is 25cm and cross range resolution 29cm. Range goes from bottom to top of the image, the direction of flight from right to left, for a gravitationally stabilised object.

Figure 4 shows the corresponding phase difference image. The phase difference image is thresholded to exclude signal 20dB below the maximum signal power. The phase runs from  $-\pi$  shown white, to  $\pi$  shown black. Zero phase difference is plotted grey.

The central scatterer at the origin of the image and object coordinate systems, lies in the image plane and hence has zero phase difference. Each axis of scatterers clearly shows a linear progression of phase difference. The scatterers on the Z axis at +5m and -5m touch the boundary at which the phase difference wraps round. It should be noted the phase difference is not proportional to the height of the scatterer out of the image plane, but a plane which is orthogonal to the radar difference vector translated into the image coordinate system.

Figures 3 and 4 show the imaging XY projections of the object. Figures 5 and 6 show the YZ and ZX projections of the object, ie in the image coordinate system. These projections are sampled in the same way as the XY image, and with the same pixel power and thresholds. The YZ and ZX projections appear noisy because of the low threshold, sampling effects and the system impulse response.

The matrix for transforming from image to object coordinate system can be used to form projections of the object in the XY, YZ and ZX planes of the body centred coordinate system. By coadding several images from different aspects, that is throughout the pass of the object, more details of the object's structure will be filled in, and the signal to noise ratio improved.

### 4. BISTATIC RADAR SYSTEM REQUIREMENTS

Two high resolution coherent imaging radar systems placed a few hundred metres apart are required. One radar operating in transmit and receive mode, the other operating in receive mode only. The distance between the radars should be set to just give unambiguous phase for the largest object to which the method is to be applied. This



maximises the phase variation across the object and optimises object feature height accuracy.

The bearing of the radars with respect to each other will depend upon the distribution of space object passes. Ideally the line between the radars should be orthogonal to the plane of motion of an object. However, to avoid excluding LEO object's with maximum nadir latitudes comparable to that of the radars, East-West bearings should be avoided.

Pulse sampling times do not need to be any more accurate than for range Doppler imaging. However, if the centring component is to be corrected by sample timing, either the radars should use a common clock, or the drift rates of synchronized clocks must be less than the equivalent of a fraction of a wavelength, over the observation period, if the clocks are synchronized at the beginning of a pass.

The pulse duration before deramping is typically a few hundred microseconds, or tens of kilometres in length, which is more than the separation of the radars. Thus if common deramp hardware is used, it will be necessary to delay one of the pulses.

## **5. MONOSTATIC CASE**

In certain circumstances ISAR interferometry of space objects can be performed with a mono-static radar. The technique can be applied to rapidly spinning objects if observed over several rotations. Given an estimate of the spin period, image pairs are formed one rotation apart. Phase difference and geometric mean power images are then formed as for the bistatic case. The aspect change of the object and hence image phases differ because of the motion of the object in it's orbit. The phase differences can then be used to infer the 3 dimensional structure of the object. We do not describe the details here.

A similar constraint on the radar to radar vector in the bistatic case, applies to the difference position vector of the object from one image to the next in the monostatic case. The difference position vector must not lie in the image plane. It can be shown that ISAR interferometry solves a problem imaging rapidly spinning objects, the ambiguity in the direction of its angular velocity vector and the cross range image scale. Resolution of this ambiguity allows the true dimensions of the object to be determined.

## **6. FUTURE WORK**

A detailed analysis of the sensitivity of height estimates to the various sources of error needs to be performed. Error sources include:

- Orbit estimation errors
- Attitude estimation errors
- Radar position errors
- Radar system noise
- Medium transmission errors
- Phase ambiguities

A second order expansion of the range difference equation shows that for recommended radar separations an additional term needs to be added to the centring component.

The simulations described above were of isolated scatterers with separations greater than the image resolution. The case where there are several scatterers within a resolution element must be considered. In the case where two scatterers occupy the same resolution element but are at different heights, the scatterer cannot be discerned and their estimated height will be a weighted average of their actual heights. In a sequence of images these scatterers should eventually fall into separate cells.

A thorough study of the radar hardware requirements: particularly pulse timing using a common clock for determining the centring corrections, and an accurate survey of the radar detector locations to millimetre precision.

Acquiring real data with a bistatic radar system to test the method. Data of a calibration sphere will test the pulse centring, data of an extended object test the 3 dimensional imaging capability of the system.

Exploit the benefits of two data sets to improve the orbit and attitude estimates of the object. The range and range rate measurements from both radars should constrain the orbit estimate.

## **7. ACKNOWLEDGEMENTS**

This paper was produced by EDS-Scicon Defence plc for the Ministry of Defence. This work has benefited much from discussion with and comments of Drs. David Lewis (EDS-Scicon) (see references 4 and 5) and Peter Liddell (DRA Military Aerospace) and Mr Stuart Eves (MoD). Their contribution is gratefully acknowledged.

## **8. REFERENCES**

1. High Resolution Radar,  
D.R.Wehner,  
Artec House, 1987.
2. Developments in Imaging Radar Systems,  
D.A.Ausherman et al,  
IEEE AES-20, 4, 363-400, July 1984.
3. Crossed orbit interferometry: theory and experimental results from SIR-B  
A.K.Gabriel and R.M. Goldstein  
Int'l J. Remote Sensing, 9, 5, 857-872, 1988.
4. Study of SAR Interferometry for Topographic Mapping: Final Report  
D.J.Lewis, D.G.Corr, EDS-Scicon, 1992.
5. Possible Applications of Interferometric SAR Techniques to  
SOI Object Analysis  
D.J.Lewis, EDS-Scicon, 1992.

## 9. SYMBOLS

- $\mathbf{s}$  Space object feature vector  $(s_x, s_y, s_z)$
- $\mathbf{p}$  Space object position vector
- $\omega$  Space object net angular velocity vector
- $\mathbf{r}$  Active to passive Radar vector  $(r_x, r_y, r_z)$
- $\lambda$  Radar wavelength
- $\phi_k$  Image k pixel phase
- $\Delta\phi$  Phase difference of image pixels
- $i_k$  Image k pixel imaginary component
- $r_k$  Image k pixel real component
- $l_k$  Distance from radar to space object feature

$\lambda (m)$	$p (km)$	$r_{\max} (m)$ $s_{\max}=25m$	$r_{\max} (m)$ $s_{\max}=50m$
0.03	250	300	150
0.03	500	600	300
0.03	1000	1200	600
0.02	250	200	100
0.02	500	400	200
0.02	1000	800	400

Table 1 Maximum Radar Separations for Unambiguous Phase

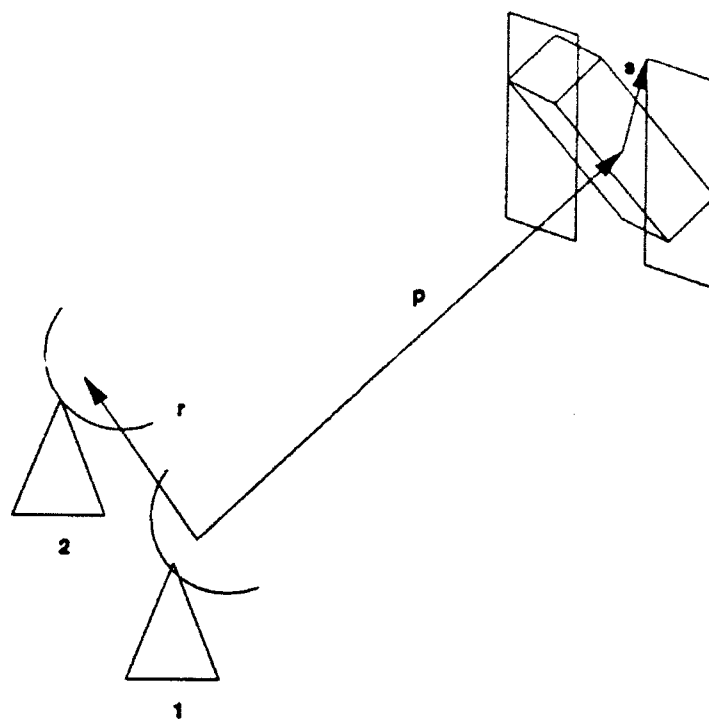


Figure 1 Imaging Radars and Space Object Geometry

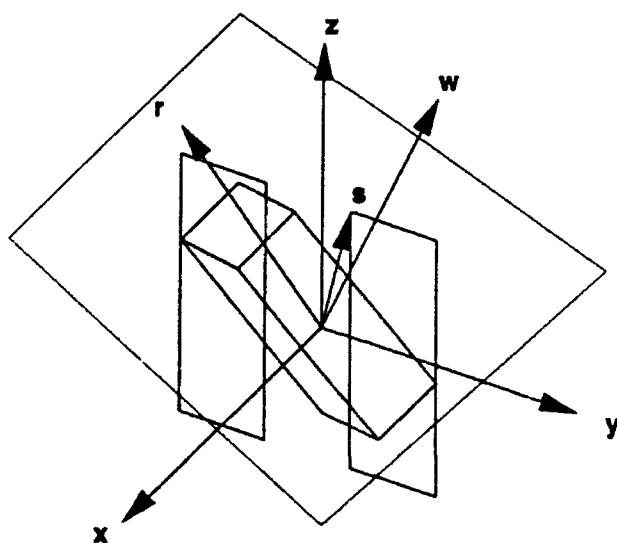


Figure 2 Image Coordinate System and Isophase Planes

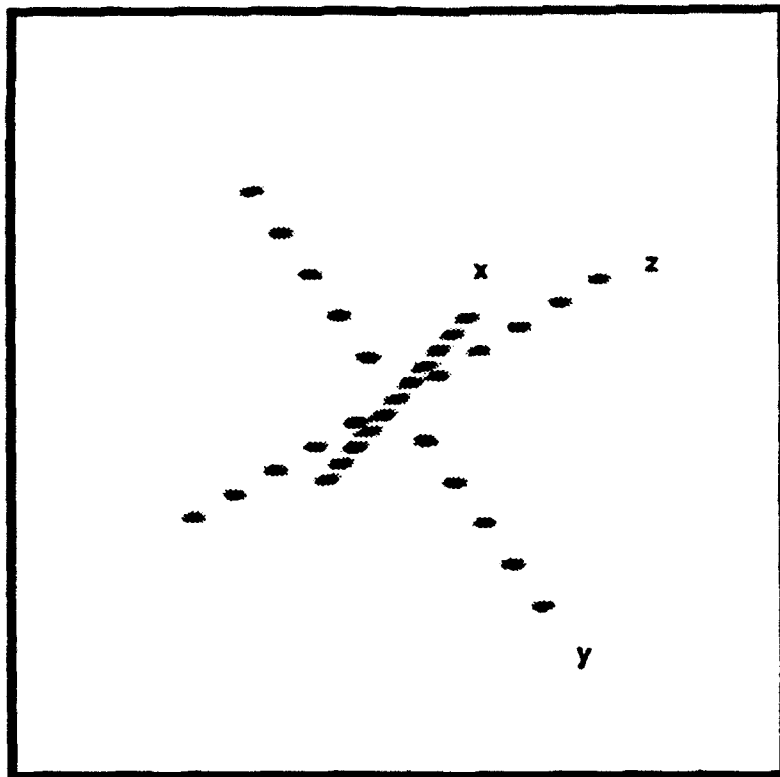


Figure 3 Simulated Object Range Doppler Mean Power Image

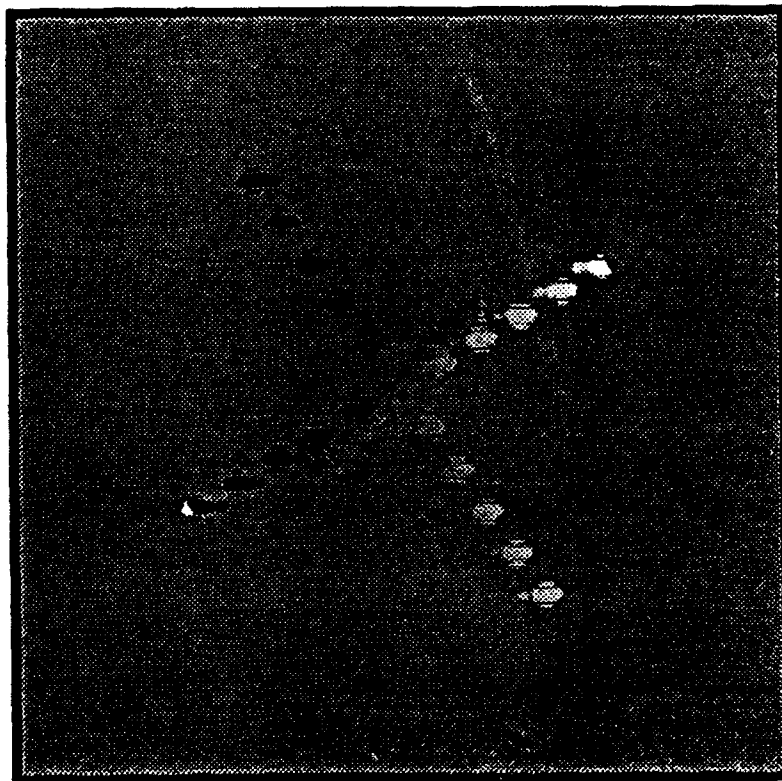


Figure 4 Simulated Object Range Doppler Phase Difference Image

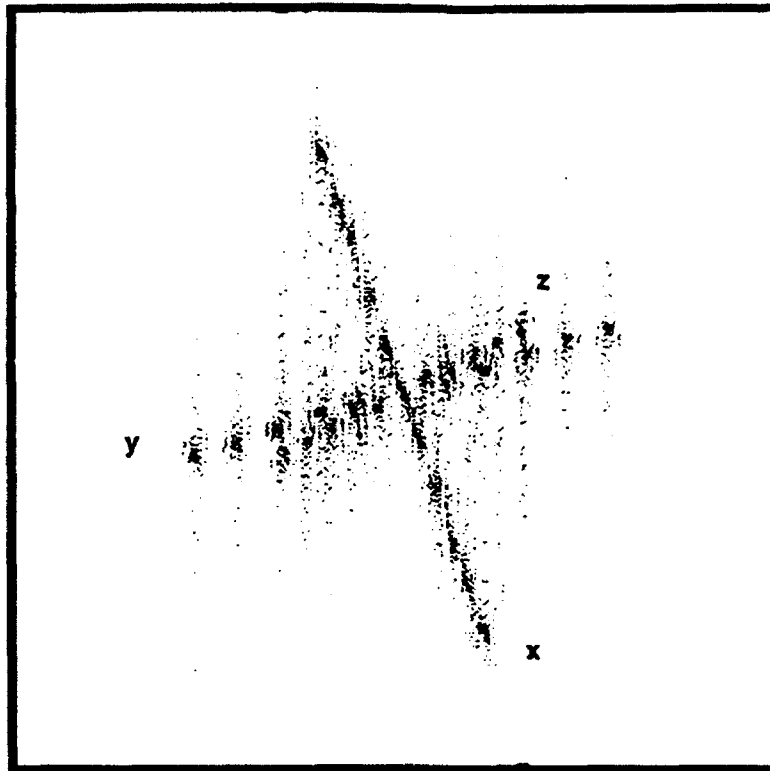


Figure 5 Simulated Object YZ Projection

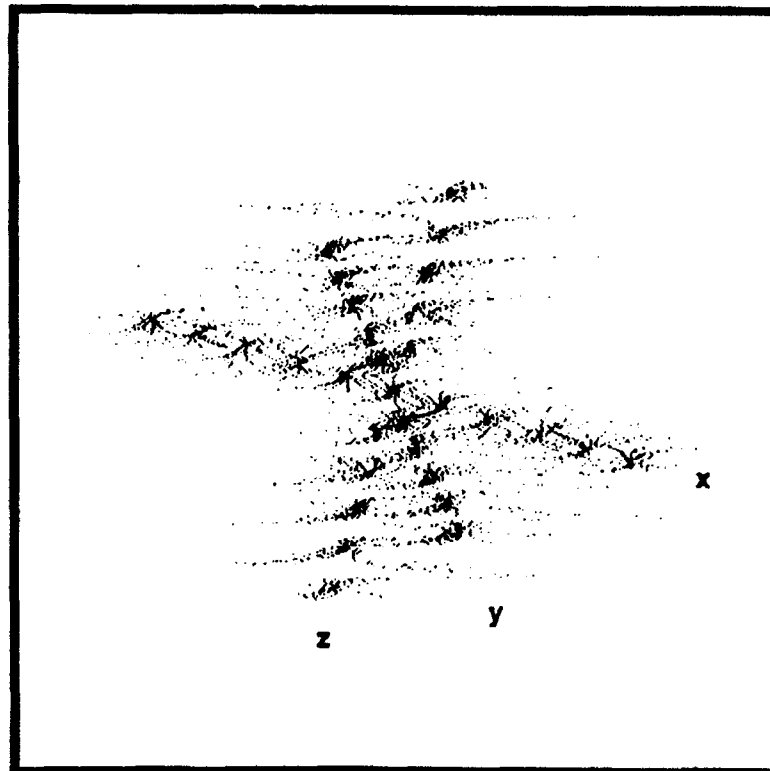


Figure 6 Simulated Object ZX Projection

**Pages 135 to 142 are intentionally left blank.**

## **The Passive Imaging Systems at the Air Force Maui Optical Station's (AMOS) 1.6m Telescope**

Capt Andrew H. Suzuki (Phillips Laboratory, PL/OL-YY), Capt Mark VonBokern (Phillips Laboratory, PL/LIMI)

**Abstract:** The Air Force Maui Optical Station (AMOS) is extensively using passive imaging techniques for space object identification (SOI). This paper discusses two passive imaging systems designed to support present and future SOI tasking requirements.

The most recent addition to the suite of AMOS operational sensors is the Passive Hybrid Imaging at the AMOS 1.6m Telescope (PHIAT) system. PHIAT began as a Phillips laboratory R & D system and was recently transitioned to an operational system that routinely supports operational USSPACECOM SOI tasking. The PHIAT system can combine predetection compensation (adaptive optics) with a variety of computer post-processing techniques to produce high resolution satellite imagery. A brief discussion of the PHIAT system and its operational requirements is presented.

Finally, this paper discusses the AMOS Daylight Optical Near-IR Imaging System (ADONIS). ADONIS is scheduled for a proof-of-concept demonstration in April 1993. ADONIS differs from the PHIAT system in that it's a daylight system and no predetection compensation (adaptive optics) is envisioned for the proof-of-concept system. The proposed proof-of-concept design and operational design constraints are presented.

**Introduction:** The traditional Air Force mission, "to fly and fight" is becoming increasingly dependent upon peripheral technologies. High resolution ground based exo-atmospheric imaging technology is crucial to the success of present and future Air Force mission profiles. The success of high resolution ground based exo-atmospheric imaging hinges on the solution to one crucial problem, mitigating the image degrading effects of atmospheric turbulence.

Atmospheric turbulence significantly degrades the performance of exo-atmospheric imaging systems. Atmospheric turbulence results in phase distortion and intensity fluctuation (scintillation). Passive imagery techniques rely on solar or self-illumination of the intended target. For ground based applications, the most common passive imaging techniques are predetection compensation (adaptive optics), post-processing, and the combination of these two methods or the hybrid technique.

The Air Force's Phillips Laboratory has been conducting ongoing research to extend existing and develop new passive imaging techniques. The results of this research are the PHIAT system and the proposed ADONIS system. This paper begins with a brief discussion of the theory behind the passive imaging techniques used by PHIAT (hybrid) and ADONIS (speckle). After the brief discussion of the theory, this paper will then discuss the actual (PHIAT) and proposed (ADONIS) systems. Finally, this paper presents the results, operational concerns, and applied research initiated by AMOS utilizing these systems.

**Theory:** The discussion of the theory will begin with a brief background discussion, followed by a discussion of the predetection compensation (adaptive optics), followed by discussions of the post-processing techniques of linear deconvolution and bispectrum (speckle masking) phase retrieval.

**Predetection Compensation:** Predetection compensation systems assumes a geometrical



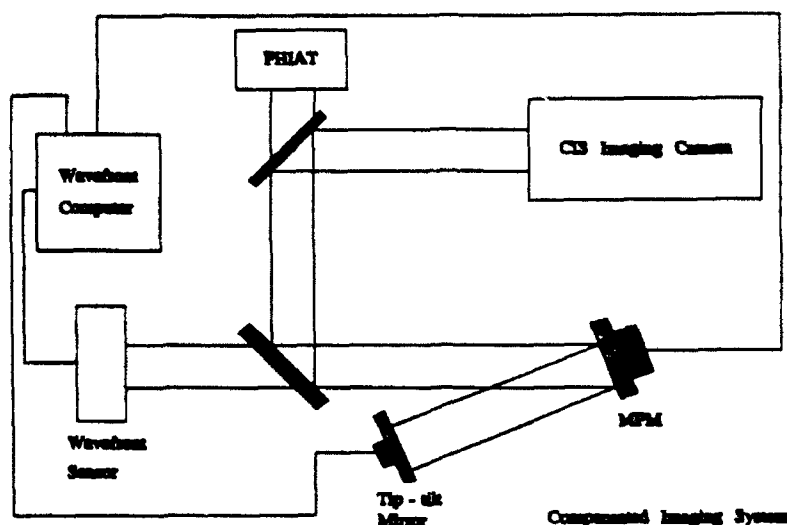


Figure 1

optics or Rytov approximation<sup>1</sup> for the wavefront aberration process. The geometrical optics view assumes that the wavefront aberration is a phase only error. Predetection compensation uses deformable mirrors to induce a conjugate aberration to the atmospherically induced phase error. The predetection compensation or adaptive optics system used at AMOS is referred to as the Compensated Imaging System or CIS. Figure 1 graphically displays the CIS system. CIS uses a wavefront sensor to sense the phase of the incoming aberrated wavefront. The incoming wavefront includes the aberrant effects of the atmosphere on the object. CIS uses a fast steering or tilt mirror to remove the lower order aberrations in the incoming wavefront. CIS then uses a monolithic piezo-electric mirror (MPM) to remove higher order atmospheric induced aberrations in the incoming wavefront. Although much of the lower order aberrations are removed, there still exists some higher order atmospheric turbulence induced aberration. To remove the residual aberration, AMOS uses post-processing algorithms to enhance the quality of the passive imagery.

**Post-Processing Compensation:** The ultimate goal of any post-processing imaging system is to provide a good estimate of the spatial representation of the object ( $o(x,y)$ ). Using a linear systems approach<sup>2</sup>, the image ( $i(x,y)$ ) is defined as a convolution of the object with the impulse response or point spread function ( $h(x,y)$ ) of the system (Eq. 1). The system includes the telescope and the atmosphere. Many times it's easier to envision this process in the Fourier domain, where the convolution operation becomes a simple multiplication (Eq. 2). To retrieve

$$\begin{aligned}
 i(x,y) &= o(x,y) * h(x,y) \\
 &= \int_{-\infty}^{\infty} \int_{-\infty}^{\infty} o(\alpha, \beta) h(x - \alpha, y - \beta) d\alpha d\beta
 \end{aligned}
 \tag{1}$$

the unaberrated object ( $o(x,y)$ ), a "deconvolution" is done, which equates to a division in the

Fourier domain (Eq. 3).

$$\begin{aligned}\mathcal{F}[i(x,y)] &= \mathcal{F}[o(x,y) * h(x,y)] \\ I(u,v) &= O(u,v) H(u,v)\end{aligned}\tag{2}$$

To begin the object spectrum ( $O(u,v)$ ) estimation process, data must be collected to define the image spectrum and system optical transfer function. The average image spectrum ( $\hat{I}(u,v)$ ) data consists of a large ensemble of short exposure images of the object. The average optical transfer function or OTF ( $\hat{H}(u,v)$ ) data is found by collecting a large ensemble of short exposure images of a reference star.

The linear deconvolution<sup>3</sup> is by far the simplest passive image reconstruction technique used at AMOS. The estimate of the object spectrum is defined by Eq. 3, where  $\epsilon$  is a factor included to prevent a divide by zero error and  $\cdot$  denotes the ensemble averaging in the spatial frequency domain. It's important to note that the linear deconvolution technique calculates the estimated object spectrum by a simple centroiding and averaging process. A better estimate is found by using the more computationally intense speckle masking technique.

$$\hat{O}(u,v) = \frac{\hat{I}(u,v)}{\hat{H}(u,v) + \epsilon}\tag{3}$$

The speckle masking technique uses a combination of the Labyrie technique<sup>3</sup> to estimate the object power spectrum and the bispectrum or "triple correlation" technique<sup>4</sup> to estimate the object phase. It's been proven that this type of estimator provides a superior object spectrum estimate over the linear deconvolution technique<sup>3</sup>. The object power spectrum estimate is accomplished using a conventional Labyrie or speckle imaging technique which is represented by the following;

$$|\hat{O}(u,v)|^2 = \frac{\langle |I(u,v)|^2 \rangle}{\langle |H(u,v)|^2 \rangle}\tag{4}$$

Using equation 4, the fourier modulus component of the estimated object spectrum is very simple to calculate. The phase spectrum estimation ( $\Psi(u,v)$ ) begins with calculating the bispectrum or triple correlation technique which follows the form;

$$\begin{aligned}B(u_1, v_1; u_2, v_2) &= I(u_1, v_1) I(u_2, v_2) I(-u_1 - u_2, -v_1 - v_2) \\ &= |B| e^{j\beta}\end{aligned}\tag{5}$$

Where  $\beta$  represents the phase of the bispectrum estimation. The bispectrum phase,  $\beta$  is found by Eq. 6 where  $\theta$  represents the image phase spectrum. The next step in the object phase estimation is to compute the average or ensemble bispectrum phase spectrum. The final step in the object phase estimation process is to reconstruct the object Fourier phases. Lohmann's

analysis postulates that the object phase is identical to the bispectrum phase. With conventional imaging systems noise effects are present that require additional consideration when calculating the object phase. This is done via a weighted least squares solution to the problem where the weighting matrix  $W(u,v)$  is obtained by using the variance of the bispectrum phase elements<sup>3</sup> (Eq. 6). The enhancement of the speckle masking technique over the linear deconvolution method lies in the improved object modulus and phase estimate found by the Labyrie technique and bispectrum. The bispectrum calculated modulus and phase estimate now follows the same deconvolution process as the linear method.

$$\beta(u,v) = W(u,v) \psi(u,v) \quad (6)$$

**System Descriptions:** This section begins by describing the PHIAT passive imaging system and concludes with a description of the proposed ADONIS system. The system descriptions include both the hardware and software used for each respective system.

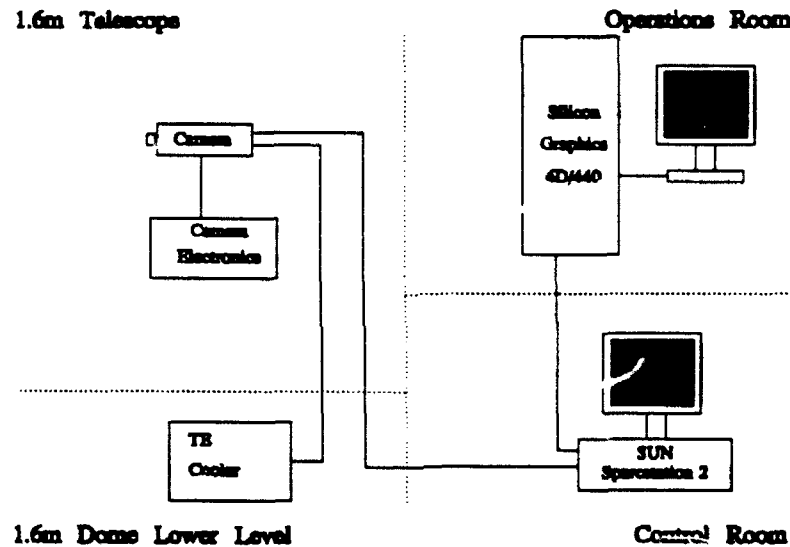


**Figure 2**

**PHIAT System Hardware:** The PHIAT camera and electronics (Fig. 2) are colocated on the rear blanchard of the 1.6m telescope with the Compensated Imaging System (CIS). The heart of the PHIAT camera system is a Photometrics CH200 camera head with a Kodak KAF 1400 CCD chip. The active area consists of a 1317 x 1035 array of 6.8  $\mu\text{m}$  square pixels. For most applications, a smaller array of 140 x 140 pixels is used to achieve the high frame rates required for speckle imagery. The camera operates at  $-40^\circ\text{C}$ . At that temperature, a quantum efficiency of 41% @ 700nm and read noise of 13 electrons make this camera ideally suited for speckle imagery applications. A computer controlled electro-mechanical shuttering system allows a user selectable range of exposure times from 5 to 99 msec. A diagram of the camera system

and optical train is shown in Figure 3.

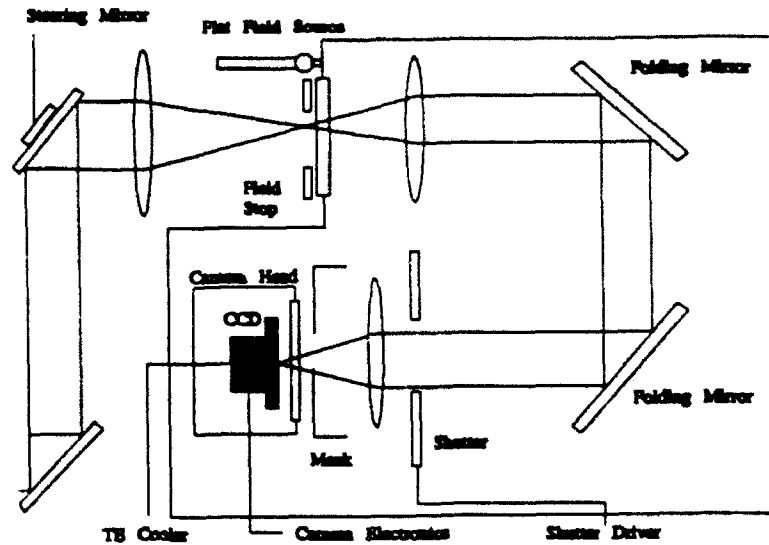


Figure 3

The camera control electronics provides all power and clock sequences to the camera head. It's here that the analog signal processing and the digitization of 12 bits/pixel occurs. The camera electronics also houses a temperature stabilization circuit to control the CCD temperature to within  $\pm 0.1^\circ \text{C}$ . The camera electronics interfaces with a VME chassis providing control signals to the camera from the SUN Sparcstation 2.

The PHIAT system receives the compensated or uncompensated imagery via a selectable filter. The filter sends part of the beam to the CIS intensified silicon intensified target camera system and the rest to the PHIAT camera system. The selective filter has a 50/50 beam splitter position and 2 wavelength selectable bandpass filters. The bandpass filters are centered at 700 nm, which is the peak of the KAF 1400 chips response curve, with bandwidths of 70 and 140 nm. A slow steering mirror is used to center the image the field of view for the PHIAT system. A computer controlled flat field source uses a rotary solenoid to position a broadband photoluminescent panel in front of the PHIAT system entrance aperture for pixel-to-pixel flat field compensation. An adjustable field stop is available for entrance aperture size adjustment. Upon entering the camera enclosure, the optical beam is passed through beam conditioning and steering optics, a electro-mechanical shutter, and a mask prior to imaging on the CCD. The mask has several selectable positions to allow access to larger portions of the CCD array.

The control and data acquisition is arbitrated by a SUN Sparcstation 2 computer system (Fig. 4). The Sun Sparcstation controls exposure time settings and data transfer the from camera system to the HDD storage devices. The IRIG timing information is also read by the SUN computer and encoded with the imagery. The main data storage devices are a 64 MByte DRAM memory for high speed data storage and 1.2 GByte HDD for additional data storage capacity. The 207 MByte internal disk drives hold the operating system and software for camera operations, image processing, and data acquisition. The tape drives are available for archiving of SOI data.

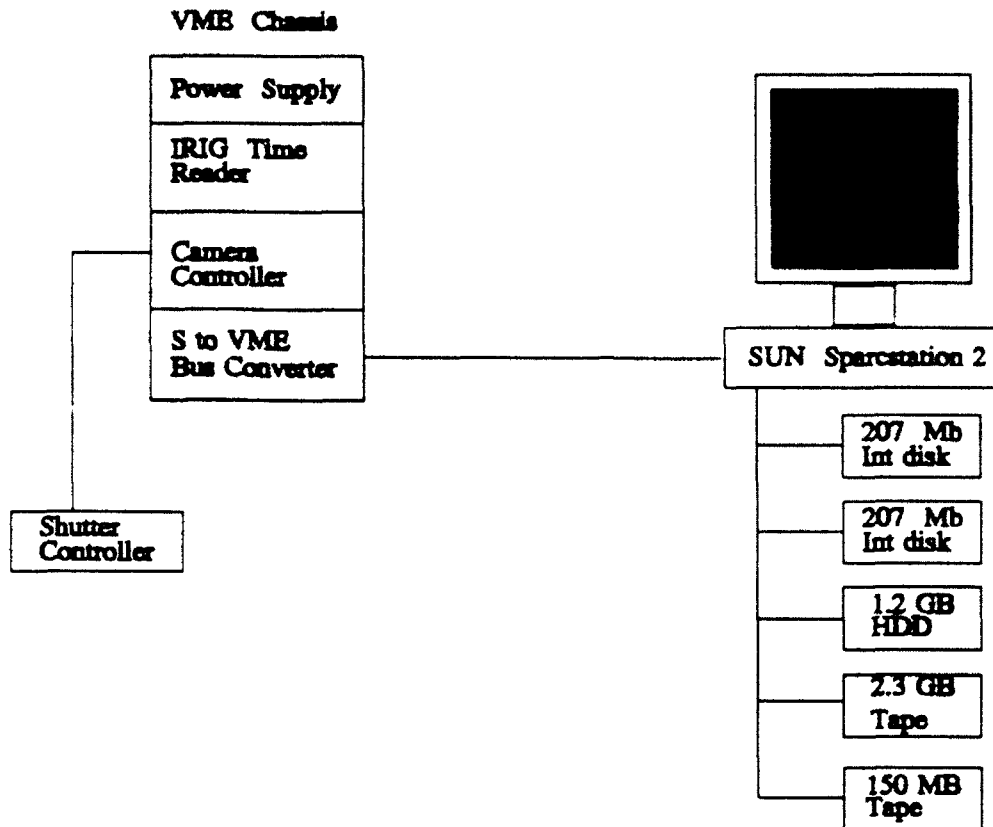


Figure 4

The bulk of the image processing occurs on the Silicon Graphics 4D/440 system. The post-processing code was adapted to take advantage of the multi-processor capability of the 4D/440.

**PHIAT Software:** The PHIAT system software consists of programs for data acquisition, display, and post-processing. The data acquisition and display software was originally an off-the-shelf version that was adapted by Phillips lab personnel to fit the PHIAT mission profile. The post-processing software was written exclusively by Phillips lab personnel and implements the linear deconvolution and bispectrum techniques. The post-processing software also compensates with flat fielding and corrects the data camera read noise.

**ADONIS System Hardware:** The ADONIS package will be located on the side blanchard of the 1.6m telescope. A tertiary mirror will divert the wavefront to the side blanchard. ADONIS will not use predetection compensation for the proof-of-concept phase. A single MIT Lincoln Labs camera system is planned for the ADONIS experiment. The camera system uses a back illuminated 64 x 64 CCD array for imaging. The CCD is operated in the 0.8 - 1  $\mu\text{m}$  band and has an advertised peak quantum efficiency of 80%. The camera has the ability for data acquisition rates up to 1000 frames per second, which is well within the coherence time of the atmosphere. A selectable zoom feature will allow a range of fields of view from 30 to 6 arcseconds. A fast steering mirror will also be included to remove atmospherically induced

wavefront tilt and residual mount jitter.

The proof-of-concept system will use microvax and trapix computer systems for system control, data storage, and image post-processing.

**ADONIS System Software:** The ADONIS system software will incorporate post-processing algorithms for object estimation and image processing algorithms. The post-processing algorithm proposed is known as the Knox-Thompson algorithm. The Knox-Thompson algorithm should provide an object spectrum estimate comparable to that of the speckle masking process.

**Operational Constraints:** AMOS is an operational electro-optic imaging site which supports routine EO data tasking generated by USSPACECOM. In response to the operational nature of the AMOS mission, many design constraints have been imposed on the passive imagery systems. Although quite general, the operational requirements ultimately drive the imaging system design. The remainder of this section presents the general operational system requirements and the resultant design criteria implemented on the PHIAT and ADONIS system.

System operation is accomplished by AMOS operators, equivalent to the USAF enlisted 3-level designation. As a result, an extensive user interface design program was undertaken prior to transition of the PHIAT from a R & D system to an operational system. User friendliness and concise documentation is a hard requirement.

The targets of interest necessitate a relatively large field of view. For ADONIS, a 20 arcsecond field of view is a requirement. The result was a redesign of the system optical train from a fixed 6 arcsecond to a selectable 30 to 6 arcsecond field of view. The PHIAT system requirements were reduced, but an increase in the current 6.9 arcsecond square is necessary. This increase may require numerous software changes in concert with optical hardware changes.

Timeliness is a fundamental requirement for AMOS imagery data. The image data timeliness goal is an end-to-end (acquisition and processing) time of 2 hours. Within this 2 hour timeframe, a minimum of 5 processed images per satellite pass is necessary. In response to these requirements, numerous software changes were made to reduce the R & D end-to-end time of 4 hours per image to 1 hour for 5 images.

The exact time when the imagery was taken is also a necessary requirement. In response to this, IRIG timing hardware and software interfaces had to be incorporated in the design of the PHIAT and ADONIS systems.

**Summary:** This paper has discussed the passive imagery systems at AMOS, both present and future. Being part of the Phillips laboratory and also supporting operational tasking, puts AMOS in a unique position. AMOS must transition laboratory R & D assets into the operational environment. With this in mind, early definition of requirements for each new system is essential.

### References

1. Goodman, Joseph W., *Statistical Optics*, Wiley-Interscience Publications, New York, 1985
2. Gaskill, Jack D., *Linear Systems, Fourier Transforms, and Optics*, John Wiley & Sons, 1978
3. Roggemann, Michael C., *Unconventional Imaging: OSA Short Course*, 1991
4. Lohmann, A. W., et. al., *Speckle Masking in Astronomy: Triple Correlation Theory and it's Applications*, Applied Optics, Vol. 22, pp 4028-4037, 1983

## **All Source Satellite Evaluation Tool**

G.D. Conner (BA&H/ADS)<sup>1</sup>, R.D. Oldach (JNIDS)<sup>2</sup>, K.A. Wilson (BA&H/ADS)

### **Overview**

The purpose of the All Source Satellite Evaluation Tool (ASSET)<sup>3</sup> is to improve satellite status monitoring capabilities for the U.S. Government. The need for rapid analysis and information dissemination is increasing as collection and foreign launch capabilities improve. Compounding this increasingly difficult problem is the routine turnover of analysts and the real threat of staff reductions. To better support the space analyst, BA&H/ADS is building a tool which: 1) provides easy access to many sources of diverse information from a single workstation; 2) automatically alerts an analyst to anomalous behavior; 3) captures current expertise in satellite behavior models and databases; 4) predicts future activity; and 5) provides report-generation tools for rapid dissemination of information.

Two major goals have shaped the ASSET development process. The first goal has been to keep the system as simple as possible. This helps to minimize the training required for analysts to use the system. Simplicity also reduces the cost of maintenance which often exceeds the cost of original system development. The second major goal of ASSET has been to increase the efficiency, consistency, and quality of the analytic process. ASSET attempts to meet this goal by providing an easy to use, uniform framework that supports the analytic process.

BA&H/ADS has delivered a workstation with integrated custom and commercial software for: anomaly detection via model-based expert system; large database management; and report generation. ASSET has been receiving operational data on a continuous basis since September of 1992. System upgrades are delivered every two to three months. Each iteration incorporates new features and serves as a platform for soliciting feedback from current users. This paper will present an overview of the current ASSET system and provide examples of a typical user session.

### **System Description**

The System Architecture depicted in Figure 1 shows the main modules of the ASSET system. The *Message Parser/Data Filter* provides the necessary connections to the outside world for message traffic. As messages are received the necessary information is parsed and reviewed for data relevance. Information pertaining to objects that is not of interest is discarded. Information on objects that are not sufficiently described to the system is held for possible future processing. Information representing objects of interest is stored in the *Database* and queued up for future processing.

---

1. BA&H/ADS - Booz, Allen & Hamilton / Advanced Decision Systems Division

2. JNIDS - Joint National Intelligence Development Staff (JNIDS)

3. This work is funded by the Joint National Intelligence Development Staff (JNIDS). The views and opinions contained in this document are those of the authors and should not be interpreted as representing the official policies, either expressed or implied, of Booz, Allen & Hamilton, JNIDS, or the U.S. Government.



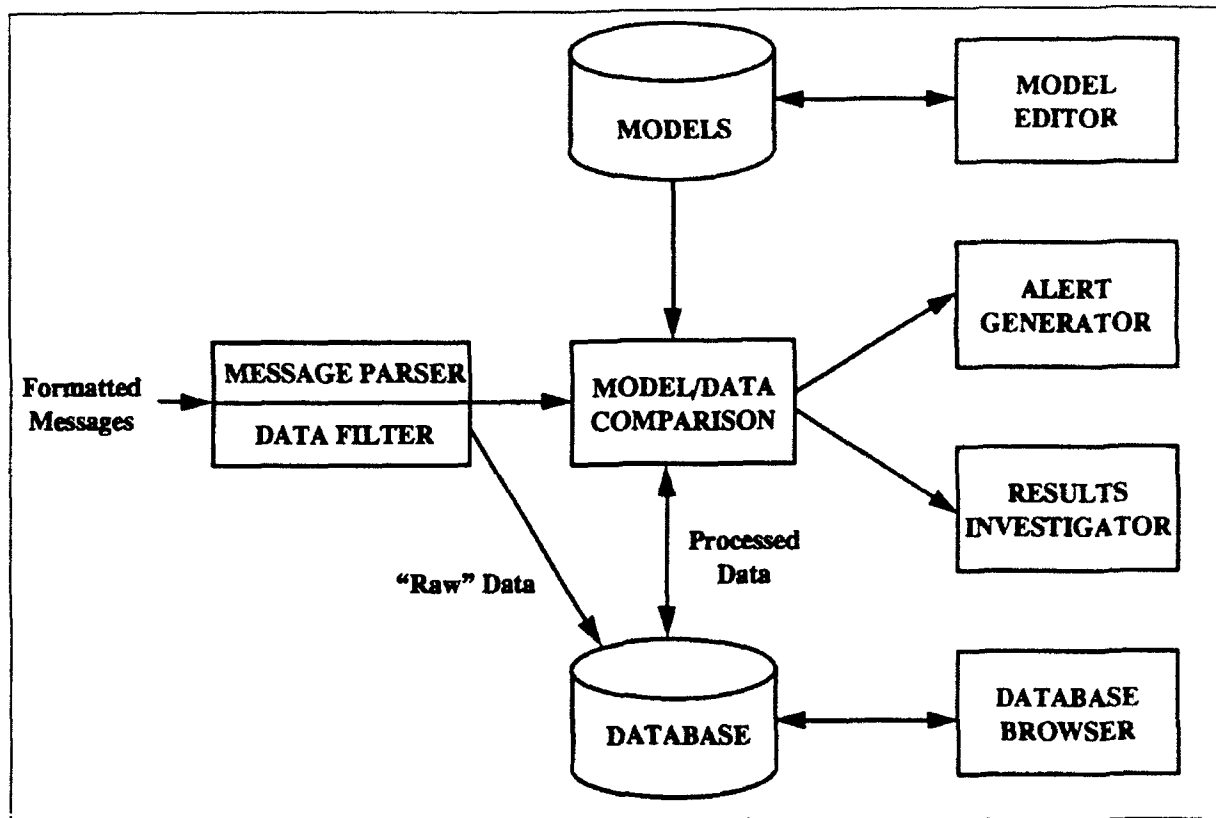


Figure 1 System Architecture

Messages that are unable to be correctly parsed are stored for further processing at a later time. This fully automated mechanism supports the continuous processing required for twenty-four hour operations.

*ASSET Models* are a set of the rules used to represent the orbital behavior of a particular group of satellites. A rule consists of a clause or group of clauses and a single action. Clauses are typically used to represent abnormal parameter ranges (e.g. Perigee < 200km) or specific sets of conditions that typically indicate impending events. Individual clauses can be associated together through a variety of logical and temporal connectors. Actions consist of a single object which contains the action type, the explanation, and the "routing" list. Actions can include behavior ranging from "Do Nothing" (essentially the rule is deactivated) to "Send Alert" which notifies specific users by electronic mail (email). The overall consequence of a rule is determined by the specified action type. Clause components and actions each have graphical representations. Because of the complex internal structure, models are stored as flat files, but are indexed through a database mechanism.

The *Database* is comprised of Domain and Bookkeeping information. Domain information contains data relating to the space object domain, such as satellite, ELSET, and booster information. Bookkeeping data consists of information that the system uses to keep track of system processing, user profile information, login times, processing results, etc.. Both types of information are used to support current and historical analysis.

The *Model/Data Comparison* module performs the comparison of the incoming data to the stored models. The module first determines which model corresponds to the incoming piece of data. The corresponding model is read into memory. Any additional data or satellite information is retrieved. The information in the data is then compared with the model. The *Alert Generator* performs any of the necessary actions as specified in the model. This includes the sending of email and the recording of processing information.

The *Model Editor*, shown in Figure 2, provides a tool with which the analyst can develop new models or edit existing ones. The models are represented as a series of objects, either clause components or actions. The right side of Figure 2 shows the list of clause components that can be used to model orbital parameters. Clause components or actions are visually represented by graphical objects. These objects are manipulated graphically via an editor that is intentionally designed to look like any standard drawing package.

The *Alert Generator* handles the generation of external alerts (electronic mail) and the associated bookkeeping information. This bookkeeping information includes records of processing results and alerts to be checked off by individual users.

The *Results Investigator* is a mechanism that allows a user to examine the results that have been generated since the last time the user ran ASSET. It presents information in both tabular and graphical form. Results investigation involves access to the Satellite Status Summary (Figure 3), the individual Satellite Alert Summary windows (Figure 4), and the Results Detail Windows (Figure 5). The *Results Investigation* application also allows the user to perform retrospective analysis. To do this the user selects a specific set of satellites and a time period. The system then

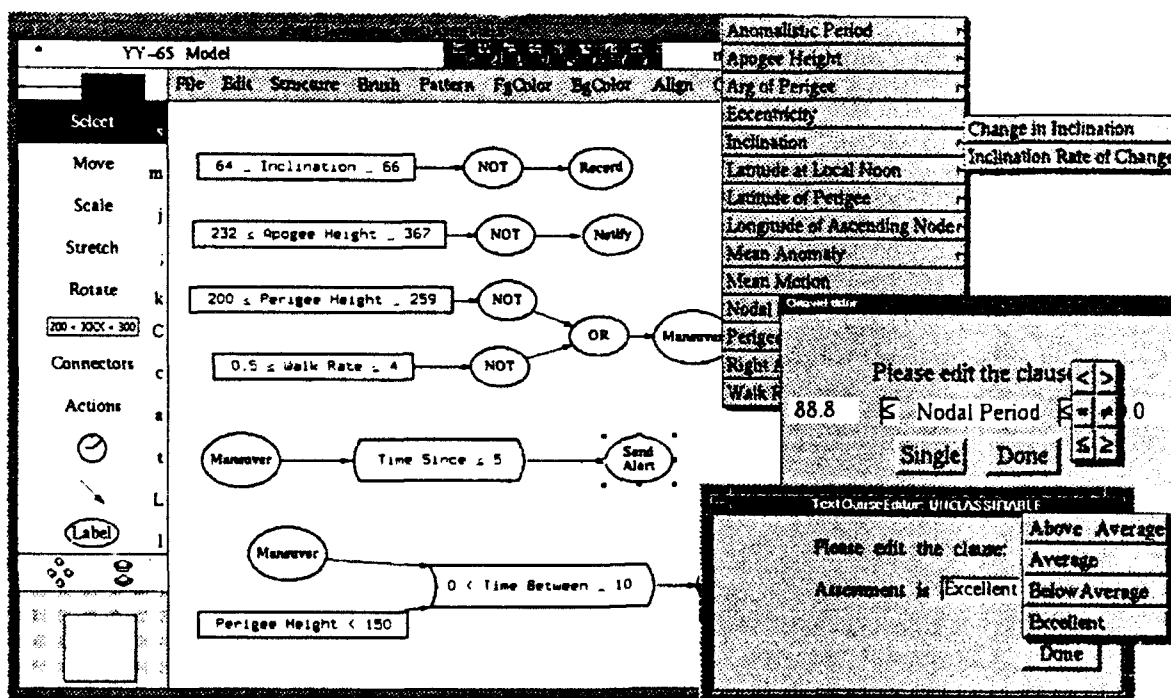


Figure 2 Model Editor

ASSET: UNCLASSIFIABLE

**Satellite Status Summary**

Object	Alerts?	Events?	DTG
21026	Yes	No	11/0109Z JUN 91
21000	Yes	No	28/1434Z JAN 91
20568	Yes	No	21/1746Z NOV 90

OK

Figure 3 Satellite Status Summary

**Satellite Alert Summary**

SSC Number: 21026  
Mission: YY  
Common Name: COSMOS 2113  
Model Name: YY-65 Model

DTG	Data Type	Number of Alerts
11/0109Z JUN 91	ORBINT	4
10/1913Z JUN 91	ORBINT	4
10/1447Z JUN 91	ORBINT	2
10/0426Z JUN 91	ORBINT	2
09/1636Z JUN 91	ORBINT	2
09/1507Z JUN 91	ORBINT	2
09/0147Z JUN 91	ORBINT	2
08/1227Z JUN 91	ORBINT	1
08/0204Z JUN 91	ORBINT	0
07/1243Z JUN 91	ORBINT	0

View History OK

Figure 4 Satellite Alert Summary

performs the model/data comparison for the specified time period. Results are presented using the same windows shown in Figures 3 through 5.

The overall intent of the Results Investigator is to provide rapid and easy access to the necessary information. The total "distance" between the high level summary and the lowest level of detail is a few "mouse" clicks. Even though data is summarized at the highest level, access is provided to the "raw" information.

At a glance the Satellite Status Summary window provides the analyst with the overall status of the satellites in his user profile. Each satellite with "new" data is represented by a single line in the summary table. The presence of Alerts and Events are noted, as well as the time of the most recent piece of incoming data. Alerts are signaled by red filled boxes as shown in Figure 3. This facility allows an analyst to quickly determine the status of his assigned satellites. Further analysis on specific satellites can be pursued, or the information can be brought to the attention of a more senior analyst. By clicking on a row corresponding to a particular satellite more detailed information can be displayed.

The Satellite Alert Summary window provides more in-depth information on a particular satellite. Each row in the table represents information on a single piece of data. The data time, type, and the

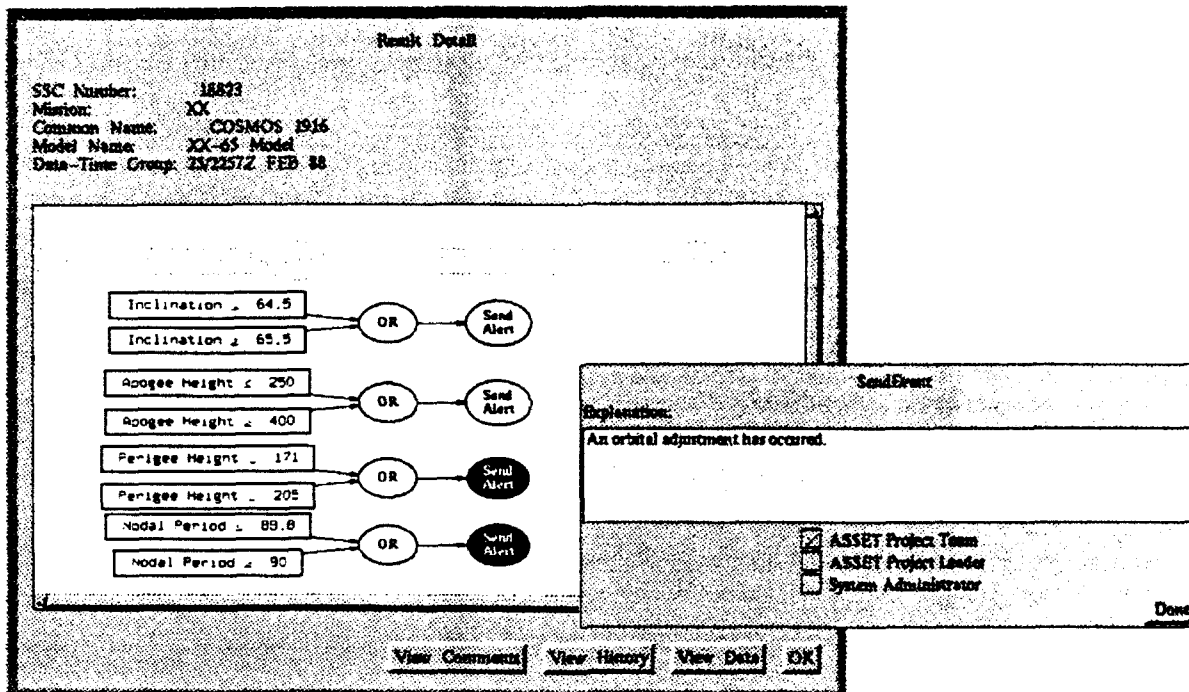


Figure 5 Result Detail Window and Expanded Explanation

number of alerts generated is displayed for each item. The View History button provides quick access to graphical and tabular displays of historical data that help put current information into context.

The Results Detail window contains a "picture" of the model, with the addition of color and shading to show the impact/results of the incoming data. Buttons along the bottom of the window provide easy access to graphical displays of historical data. They also provide a mechanism by which the analyst can view comments that have been previously entered about the satellite. This same mechanism can be used to add new comments if desired.

Analyst's comments provide a running commentary/history that represents a "chron file". Historical comments can be used as a training aid for satellite familiarization or as part of a normal turn-over procedure. ASSET provides a framework by which the triad of the comment history (narrative information), the satellite model (structured parametric information), and raw data can be unified to capture and mimic the expertise of the senior analyst.

The *Database Browser*, shown in Figure 6, is used to retrieve and display information from the ASSET database. The browser allows users to search and view selected topics in the Database. The interface is customized by the subject being viewed. For example, the window configuration and data display capabilities are different for ELSETS and Satellites. The browser provides a "Point and Click" interface to the information stored in the Database. This interface shields the user from the details of tables, joins and other vulgarities of SQL<sup>4</sup>. Figure 7 illustrates the various methods of displaying data.

4. Structured Query Language - A language used to query the relational databases used in ASSET

Close Select Subject Predefined Query Save Query Clear Query Help

### Element Set (ELSET)

**Fields**

- Object Number
- Combined Name
- Common Name
- International Designat
- Classification
- Date
- Elset Number
- Inclination
- Mean Motion
- Mean Anomaly
- Epoch Revolution

**Restrictions**

**Search**

Select All Display View All

Edit Omit Delete

**Database Query**

Combined Name ----> 21026 COSMOS 2113

OR

Combined Name ----> 21000 COSMOS 2108

OR

Combined Name ----> 20568 COSMOS 2072

Obj #	20568	ELSET #	1	DTG	13/1845Z	APR 9
Obj #	20568	ELSET #	1	DTG	13/2014Z	APR 9
Obj #	20568	ELSET #	2	DTG	13/2312Z	APR 9
Obj #	20568	ELSET #	3	DTG	14/0337Z	APR 9
Obj #	20568	ELSET #	5	DTG	14/0507Z	APR 9
Obj #	20568	ELSET #	6	DTG	14/0935Z	APR 9
Obj #	20568	ELSET #	7	DTG	14/1232Z	APR 9
Obj #	20568	ELSET #	8	DTG	14/1830Z	APR 9
Obj #	20568	ELSET #	9	DTG	15/0929Z	APR 9
Obj #	20568	ELSET #	10	DTG	15/1627Z	APR 9
Obj #	20568	ELSET #	11	DTG	16/1224Z	APR 9
Obj #	20568	ELSET #	12	DTG	17/1051Z	APR 9
Obj #	20568	ELSET #	13	DTG	17/1619Z	APR 9
Obj #	20568	ELSET #	14	DTG	17/2119Z	APR 9
Obj #	20568	ELSET #	15	DTG	18/1345Z	APR 9
Obj #	20568	ELSET #	16	DTG	18/2242Z	APR 9
Obj #	20568	ELSET #	17	DTG	19/1509Z	APR 9
Obj #	20568	ELSET #	18	DTG	20/0304Z	APR 9
Obj #	20568	ELSET #	19	DTG	20/0903Z	APR 9
Obj #	20568	ELSET #	20	DTG	20/1801Z	APR 9
Obj #	20568	ELSET #	21	DTG	21/0726Z	APR 9
Obj #	20568	ELSET #	22	DTG	21/2053Z	APR 9
Obj #	20568	ELSET #	23	DTG	22/1746Z	APR 9
Obj #	20568	ELSET #	24	DTG	23/1437Z	APR 9

AND

OR

NOT

Figure 6 Database Browser

## Twenty-Four Hour Monitor

The *Twenty-four Hour Monitor* is a process that runs continuously. Each time a new piece of data is received by ASSET, an entry is added to the "monitor data queue". The Twenty Four Hour Monitor polls this queue to find out if there are any new entries to process. When there is data to be processed, the monitor retrieves the oldest entry from the queue and uses that information to retrieve the corresponding satellite information from the database. Only satellites that have been assigned system models are further processed. Next, the monitor loads the appropriate system model and compares the data to the model. The processing results are then stored in the database. Once the monitor successfully processes the data and stores the results, it removes the processed entry from the queue, and polls the queue for the next entry.

## Current Status/Accomplishments/Prototyping Methodology

The ASSET contract was awarded in January of 1991. The first installation of hardware and software at USSPACECOM occurred at Iteration 1 in September of 1991, just nine months after contract start. New versions or iterations of software are delivered approximately every two to three months. The system has been receiving operational data since September of 1992, at which time ASSET began twenty-four hour monitoring. We are currently developing Iteration 8. The rapid prototyping methodology has allowed us to immediately incorporate analyst feedback as well as respond to a dramatically changing political environment.

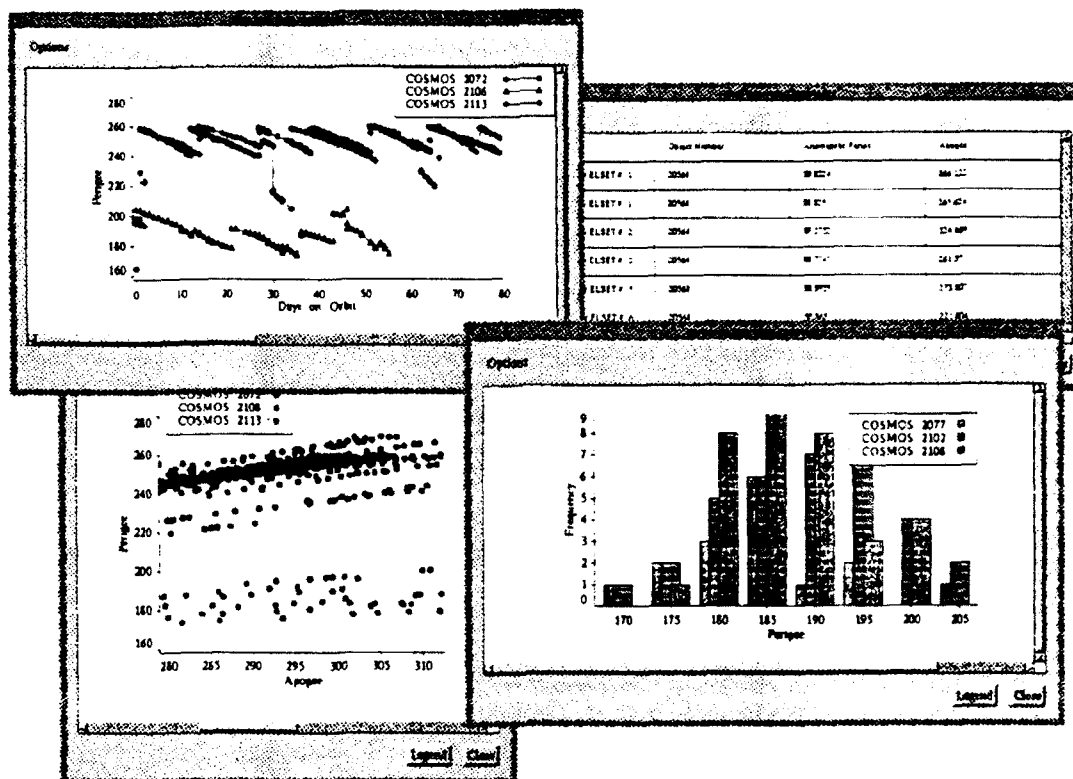


Figure 7 Sample of the Available Plots

ASSET provides the space analyst with a variety of tools. Much of the previous processing involved hours of "pencil and paper" analysis. ASSET facilitates the concept of single point access to the required information.

The processing results of ASSET are all available within a few "mouse" clicks. This provides a user interface that is easy to use and learn.

Alerts detected by the system can be handled as they are generated by the *Twenty-four Hour Monitor* or as the analyst is ready to process them. This is accomplished through the electronic mail facility and the result processing records. Electronic mail notification provides a method of user notification that is already part of the user environment. It handles the problem of whether the user is currently on the system. It also allows the forwarding and sending of mail outside of the current workstation. A visual display is available to the user if a session is running.

In the past many "expert" systems have failed not because the technology did not solve/assist in the solution, but because the models themselves added to the problem. Model maintenance has been the downfall of many systems. ASSET has avoided this problem by following two important strategies. The first has been to depict the models to the user in a form that is easy to construct and understand. We chose a "palette" approach that represents models as graphic objects. Many users already have experience with the various graphical drawing packages that are widely available on personal computers. The selection of this paradigm has enabled ASSET to construct and present models in a readily understandable form. The use of the model in the explanation facility also reinforces the understandability and acceptability of the models. The second strategy was to iden-

tify the management of models as a critical area to be addressed. A tool has been designed and partially implemented that provides user's with the capability to experiment with and test the interaction of models with data. This tool can be used to test new or existing models and determine their likely impact on overall system performance. In the future statistical tools will also be developed to assist in model building.

ASSET includes tools that allow easy access, display, and maintenance of database information. These tools are designed for the senior ASSET users. They facilitate and automate many of the necessary database maintenance functions that are normally provided by other support personnel, namely system or database administrators. These tools help reduce the overhead normally associated with sophisticated software applications.

In response to the changing user requirements and geopolitical situations, ASSET was able to generalize the original modeling capability that had been developed for the project. Initially ASSET was to develop models for a specific set of satellite domains. After developing models for the first few domains, the commonalities between satellite models were noted. By developing a more general system than was originally envisioned, it is expected to have saved at least two million dollars. The changes increased flexibility as well as user empowerment. The changes allowed users to develop models versus the contractor. Some detailed calculation and specific event type modeling was lost to the generalization process, but the added flexibility has more than offset this loss. The added flexibility greatly facilitated the ease with which ASSET was able to respond the world changes. This flexibility increases the useful "lifetime" of ASSET by providing the capability to easily build and edit models to represent new satellite systems.

ASSET maintains profiles on the interest's of each user. User's have the ability to change the profiles. Profiles contain information on the specific and general type of satellites that are of interest. The purpose of profiles is to reduce the amount of extraneous information presented to the user.

### **Summary**

ASSET has already met or exceeded most of the original goals established for the project. The key to continued success for ASSET lies largely in the hands of the space analysts. The ASSET project has always been responsive to the analyst's needs and preferences. This has been reflected by the warm reception that USSPACECOM has shown to ASSET. Within a week of routinely receiving operational data, the ASSET system was demonstrated to the Chairman of the Joint Chiefs of Staff.

ASSET currently runs on DEC/ULTRIX and SUN/UNIX platforms running X Windows. The adherence to open systems standards such as UNIX, X Windows and the use of C++/C for implementation should facilitate ease of maintenance. Following standard user interface guidelines should reduce the user training requirements and allow expected functions to carry over between applications, like "Cut and Paste" between application windows. The tools developed for managing the models and the databases should also reduce overall lifecycle costs. All project documentation is kept on-line for ease of maintenance, access, and reusability. The multi-process client server architecture should allow this system to be distributed over multiple workstations should the need arise. ASSET will be accessed from a user's workstation much like any other application such as a word processor or spreadsheet.

## ORBITAL DEBRIS ENVIRONMENT CHARACTERISTICS OBTAINED BY MEANS OF THE HAYSTACK RADAR

Thomas E. Tracy (NASA/LESC), Eugene G. Stansbery (NASA), Mark J. Matney (NASA/LESC) and John F. Stanley (NASA)

### ABSTRACT

This paper describes the collection and analysis of space debris data. Sizes down to less than 1-cm diameter were detected by the Haystack radar during a collection period between October 1990 and October 1992. A "beam park" mode of operation was used whereby the radar was held in a fixed position and debris passed through the field of view.

The analysis includes physical size estimates from the obtained radar cross sections (RCS), orbital debris flux calculations based upon the probability of detections within the half-power radar beam volume, and the occurrence of debris "clusters" within the general population. In addition, a weighting function applied to the flux calculations is described.

### HAYSTACK DESCRIPTION

The Haystack radar is a high power, X-band, monopulse tracking radar with very high sensitivity. The operating efficiency at 10 GHz (3-cm wavelength) is approximately 36 percent, corresponding to a gain of 67.2 dB and a half-power beamwidth of 0.058 degrees. (ref. 1) Single pulse signal-to-noise on a 1 square meter target at 1000 km for the 1.023 millisecond waveform used in debris search is 58 dB. This sensitivity allows objects as small as 1 centimeter diameter to be viewed at ranges greater than 1000 km.

For debris observations, the radar is locked into predetermined "staring" elevation and azimuth positions. The most common elevation positions, and the ones used exclusively in 1992, were 90, 20, and 10 degrees. For all elevations other than 90 degrees the radar is pointed due south. Debris (and known satellites) pass through the radar field of view. A real-time Processing and Control System (PACS) has been programmed to record data only during periods of detection. In this way many hours of detection can be performed without an impractical amount of recording.

The beginning of the receive window for each elevation angle was set at a range corresponding to 350 km of altitude for the 1990 and 1991 observations and at a range corresponding to a 300 km altitude for 1992. The entire range window spans 1138 km. Real-time debris detection consists of the computation of a sliding 12-point noncoherent average of the data for each range bin and doppler cell. If the averaged signal-to-noise ratio in any doppler cell



exceeds the threshold value of  $-5.35$  dB then the data is recorded to disk. Later, at JSC a higher threshold of  $1.08$  dB above noise is applied which amounts to the allowance of only 1 false alarm every 10 hours.

#### SIZE ESTIMATION

Due primarily to limited aspect angle, it is not possible to absolutely determine the size of every individual object as it passes through Haystack's beam. However, a statistical relationship has been established.

Based upon physical principles, static RCS data from 45 hypervelocity impact debris fragments, orbital debris multi-frequency RCS data collected by the Kwajalein radars, and theoretical modelling, an orbital debris size estimation model has been developed which allows physical size to be derived from an object's PP and OP RCS returns. This algorithm, which has been developed in stages as more information has become available, is concerned primarily with object sizes from 1 to 20 centimeters. (ref. 2)

Because of the statistical nature of the size estimations, the non-homogenous distribution of orbital debris (i.e. one volume of space is not equivalent to every other volume), and the temporal changes which occur it is necessary to accumulate a significant number of observations. To-date over 1500 hours of useful beam park observations have been accepted.

#### SAMPLE DETECTIONS

A pictorial representation of some of the data received by the radar and derived from subsequent processing is shown in Figures 1 through 4 for two satellites of disparate size. The first set of plots is for a known cataloged object, with International Designation 1965-051A (Satellite I.D. 1430). Its common name is Tiros 10.

Tiros 10 flew through the Haystack radar beam during September 1991 while the radar was parked at 20 degrees. The slant range of Tiros from the radar was 1718 km corresponding to an altitude of 773 km. The high signal-to-noise of this object, as seen in Figure 1, for both the principal polarization (PP) return and the orthogonal polarization (OP) return indicated that it was a real, non-spherical target and probably of significant size.

NASA software programs estimated the size of Tiros 10 to be approximately 2.3 meters in diameter. This compares to a catalog estimated size of 1.8 meters in diameter.

The second example of Figures 3 and 4 show similar plots for a debris target of only 1.1 centimeters. The observation again took

place in September 1991, this time with the radar parked at 90 degrees. The altitude of this object was 975 km. It is noteworthy that even at this range the Haystack waveform has the sensitivity to detect this object with greater than 20 dB signal-to-noise.

Occasional undesired observations such as sidelobe, off-axis ( $> 6\text{dB}$  two-way), arcing, and range-folded detections are screened from the final database. This is done by a combination of software decision making and engineering analysis.

#### ORBITAL DEBRIS CLUSTERS

A review of all Haystack detections thus far accumulated has revealed the existence of debris "clusters". These multiple objects are seen to travel together in both space and time. Their estimated sizes tend to be 0.5 to 5.0 cm in diameter.

The clusters discovered so far have existed within the altitude regime of approximately 850 km to 1000 km. This may be due to a number of factors: the preponderance of known orbiting satellites within this region, documented past satellite breakups and lack of drag effects which allow the debris to separate at a much slower rate than would be possible at lower altitudes.

While their total contribution to the overall debris population is probably less than 1 percent, the verifiable existence of these clusters may be noteworthy. In the future attempts will be made to extrapolate back to the originating satellite(s). The type of debris observed may reveal some clues as to breakup mechanism - explosion from within, catastrophic collision, or partial collision. It is suggested that in the future, when available, Haystack or the newly constructed HAX radar be requested to scan suspected breakups as soon as possible after the event. This would provide a wealth of information regarding total number of debris pieces introduced into the environment, their size distribution, and their spread rate. By being able to observe debris clusters with individual members less than 1 cm in diameter and tracing such swarms back to their point of origin it may be possible to confirm non-catastrophic satellite breakups which would otherwise go undetected.

An example of a debris cluster is circled in the altitude vs. time plot of Figure 5. Each dot represents a detection with an integrated signal-to-noise ratio (SNR) greater than 5.5 dB. An enlargement of that area (Fig. 6) displays 12 detections consecutive in time. Objects #2 and #6 are visibly outside of the potential "cluster" and are not further considered. Object #3 is below the final SNR threshold of 6.08 dB and is considered noise.

When the monopulse path through the radar beam is plotted (Fig. 7) for the remaining 9 objects a remarkable consistency in direction is seen. Figure 7 may be considered a cross section of the Haystack radar beam. Each debris path is superimposed upon this

cross section. Of the nine remaining objects #5 has the lowest SNR value of 6.89 dB. The large dot represents the first appearance within the beam and its path follows the attached line in chronological order. The object numbers remain the same.

#### RADAR PERFORMANCE MODEL (RPM)

The radar performance model calculates the collection area, and the average probability of detection over that collection area, as a function of the object size, the range to the object, and the orbital inclination of the object. The model uses well-established techniques for calculating the probability-of-detection of scintillating objects (refs. 3 and 4) as a function of SNR, threshold level, number of pulses integrated, and target fluctuation characteristic. The number of pulses integrated is set to 12 which is the same number used by the Haystack radar during data collection. The threshold level used in the performance model is 6.08 dB SNR. This threshold gives a false alarm rate of 0.1 per hour.

A separate program calculates the orbital debris flux for each object size step, altitude step, and inclination step. The program then reads the appropriate probability-of-detection and edge-to-edge distance from the random access file created by the RPM and calculates the expected detection rate.

Results from all processing of the data taken during the first half of 1992 are presented in Figures 8 and 9.

#### DEBRIS FLUX WEIGHTING FUNCTION

As stated above, an estimation of debris size is derived from each object's monopulse corrected RCS. If there were equal numbers of different sized objects, then these results could be integrated directly to obtain a debris flux plot. However, it is known from previous studies that the number of objects in orbit increases geometrically with decreasing size.

Bohannon et al. (ref. 2) were able to construct a mean size function relating RCS to average object size (Fig. 10). In addition they were able to construct the probability function of an object of a particular size being measured with an unusually high or low RCS, due to variable aspect angle (Fig. 11). When Haystack sees an individual object with some RCS we do not know if it is seeing an object with a size consistent with that RCS, or a small object with a high signal return, or a large object with a low signal return.

Because the number of small objects in orbit predominate, it is more likely that a small object is being measured with a high RCS

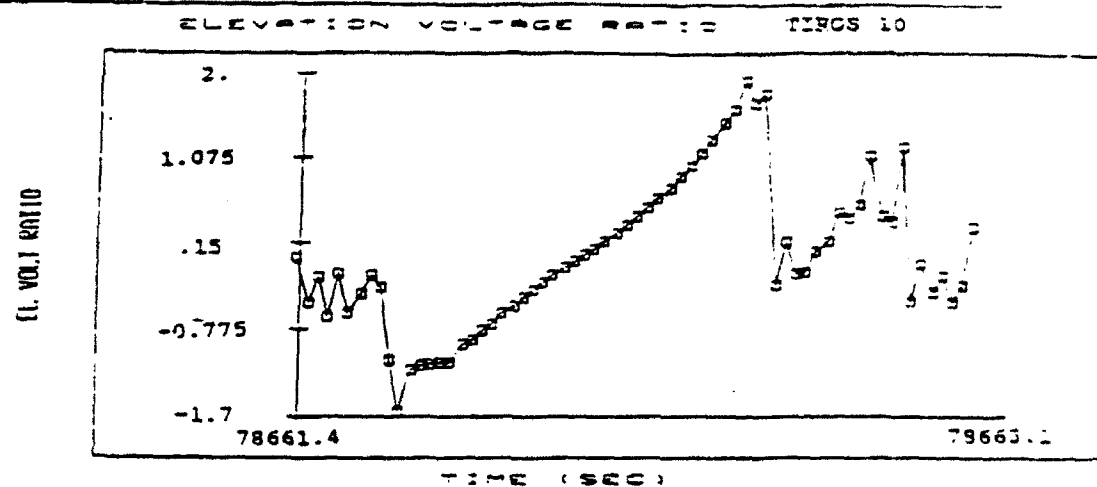
than a larger object with a small RCS. The functions (Fig. 12) must be weighted for this type of size distribution. By comparing some "a priori" size distributions to those actually measured by the Haystack radar it is possible to obtain a good fit by trial and error.

Figure 13 shows a characteristic cumulative distribution of Haystack RCS measurements (showing the number of objects counted with RCS equal to or greater than the given value) with a theoretical fit. By transforming the basic RCS measurements into size using the mean curve (Fig. 10), we may compare this "simple" distribution against the theoretical size distribution chosen as a good fit by trial and error. As can be seen in Figure 14, the results match the observed Haystack distribution well for object sizes  $> 1$  cm, demonstrating that some of the "bumps" in the original Haystack data are effects which may be corrected. For smaller objects ( $< 1$  cm) the fit is not as good probably because the RCS functions are extrapolations from larger measured objects and may break down for sizes  $\ll 1$  cm. By introducing this weighting function, an improved flux curve results.

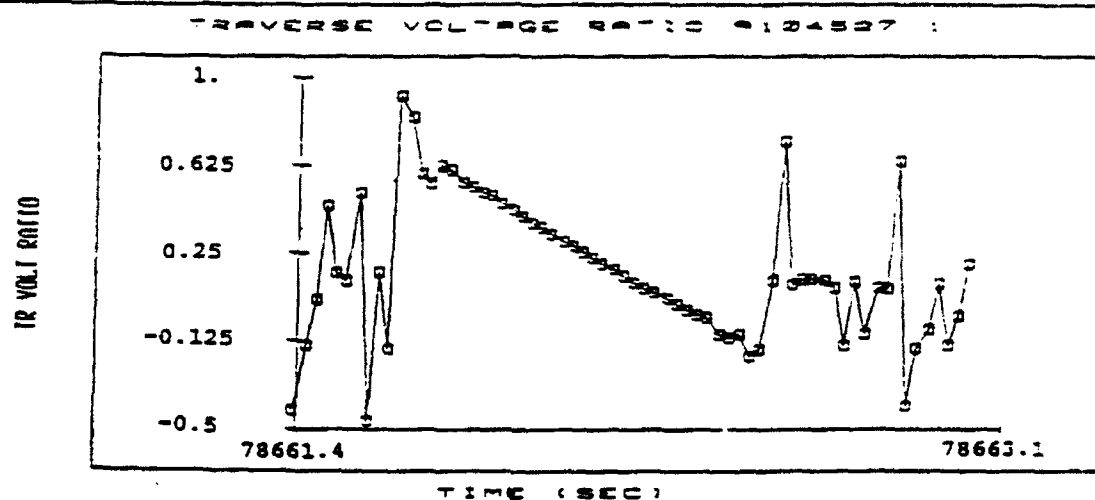
#### REFERENCES

1. Coster, A.J. "Radar, Laser, and Telescope Parameters of Various Lincoln Laboratory Affiliated Facilities", MIT Lincoln Laboratory Memo 91M-0703, June 1991.
2. Stansbery, E.G., Bohannon, G., Pitts, C.C., Tracy, T.E., Stanley, J.F., "Characterization of the Orbital Debris Environment Using the Haystack Radar", NASA JSC-32213, April 1992.
3. Fehlner, L.F., "Marcum and Swerling's Data on Target Detection by a Pulsed Radar", Johns Hopkins University Applied Physics Laboratory Report TG-451, July 1962.
4. Blake, L.V. "A FORTRAN Computer Program to Calculate the Range of a Pulse Radar", Naval Research Laboratory Report 7448, August 28, 1972.

(c)



(b)



(a)

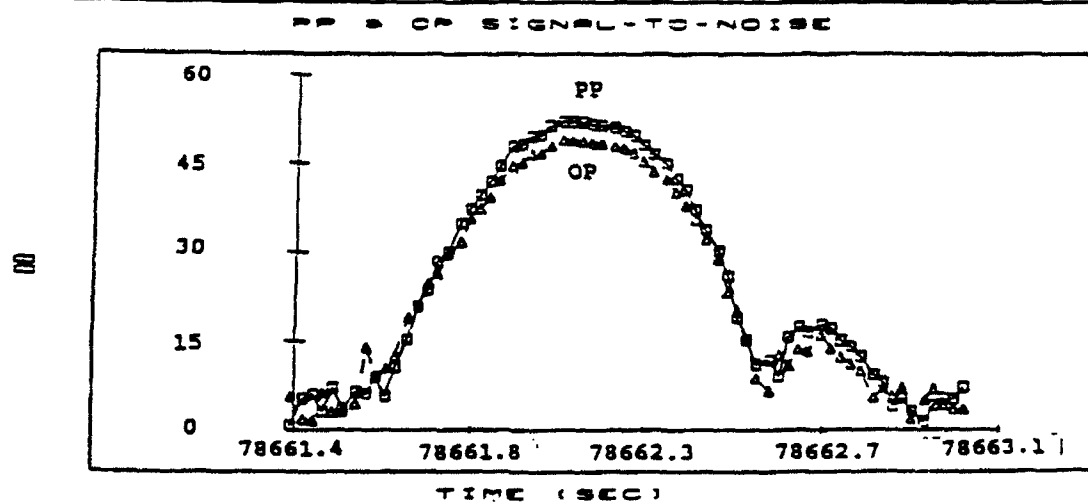
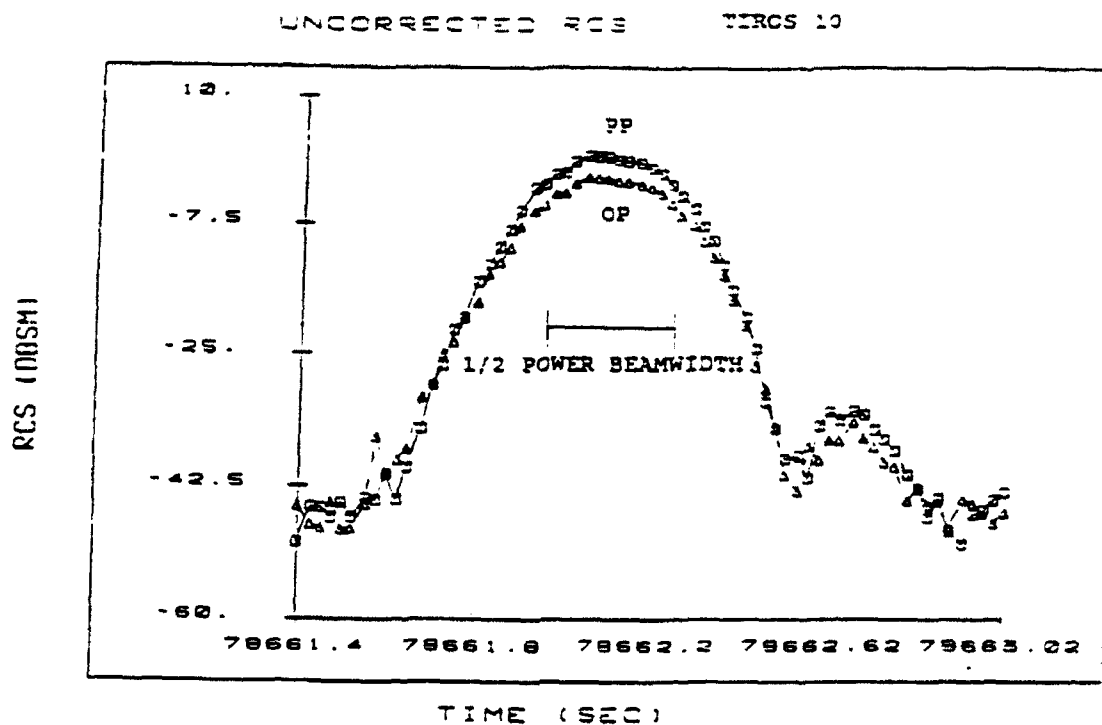


Figure 1. Tiros 10 (a) signal-to-noise in dB, PP and OP (b) traverse voltage ratio (c) elevation voltage ratio

(a)



(b)

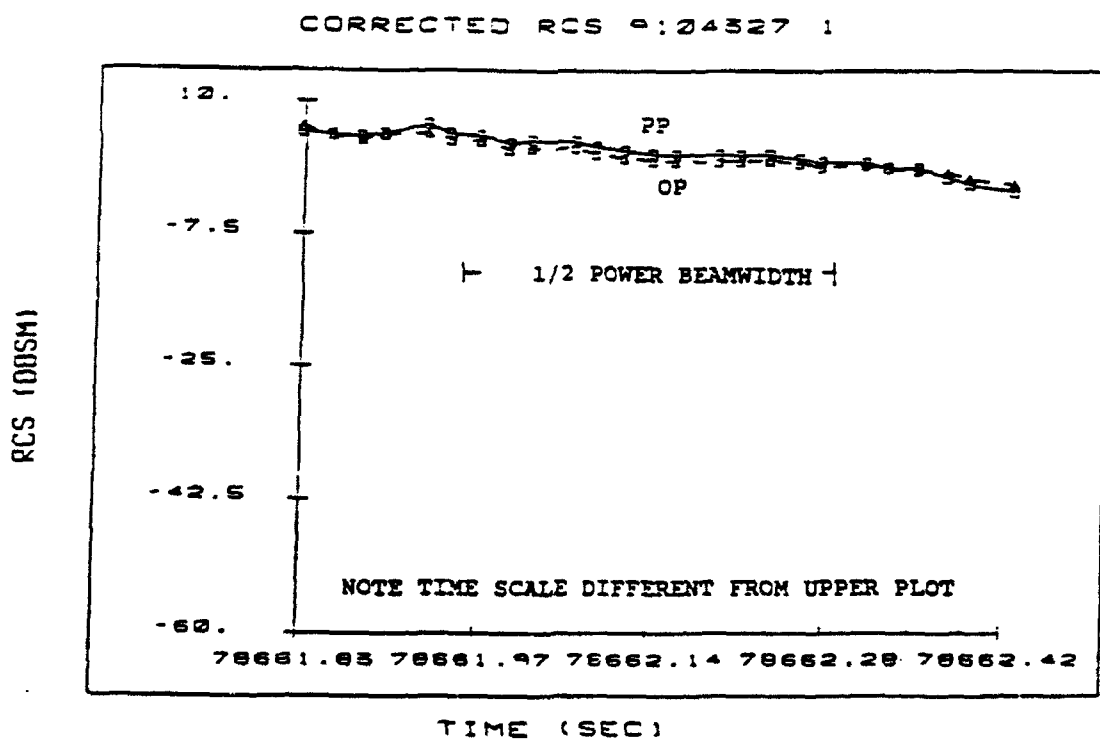
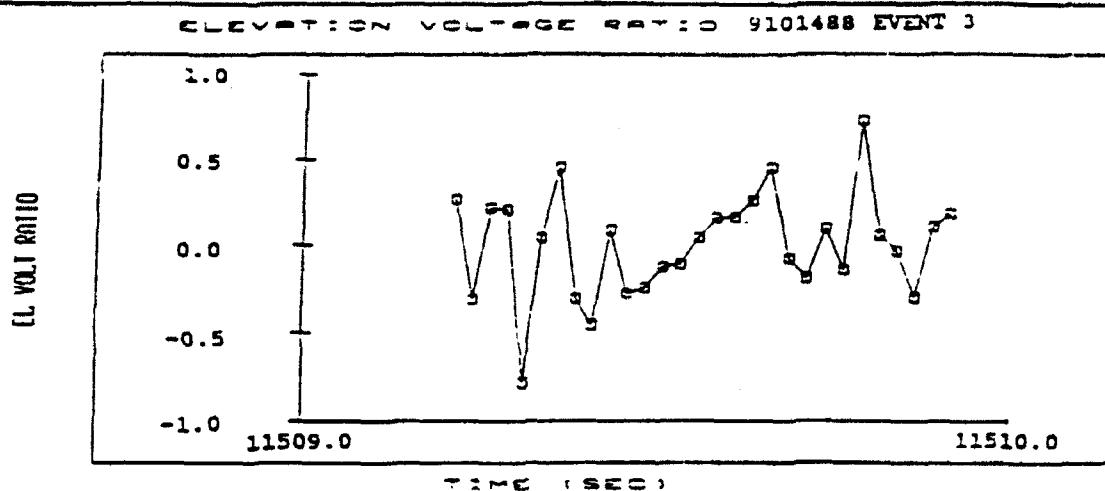
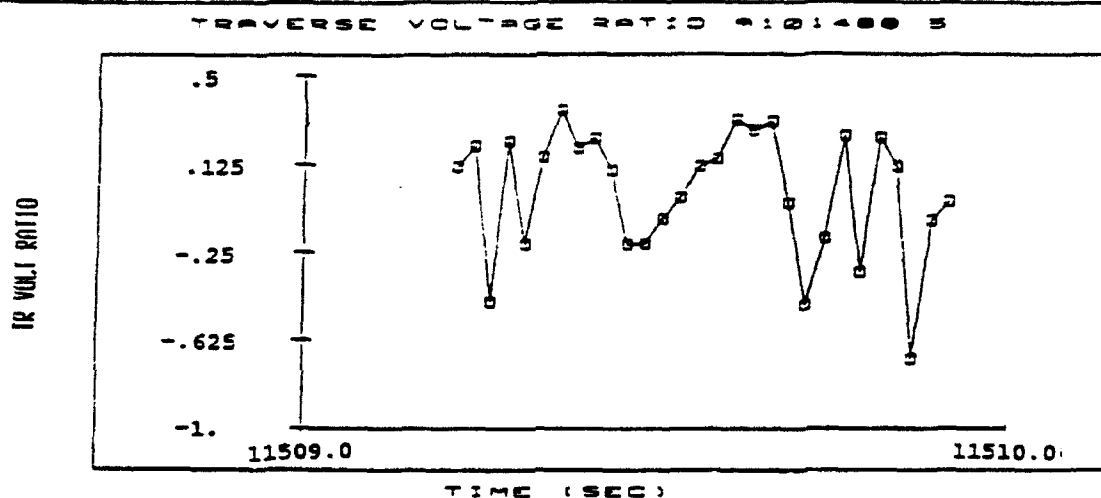


Figure 2. Tiros 10 (a) uncorrected radar cross section  
(b) corrected radar cross section

(c)



(b)



(a)

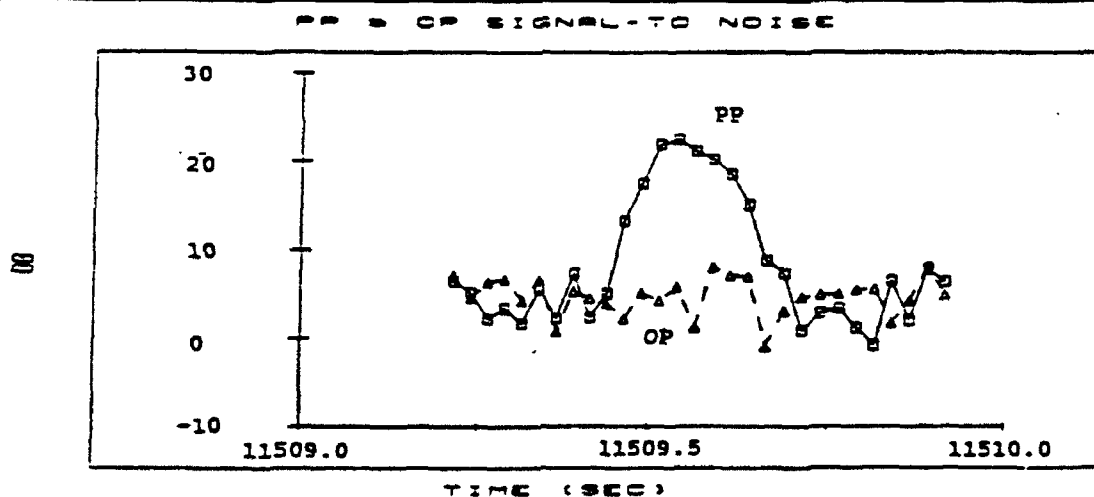
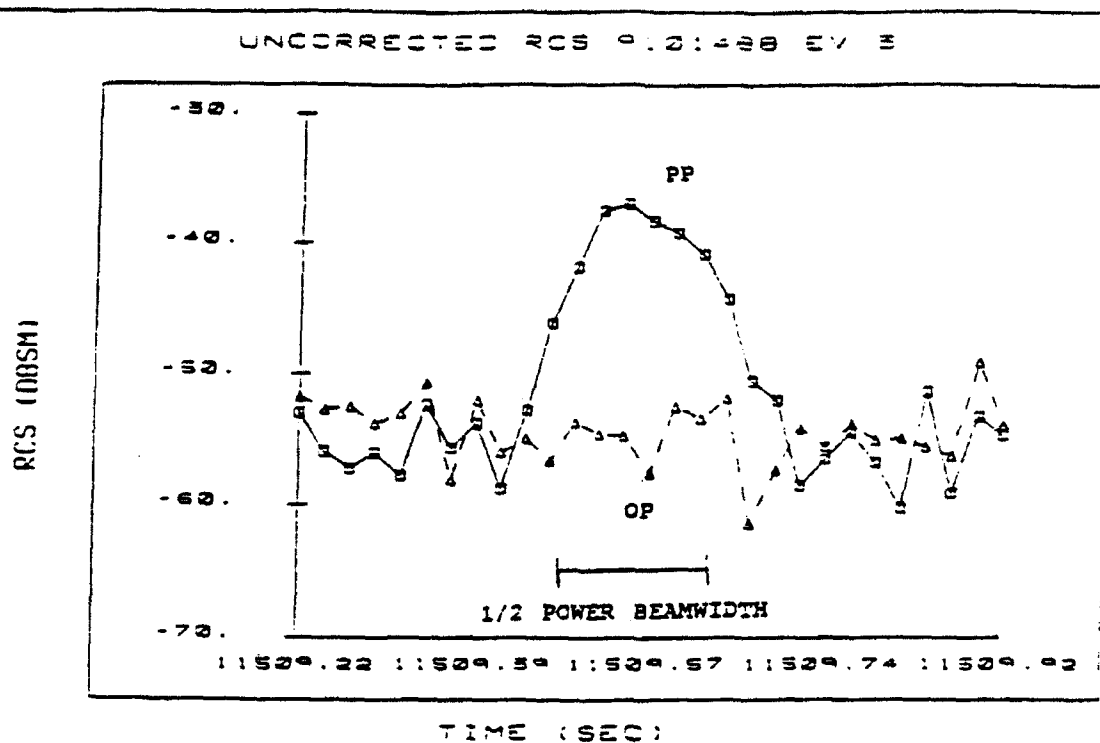


Figure 3. Example detection of 1.1 cm diameter debris object  
(a) uncorrected signal-to-noise in dB, PP and OP  
(b) traverse voltage ratio (c) elevation voltage ratio

(b)



(a)

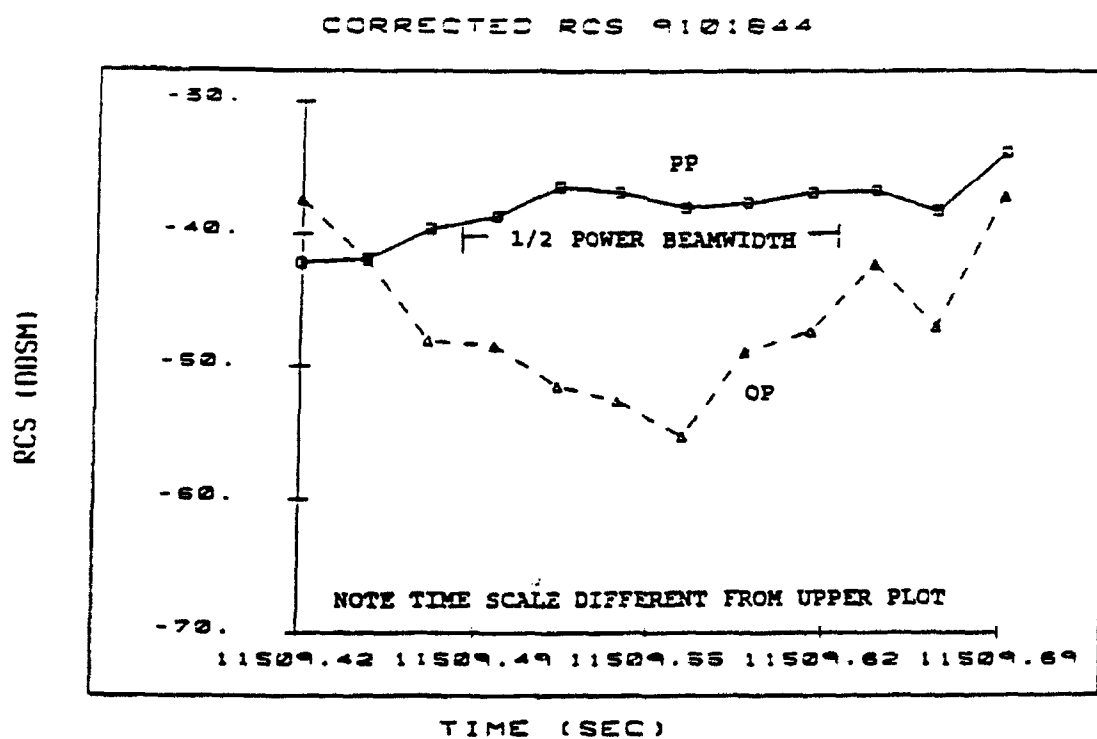


Figure 4. Example detection of 1.1 cm diameter debris object  
(a) corrected radar cross section  
(b) uncorrected radar cross section



# Debris Events Altitude vs. Time Julian Day = 91293

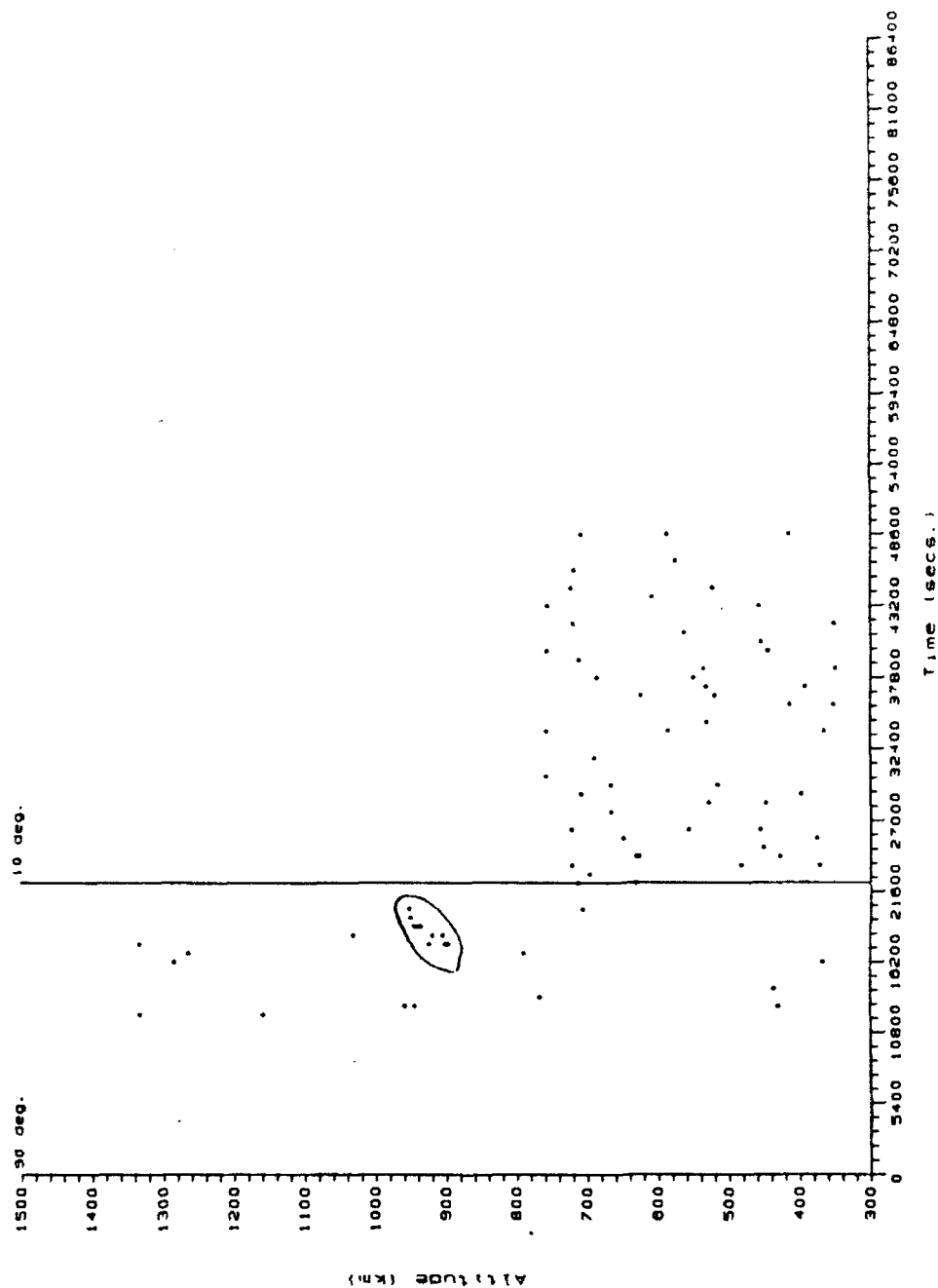


Figure 5. Altitude vs. Time detection plot. Each dot represents a detection with integrated signal-to-noise greater than 5.5 dB. Beam staring was done this day, 10-Oct-91, at 90 deg. and 10 deg. elevations.

● 2

ENLARGEMENT

● 6

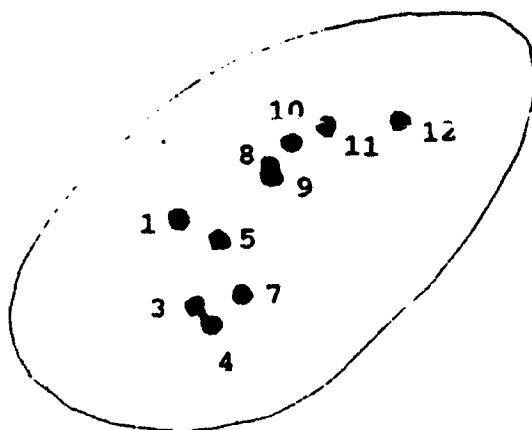


Figure 6. Enlargement of encircled area from figure 5. Each detection consecutive in time, beginning with #1, is labelled.

# TRAVERSE AND ELEVATION OFFSETS DERIVED FROM MONOPULSE VOLTAGE RATIO

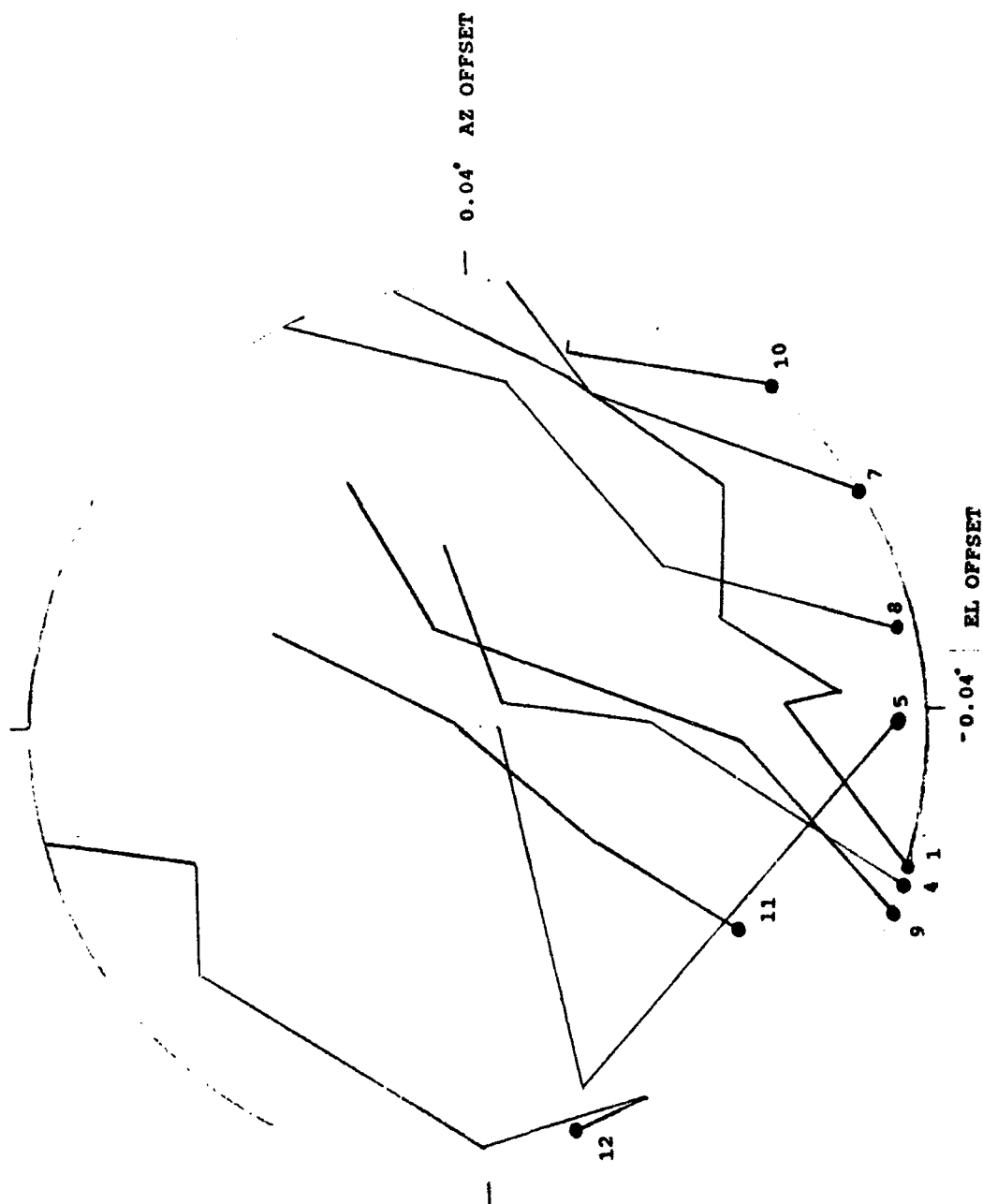


Figure 7. Simulated Cross Section of the Haystack Radar Beam. The monopulse derived flight paths of each object are superimposed. The large dot represents a starting location. Each object then follows the path of its attached line.

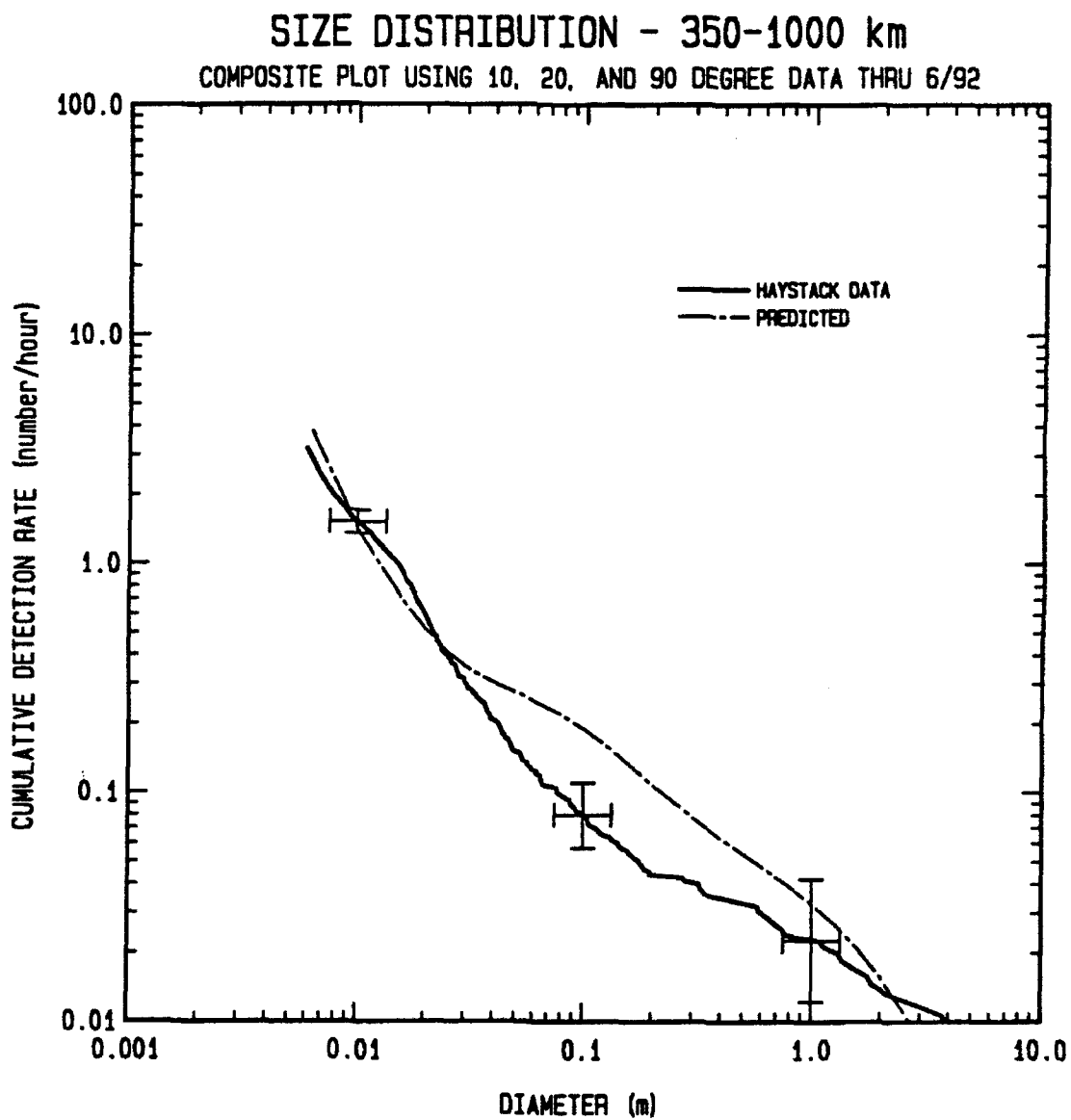


Figure 8. Composite Plot of Detection Rate vs. diameter using data collected at 10, 20, and 90 degrees.

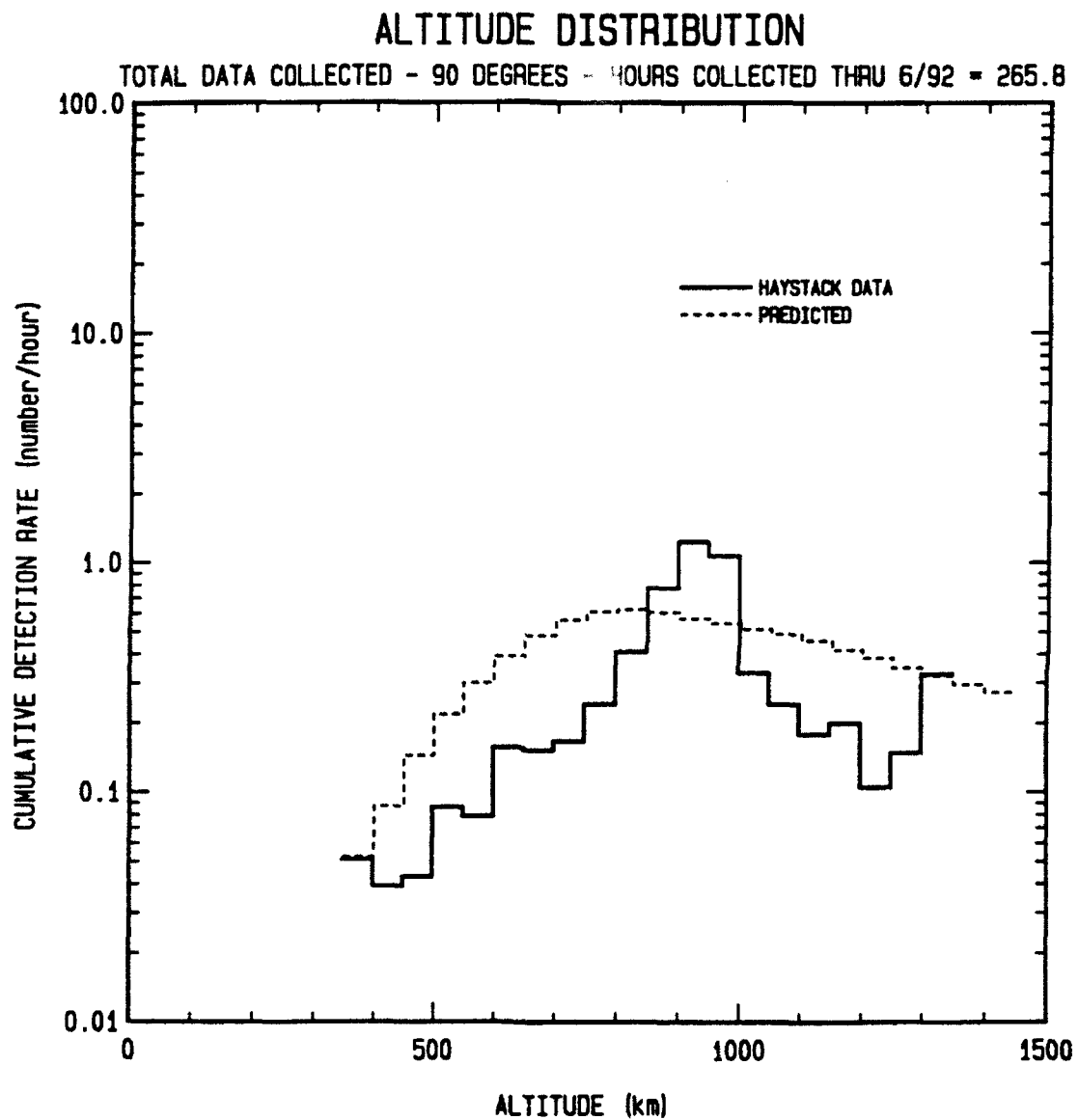


Figure 9. Altitude Distribution.

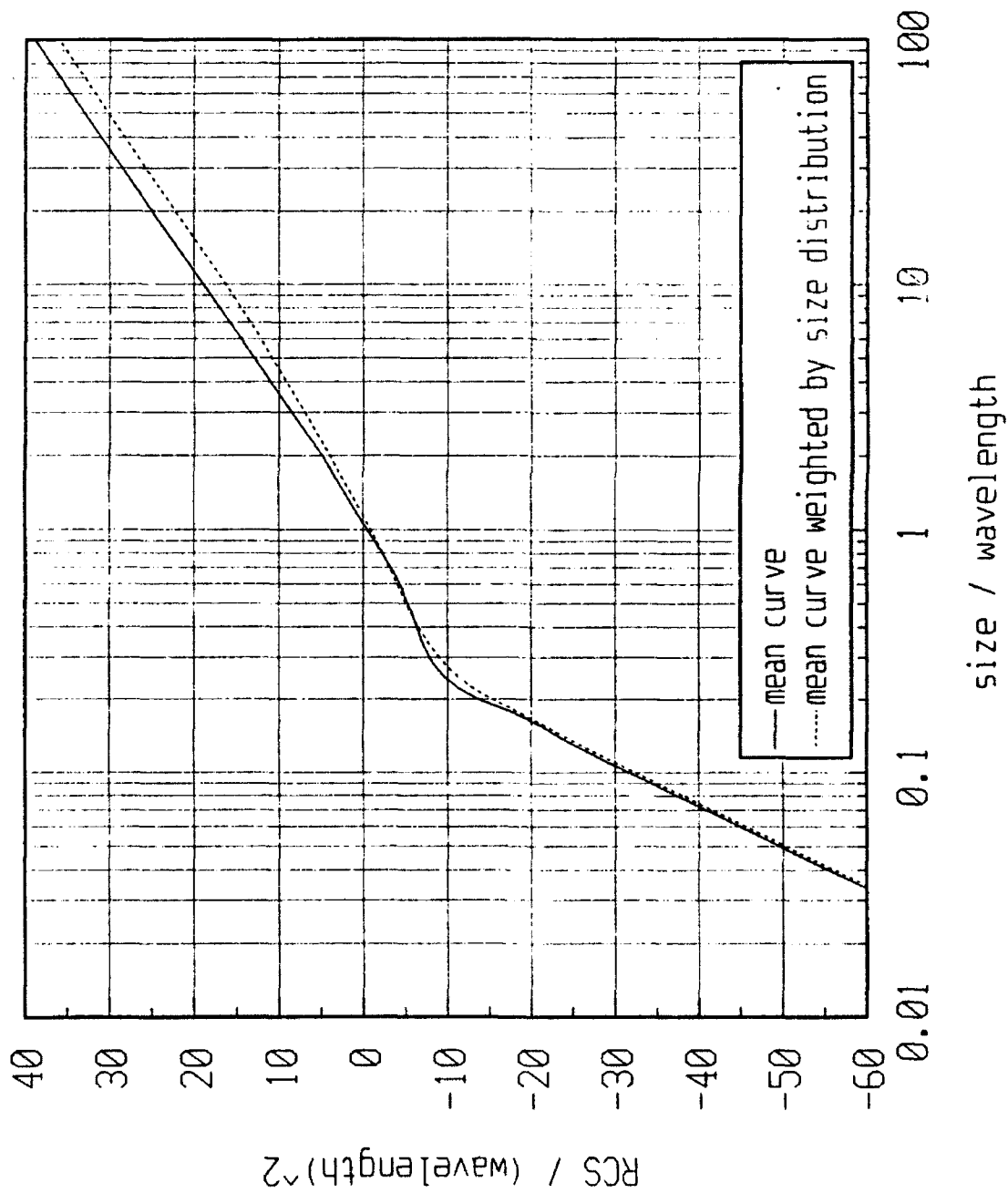


Figure 10. Mean Size Function Relating RCS to Average Object Size.

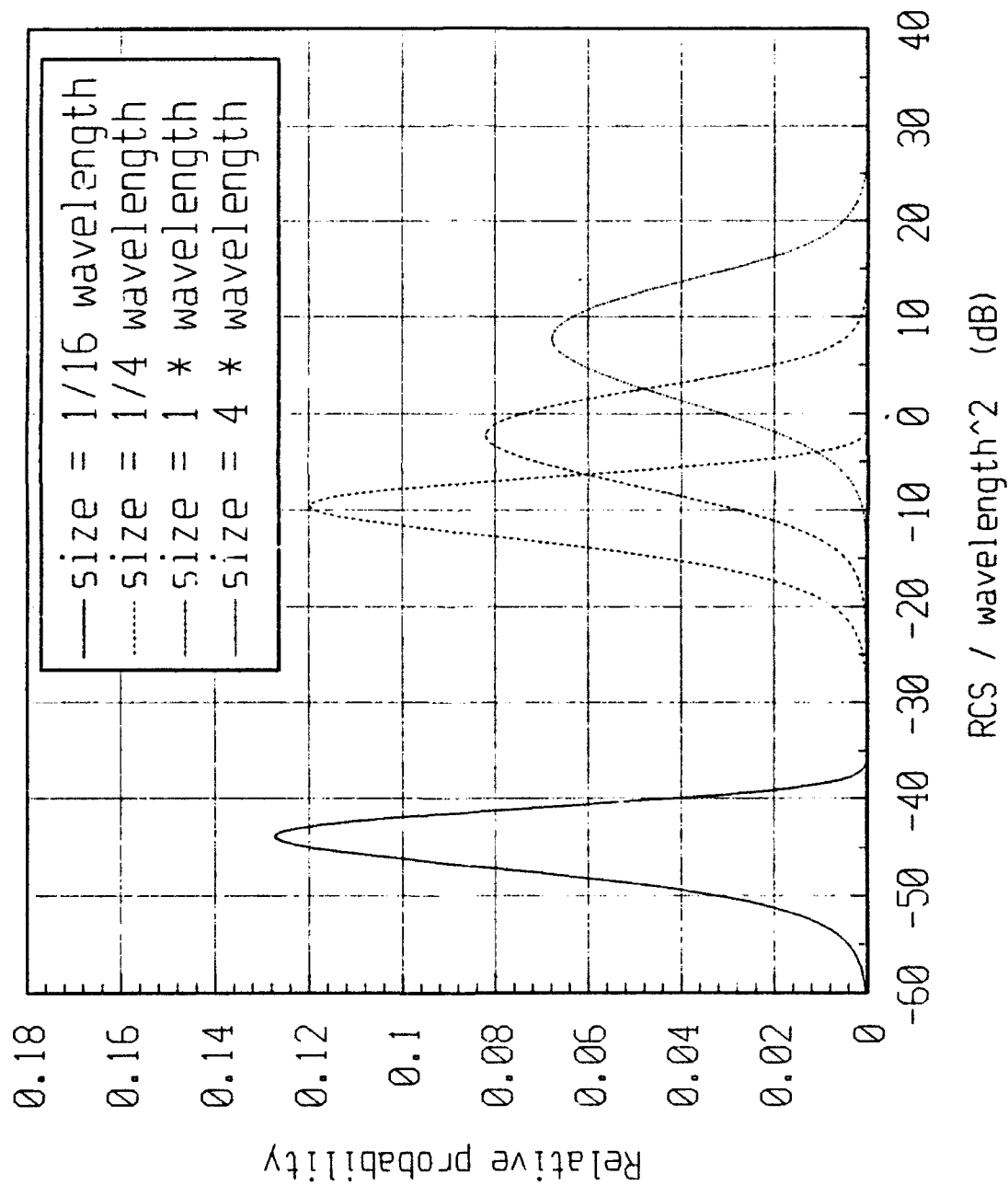


Figure 11. Probability Function for an Object of a Particular Size Being Measured with a Particular RCS.

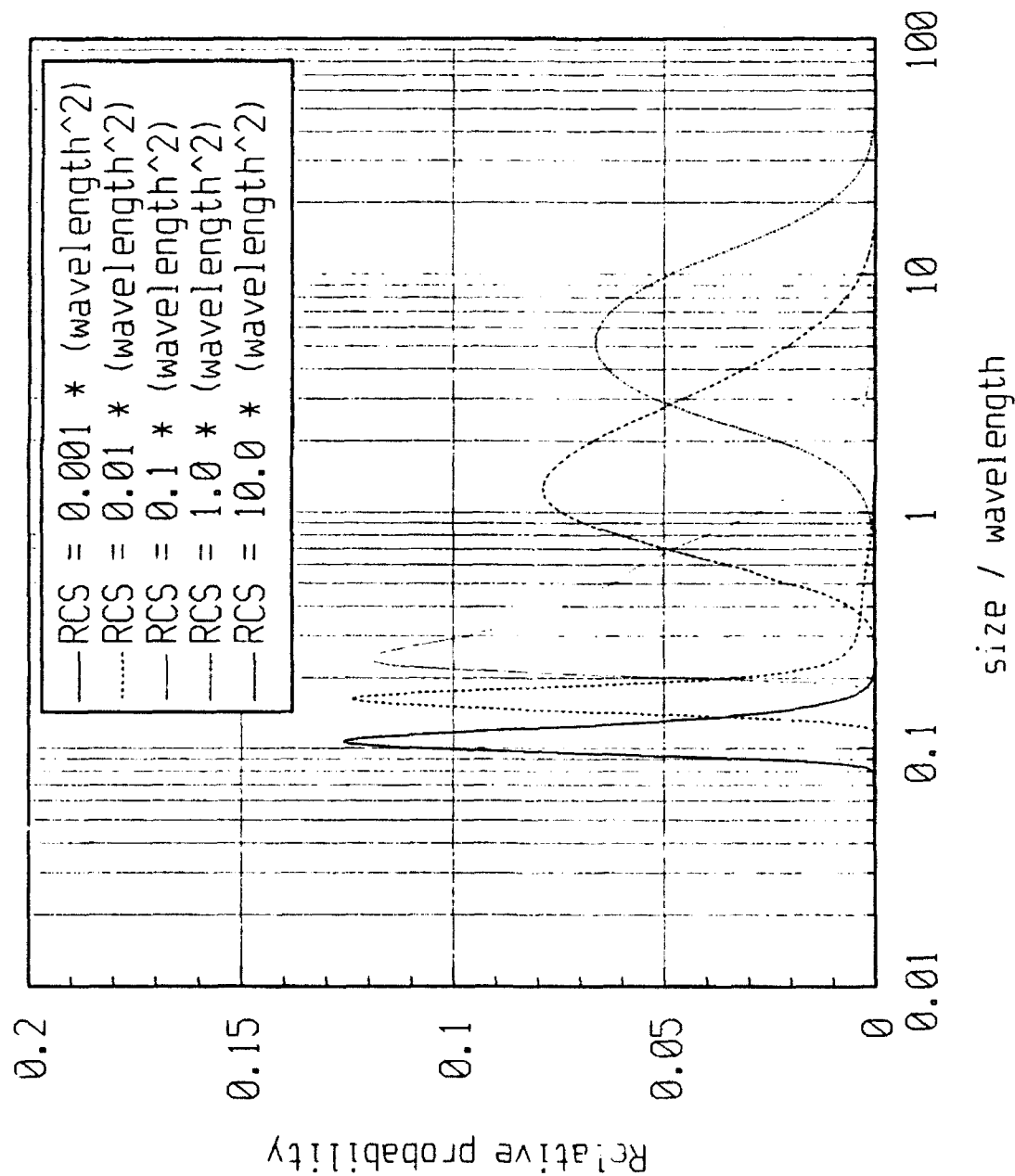


Figure 12. Probability Distribution Showing the Relative Contributions of Different Sizes to a Single RCS Measurement.



# Model Fit to Haystack Data

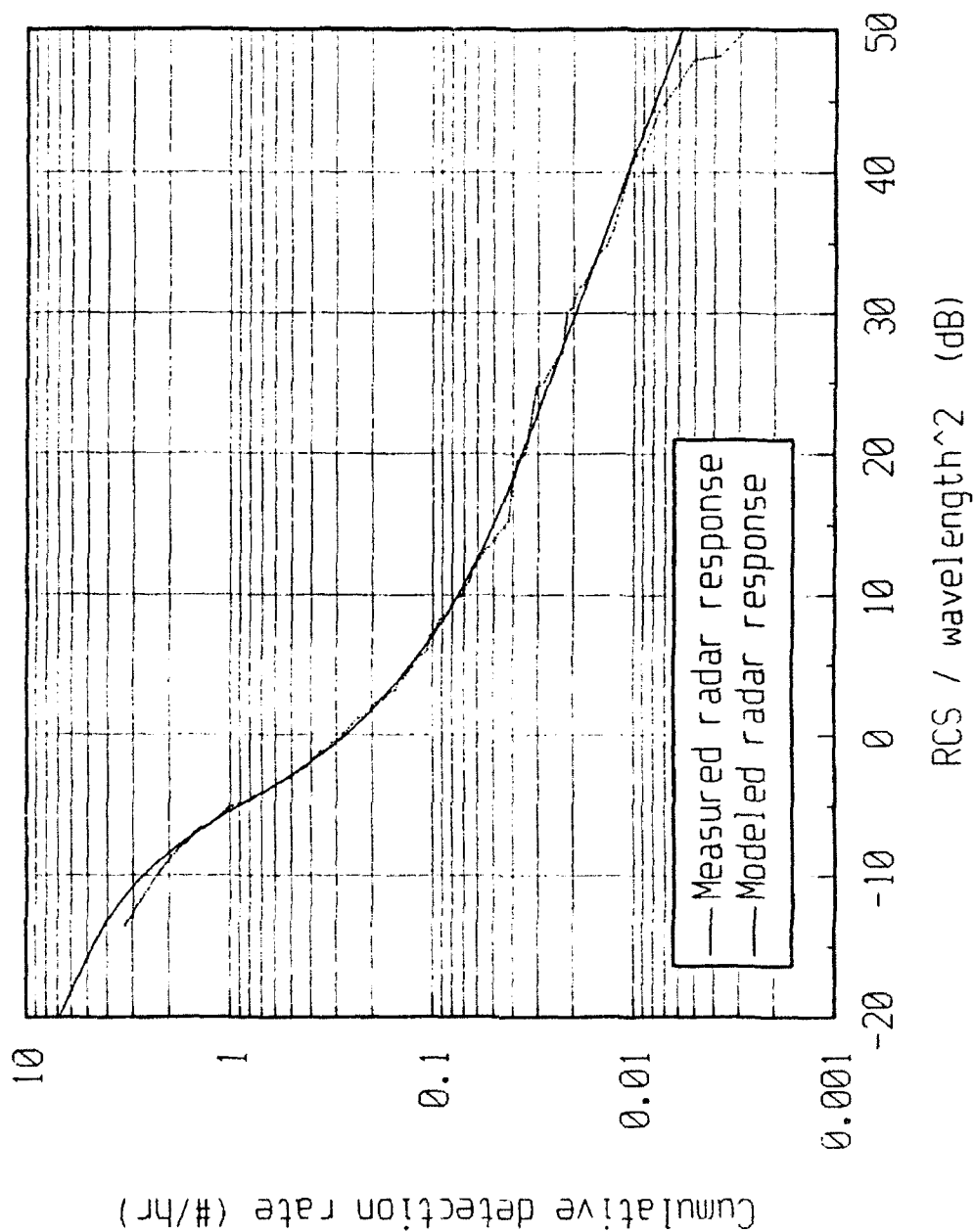


Figure 13. Characteristic Cumulative Distribution of Haystack RCS Measurements Compared to a Theoretical Fit (Modeled Radar Response).

# Model Fit to Haystack Data

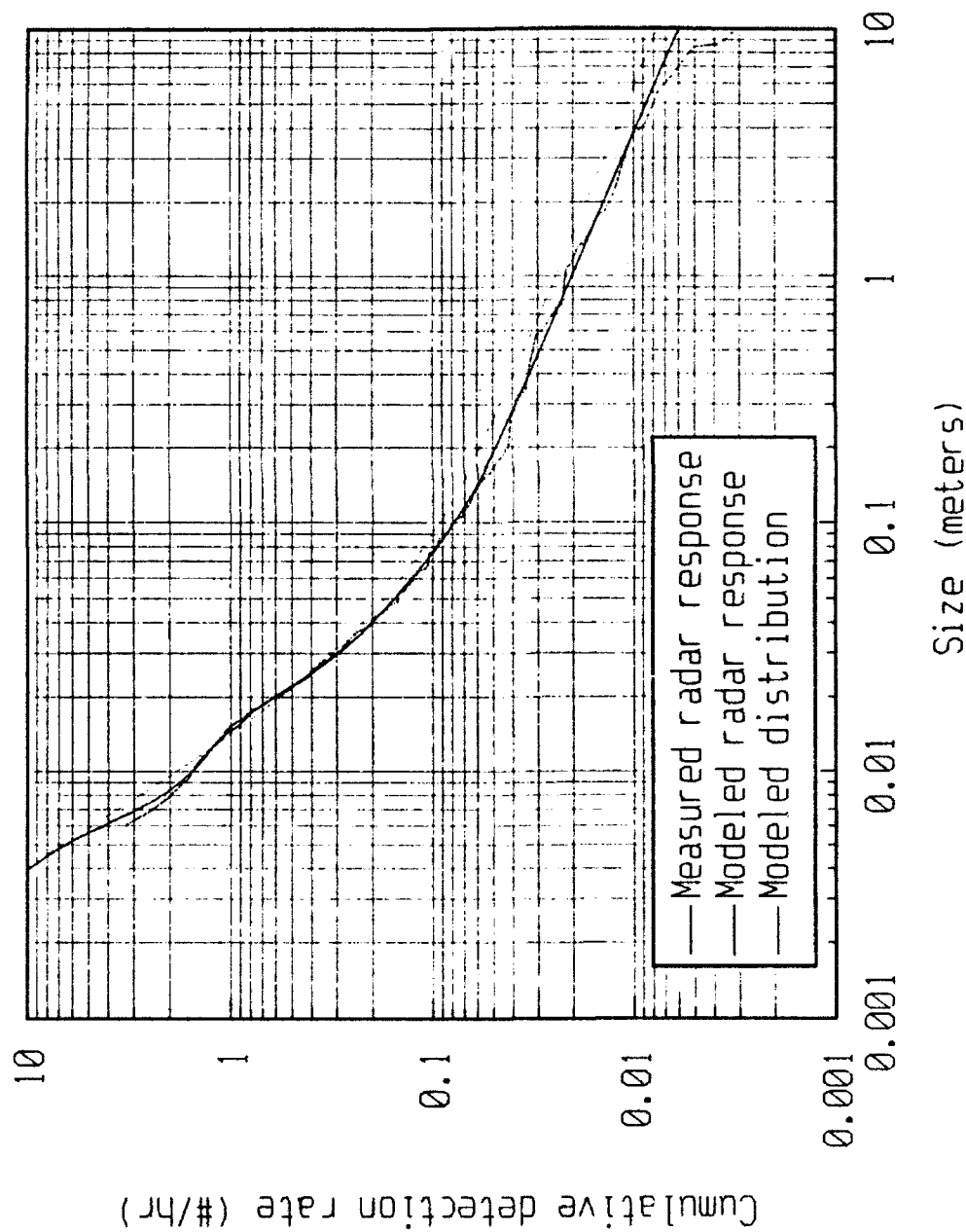


Figure 14. The RCS Measurements from a Characteristic Cumulative Distribution of Haystack RCS are Changed to Size Measurements and Compared Against the Modeled Radar Response and a Modeled Distribution.

## A Study of Systematic Effects in Eglin (AN/FPS-85) RCS Data

K.G. Henize (NASA/JSC), P.D. Anz-Meador (Lockheed ESC), T.E. Tracy (Lockheed ESC)

### Background

As a part of ongoing studies at the NASA Johnson Space Center concerning the frequency and distribution of orbital debris, 47 updates of RCS values received in electronic form from the US Space Command (primarily from the AN/FPS-85 radar) have been archived since 1977. These are used not only to derive diameter distributions necessary in modelling the space environment but also as an independent source of size from which Bond albedoes may be derived when calibrated optical observations are available. In these studies it is important to understand and eliminate both random and systematic effects in the data to the greatest possible extent.

The random scatter in the individual monthly observations of any given object may be minimized by finding either the mean or median of all available observations for that object. However, before combining observations, it is necessary first to eliminate the discernable systematic effects. Potential effects to be considered include the effects of Mie and Rayleigh scattering, changes in the system calibration and ionospheric effects related to solar activity. The effects of system calibration and of solar activity are the subject of this paper. Statistical methods for correcting Mie and Rayleigh scattering in the Eglin data have been discussed by Stansbery et al (1991).

Several studies of Eglin RCS data (Gaposchkin and Sridharan 1988, Badwhar and Anz-Meador 1989, Burns 1990) have shown that values published prior to 1990 are too large by a factor of about two. As a result of recommendations made by Burns (1990) the calibration of the reported RCS was altered in mid-1990 (Baker 1993 - can't we do better?) Our interest in using not only the most recent but also the older RCS data at our disposal led us to examine the data in our 47 monthly updates to determine the magnitude of the effect of the 1990 recalibration and to search for other changes over the years due either to unreported calibration changes or to effects caused by ionospheric changes related to solar activity.

### Data Selection and Processing

To provide a broad statistical base for this study, we have chosen three groups of objects: six USA calibration spheres of various sizes, 19 Cosmos satellites reputed to be two-meter spheres and 352 so-called "eight-balls" launched by the USSR. The six US spheres have well-documented sizes, shapes and surface characters and can be expected to show the least scatter for each individual object. The Cosmos two-meter spheres were included to extend the statistical base to larger sizes and to a wider range of orbital inclinations and heights. However, our data cast doubt on the uniformity of their sizes

and/or surface structures. The eight-balls have been included in spite of their somewhat dubious size and shape, in the expectation that they are at least uniform in size and shape and that their sheer number would strengthen the overall statistical result, especially the relative changes from month to month. The results justify this judgement.

In order to facilitate comparison of this variety of objects, the RCS values have been normalized by dividing them by the "expected" RCS. For the US spheres the expected RCS is the geometrical cross section based on the known diameter multiplied by the scattering coefficient for a perfectly conducting sphere of that size. For the seven two-meter spheres finally accepted as such, the expected RCS (3.01) was likewise taken to be the geometrical cross section (3.14) multiplied by the scattering coefficient.

The expected RCS of 0.7 square meters selected for the eight-balls is somewhat arbitrary since only approximate dimensions are known for these objects. The RAE Table of Earth Satellites (King-Hele et al 1990) gives the shape as "spheroid" and the size in meters as "1.0 long?, 0.8 dia?". An ellipse of these dimensions has an area of 0.63 square meters. Use of this value produced normalized RCS's somewhat higher than those for the US calibration spheres. A value of 0.7 gives excellent agreement between the two data sets (especially for the well-calibrated period after 1990.5) and is the ellipse area if the length of the spheroid were increased by 10%. The fact that the Eglin radar tends to see the maximum cross section for these objects suggests that the objects are gravity-gradient stabilized and thus are seen nearly broadside-on at the Eglin viewing angle.

It should be noted that care has been taken to eliminate false (i.e. default) RCS values and values which are identical to the previous month's values, an indication that the RCS's were not updated. We have also weeded out several inordinately high or low values in each group by excluding all normalized RCS's more than a factor of ten greater than or less than the expected RCS.

The six USA calibration spheres and the 19 Cosmos objects originally selected are listed in tables 1 and 2 respectively.

The month-by-month means for each of the three groups are displayed in figures 1, 2 and 3. These plots display not only the means but also error bars representing the standard error of the means. The numerical data for each monthly point is given in tables 3, 4 and 5. Perhaps the most pertinent data in these tables are the number of objects included in each monthly mean. These vary because the RCS was frequently not updated for a particular month.

### Discussion

The three plots show a remarkable similarity considering the diverse nature of the groups. The three points from 1977 to

early 1980 and the points following mid-1990 are in nearly perfect agreement among the three groups as a perusal of the tabular data will attest. From mid-1980 to mid-1983 there is a general scatter of points about a normalized RCS of about 1.2. This is followed by a rapid increase to a normalized value of about 2.0 for the interval from mid-1983 through mid-1990. Between 1990.45 and 1990.54 there is a sharp decrease by a factor of 1.9 in the RCS values indicative of the calibration change which took place at that time.

The increase in mid-1983 may be attributable either to an undocumented calibration change of "between 1 and 2 db" reported by Baker (1993) or to an ionospheric effect related to the rapid decrease in solar activity which took place during this time period. However, if the effect is due to solar activity, then a corresponding decrease in the reported RCS's should be observed during the rapid increase in solar activity between 1987 and 1990. Although such an effect is not readily evident it is possible that it is masked by the low time resolution of the available data or by the lack of documented data on the history of calibration and/or operational changes in the radar.

We have derived a set of time-dependent calibration factors from the data presented in tables 3-5 and figures 1-3. These are given in table 6. The adopted factors represent a subjective averaging between the US sphere data and the eight-ball data.

These calibration factors may be checked by using them to calculate a mean RCS for each satellite. These data are reported in tables 1 and 2 as the "mean" cross section. The eight-balls are too numerous to tabulate and, instead, we present for them a histogram of the derived RCS's in figure 4. It should be noted that the derived RCS's for the US spheres tend to be slightly smaller than the "adjusted" RCS while the reverse is true for the eight-balls. This is the result of the fact that the normalized RCS's for the eight-balls run somewhat larger than the normalized RCS's for the US spheres, particularly in the interval from 1981 to 1986 (see figures 1 and 3). Thus, the resulting mean calibration factors over this interval are not perfect for either set of data. The reason for such an effect is not clear. It may be tempting to relate the effect to solar activity (which went through a sharp decline during this interval) but there is no distinction between the two groups of objects which can explain why they were affected differently.

### USSR Spheres

The USSR spheres deserve special comment. The original list of nineteen objects was suggested to us by Duff (1992). We found that several objects had unusually low RCS's and that this was correlated with type of orbit. Therefore we analysed the data by orbit groups with the results seen in table 2. Only group D (with 83 deg inclinations and moderate eccentricity) and group E (two objects in unique orbits) gave mean RCS's near the

expected value. Subsequently, Johnson (1993) offered his opinion that only group D can be trusted to be two-meter spheres.

The group D data in figure 2 lends confirmation to the overall pattern of time changes in the RCS's but, in view of the fact that the standard errors divided by the means run roughly twice as large as those for the US calibration spheres, we have given no weight to these objects in forming calibration factors. The data given in table 4 is offered mainly as information to those who may be tempted in the future to use any of these objects for calibration.

Group A is especially notable in that it contains the anomalously small objects - all having about 0.6 times the expected cross section. The fact that all four objects in this orbit group share the anomaly strongly suggests that they are a distinct group with different physical characteristics. Whether this indicates a smaller size or low-reflecting surface material is a matter of conjecture.

At first it was suspected that the differences between the groups might be ionospheric effects but no consistent pattern to support this concept is evident.

#### References

Badhwar, G.D. and Anz-Meador, P.D., 'Determination of the Area and Mass Distribution of Orbital Debris Fragments', Earth, Moon, and Planets 45, 29-51, 1989.

Baker, G., private communication, 1993.

Burns, W.S., 'AN/FPS-85 Radar Cross-Section Calibration', Lincoln Laboratory Project Report STK-150, 1990.

Gaposchkin, E.M., and Sridharan, R., 'FPS-85: A Radar That Refuses To Die', 1988 Space Surveillance Workshop, MIT Lincoln Laboratory, Boston, MA., 1988.

Johnson, N.L., private communication, 1993.

King-Hele, D.G., Walker, D.M.C., Winterbottom, A.M., Pilkington, J.A., Hiller, H., and Perry, G.E., The R.A.E. Table of Earth Satellites 1957-1989, The Royal Aerospace Establishment, Farnborough, Hants, England, 1990.

Duff, G., private communication, 1992.

Stansbery, E.G., Pitts, C.C., Bohannon, G., Zechar, C., Tracy, T. and Stanley J.F., 'Size and Orbit Analysis of Orbital Debris Data Collected Using the Haystack Radar', JSC-25245, NASA, 1991.

Table 1. Data for US calibration spheres.

SATNO	NAME	DIAM (M)	CROSS SECTION*			ERR OF MEAN	NR	INCL	APHT	PERHT
			GEOM	ADJ	MEAN					
900	CALSPHERE 1	0.36	0.102	0.039	0.037	0.002	23	90.0	1050	1015
902	CALSPHERE 2	0.36	0.102	0.039	0.039	0.002	17	90.0	1075	1051
1361	LCS 1	1.13	1.003	0.822	0.858	0.048	28	32.1	2803	2778
1520	CALSPHERE 4A	0.36	0.102	0.039	0.036	0.002	22	90.0	1182	1078
2909	SURCAL 1508	0.41	0.132	0.074	0.064	0.005	16	70.0	863	855
5398	LCS 4	1.13	1.003	0.822	0.780	0.025	36	87.6	880	771

\* Cross sections are in square meters. GEOM gives the geometrical cross section; ADJ gives the cross section adjusted for scattering coefficient; MEAN is the mean of the monthly values after correction for the calibration factors given in table 6.

Table 2. Data for Cosmos objects originally thought to be two-meter spheres.

GROUP	SATNO	NAME	DIAM (M)	CROSS SECTION			ERR OF MEAN	NR	INCL	APHT	PERHT
				GEOM	ADJ	MEAN					
A	10512	COSMOS 967	2.000	3.142	3.006	1.766	0.389	15	65.8	1002	960
	11750	COSMOS 1171	2.000	3.142	3.006	1.979	0.169	19	65.8	1008	963
	12149	COSMOS 1241	2.000	3.142	3.006	1.717	0.175	14	65.8	996	986
	13259	COSMOS 1375	2.000	3.142	3.006	1.632	0.174	20	65.8	1014	976
B	8043	COSMOS 752	2.000	3.142	3.006	3.820	0.277	4	65.8	514	481
	12852	COSMOS 1310	2.000	3.142	3.006	4.041	0.371	6	65.8	411	377
	13750	COSMOS 1427	2.000	3.142	3.006	3.442	0.182	6	65.8	441	412
	14668	COSMOS 1534	2.000	3.142	3.006	3.118	0.301	10	65.8	487	460
C	13033	COSMOS 1333	2.000	3.142	3.006	5.126	0.354	13	82.9	1013	965
	15077	COSMOS 1577	2.000	3.142	3.006	4.872	0.517	12	83.0	1008	954
D	7337	COSMOS 660	2.000	3.142	3.006	3.509	0.232	26	83.0	1725	387
	8744	COSMOS 807	2.000	3.142	3.006	3.913	0.306	31	82.9	1748	387
	11796	COSMOS 1179	2.000	3.142	3.006	3.712	0.611	20	82.9	778	270
	12138	COSMOS 1238	2.000	3.142	3.006	3.795	0.714	16	83.0	1858	399
	12388	COSMOS 1263	2.000	3.142	3.006	2.869	0.257	11	83.0	1862	390
	14075	COSMOS 1463	2.000	3.142	3.006	2.747	0.272	11	82.9	1346	298
	14483	COSMOS 1508	2.000	3.142	3.006	3.242	0.364	8	82.9	1932	394
E	15080	COSMOS 1578	2.000	3.142	3.006	3.417	0.432	9	50.7	1485	293
	17042	COSMOS 1786	2.000	3.142	3.006	2.913	0.139	2	64.9	2562	189

Table 3. Month-by-month RCS statistics for US calibration spheres.

OBS	YR	TRCS	NR	MNMON	STDMON	ERRMEAN	MIN	MAX
1	1977.13	0.039	6	1.21827	0.288723	0.117871	0.81795	1.51795
2	1978.13	0.039	6	1.08542	0.219468	0.089597	0.93443	1.52051
3	1980.13	0.039	6	0.76434	0.048866	0.019949	0.69343	0.81351
4	1980.96	0.039	5	1.17057	0.524555	0.234588	0.63784	1.99574
5	1981.04	0.822	1	1.27664	.	.	1.27664	1.27664
6	1981.13	0.039	3	1.23061	0.299216	0.172752	0.97336	1.55897
7	1981.29	0.822	2	1.08321	0.225552	0.159489	0.92372	1.24270
8	1981.54	0.039	2	1.21225	0.091469	0.064678	1.14757	1.27692
9	1981.71	0.822	1	1.18418	.	.	1.18418	1.18418
10	1982.13	0.039	4	0.98225	0.206328	0.103164	0.78462	1.26667
11	1982.29	0.039	3	1.14109	0.178447	0.103026	1.00769	1.34380
12	1982.54	0.039	2	1.25827	0.038889	0.027499	1.23077	1.28577
13	1982.79	0.039	3	0.98020	0.085969	0.049634	0.92308	1.07908
14	1983.13	0.039	4	1.01781	0.111374	0.055687	0.87436	1.10769
15	1983.29	0.822	1	1.04307	.	.	1.04307	1.04307
16	1983.71	0.822	3	1.86021	0.451179	0.260488	1.36154	2.24015
17	1983.87	0.039	5	1.68108	0.230129	0.102917	1.29744	1.87798
18	1984.04	0.822	3	1.66193	0.034923	0.020163	1.62202	1.68686
19	1984.29	0.039	3	1.47473	0.286285	0.165287	1.16410	1.72798
20	1984.54	0.039	6	1.72639	0.222162	0.090697	1.40405	1.98718
21	1984.79	0.822	2	1.51715	0.162239	0.114720	1.40243	1.63187
22	1985.13	0.039	5	1.69630	0.220938	0.098807	1.46351	2.01026
23	1986.45	0.039	6	2.15470	0.233905	0.095491	1.97080	2.56410
24	1986.79	0.039	4	1.91653	0.125895	0.062947	1.79487	2.05128
25	1987.45	0.039	5	2.05309	0.300272	0.134286	1.79487	2.56410
26	1988.29	0.039	5	1.80495	0.338087	0.151197	1.53846	2.27494
27	1988.46	0.039	4	1.88331	0.315099	0.157550	1.41119	2.05128
28	1988.54	0.822	2	1.96472	0.352693	0.249392	1.71533	2.21411
29	1988.62	0.822	1	1.58151	.	.	1.58151	1.58151
30	1988.71	0.039	4	1.69989	0.280489	0.140244	1.28205	1.87348
31	1989.45	0.039	4	1.74855	0.704867	0.352434	0.76923	2.30769
32	1989.62	0.039	5	1.51533	0.733896	0.328208	0.81081	2.56410
33	1990.37	0.039	4	1.82805	0.602807	0.301403	0.94595	2.30769
34	1990.45	0.039	6	2.15417	0.368266	0.150344	1.79487	2.74939
35	1990.54	0.039	5	1.05313	0.455826	0.203852	0.51282	1.62162
36	1990.96	0.039	5	0.57511	0.437021	0.195442	0.25641	1.15572
37	1991.79	0.039	6	0.96712	0.063859	0.026070	0.86703	1.04615



Table 4. Month-by-month RCS statistics for Cosmos objects originally thought to be two-meter spheres.

QBS	YR	TRCS	NR	MNMON	STDMON	ERRMEAN	MIN	MAX
1	1977.13	3.01	2	1.40870	0.01518	0.010731	1.39797	1.41944
2	1978.13	3.01	2	1.28902	0.33126	0.234236	1.05478	1.52326
3	1980.13	3.01	2	0.70635	0.17530	0.123953	0.58239	0.83030
4	1980.96	3.01	3	1.16550	0.16134	0.093150	1.02156	1.33990
5	1981.13	3.01	2	1.76131	0.92138	0.651512	1.10980	2.41282
6	1981.29	3.01	3	1.31176	0.27871	0.160912	1.13289	1.63289
7	1981.54	3.01	5	1.41592	0.13204	0.059052	1.28159	1.56163
8	1981.71	3.01	1	1.26831	.	.	1.26831	1.26831
9	1982.13	3.01	4	1.21548	0.43460	0.217301	0.89243	1.85329
10	1982.29	3.01	2	1.24640	0.01041	0.007359	1.23904	1.25375
11	1982.54	3.01	3	2.16095	0.78643	0.454048	1.32508	2.88625
12	1982.79	3.01	1	1.45894	.	.	1.45894	1.45894
13	1983.13	3.01	2	1.36214	0.33366	0.235930	1.12621	1.59807
14	1983.29	3.01	1	0.97236	.	.	0.97236	0.97236
15	1983.71	3.01	4	2.45026	0.34693	0.173465	2.16110	2.94854
16	1983.87	3.01	2	2.40133	1.09143	0.771761	1.62957	3.17309
17	1984.04	3.01	2	2.07952	0.22743	0.160814	1.91870	2.24033
18	1984.29	3.01	2	1.69844	0.26363	0.186412	1.51203	1.88485
19	1984.54	3.01	1	2.98502	.	.	2.98502	2.98502
20	1984.79	3.01	1	2.63140	.	.	2.63140	2.63140
21	1985.13	3.01	2	2.08874	0.55375	0.391561	1.69718	2.48030
22	1986.45	3.01	6	1.95903	0.57917	0.236447	1.11296	2.63787
23	1987.45	3.01	3	2.02436	0.24844	0.143440	1.73754	2.17276
24	1988.29	3.01	7	1.66540	0.30178	0.114061	1.27243	2.02326
25	1988.46	3.01	4	1.82309	0.43408	0.217040	1.29900	2.35216
26	1988.54	3.01	3	1.86047	0.74266	0.428777	1.12625	2.61130
27	1988.62	3.01	2	1.95349	0.16914	0.119601	1.83389	2.07309
28	1988.71	3.01	3	1.78738	0.37053	0.213927	1.36545	2.05980
29	1989.45	3.01	5	1.81329	0.48807	0.218271	1.20930	2.35548
30	1989.62	3.01	5	2.32226	0.34897	0.156065	1.83056	2.75415
31	1990.37	3.01	6	1.88040	0.70197	0.286577	0.87375	2.55482
32	1990.45	3.01	3	2.00332	0.73547	0.424626	1.19269	2.62791
33	1990.54	3.01	6	1.05703	0.54217	0.221341	0.39867	1.79734
34	1990.96	3.01	6	0.77243	0.50728	0.207097	0.31229	1.61130
35	1991.45	3.01	6	0.99169	0.15051	0.061444	0.86047	1.22259
36	1991.79	3.01	6	0.99157	0.28713	0.117220	0.49777	1.28299

Table 5. Month-by-month RCS statistics for 352 eight-balls.

OBS	YR	TRCS	NR	MNMON	STDMON	ERRMEAN	MIN	MAX
1	1977.13	0.7	128	1.31027	0.44111	0.038989	0.41129	2.98486
2	1978.13	0.7	138	1.07227	0.40025	0.034072	0.28500	3.15471
3	1980.13	0.7	164	0.80412	0.25582	0.019976	0.11171	1.72757
4	1980.90	0.7	142	1.17904	0.45440	0.038133	0.26000	3.71186
5	1981.04	0.7	20	1.64043	0.79588	0.177963	0.69114	3.56929
6	1981.13	0.7	28	1.43398	0.78769	0.148860	0.29329	4.94671
7	1981.29	0.7	59	1.34514	0.61128	0.079582	0.17900	3.24886
8	1981.54	0.7	55	1.26461	0.63722	0.085923	0.18543	4.14586
9	1981.71	0.7	15	1.51196	0.54087	0.139653	0.46229	2.86643
10	1982.13	0.7	76	1.34510	0.66870	0.076705	0.19671	3.40614
11	1982.29	0.7	46	1.55373	0.90667	0.133681	0.14671	4.92529
12	1982.54	0.7	156	1.56201	0.69619	0.055740	0.10357	3.70671
13	1982.79	0.7	98	1.28387	0.60116	0.060727	0.23714	3.23971
14	1983.13	0.7	118	1.33983	0.56404	0.051924	0.21814	3.28886
15	1983.29	0.7	18	1.81944	0.63537	0.149759	0.45800	2.74500
16	1983.71	0.7	148	2.24352	1.14620	0.094217	0.31743	6.91714
17	1983.79	0.7	32	2.28895	1.11352	0.196845	0.35500	5.30986
18	1983.87	0.7	117	2.17499	0.87987	0.081344	0.49943	5.34314
19	1984.04	0.7	80	2.21516	1.13959	0.127410	0.26129	5.41914
20	1984.29	0.7	125	2.02672	0.98411	0.088022	0.21186	6.30600
21	1984.54	0.7	164	2.18091	1.04423	0.081541	0.34171	5.81171
22	1984.79	0.7	152	1.99760	1.04924	0.085105	0.52057	8.28700
23	1985.13	0.7	161	1.90545	0.92504	0.072903	0.24771	7.89557
24	1986.45	0.7	302	2.04844	0.98036	0.056413	0.30000	7.00000
25	1986.62	0.7	143	1.90424	0.83700	0.069994	0.77443	7.00014
26	1986.79	0.7	300	2.03586	0.95190	0.054958	0.60000	6.65714
27	1987.20	0.7	8	0.85000	0.76253	0.269596	0.44286	2.28571
28	1987.45	0.7	168	2.13257	0.91216	0.070375	0.50000	6.70000
29	1988.29	0.7	213	1.82475	0.61997	0.042480	0.44286	6.07143
30	1988.40	0.7	143	1.99610	0.79957	0.066864	0.31429	4.34286
31	1988.54	0.7	54	1.98677	0.78962	0.107453	0.34286	4.12857
32	1988.62	0.7	49	2.10787	0.82877	0.118396	0.48571	4.81429
33	1988.71	0.7	69	2.04348	0.80009	0.096320	0.90000	5.47143
34	1988.96	0.7	7	2.02245	0.57285	0.216516	1.27143	2.71429
35	1989.45	0.7	290	1.95429	0.97717	0.057381	0.21429	6.60000
36	1989.62	0.7	208	1.95405	0.97306	0.067470	0.22857	6.34286
37	1990.37	0.7	334	1.89880	0.92350	0.050532	0.18571	5.22857
38	1990.45	0.7	181	1.99400	1.07061	0.079578	0.34286	6.42857
39	1990.60	0.7	338	1.01378	0.55762	0.030330	0.10000	3.18571
40	1990.96	0.7	332	0.62844	0.38033	0.020873	0.11429	2.22857
41	1991.45	0.7	351	0.96085	0.34978	0.018670	0.15714	2.14286
42	1991.79	0.7	351	0.95649	0.35764	0.019089	0.10614	3.66429

Table 6. Adopted monthly calibration factors.

Date	Calibration Quot.	Factor
1977.126	1.30	0.769
1978.126	1.05	0.952
1980.126	0.75	1.333
1980.956	1.10	0.909
1981.000		
to	1.25	0.800
1985.500		
to	1.90	0.526
1990.500		
1990.537	1.00	1.000
1990.956	0.55	1.818
1991.454	1.00	1.000
1991.788	1.00	1.000

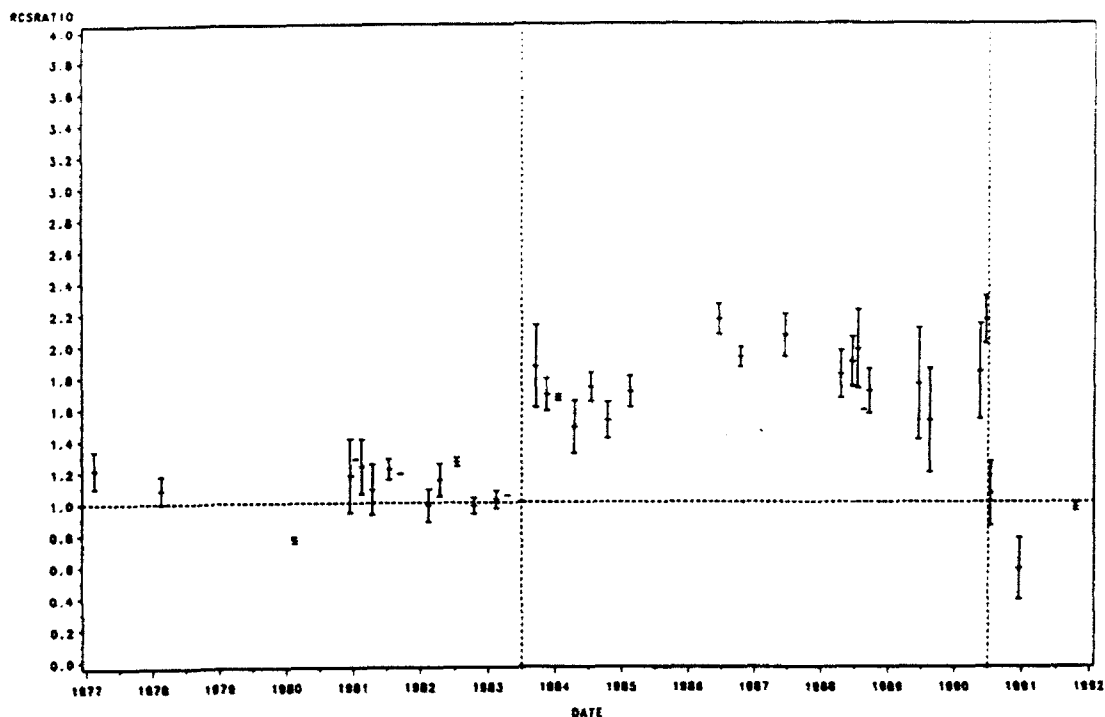


Figure 1. Monthly mean values of normalized RCS (RCSRATIO) vs. date for six USA calibration spheres. Data for each satellite is normalized by dividing the published RCS by the "expected" cross section (see text). Error bars depict the standard error of the mean at each date. Vertical dotted lines designate dates at which known calibration adjustments took place.

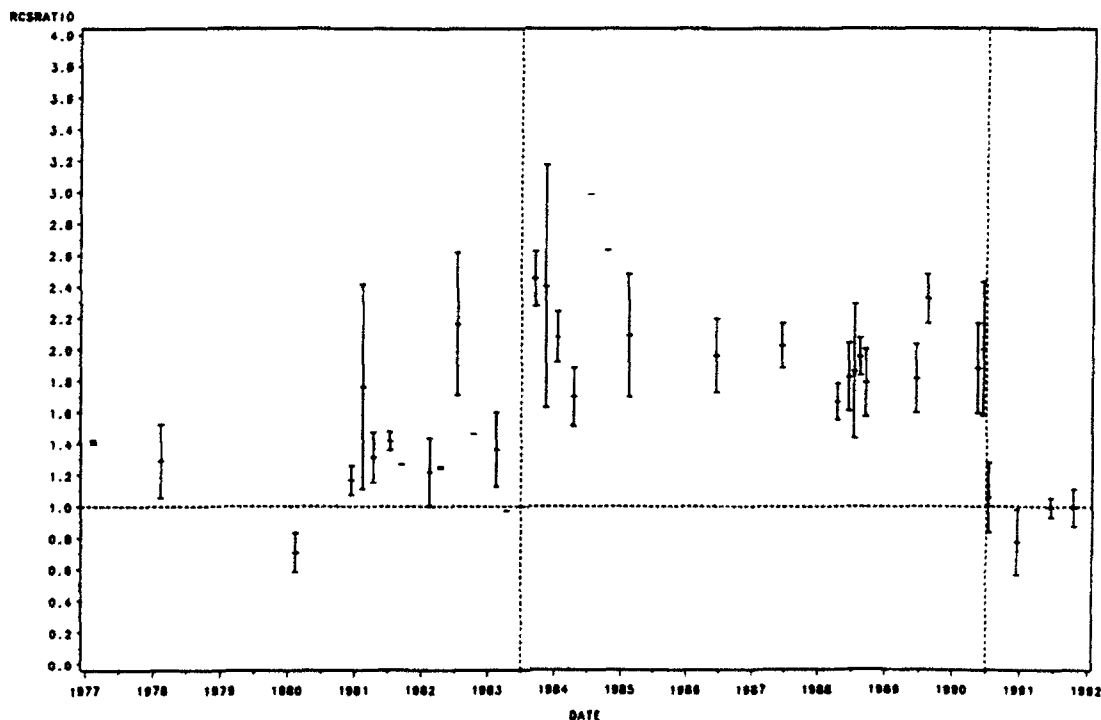


Figure 2. Monthly mean values of normalized RCS (RCSRATIO) vs. date for the seven USSR two-meter spheres in group D of table 2. RCS is normalized by dividing by 3.01, the expected RCS for a two-meter perfectly conducting sphere.

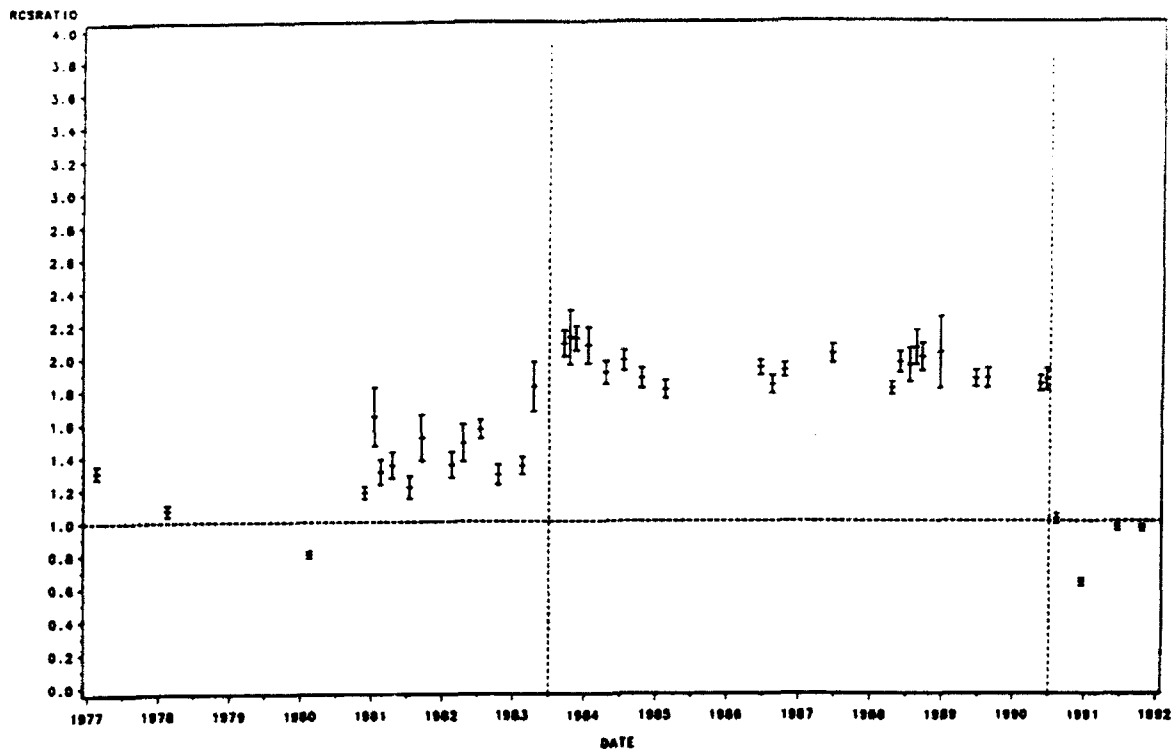


Figure 3. Monthly mean values of normalized RCS (RCSRATIO) vs. date for 352 Cosmos eight-balls. RCS is normalized by dividing by 0.70, the estimated eight-ball cross section.

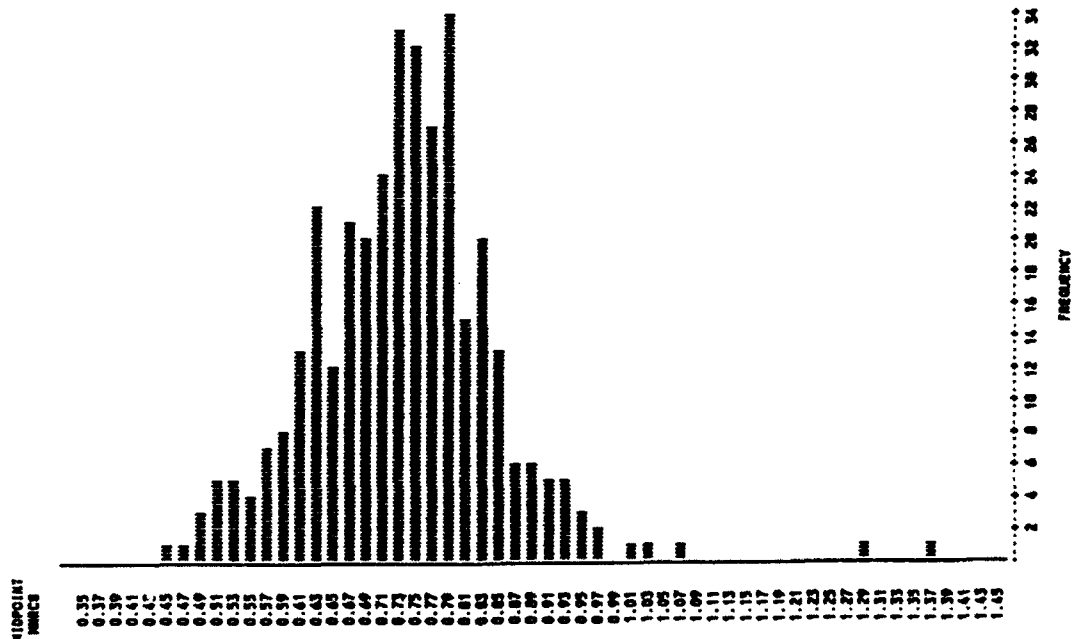


Figure 4. The distribution of eight-ball mean RCS's. The mean for each object is the mean for all monthly values for the object after multiplication by the factors in table 6. The median value lies at 0.74 square meters - slightly larger than the adopted "expected" value of 0.70.

# Debris Correlation Using the Rockwell WorldView Simulation System

M. F. Abernathy, J. Houchard, M.G. Puccetti (Rockwell Power Systems)  
and J. V. Lambert (Rockwell Space Systems Division)

## Introduction.

This paper describes the use of sky simulation tool to facilitate the tracking and categorization of candidate debris objects. One of the problems in cataloging space debris is separating it from the myriad of non-debris objects visible to observatories. In addition to the distraction of celestial bodies, some several thousand objects orbit the planet. This paper describes how the sky simulator (Rockwell WorldView) is used to provide a video overlay to assist human operators in correlating known versus unknown space objects (debris). The methods employed in developing the simulator are described, along with validation procedures. We will present video showing the system in operation producing correlation overlays in real time.

## Rockwell WorldView

The simulation tool used for this work is Rockwell WorldView, an observatory simulation program. This 3 dimensional geometric simulation tool uses star catalogs (such as Yale Bright Star and Astrographic Catalog Reference Stars), and the NORAD space object catalogs to compute the sky as seen from a particular sensors field of view, for a given set of mount pointing angles at a particular site location and time. The user may set these parameters and may select which space objects are used from the catalogs, and may select stars by catalog and by maximum visual magnitude. By overlaying the simulated sky (including stars and predicted satellite tracks) on the video from telescope cameras, operators may distinguish unexpected objects by tagging these objects and handing them over to a tracking telescope. Figure 1 shows a schematic diagram of the system. Unlike traditional simulations Rockwell WorldView incorporates pointing data and video from mounts which in turn drives the simulated star field and

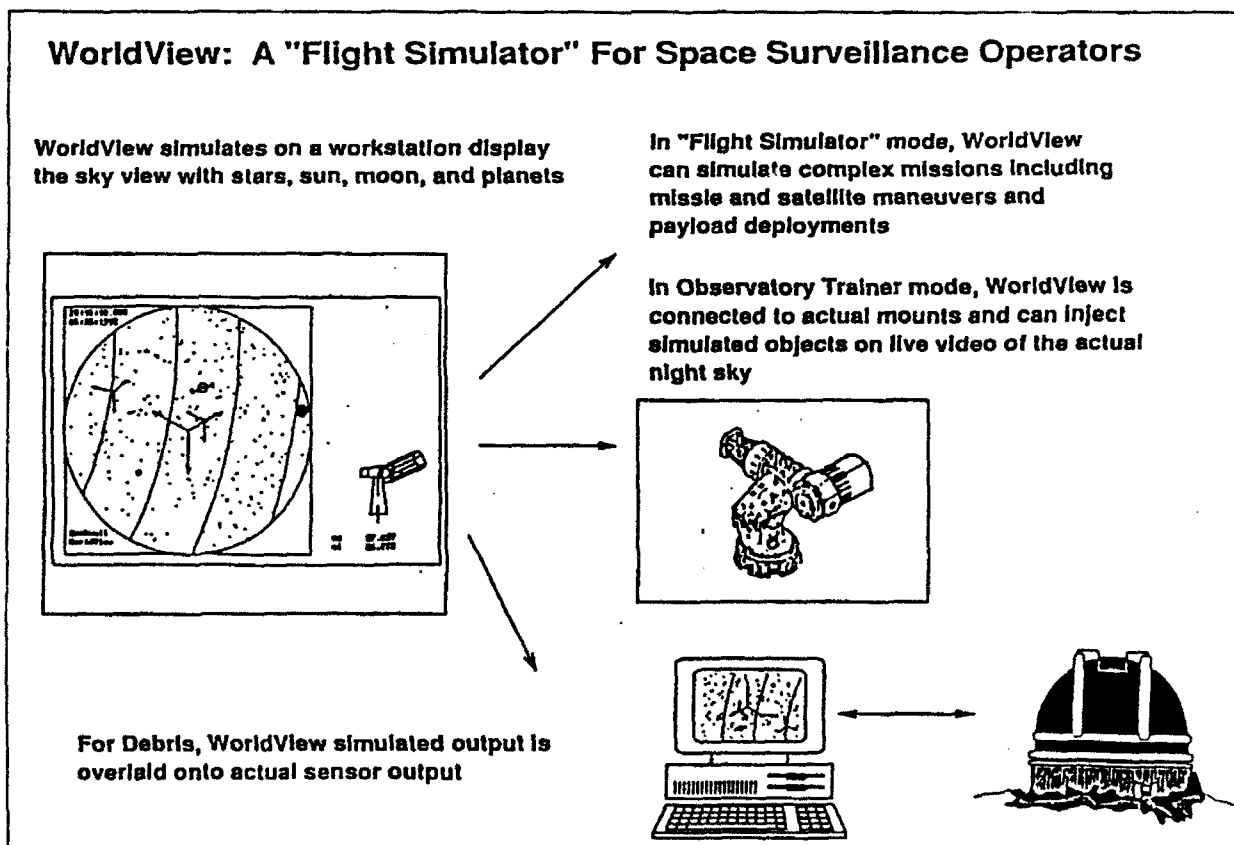


Figure 1 Overview of the Rockwell WorldView System.

satellite track overlay in real time. The result is a real-time video display containing real sky imagery with an overlay that moves with the telescopes.

Figure 2 shows a typical Rockwell WorldView console. Annotated by time information at upper left, the simulated sky view from the focal plane contains all 3d rotations induced by mount movement. Stars and other celestial objects are seen in the background, along with lines of constant declination to aid user orientation. Stars may be selected from several star catalogs, and may be limited according to minimum brightness, if needed. The satellites in this particular mode are represented as axis triplets showing velocity vector, object local nadir, and an axis normal to the direction of travel. (For debris missions objects are represented as with sky tracks that show the path of the expected satellites over time.) In the lower left corner mount pointing angles are given in degrees, and a 3d wireframe of the telescope (as viewed from due south of the mount) provides the user a graphical representation of the pointing information.

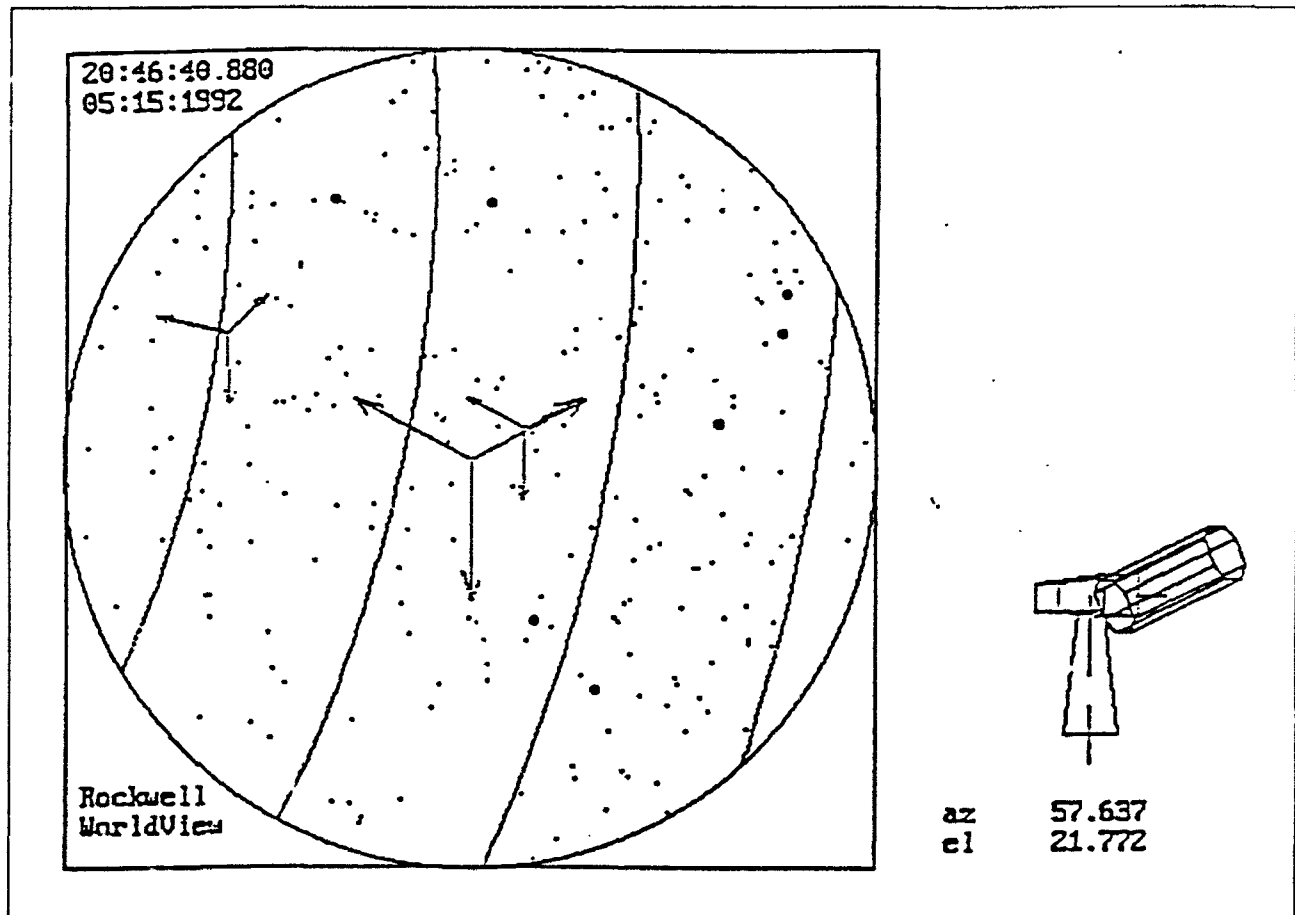


Figure 2 Typical Rockwell WorldView Console Screen.

WorldView simulates geometric views of the celestial sphere and near earth space at the focal plane of a telescope. It calculates the position of natural celestial objects (stars, sun, moon, planets) and artificial satellite vehicles as viewed from specific sites and sensors. These calculations are based on star field databases, ephemeris calculations for the planets and two-body propagators for the requested satellites. Each satellite requires only a single position and velocity state vector. Given a time frame, WorldView can simulate the user configured scenario for actual or planned missions and display a graphical output. WorldView is written in C++ using object oriented programming techniques and is based on a general purpose, three dimensional object library where a master coordinate system is created and an unlimited number of local coordinate systems are produced to render the desired view. This allows WorldView to easily simulate complex telescopes, mounts, viewing conditions, and satellites.

Using a secondary process and a shared memory table, WorldView can be connected to a physical telescope using actual encoder information. In this way, mount control systems and operator response can be tested before the actual mission takes place. The site mount control system will control the telescope and WorldView will generate the appropriate space scene using the actual mount angles. The design allows multiple sensor output on different telescopes to be simulated simultaneously. In this mode the live video from the camera may be overlaid by the simulated skyview, and the telescope pointing angles are derived from the real rather than simulated telescope.

Other analytical capabilities have allowed WorldView to be used to design satellite missions.

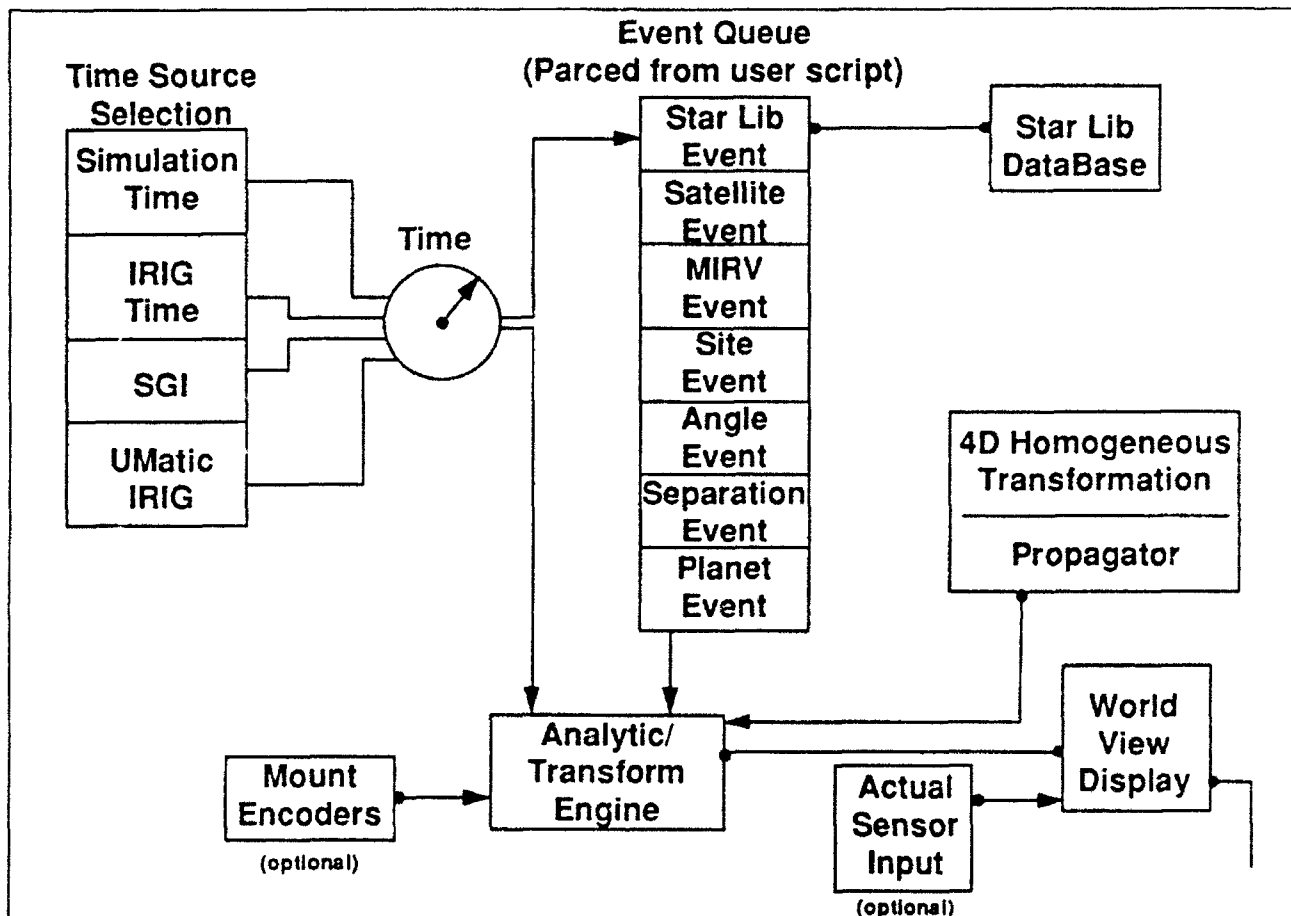


Figure 3 Rockwell WorldView Object-Oriented Design.

## Simulation Methodology

WorldView is an event driven simulation tool driven by a Gregorian calendar with a user selected time step. As the software runs, events are queued and when proper conditions are met an event is executed (see Figure 3). During a typical Worldview simulation, a user may request some satellite action at a specific time or position. For many events, the actual time or position is determined dynamically using current conditions of the simulation. In order to simulate this, earth rotation, satellite motion and satellite interactions are taken into account at each step. For such user specified events, range separation, slant range, telescope position, type of mount and sensor field of view dictates the final graphical output. Tabular information is also produced for each simulation time step. Graphical could, for example, include a series of images illustrating the stars, sun, moon, planets, and satellites of interest as viewed from a given telescope (e.g. AMOS/MOTIF 1.6M at MSSS). The initial conditions of the simulation and the desired graphical output is configured by the user.

WorldView has been developed for both the Personal Computer/DOS and Unix/XWindow based platforms. The PC/DOS version requires the user scenario to be input through an ASCII file while the XWindow version will have a more sophisticated graphical interface.

The following event types are currently supported in the user script language:

#### SATELLITE\_LAUNCH\_EVENT

Defines a new satellite or missile using a state vector.

#### SATELLITE\_MIRV\_EVENT

Ejects a secondary vehicle from a parent satellite or missile with at a user specified time and velocity vector in the defined satellite reference frame.

#### SATELLITE\_MIRV\_EL\_EVENT

Same as a SATELLITE\_MIRV\_EVENT except the user does not enter the time of ejection but instead the topocentric elevation of the current site. The simulation will thus determine the ejection time relative to the input elevation.

#### SATELLITE\_TRACK\_EVENT

At the user requested time, the simulation telescope will be pointed at the requested satellite or missile. Until the next SATELLITE\_TRACK\_EVENT or TELESCOPE\_EVENT the simulation view will follow the object. All other simulated object positions will be calculated from this moving view.

#### SATELLITE\_TRACE\_EVENT

At the user requested time, a trace of where the satellite has been or will be is displayed. The start time and stop times of the trace are selected by the user.

#### SATELLITE\_MIGRATION\_EVENT

Allows a satellite to migrate with a linear velocity from its current position to intercept another satellite.

#### SATELLITE\_ORIENT\_EVENT

Orients the satellites or missile frame with a 3X3 earth centered inertial reference matrix.

#### SATELLITE\_MANEUVER\_EVENT

At the user specified time the requested satellite or missile will undergo a roll or pitch or yaw maneuver.

#### TELESCOPE\_EVENT

Allows the user to enable or select a new type of telescope at the given time. Az/Pol/Dec, Az/El, and RA/DEC mounts are currently simulated. Once the type of telescope is selected the simulated view is that of the selected telescope. If requested, a small model of the telescope is displayed next to the simulated view.

#### DISPLAY\_TALO\_EVENT

Useful primarily for missile tests, this event will display the Time (in seconds) After LiftOff on the simulated view.

#### STARPLOTTER\_EVENT

At the user requested time and until otherwise requested a star field will appear in the simulated view. This event will determine or change the currently selected magnitude range of the stars displayed. The displayed stars are scaled in size relative to their magnitudes. An option for color coded stars relative to their spectral output is included.

#### PLANETPLOTTER\_EVENT

This event will either enable or disable display of the planets in the selected view.

#### DATALOG\_EVENT

This event will provide tabular output of state vectors, site, telescope, range and events as the simulation progress. This event can be used to selectively record events.



#### MOVIE\_EVENT

For the Personal Computer version this event allows movies of generated simulation frames to be stored for later playback. Workstation class hardware does not require this event since the simulation can be run at real-time rates.

#### CHANGE\_TIMESTEP\_EVENT

Except when slaved to an actual mount, WorldView uses an internal software controlled clock. This event allows the time step to be configured by the user at any time in the simulation. This is important since the simulation objects are calculated a discrete times and events times will be quantized to the selected time step. Increasing the time step will provide faster simulations but greater quantizing error. This event allows the user to reduce the quantizing error if necessary a critical times without significantly slowing the simulation.

#### RANGE\_SEPARATION\_EVENT

The user can select any two missiles/satellites and a range at which this event is to occur. When the simulation detects this range, the current simulation time and other data is stored to the tabular log.

#### ANGLE\_SEPARATION\_EVENT

The user can select any two missiles/satellites and a angle at which this event is to occur. When the simulation detects this angle separation as viewed from the site, the current simulation time and other data is stored to the tabular log.

#### Test Cases: AMOS and Diego Garcia Data

Before the simulation could be used to search debris, it had to be validated using live video and live mount pointing angles. Owing to interfacing issues this was most easily accomplished with the AMOS mounts. A simulated missile engagement was run with 26 simulated targets overlaid against live video from the 1.6 meter mount. The result was that operators acquired and tracked simulated targets using a real telescope in real time (30 frames of video per second). Because WorldView is driven by the telescope pointing angles measured from the encoders, mispointing would cause the target to slip off the video monitor exactly as would an actual target signature. This provided validation of the telescope-in-the-loop concept.

The next step was to apply this to the debris search process, using simulated sky tracks for catalogued objects to permit the operators to separate debris from catalogued objects. The video tape presented includes imagery from a 2 degree field of view telescope located at Diego Garcia. This video also includes a sky simulation image which is color coded and overlaid on the collected video data. This simulation was done on Silicon Graphics 4D/440 computer in real-time. In order to achieve this star-sorting methods, and known-object pre-sorting methods are employed to optimize CPU performance. After configuring the simulation for the mount location, type and sensor field of view to be incorporated, the computer program first searched the catalog for objects appearing in the observation period, and computed sky tracks (which are the traces of the objects path against the celestial sphere).

Next the simulation clock is set to the same time as the start of the video collected, and the video is played at real time into the simulator. Since this particular data is for a staring telescope, real time hook-up was not required and the mount pointing angles were given for a simulated statically pointed telescope. The resultant video (see Figure 4) is shown to the operators. Objects which cross the field of view, without having an apparently similar skytrack are most probably debris. In the video tape shown 2 possible debris events were seen on the raw video, but with overlay it is apparent that they are lay along lines closely parallel to the sky tracks. Thus keeping operators from wasting time on cataloged objects, and permitting them to concentrate on uncorrelated objects. This same method may now easily be applied to live, scanning acquisition telescopes, however, this requires live input of mount pointing angles.

As can be seen in the resultant imagery the approach was successful. Some adjustment of the sensor field of view (FOV) was required, as actual FOV varied from the nominal. As seen in Figure 4 a relatively good alignment between simulated and actual stars was observed. At AMOS, an experiment is planned to allow operators to view on separate monitors the WorldView simulation and the actual sensor data. This is expected to enhance the operators ability to track uncorrelated debris.

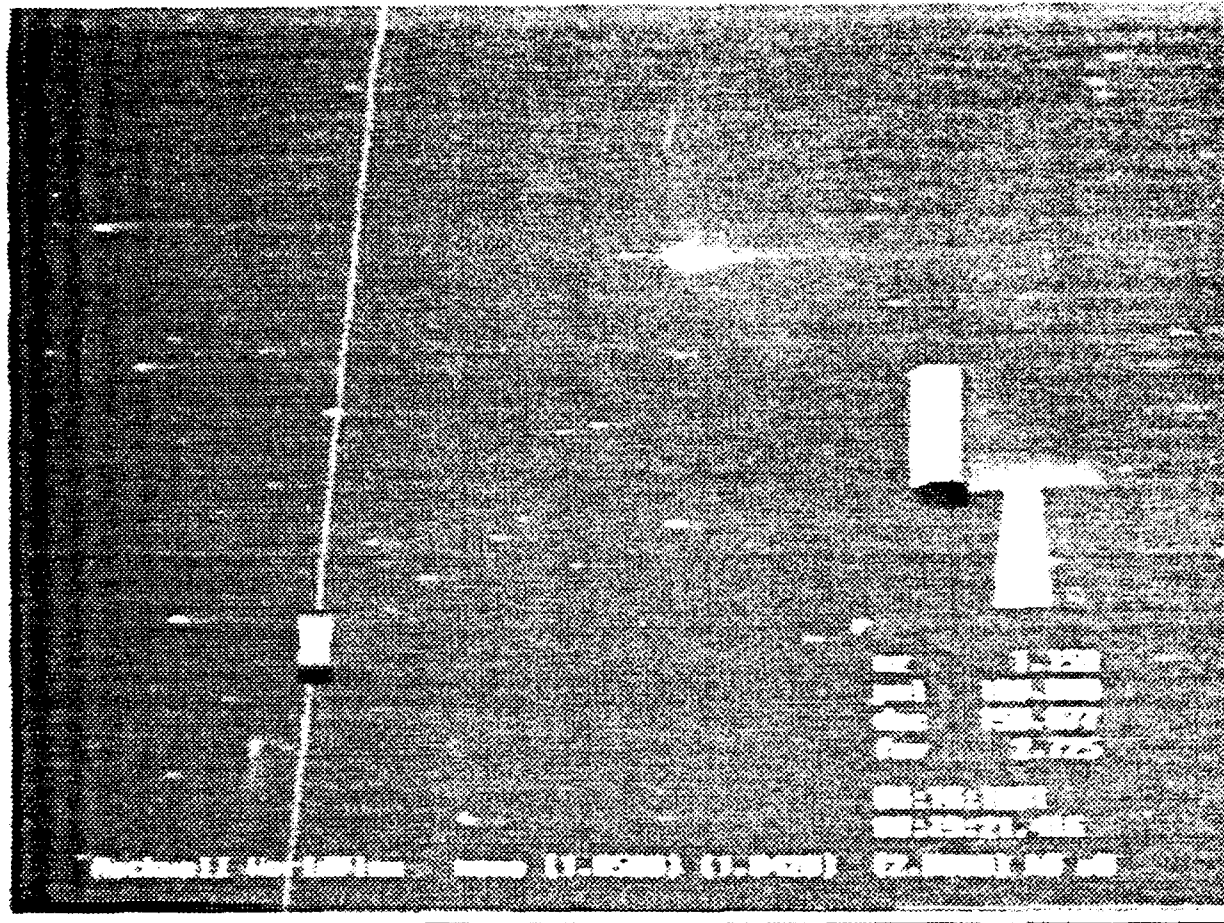


Figure 4 WorldView Console Configured for Debris Tracking

#### Whats Next For WorldView

A full X-Window user interface is currently being implemented which will allow elaborate mission scripts to be generated quite easily

A set of user events will allow mission anomalies to be invoked instantly by test directors

Ties to an SQL database of satellites will be required for debris overlays.

A telescope trace event will allow search patterns to be shown in the field of view

Modeling thrusting targets and/or tabular data input events

A library of 3-dimensional object shapes (missiles, plumes, satellites etc) for use with the simulations

### Summary

Rockwell WorldView has many of the foundational components required to support complex space simulations. The event driven nature of the software and the object-oriented design allows new components to be easily added. Successful testing the simulation with actual mission data and actual telescopes was completed. Many areas of space surveillance including mission planning and debris studies could be supported with this tool. The simulation capability also provides the means to design actual missions. Future work will include a full-featured graphical user interface with a number of display widgets.

When fully developed, WorldView will be enormously beneficial to space surveillance sites. Many missions are preplanned and rehearsed extensively due to the one-time, high cost nature of space surveillance experiments. A geometrically accurate real-time simulation of the mission as viewed from a particular mount/sensor at a particular site is possible with moderate computer processing capabilities.

### Acknowledgements

This project was entirely funded under Rockwell Independent Research and Development. The authors wish to thank Major Brett Smith and Captain D. Kuo, USAF for providing test data for this project. The authors also wish to acknowledge Mr. John Clark of the USAF SPACECOMMAND who conceived of this approach to identifying space debris.

## Orbital Debris Correlation and Analysis at the Air Force Maui Optical Station (AMOS)

*Richard K. Jessop, John Africano, John V. Lambert, Robert Rappold*  
(Rockwell International, Colorado Springs, Colorado)

and

*Robert Medrano, Paul Kervin*  
(Phillips Laboratory, Maui, Hawaii)

and

*Kenneth E. Kissell*  
(Rockwell Power Systems, Maui, Hawaii)

### ABSTRACT

The Air Force Maui Optical Station (AMOS) is conducting searches, measurements, and analyses of orbital debris for the Air Force Phillips Laboratory and Air Force Space Command in support of the Air Force Orbital Debris Measurements Program.

Algorithms and software have been developed for correlation of objects observed on GEODSS video with the Space Command satellite catalogue and with previously observed but uncorrelated objects. The developed algorithms apply gross and fine filters to reduce the number of candidate catalogued objects from further consideration. The software uses an object-oriented approach that closely models the problem/analysis domain and performs analysis verification both at compile time and during run time.

Techniques have also been developed for determining the magnitude or brightness of both correlated and uncorrelated objects using calibration star fields. From the identified (correlated) objects, plots of radar cross section (RCS) versus normalized magnitude are produced. A size may then be assigned to the debris objects assuming that the optical properties of these objects are similar to the optical properties of the correlated objects.

### I. Correlation Software

Ideally, in performing orbital debris correlation each catalogued element set is propagated to an observation time, and its position and velocity vector are compared to the position and velocity of an observation. By correlation, the propagated element set state vector and an observation state vector are within some tolerance of time, position, and velocity. For those element sets that appear to be correlated, a method to verify proper identification is still necessary.

For those element sets/observations that appear to be uncorrelated, there are two possible explanations. First, the observed object is a true uncatalogued object (i.e., an observation was recorded but no element set correlated). Second, the catalogued object should have been in the field of view but was not (i.e., no observation was recorded but element set propagation indicates that there should have been one). In the former explanation, we must be careful that the observation is not of a sensitive (e.g., classified) object. In the latter explanation, we must determine if the object has a maneuvering capability and/or if non-standard environmental forces were present. Element set information can be augmented with a maneuvering capability flag and augmented with the magnitude and duration of that capability. If the observation is of a breakup fragment or true space debris object, drag parameters must be estimated for proper subsequent propagation, and

these newly generated element sets must be included within the current catalog for all subsequent correlation analyses.

In reality, the previous process description is computationally expensive and therefore takes a greater amount of time than may be available to an analyst in an operational environment. Propagation of every element set is a brute force method and still may result in incorrect correlations or uncorrelations, and missed correlations. Propagation also assumes ballistic movement by the satellite and a nominal orbital environment. Although this problem is alleviated somewhat by having the most current element set possible, this may not be operationally feasible.

As a result, filters must be applied in order to reduce the number of candidate element sets propagated. Extensions to the current data formats must be designed and should be easily implemented within the existing architecture. Finally, since new analysis techniques are being developed, validity checks must be added to ensure quality. These topics will be discussed in the next several sections.

The filters can be classified into two types: gross and fine. The objective of the gross filters is to reduce the number of candidate element sets considered based solely on their orbital parameters or at most one propagation. The objective of the fine filters is to again reduce the number of candidate element sets by propagation but by avoiding any coordinate system transformations. The final correlation process involves propagation, coordinate system transformations, and proximity determinations.

The first gross filter applied involves the angular momentum vector of the element set object and the sensor position vector at the time of the observation. The candidate element set is propagated once sometime between the observation start and stop times. The angular momentum vector is calculated from the position and velocity vectors. The site position vector is calculated and is dotted with the angular momentum vector. The complement of this angle is calculated in order to determine the angle between the plane of the orbit and the site position vector. The apogee distance is then calculated. Using these quantities and the law of cosines, an angle is calculated between the site's horizon plane and the element set orbital plane out to apogee to determine whether or not the element set object at apogee can be viewed from the site, see Figure 1. There are two drawbacks to this approach: it requires the previously described algorithm to be applied to every element set, and all of the very high altitude satellites will always pass this filter.

The second gross filter applied involves how the selection query submitted to the data repository is generated. Since the data repository is a relational database, the query must be based on actual stored fields. The problem involves what ranges of values should be used on the various fields. The two fields used are inclination and altitude. The estimated orbital inclination of the observed debris object is first calculated using a circular orbit assumption. A reference database of 54 previously correlated observations consisted of the circular orbit parameters and the "true" parameters derived from the correlated element set. A linear least squares regression of the "true" inclination showed a high degree of correlation. A least squares forecast is used as a point prediction of the "true" inclination and then a 95% confidence interval is constructed about this inclination prediction. The confidence interval boundary constitutes the range of values to be used in the inclination query.

In a similar manner, the estimated orbital altitude of the observed debris object is first calculated using a circular orbit assumption. Depending on the eccentricity of the object's orbit, the estimated altitude may contain significant errors, however. A reference database of 50 previously correlated observations served as the basis for the error

analysis. Each of the 50 debris objects was propagated one full orbit with an altitude analysis at one minute intervals along the path. At each interval, the "true" orbital altitude was calculated along with the estimated altitude derived from the circular orbit algorithm. Next, the average altitude error for one full revolution was calculated for each of the 50 correlated objects. A linear least squares regression of the average altitude error on the orbital eccentricity again showed a high degree of correlation. The orbital eccentricity of a candidate correlate's element set is retrieved and used to calculate a point prediction for the average altitude error. A 95% confidence interval is constructed about this altitude prediction. The confidence interval boundary constitutes the range of values to be used in the altitude query.

Two fine filters are then applied to the element sets surviving the gross filters. The first fine filter simply determines if the propagated position vector has broken the horizon plane. If the dot product of the earth-centered site vector and the propagated satellite position vector is greater than one earth radii, then the propagated object is above the site's horizon. The second fine filter applied checks to see whether or not the element set object is in sunlight. This could account for the problem of no observation recorded but element set propagation implying there should have been one.

The extendibility of the data formats results from the use of a relational database management system (RDBMS). An RDBMS allows a developer to create new data formats and/or modify existing data formats with little to no effect on data already contained in the database. For example, the first database constructed obviously contained all of the fields of the standard 2-card element set. However, this information is not complete with regard to debris correlation processing and required task results. Some of the missing information includes the ability of a catalogued object to maneuver, dynamic, optical, and radar characteristics, as well as information that can be computed from the standard fields such as perigee and apogee altitudes, semimajor axis, and period. There may very well be additional information that requires storage that have not yet been anticipated. These fields can either be added to the existing database tables or new tables can be created. No information is lost if new tables are created and only one field (a unique identifier, the satellite number) needs to be duplicated. Access of the data is made through an industry standard query language either through a utility that comes prepackaged with the database or through any programming language.

Data storage as well as queries can be optimized as needs dictate. For example, since queries are generated specifically on the inclination and altitude, high speed access indices can be set on these fields. This allows orders of magnitude performance improvement as compared to accessing raw data file formats. There are other advantages of using an RDBMS that will not be elaborated upon. The reader is encouraged to consult any database textbook that describes this technology.

Validity checking of the software is implemented by the insertion of numerous assertion statements and by the introduction of a dimensional data type. An assertion statement is a combination of a conditional and a termination statement. If the condition is not met, a serious problem is implied to have occurred, and program execution terminated. The conditions insure that assumptions about specific values are correct. If these values are not in the expected range, then a statement is output to the user/developer explaining the failed condition and the exact location in the code of the error. This allows the developer to remedy the defect as efficiently as possible. A dimensional data type allows the programmer to work in units of length, time, angle, and other dimensions. These units are independent of unit of measure.

## II. Optical Brightness Determination and Analysis

The basic goals of the photometric calibration or the determination of the equivalent V (visual) magnitude or optical brightness for objects detected on the GEODSS video tape is to estimate the V magnitude of the object, relating this to object size, and determine the limiting magnitude for each tape to normalize the detection rates for calculation of the debris population.

The techniques developed for determining the V magnitude from the video tapes are similar to the techniques used in photographic photometry. The basic assumption is that equal intensities produce equal video effects under similar conditions. Calibration star fields containing stars with photoelectrically determined V magnitudes, are observed at the beginning and/or end of each GEODSS video tape. An intensity in volts is measured for each calibration star in the calibration field using a Colorado Video Integrator and Display Unit. A calibration curve for each video tape is produced. A typical calibration curve is shown in Figure 2, which is a plot of voltage versus V magnitude. The voltages for uncorrelated as well as the correlated objects are then referenced to the calibration curve for brightness determination.

The results from fourteen hours of observations are now presented. During this period 76 objects were detected of which 48 (or 63%) were correlated. We have determined the V magnitude for all of the objects and plotted their normalized magnitude (magnitude of the object at a range of 1000 km) against the radar cross section (RCS) for each correlated object (filled circles) in Figure 3. The uncorrelated objects are plotted as open triangles and arbitrarily assigned an RCS of  $-2$ . The two dotted lines are where specular spheres would lie if they had albedo's of 1.0 (lower dotted line) or .08 (upper dotted line). Finally the solid line is the least squares line fit to the correlated data. Note that the smallest correlated object has an RCS corresponding to a diameter of about 8 cm.

While this is a very limited data set, a couple of interesting results are suggested by Figure 3. The slope of the least squares line fit suggests that the larger RCS objects may have a higher albedo than objects having smaller RCS's. There are also some very bright uncorrelated objects. If these objects behave like the correlated objects then they are fairly large (several meters!) yet are uncatalogued by radars.

## III. Summary

Because of the operational requirements of the correlation software, methods other than brute force are required. This paper described various process filtering techniques, data design and implementation techniques, and software development approaches that contributed to make the orbital debris correlation process operationally viable.

Preliminary analysis of a very limited sample of GEODSS video tapes indicate that there may be some large pieces of space debris which are uncatalogued by the radars. There is also an indication that the smaller pieces of debris have a smaller albedo than larger pieces.

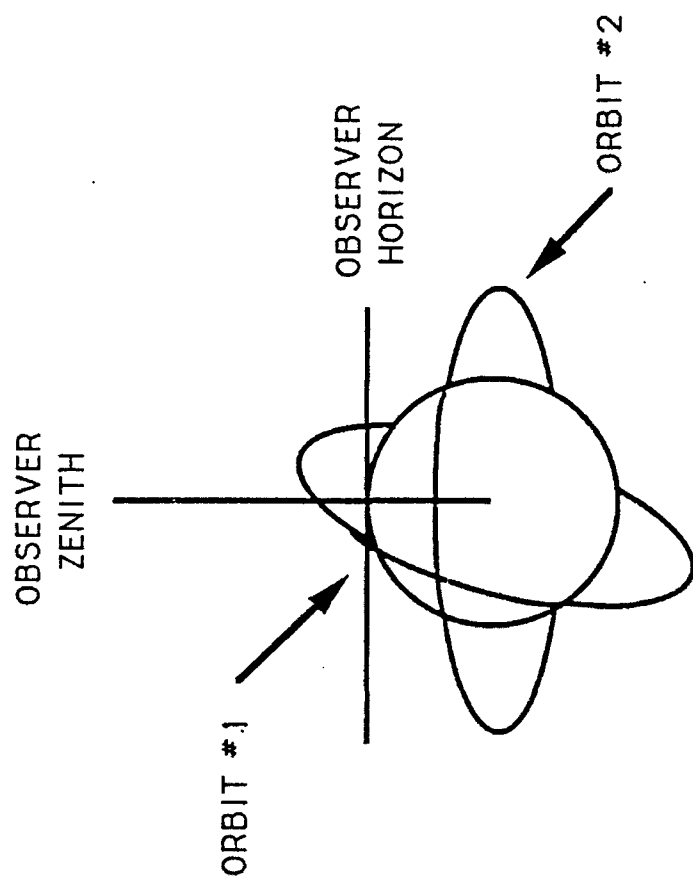


FIGURE 1: ORBIT HORIZON BREAK TEST. (Orbit #1 passes horizon test; Orbit #2 fails horizon test and is eliminated from further consideration.)



FIGURE 2: VIDEO CALIBRATION CURVE

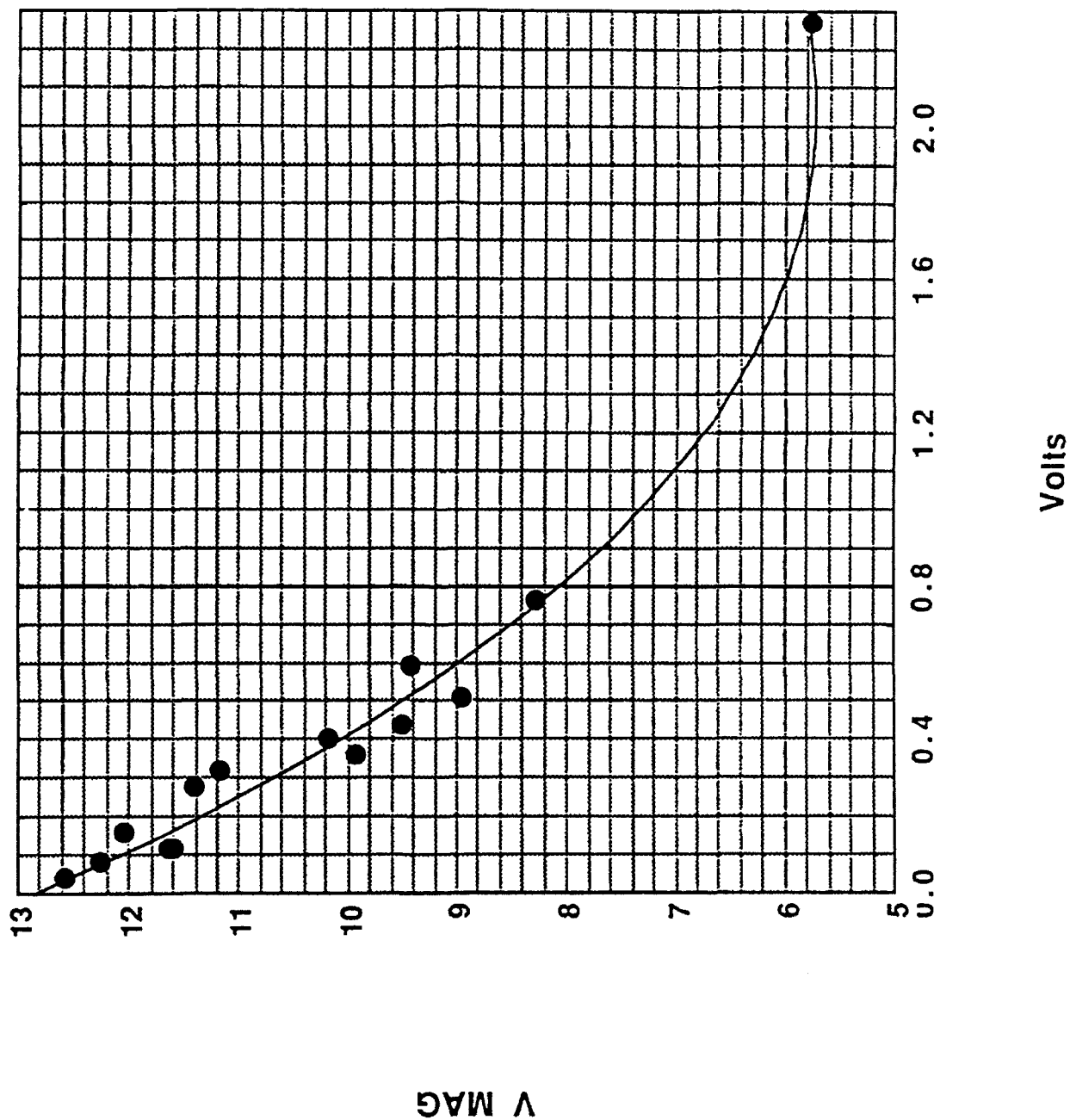
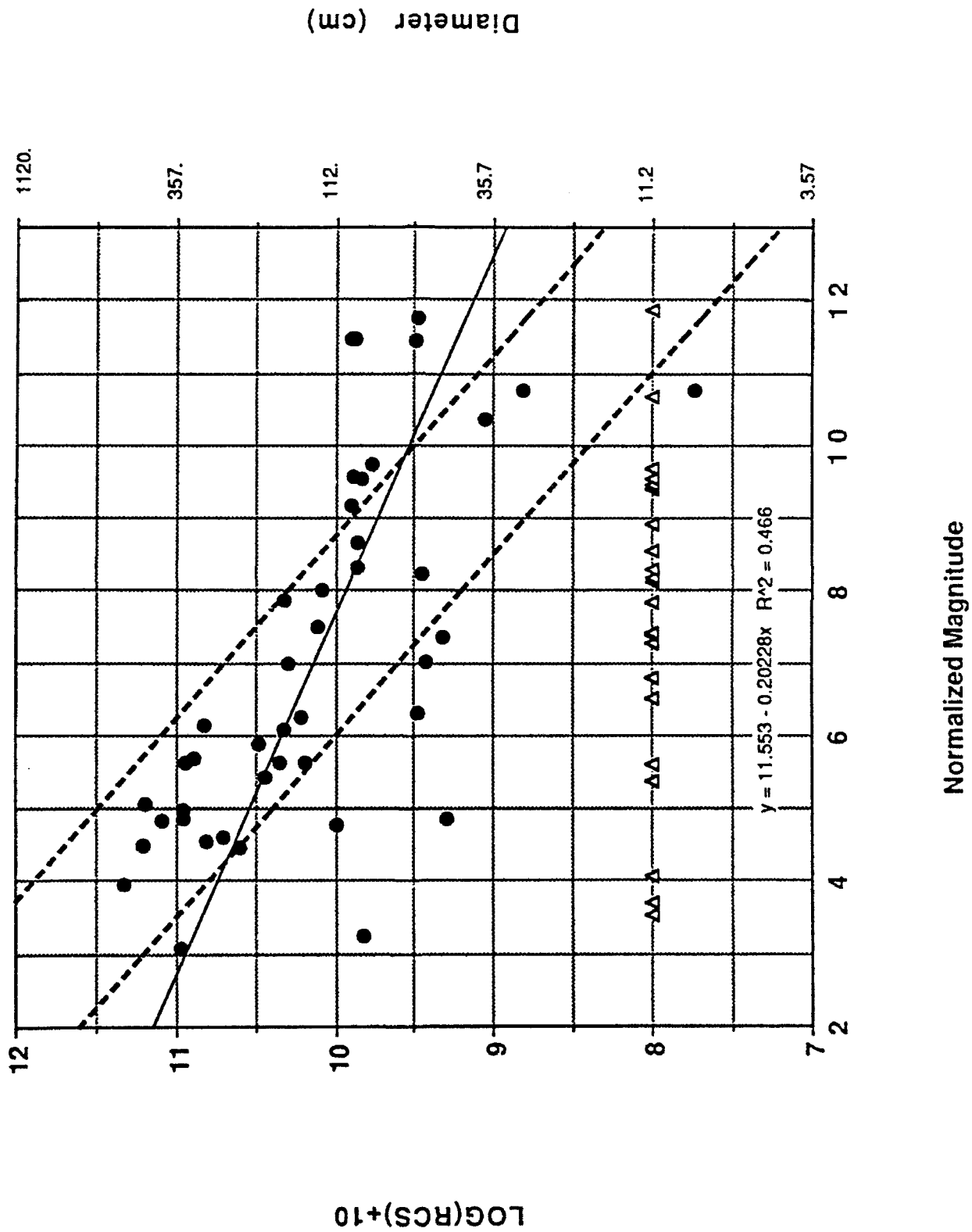


FIGURE 3: DEBRIS RESULTS



# Real Time Orbit Determination of Orbital Space Debris

S. D. Kuo (Air Force Maui Optical Station, PL/OL-YY)

## ABSTRACT

The Air Force Maui Optical Station (AMOS) is currently cataloging pieces of space debris using the GEODSS 24 inch auxiliary telescope with a 6 degree field of view. A new method has been implemented that permits real time determination of the orbital element set of a previously uncataloged piece of debris. Using the Prototype AMOS Computer Control System (PACCS), two observation points are recorded when a piece of debris passes through the auxiliary telescope field of view. These two observation points are fit to a circular orbit and an estimated slant range is obtained. Using the range, the azimuth (az), and elevation (el) of the observation points, a state vector can be estimated. This vector is then propagated and fed into PACCS which then generates an orbital track for the Beam Director/Tracker (BD/T) mount. The BD/T then follows this track and acquires the debris with its one degree field of view camera. The operator then brings the debris onto the boresight camera and takes position readings to update the track file. After several readings along the track, a very accurate element set can be generated for this piece of debris.

## 1. Introduction

The Air Force Maui Optical Station (AMOS) has been tasked to detect, track, and catalog pieces of space debris as part of the ongoing Air Force Space Command orbital debris measurement program. A new method has been developed using the GEODSS auxiliary telescope (Aux) to make real time orbital estimates of any pieces of debris that come through the field of view. Based on these estimates, a second mount at AMOS, the Beam Director/Tracker (BD/T), can be slewed along the track to acquire the debris. The BD/T can then generate an updated state vector of the target based on Kalman filter marks of the debris position. This whole process of handing off from GEODSS to the BD/T can occur within 10 seconds after the debris passes through the Aux and is done by a single operator (excluding the GEODSS operator).

## 2. Theory

The initial estimation of the orbital parameters is determined from two optical observation points and the time for the debris to cross the two points. These points are in the topocentric coordinate frame (azimuth and elevation) and can be fitted to a circular orbit. This algorithm was developed by Dr. John Lambert of Rockwell Power Systems and sets the orbit radius of the debris equal to the earth's radius and increases it until the calculated radius and its earth centered angular rate is equal to the observed rate.

Using Lambert's algorithm we obtain the estimated circular orbit radius  $R$ , the earth centered position vectors  $r_1$  and  $r_2$ , the orbital arc  $\Psi$  transversed between the two observation points, the latitude and site-relative longitude of the debris sub-points  $lat_1 lon_1$  and  $lat_2 lon_2$ , and the slant range from the site to the debris  $D_1$  and  $D_2$  (see Figure 1).

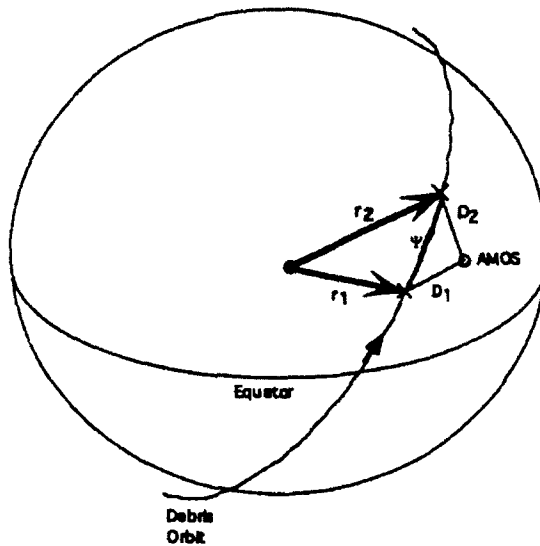


Figure 1. Values Determined from Circular Orbit Approximation

While only the slant range is used for calculating the estimated track for the BD/T, it is still useful to generate an initial estimate of the the 2-line element set based on the circular orbit approximation.

The inclination can be determined from the unit vector  $N$  and the unit vector  $k$  in the earth centered inertial (ECI) coordinate frame (the  $z$ -axis pointing to the North Pole).  $N$  is the unit vector normal to the orbital plane and is the cross product of the position vectors

$$N = r_1 \times r_2 / (R^2 \sin \psi) \quad (1)$$

and inclination  $i$  is the angle between  $N$  and  $k$ .

$$i = \arccos(N \cdot k) \quad (2)$$

The mean motion  $n$  can be found using the orbit radius  $R$

$$n = (\mu / 2\pi) R^{3/2} \quad (3)$$

where  $\mu$  is the gravitational parameter.

The mean anomaly  $M$  at the second observation point can be found using the debris sub-points. Using spherical geometry and the law of sines we see from Figure 2

$$M = \arcsin \left( \frac{\sin(\text{lat}_2) \sin(\pi/2)}{\sin(i)} \right) \quad (4)$$

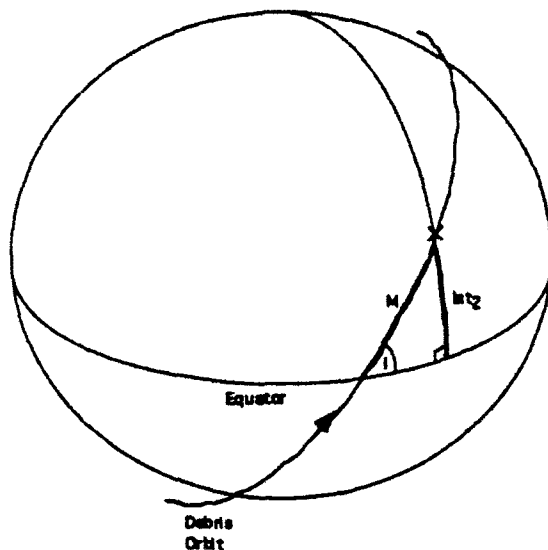


Figure 2. Determination of Mean Anomaly

Since the orbit is circular, eccentricity is 0 and the argument of perigee is undefined (set to 0 in the code). The epoch time is that of the second observation point and the drag terms are set to zero.

The only remaining element that needs to be found is the right ascension of node (ran)

$$\text{ran} = \text{lst} + \text{lon}_2 + \Delta\lambda \quad (5)$$

where lst is the local sidereal time and  $\Delta\lambda$  is the angular distance along the equator from the debris sub latitude point to the ran. Again using the law of sines and referring to Figure 3

$$\Delta\lambda = \arcsin \left( \frac{\sin(M) \cos(i)}{\cos(\text{lat}_2)} \right) \quad (6)$$

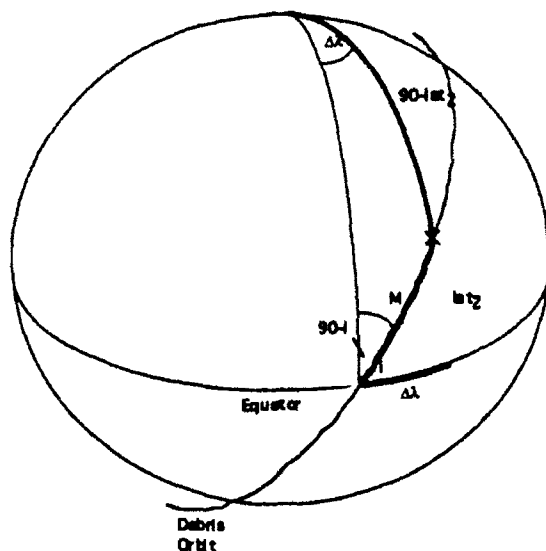


Figure 3. Determination of  $\Delta\lambda$  for Right Ascension of Node

The sign value of  $\Delta\lambda$  depends on three conditions: if the debris passing over the site is ascending/descending, posigrade/retrograde, and if the observation point was above/below the equator. Determination of each of these three conditions can be found by examining the 2 debris sub latitude and longitude points. The eight possible cases and the sign of  $\Delta\lambda$  in each one are illustrated in Figure 4. A check is made on the mean anomaly and RAN by adjusting them by 180 deg if the pass is descending.

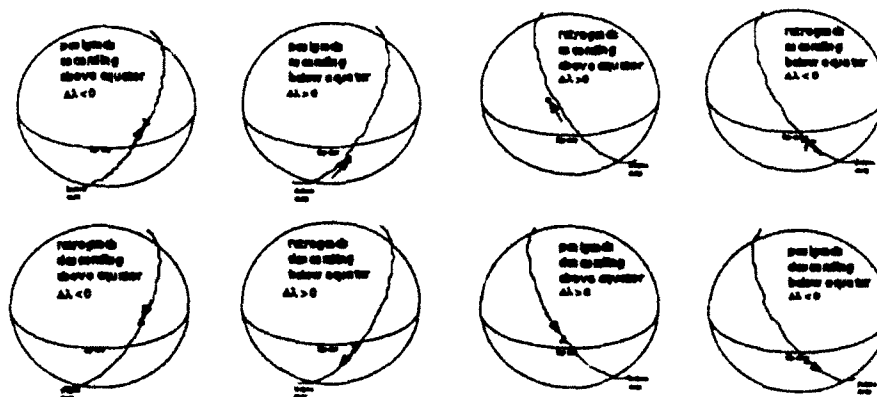


Figure 4. Determination of Sign of  $\Delta\lambda$  Based on Debris Orientation

To actually handoff the debris from GEODSS to the BD/T a state vector is estimated based on the two observation points. Using the estimated slant range  $D_1$  and  $D_2$  from above and the azimuth and elevation of the two points, an ECI position vector  $r_1$  and  $r_2$  can be calculated for the two points. By taking the difference between the two vectors and the elapsed time between the two observation points, the ECI velocity vector  $v_2$  can be found at the second point

$$v_2 = \frac{r_2 - r_1}{\Delta t} \quad (7)$$

The full ECI state vector can now be found at point 2 by combining  $r_2$  and  $v_2$  and then propagated using a third order Runge-Kutta two body orbit propagator.

Once the BD/T has acquired the debris based on the initial state vector estimation, update marks are taken on it after it has been centered on the boresight. These marks are put through a Kalman filter and then used to update the initial state vector for a better track fit (Myers). The final updated state vector can then be propagated forward or converted back into an element set in order to attempt acquisition on the next rev. For conversion back to an element set the algorithm used is outlined in "Fundamentals of Astrodynamics" (Bate, Mueller, White, p. 61) where the angular momentum, node, and the eccentricity vectors are computed from the ECI position and velocity vectors. The orbital elements are then computed from the angles between the various vectors. Due to the low eccentricity orbits of many pieces of debris, the eccentricity vectors were normalized by the eccentricity  $e$  as determined by the specific mechanical energy  $T$

$$T = \frac{V^2}{2} - \frac{\mu}{R} \quad (8)$$

$$e = \sqrt{1 + \frac{2TH^2}{\mu^2}} \quad (9)$$

where  $R$ ,  $V$ , and  $H$  are the position, velocity, and angular momentum vectors, respectively.

### 3. Equipment and Procedure

GEODSS and AMOS are located on top of Mt. Haleakala on the Island of Maui and are run by AF Space Command and the Phillips Laboratory, respectively. The GEODSS telescope used for the debris observation is a folded Schmidt optical system with a 15-inch aperture on an equatorial mount. A silicon intensified target (SIT) Vidicon tube is used and has a diagonal field of view (FOV) of  $6^\circ$ . The tracking mount used is the 80 cm Cassegrain AMOS BD/T and has mounted on it a  $5^\circ$  FOV intensified SIT (ISIT)

boresight camera behind the tertiary mirror and a  $1^\circ$  FOV acquisition camera mounted to the side of the mount. The mount control system used to drive the BD/T is the Prototype AMOS Computer Control Systems (PACCS). It uses a Silicon Graphics 4D/440 multi-processor workstation as well as a PIXAR image processing computer. A 386PC digitizes the incoming Aux video and overlays a crosshair and mouse cursor on it for display to the operator.

After the Aux is positioned at its fixed azimuth and elevation stare angles, the BD/T is also set to the same angle. When the operator observes the debris passing through the Aux, he moves the mouse cursor and takes two observation points. For the highest probability of handoff to the BD/T the first point should be near the entry point and the second near the exit point. The azimuth and elevation of each observation point is determined by the pixel offset of the cursor from the crosshairs. Since the crosshair is boresighted with the fixed azimuth and elevation the Aux is pointing at, and applying the appropriate plate scale calibration and coordinate transformation from right ascension-declination (ra dec) to az el, the two points can each be assigned an az el position. After the second point has been taken and the estimated state vector calculated, the operator takes control of the BD/T and attempts

acquisition on the 1° camera. By putting offsets into the mount position, the debris is centered on the boresight camera and marks taken on it. Marks are taken for as long as the debris is visible in the boresight camera and fed into the Kalman filter to determine a final ECI state vector. If the debris is bright enough, the PIXAR video tracker may be used to keep it centered on boresight automatically.

#### 4. Results

Since this tracking system is in the developmental stage, tests have only been done against satellites and no pieces of debris have been acquired yet. To test the handoff from GEODSS to the BD/T the Aux was positioned to an angle where a known satellite was going to pass through. Against the approximately 30 satellites tested, 60% of them were handed off to the BD/T. These were then tracked for the rest of the pass using Kalman marks to update the state vector.

Originally it was thought that the element set generated by the circular orbit approximation would be sufficient to for the BD/T to track with. However when propagated using GP4 the track was far enough off that the BD/T would not have acquired it.

Table 1 shows an actual element set and the one generated using the circular orbit approximation based on the two observation points.

Table 1. Comparison of Actual vs Estimated Orbital Elements

	Actual	Circular Approximation	Track w/ Kalman Marks
Inclination (deg)	82.5522	84.35291	82.5643
Eccentricity (deg)	0.0017474	0	0.004277
Right Ascension of Node (deg)	256.2581	253.126365	254.42313
Argument of Perigee (deg)	76.7709	n/a	77.8057
Mean Motion (rev/day)	13.16009284	12.72936	13.241272
Perigee Height (km)	1186	1370	1136
Apogee Height (km)	1213	1370	1201
Period (min)	109.42	113.1243	108.75

Since the orbit of the satellite has a low eccentricity (.001) most of the terms are in good agreement. The ECI state vector that was then generated from the two observation points was then propagated out as a track file for handoff to the BD/T. Figure 5 compares the actual track against the estimated one in azimuth, elevation,



and their root sum square (RSS).

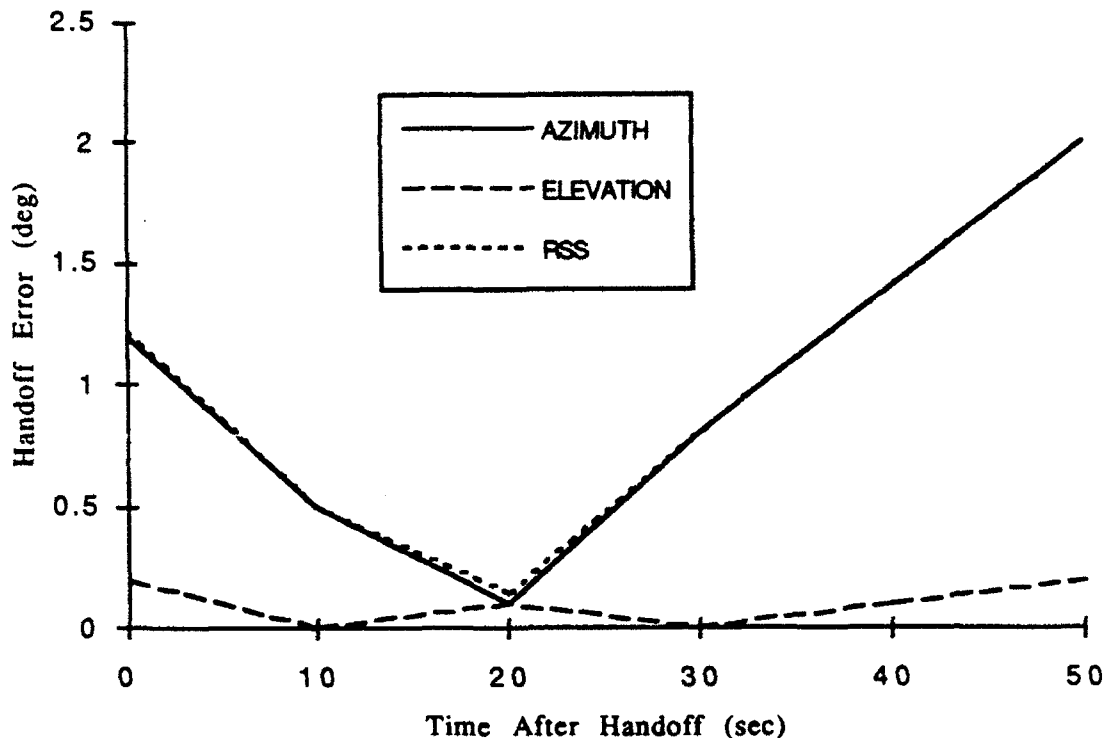


Figure 5. GEODSS to BD/T Handoff Error

If no corrections are made to the estimated track the satellite would stay within the BD/T acquisition camera ( $1^\circ$  FOV) for just about 30 seconds. After the target was centered on the boresight TV, 43 Kalman marks were taken to update the state vector over a 12 deg orbital arc. Table 1 shows the element set transformed from the state vector for the satellite. All the elements have been improved over the initial estimation from the circular orbit approximation. What remains to be seen is whether this is accurate enough to reacquire the satellite on the next rev. Based on the difference between the actual and estimated (from the state vector) mean motion, there will be a  $\pm 20$  sec along orbit error.

## 5. Conclusion

There is now a capability at AMOS to chase debris observed passing through the GEODSS AUX by generating an estimated state vector and passing it on to the BD/T. By being able to obtain a longer observation period with the BD/T better orbital information can be obtained on the debris. While no debris or test satellites have been acquired on the next rev, there will a concerted effort to do this in the coming months. Based on the comparison between the actual and estimated element sets of a test satellite it should be possible to pre-position the AUX and watch the debris pass through on the next rev (assuming it is still lit). If this occurs another handoff can be attempted to the BD/T. With another track on the second rev it should be possible to generate an extremely accurate element set on the debris. One advantage of this

system is that the AUX can continue in its stare mode to look for other debris while the BD/T tracks the debris that was handed off to it. Future work will use multiple chase mounts working with the single AUX video.

#### 6. Acknowledgements

I would like to thank the following people at Rockwell Power Systems for assisting me on this project: Dr John Lambert, John Africano, and Richard Jessop of RPS Colorado Springs and Wes Freiwald, Bob Brem, and Dr. Ken Kissell of RPS Maui. The mount control software was developed by Don Brown of Textron Defense Systems and Don Fronterhouse of Strategic Simulations, Inc.

#### 7. References

1. Lambert, John. "Circular Orbit Determination From Two Angular Position Observations." Rockwell Power Systems Colorado Springs. 1992
2. Myers, W. L. "AMOS Trajectory Estimator Simulation." AVCO Everet. 1972
3. Bate R., Mueller, D., and White, J. Fundamentals of Astrodynamics. Dover Publications, Inc. 1971.

## Surveillance for Comets and Asteroids Potentially Hazardous to the Earth

B.G. Marsden (Harvard-Smithsonian Center for Astrophysics)

Although comets, meteors and even meteorites were obviously known to ancient civilizations, an appreciation of coherent connections among these phenomena has developed surprisingly recently. All were widely believed to be events occurring in the atmosphere, and—at least in the western world—thought was strongly influenced by the ideas of Aristotle, which held that they were originally produced by evaporation of material from the earth. The thought of comets as celestial portents seems to have developed in several different traditions, although maleficence was generally considered symbolic, rather than physical.

The Chinese were particularly meticulous about recording these phenomena, and a report in the year 616 discussed the fall of a meteorite on a rebel camp, where it crushed more than ten people to death.

In Europe, however, there was far less enlightenment. The latter half of the fifteenth century brought scientific attempts to make parallactic determinations of the distances of comets, as well as the earliest preservation of a meteorite observed to fall there. However, the parallactic measurements seem to have served only to support the Aristotelian philosophy, and subsequent centuries brought denials that stones fell from the sky at all.

European enlightenment required several more steps: Tycho Brahe's demonstration that the comet of 1577 had to be farther away than the moon, Isaac Newton's demonstration that the motion of the comet of 1680 was consistent with the law of gravitation, Edmond Halley's 1714 suggestion that the high speeds of meteors suggested the injection of extraterrestrial material into the atmosphere, Ernst Chladni's 1794 demonstration that the existence of iron meteorites seemed also to require an extraterrestrial origin, and Edward Howard's 1801 chemical analysis showing that several stony meteorites must have had a very similar origin.

The year 1801 also brought the discovery of the first asteroid. With their general confinement to the region between Mars and Jupiter, the asteroids were not obviously immediate candidates for association with comets, meteors or meteorites, but subsequent research would change this situation.

The idea that comets might strike the earth, and to do so with devastating results, seems first to have been considered by Jakob Bernoulli, who in 1682 made a completely nonsensical prediction that the 1680 comet would do so in 1719. In an equally nonsensical publication, William Whiston in 1696 discussed the possibility that a cometary near miss was responsible for the Deluge; he later also selected the 1680 comet as the one responsible and—using the erroneous revolution period supposed by Halley for this comet—predicted the end of the world at the comet's next return in 2255. In a more serious paper presented to the Paris Academy in 1773, Joseph Lalande discussed the possibility of collisions between comets and the earth and caused an unfortunate scare that such an event was imminent. In 1777 Anders Lexell showed that a comet observed seven years earlier had made what is still the record confirmed closest distance to which a comet is known to have approached the earth, little more than 2 million km.

The magnificent display of Leonid meteors in the eastern U.S. in November 1833 removed all doubt of an extraterrestrial origin, showing clearly that the Leonids had to be in orbit about the sun. Denison Olmsted conceived the idea that they consisted of a particles forming some kind of nebulous "comet". His deduction, from the fact that Leonids came in neighboring Novembers, that the revolution period was a submultiple of one year, specifically half a year, seemed unlikely, particularly with the realization soon afterward that the Perseid meteors observed each August behaved in much the same way. Given that there had been another great Leonid display in 1799, Wilhelm Olbers suggested in 1837 that the period of the Leonid clump might be 34 years, which is close to the truth. It was Olbers who suggested that the shape of the tail of the comet of 1811 indicated the presence of some kind of repulsive force in comets, a hypothesis later echoed by Friedrich Bessel with regard to Halley's Comet in 1835. In 1839 Adolph Erman first proposed the modern notion that meteoric material essentially stretches all around an orbit, which the earth could then intersect annually. No immediate connection seems to have been made between these thoughts, nor was it seriously considered at the time that reaction to the Olbers-Bessel force could be responsible for the nongravitational influence established by Johann Encke as decreasing the revolution period of the comet that now bears his name (and thought by him to be due to the comet's passage through a resisting medium), although Josef Morstadt did relate the Leonid meteor stream to material from the tail of a comet—but not the correct comet. The comet he did consider was Biela's, the observed break-up of which was another manifestation of the kind of process that produces meteors—as well as an indication that there can be more than one dangerous object in essentially the same earth-approaching orbit.

The first direct—and correct—connection between a meteor stream and a comet came in 1866, when Giovanni Schiaparelli showed that the Perseids moved in precisely the orbit of P/Swift-Tuttle, a comet discovered four years earlier and determined to have a revolution period of rather more than a century. Other comet-meteor associations were soon forthcoming. In 1873 the asteroid Aethra was found to cross the orbit of Mars, while with the discovery of Eros in 1898 an asteroid was known that could regularly approach the earth to within some 25 million km. With the introduction of photography as a discovery tool, the 1890s also saw greater systematization of searches for both asteroids and comets.

At its discovery in 1913 many observers were prepared to dismiss P/Neujmin 1 as an asteroid, although under very careful scrutiny evidence for a coma was detected. When Hidalgo was found seven years later there was no such immediate scrutiny, although more recent observations have not shown any direct reason to drop its asteroidal appellation in favor of a cometary one. But the two objects have rather similar orbits with revolution periods somewhat larger than that of Jupiter and perihelion distances somewhat larger than the aphelion distance of Mars.

In 1927 P/Pons-Winnecke passed some 5 million km from the earth, the closest ever predicted in advance for a comet, and it afforded Fernand Baldet the opportunity of scrutinizing its central region, both micrometrically and photometrically; the latter technique made it probable that, although a comet's coma may extend for hundreds of thousands of km, P/Pons-Winnecke did not have a solid nucleus as large as 0.6 km across. In that same year, Russian scientists first visited the site at Tunguska where an enormous atmospheric blast 19 years earlier had knocked down trees for in the taiga forest for several tens of kilometers

around; an early hypothesis was that the event was due to an interaction with a small comet. In 1932 there came the discovery of Apollo, the first asteroid (of the order of 1 km across) known to cross the orbit of the earth and clearly to be capable of a collision, and within five years the searches had also produced Adonis and Hermes.

It may be difficult to appreciate the points now, but around the year 1950 there were still two rather widespread, but completely erroneous, beliefs. One was that comets consisted solely of meteoric particles, i.e., that there was no solid nucleus. The other was that the craters on the moon, as well as terrestrial craters like Meteor Crater in Arizona, were volcanic in origin. The former belief may be reasonable if one accepts that comets can accrete material and does not try to interpret the observed cometary spectra in any detail; the latter belief has merit if one accepts the former, regards meteorites as exclusively coming from asteroids, and does not consider earth-crossing asteroids to be either particularly numerous or in any way related to comets.

While Fred Whipple's development of the icy-conglomerate model provided an important turning point in the understanding of comets, this was only part of the issue. The model could explain spectra and nongravitational effects on cometary motions, but it could still leave cometary nuclei with insufficient rigidity to yield meteorites. The Prairie network of cameras established to triangulate on tracks of bright fireballs in order to search for resulting meteorites indeed yielded many fireballs but only one stony meteorite. As for the meteoritic nature of craters, Eugene Shoemaker concluded this in the Arizona example by appreciating that the fusion of silica glass on its floor from quartz required temperatures substantially higher than those of any lava flows; the observed fall of the Sikhote Alin iron meteorite in 1947 also helped the cause, and Ralph Baldwin produced a convincing case for the impact nature of the lunar craters. The rapidly increasing discovery rate of asteroids of Apollo type, on the one hand invited comparisons of their reflectance spectra with those of main-belt asteroids and the association with meteorites of various types, including irons; while in other cases it rendered support to the hypothesis that some of these objects are defunct cometary nuclei, an idea discussed in some detail by Ernst Öpik around 1963.

The possible asteroid-comet connection remains confused. "Asteroidal" comets like P/Neujmin 1 are rarities in that their motions are not affected by detectable nongravitational forces. The asteroid Phaethon, which goes closer to the sun than any other known, was recognized in 1983 as the parent of the Geminid meteor stream. The as-yet-unnamed asteroid (4015) 1979 VA was identified in 1992 with P/Wilson-Harrington, an object that was clearly of cometary appearance on the two exposures on its discovery night in 1949 but that has otherwise appeared completely asteroidal. Some meteorites, notably a class of carbonaceous chondrites, are considered by many to be from comets. No meteorite is ever known to have fallen during a meteor shower.

A recent publication by Chris Chyba makes it rather clear that, when proper allowance is made for aerodynamic drag, the object that produced the Tunguska event in 1908 was not cometary, but a typical stony asteroidal object originally some 60 m across. It is indicated that a Tunguska-type explosion is a common fate for stony asteroids of around this size, irrespective of the angle of incidence. Vertical entry would make the explosion closer to the ground, and a somewhat larger object could reach the ground. The estimated energy of the

Tunguska event, some 15 megatons, seems to be comparable to that of the Meteor Crater event, but the higher density and strength of an iron object allow it to strike the surface. It is considered possible, though unlikely, that Tunguska was more of a carbonaceous origin, but cometary origin is now ruled out, for a low-density, low-strength object would safely lose its energy entirely to ablation much higher in the atmosphere.

"Tunguska" events are believed to occur every century or two, and there are perhaps a million asteroids in the appropriate size range. For a given impactor size iron objects constitute perhaps 3 percent of the whole; it is estimated that Meteor Crater occurred some 50 thousand years ago. While these events obviously produce an enormous amount of local damage, computations by Brian Toon indicate that impactors must be about 1 km or more across in order to produce truly global damage. In such a case the danger to human life would come mainly from starvation, as the agricultural cycle is disrupted for an extended time as the material composing the objects pervades the atmosphere. This effect would be much the same for an asteroidal impact on the ground and for the disruption of a comet in the atmosphere. There must currently be some 3000 potential impactors down to 1 km across, perhaps 5 percent of them short-period comets, and impacts can be expected to occur at intervals of hundreds of thousands of years. The supply of impactors is easily maintained, at least in the cometary (or ex-cometary) case, by perturbations by Jupiter and the other outer planets on objects in much larger orbits. The supply mechanism in the asteroidal case is not so clear, although Jack Wisdom's study of chaotic motion indicates a likely source in the main belt where revolution periods are approximately one-third that of Jupiter. A small fraction of the impactors would be long-period comets, but the continuous supply from the outer part of the solar system makes it meaningless to speak about their number.

Finally, there is the type of impact that produces mass extinctions of species. These are objects, probably mainly intermediate-period and long-period comets, 10 km and more in diameter, and that strike the earth at intervals of tens of millions of years.

In the case of the short-period objects, with revolution periods of a few years and their aphelia generally out to around the orbit of Jupiter, there are likely to be numerous opportunities for discovery before the devastating strike. Thanks mainly to the systematic photographic searches begun by Shoemaker and Eleanor Helin with the wide-field Schmidt telescopes at Palomar in the early 1970s (but since 1980 the searches have been separate programs), we now know about 100, or perhaps 3 percent, of the potential earth impactors 1 km across and more. Another 100 or so smaller objects are known, in some instances with diameters as small as 10 m, but these obviously represent an almost negligible fraction of the potential Tunguskas. Most of the very smallest objects have been discovered in the Spacewatch Project. Conceived and largely executed by Tom Gehrels at the University of Arizona, Spacewatch is a real-time, scanning-CCD, survey with a 70-year-old, 0.9-m telescope at Kitt Peak. Although Spacewatch is much more sensitive than photographic searches are to faint objects close to us and moving rapidly across the sky, its small scan field puts it at a disadvantage as regards sky coverage, and in a given interval of time Spacewatch covers only one-tenth as much sky as the Palomar searches do. The fourth most active search program at the present time is carried out at the Anglo-Australian Observatory in New South Wales and consists of the examination of very deep Schmidt plates taken for other purposes.

The mere act of discovery of an object counts for naught if the object is not also followed up with further astrometric observations and orbit computations—a progressive process that can also usefully involve the identification of much earlier observations, either directly in the historic record or by re-examination of past photographic plates. Physical observations are also very desirable in order to learn something about the nature of the enemy.

All four search programs, as well as the follow-up activities, are carried out on shoestring budgets; the Anglo-Australian observer, for example, has technically been unemployed since the end of 1992. At the request of the U.S. Congress, NASA examined ways by which the rate of discoveries of near-earth objects could be substantially increased. The NASA study recommended the construction of six to eight new telescopes of aperture 2-3 m and 2-3-degree usable field, with CCD detectors and image-processing systems capable of recording moving objects down to magnitude 22.

Equally distributed in both hemispheres of the earth and suitably coordinated, this "Spaceguard" survey would be able to observe many of the near-earth objects around aphelion, where they spend most of their time. Generally confined to observe in the region of the sky extending 30 degrees on each side of the opposition point in longitude and 60 degrees on each side in latitude, Spaceguard would yield well over 90-percent of the objects more than 1 km across in the course of a 25-year search. Completeness would be to more than 60 percent for 0.5-km objects. The total cost of construction and operation of the survey for 25 years is estimated as less than \$300 million. If an object is recognized to be on a collision course with the earth, it is likely that there would be considerable notice—certainly decades, and probably centuries or more. An advance space mission to the object could presumably ensure that the object's velocity is changed by the millimeters per second necessary to avoid earth impact.

Spaceguard would also contribute to the discovery of smaller objects when they are in the vicinity of the earth, but it would have to continue long beyond 25 years in order to find a useful fraction of the Tunguska-sized objects. One unexpected hit with substantial local damage during a 100-year survey would in fact be rather probable.

The continuing survey would also be desirable for the long-period comets, where there is essentially no chance of discovery more than two years before impact. Chances are good that discovery of a comet likely to do global damage could be made at least 100 days before impact, however, and this is also thought sufficient to allow the object to be deflected. Although the chance of a hit by a long-period comet is small compared to a hit by a comparably-sized short-period object, it is important to note that more than a quarter of the long-period cometary impactors—mainly those with orbits nearly perpendicular to the earth's—would never be in the Spaceguard opposition search field. Alleviation of this problem requires extensive augmentation of the field, and this could well involve a three-fold increase in the number of telescopes used. With regard to the asteroids, we can also consider augmenting the search field to discover more of those objects with aphelia only slightly beyond or even at the earth's orbit and that are therefore rarely, if ever, at opposition.

The recent fuss concerning the possibility that the Perseid comet P/Swift-Tuttle might hit the earth in 2126 got rather out of hand, but the example is a particularly interesting

one. Although orbit determinations from the observations in 1862 suggested that this comet would return within a year or two of 1981, and certainly no later than 1986, it did not in fact reappear until 1992. This possibility had been anticipated in view of a suggested identity of the comet with one observed in 1737, but the new representation of the orbit shows severe systematic departures from the 1862 observations. Since the minimum separation of the orbits of the comet and the earth at the next return is only 400 thousand km, and since reasonable uncertainty in the comet's nongravitational parameters seemed to include the close approach date, it was appropriate to draw attention to the need for further observations. Further observations have been forthcoming, but the most significant of them were from the distant past, namely, in A.D. 188 and 69 B.C. While the short-term 1862 problem remains, the essential features of the long-term motion over the past two millennia are now understood. It is therefore very likely that nongravitational forces will not act to bring an earth encounter in 2126 or at any other time during the next millennium. Sample computations do indicate the possibility of interesting approaches by this comet for more than ten thousand years in the future, and with an impact velocity of 60 km/s and a supposed nuclear size of 10 km or so, P/Swift-Tuttle is therefore a potential long-term threat in the species-extinction class.



Pages 219 to 228 are intentionally left blank.

## Signal Processing and Interference Mitigation Strategies in NASA's High Resolution Microwave Survey Project Sky Survey\*

G.A. Zimmerman, E.T. Olsen, S.M. Levin, C.R. Backus, M.J. Grimm, S. Gulakis, and M.J. Klein (JPL)

The NASA High Resolution Microwave Survey (HRMS) project's Sky Survey is one of two complementary strategies NASA is using to search for evidence of extraterrestrial technology. The Sky Survey will observe a simultaneous dual-polarization bandpass of at least 300 MHz at a frequency resolution of 19 Hz as it performs its primary objective of searching the entire sky for extraterrestrial narrow band signals over the 1 GHz to 10 GHz frequency range. The system will be sensitive at the one-sigma level to RF inputs of from  $1 \times 10^{-21}$  to  $3 \times 10^{-21}$  Watts at the antenna feed. The survey will use existing radio telescopes, including NASA's Deep Space Network (DSN) 34-meter antennas for a search period of approximately 6 years. This paper will discuss the algorithms and hardware in the currently deployed 40 MHz Sky Survey prototype system and those planned for the full bandwidth operational system. The varying interference environment across the 1 to 10 GHz survey bandpass necessitates extensive interference mitigation. The RF system is designed with a wide dynamic range to pass the full bandwidth to the spectrum analyzer without spreading radio frequency interference (RFI) signals into uncorrupted frequencies. The planned operational system will use slightly different preprocessing from the prototype to produce a polyphase-DFT filter bank spectrometer whereas the prototype system uses a windowed FFT. The enhanced sidelobe rejection of the polyphase-DFT filter bank will not only isolate spectrally the effects of RFI, but will also improve the sensitivity of the system to weak signals in noise. The presence of RFI in the wideband input also challenges real-time dynamic noise power estimation, required for constant false-alarm-rate signal detection. An RFI-robust noise power estimate is computed using order statistics to sample the probability distribution function of the noise. Ordinarily, obtaining order statistics would require real-time sorting or histogramming of the input data stream, but the high data throughput in the HRMS Sky Survey makes this impractical. The prototype system employs a two-level hardware histogramming technique to obtain specific order statistics. In the operational system, however, by limiting the dynamic range within which the noise power is to be estimated, simple I/O efficient techniques based on a priori estimates can be used. Finally, RFI passing the detection filters is dealt with by a combination of software algorithms and frequency masking hardware.

\*This work was performed at the Jet Propulsion Laboratory, California Institute of Technology, under a contract by the National Aeronautics and Space Administration.

REPORT DOCUMENTATION PAGE			Form Approved OMB No. 0704-0188	
<small>Public reporting burden for this collection of information is estimated to average 1 hour per response, including the time for reviewing instructions, searching existing data sources, gathering and maintaining the data needed, and completing and reviewing the collection of information. Send comments regarding this burden estimate or any other aspect of this collection of information, including suggestions for reducing the burden, to Washington Headquarters Services, Directorate for Information Operations and Reports, 1215 Jefferson Davis Highway, Suite 1204, Arlington, VA 22202-4302, and to the Office of Management and Budget, Paperwork Reduction Project (0704-0188), Washington, DC 20503.</small>				
1. AGENCY USE ONLY (Leave blank)	2. REPORT DATE 1 April 1993	3. REPORT TYPE AND DATES COVERED Project Report		
4. TITLE AND SUBTITLE  Proceedings of the 1993 Space Surveillance Workshop		5. FUNDING NUMBERS  C — F19628-90-C-0002		
6. AUTHOR(S)  R.W. Miller and R. Sridharan (Editors)				
7. PERFORMING ORGANIZATION NAME(S) AND ADDRESS(ES)  Lincoln Laboratory, MIT P.O. Box 73 Lexington, MA 02173-9108		8. PERFORMING ORGANIZATION REPORT NUMBER  STK-206 Volume I		
9. SPONSORING/MONITORING AGENCY NAME(S) AND ADDRESS(ES)  ESC Hanscom Air Force Base Bedford, MA 01730		10. SPONSORING/MONITORING AGENCY REPORT NUMBER  ESC-TR-93-207		
11. SUPPLEMENTARY NOTES  None				
12a. DISTRIBUTION/AVAILABILITY STATEMENT  Approved for public release; distribution is unlimited.		12b. DISTRIBUTION CODE		
13. ABSTRACT (Maximum 200 words)  <p>The eleventh Annual Space Surveillance Workshop hosted by MIT Lincoln Laboratory was held 30–31 March and 1 April 1993. The purpose of this series of workshops is to provide a forum for the presentation and discussion of space surveillance issues.</p> <p>This <i>Proceedings</i> documents most of the presentations from this workshop. The papers contained were reproduced directly from copies supplied by their authors (with minor mechanical changes where necessary). It is hoped that this publication will enhance the utility of the workshop.</p>				
14. SUBJECT TERMS		15. NUMBER OF PAGES 240		16. PRICE CODE
17. SECURITY CLASSIFICATION OF REPORT Unclassified	18. SECURITY CLASSIFICATION OF THIS PAGE Unclassified	19. SECURITY CLASSIFICATION OF ABSTRACT Unclassified	20. LIMITATION OF ABSTRACT Same as report	